
Global Launcher Trajectory Optimization for Lunar Base Settlement

Master of Science Thesis



Antonio Pagano
May 3, 2010

Preface

Per quanto banale possa sembrare tutto quello che sar  detto in queste righe, mai banalit    stata tanto pi  lieta e soddisfacente. Con un italiano che comincia a vacillare (non che l'inglese sia un capolavoro, per carit ), la parte che attendevo con pi  ansia   arrivata. E' arrivato il momento di ringraziare, ma mai smetter  di farlo, tutte le persone che mi hanno permesso di realizzare questo "piccolo passo" nella mia vita e che spero abbia un grande peso nel mio futuro. Il grazie pi  grande va a mamma, pap  e alla mia sorellina che sono la base della mia vita e le fondamenta del mio futuro. Grazie a loro, moralmente ed economicamente, ho potuto seguire i miei sogni e sono stati il mio trampolino per tutto quello che verr  in seguito. Grazie per tutto quello che hanno fatto, per quello che mi hanno dato e insegnato. Vivere lontano da loro ha risollevato in me l'orgoglio di essere italiano e mi ha fatto scoprire la fortuna di avere delle tradizioni in cui la famiglia ha un ruolo predominante.

Un grazie immenso va alla mia ragazza, Valentina, che supportandomi e sopportandomi, ha reso meno pesante la distanza fra noi (quasi quanto i miei *achiulei*). Il suo supporto morale nei momenti pi  difficili   stato determinante come non mai. Un grazie ai miei amici palesi (i bitontini e i baresi sono stati adottati dai palesi per cui lo sono anch'essi) che hanno sopportato le mie pazzie e con cui ho passato momenti felici e di puro divertimento tra *magnate*, *cazzeggio*, Peroni e sfide iperultracompetitive di Pictionary.

Eventually, it is time to thank the people that have shared this international experience with me. Along my path, I have met mostly Italians and yet Portuguese, Spanish, Dutch, German, Indians students, that have broaden my point of view and showed me different cultures and ways to live and appreciate life. Wonderful moments have been lived with all of them that will never be forgotten.

I particularly would like to thank my supervisor Dr. ir. Erwin Mooij. He has taught me to be more critical towards engineering problems, has always pushed one step further and has shown me the way through the difficulties encountered. I would like to thank Ir. Ron Noomen for his enthusiasm in teaching and help with the orientation of my graduation project.

A special thank goes to my friends of "the ninth floor" with whom I shared the last 8 months. Coffee breaks, darts, table tennis matches, space bars, cakes and free food have characterized the social moments that our brains needed. I will miss all of them and all the moments-for-sharing-ideas.

The task I had to perform made me grow not only in the specific field I was involved, but also made me think about the issues related to it. Besides my academic growth, I am happy I have learned how to juggle and play a good table tennis. The first will make me earn some money in the streets when no jobs will be available and the second has become one of my favourite sports which I will try to play any place I go.

Concerning my empire, that faces the west side of the ninth floor and that is everyday attacked by Vivek's troops, from the east, it will live a moment of glory for the final assault. The eastern menace will be defeated and peace will reign in this world.

I would like to thank my body that supported me in the last period of this work by taking the burden of the tiredness that my will gave to it.

Besides these thanks and jokes, there is a series of statements I would like to share with you, readers, taken from the last lecture by Dr. Randolph Frederick Pausch, professor of computer science at Carnegie Mellon University. It is about achieving your childhood dreams:

- When you are screwing up and nobody is saying anything to you anymore, that means they gave up.
- Experience is what you get when you did not get what you wanted.
- The brick walls are there to give us a chance to show how badly we want something because brick walls are there to stop people who do not want it badly enough.

- Wait long enough and people will surprise and impress you.
- The best way to teach somebody something is to have them think they are learning something else.

I thank all the people I have met along my path, I am a bit of each of them.

Ringrazio tutti coloro che ho incontrato lungo il mio percorso, sono fatto di pezzettini di loro.

Antonio Pagano

Delft, April 11, 2010

Summary

In the past few years, a new spirit for the exploration of the Solar System spread among the space community. A new race to the Moon started in which each space agency was running on its own.

This goal is meant to be the first step for the exploration of new planets, first we should be able to familiarize with a new way of living in a different environment and adapting to it and testing new technology.

Besides that, at the rate we are consuming the terrestrial resources, we will soon run out of them. This will put us in front of a dramatic change in our life style. Moreover, it is not unlikely that an asteroid could impact the Earth, causing extinction for many species and difficulties to survive. Then, also for these unpredictable reasons, exploring and adapting to new planet environments is the goal for coming generations.

Following the new spirit, a project about a mission to the Moon was addressed by Mr. Ortega Ortega [2008], from ESA-ESTEC, in order to improve the development of the open source software Space Trajectory Analysis (STA). In fact, the project resulted in a feasibility study to assess a lunar mission to build a permanent lunar base.

The feasibility study is divided in three parts, that are, in execution order, the ascent of a launcher, the transfer from the Earth vicinity to the Moon and the lunar landing. In each phase, the focus is delivering the payload, that could either be cargo, crew or supplies, from the beginning of each phase to the end of it. Here, only the launching of the lunar payload into an orbit about the Earth will be dealt with. Therefore, the research question for this work is:

Is it possible, by means of existing launch vehicles, to set a permanent manned base on the South Pole of the Moon, before July 1, 2020?

Since bringing material to the Moon and building a base requires a big effort in launcher capability terms, the research will focus on the maximization of the payload mass for each launcher. The ascent trajectory problem originates from the fact that, in a launch, 97-98% of the total mass of the vehicle is structural and propellant mass. This means that only 2-3% can be used as payload and, at the same time, is the reason for which we strive for gaining every single kilo. The heaviest launch vehicles available today will be analyzed among which the Ariane 5, Proton, Atlas V, Delta IV and Vega.

In this thesis, the problem will be tackled by formulating it as an initial value problem (IVP), in which, given the launcher's initial conditions, the state vector is propagated by means of an integrator. During the flight, the vehicle will follow a guidance programme, expressed through mathematical laws whose parameters can be tuned. Moreover, the launcher will be subjected to constraints dictated by mechanical and thermal properties of the same. In order to find those trajectories that give the largest payload mass, an optimization method based on particle swarm (PSO) will be applied in order to find the best tuning of the guidance parameters, taking into account the constraints and the final orbit to be achieved. This step relies on the global optimization by using single and multi-objective ways.

The first step of the entire mission is to provide permanent communication between the astronauts on the Moon and the operation center on Earth. Two communication satellites in a Halo orbit around the Lagrangian point L_2 of the Earth-Moon system permits to have a complete coverage of the South Pole. The results show that Vega, for the three different parking orbit inclinations evaluated (5.5° , 28.5° and 51.6°), can inject 3,453 kg, 3,475 kg and 3,172 kg of payload. However, it is not possible to launch at a 5.5° orbit inclination as, from the analysis of the transfer to the Halo orbit, a payload mass of 3,491 kg is needed. Therefore, a final orbit inclination of 28.5° is chosen because the payload mass obtained is the highest and it offers also a safety margin about the mass involved.

Concerning the other launchers needed for the building phase of the lunar base, it is evident that Ariane 5 delivers the largest payload mass with 25 tons. The Atlas V, in the 552 version, and the Proton M follows with about 24 and 23 tons. The preliminary analysis for the Delta IV Heavy and the Atlas V HLV showed some leaks in the software and the particular deficiency to cope with several throttle strategies. Moreover, not much can be said from the results obtained from the optimizations of these two launchers since the optimization process was not successful.

The combined results from the analysis of the ascent, Earth-Moon transfer and landing phase (preliminary phase) show that a payload of about 4-5 tons can be delivered on the Moon.

The choice to rely on one launcher only for the complete mission is not wise. An assessment of the facilities and equipment needed for the base had already been performed. In the same study, the total mass obtained for the base (comprehensive of structure, rovers, etc.) was about 120 tons. From the results obtained, a rough estimation of the launches needed has been given resulting in 48 launches, 16 of which are manned, to be fulfilled in 4.5 years.

Actually, to build the lunar base where a huge effort mass-wise and time-wise is needed and it is advisable to use more than one launcher in order to keep a high rate of launching. In fact, a launch campaign may keep busy a launch site and pad for about 3 months. This would lead to a launch rate of 4 per year, whereas if two or three launchers are used, the rate can be up to 12 per year. Moreover, it is extremely recommended to perform such a mission in an international cooperation. This is also the best choice if one wants to build a lunar base in a limited time period.

Concerning the manned flights, the absence of a spacecraft able to host a crew to the Moon is a crucial point to the whole mission. Therefore, in order to assemble the base and accomplish the whole mission, it is mandatory to have such a capability.

Nomenclature

Latin Symbols

a	Semimajor axis	[m]
a_x	Acceleration along x-body axis	[m/s ²]
\mathbf{C}	Transformation matrix	[-]
C_D	Drag coefficient	[-]
C_L	Lift coefficient	[-]
D	Drag	[N]
E	Eccentric anomaly	[rad]
\mathbf{e}	Eccentricity vector	[-]
e	Eccentricity	[-]
e	Ellipticity	[-]
\mathbf{F}	Force vector	[N]
\mathbf{g}	Gravitational acceleration vector	[m/s ²]
\mathbf{h}	Angular momentum	[m ² /s]
h	Height	[m]
\mathbf{I}	Identity matrix	[-]
I_{sp}	Specific impulse	[s]
i	Inclination	[rad]
J_2	Gravity field harmonic	[-]
L	Lift	[N]
M	Mach number	[-]
m	Mass	[kg]
M	Mean anomaly	[rad]
\dot{Q}	Heat rate	[W/m ²]
q_{dyn}	Dynamic pressure	[N/m ²]
\mathbf{r}	Position vector	[m]
r	Modulus of position vector	[m]
R_E	Equatorial radius of the Earth	[m]
R_N	Nose radius	[m]
R_p	Polar radius of the Earth	[m]
R_s	Radius at the surface of the Earth	[m]
S_{ref}	Aerodynamic reference area	[m ²]
T	Thrust	[N]
t	Time	[s]
u, v, w	Cartesian velocity components	[m/s]
\mathbf{V}	Velocity vector	[m/s]
V_G	Modulus of groundspeed based velocity	[m/s]
X, Y, Z	Axes	[-]

Greek Symbols

α	Angle of attack	[rad]
β	Sideslip angle	[rad]
γ	Flight path angle	[rad]
δ	Geocentric latitude	[rad]
θ	Pitch angle	[rad]
θ	True anomaly	[rad]
λ	Geocentric longitude	[rad]
μ	Gravitation parameter	[m ³ /s ²]
ρ	Atmospheric density	[kg/m ³]
τ	Time of perigee passage	[s]
φ	Roll angle	[rad]
χ	Heading angle	[rad]
ψ	Yaw angle	[rad]
Ω	Right Ascension of the Ascending Node	[rad]
ω	Argument of pericenter	[rad]
ω_e	Rotational rate of the Earth	[rad/s]

Acronyms and Abbreviations

DA	Direct Ascent
DG-MOPSO	Double Grid Multi-Objective Particle Swarm Optimization
EM	Earth-Moon
ESA	European Space Agency
GA	Genetic Algorithm
ISS	International Space Station
LEO	Low Earth Orbit
LLO	Low Lunar Orbit
LOI	Lunar Orbit Injection
NSGA-II	Non Dominated Sorting Genetic Algorithm II
PAES	Pareto Archived Evolution Strategy
PSO	Particle Swarm Optimization
RAAN	Right Ascension of the Ascending Node
RSS	Root Sum Square
S/C	Spacecraft
TLI	Trans-Lunar Injection

Indices

0	Initial condition
A	Aerodynamic frame, groundspeed based
B	Body frame
cm	Center of mass
e	Earth
E	Equatorial
f	Final
G	Gravitational
G	Groundspeed based
I	Inertial planetocentric frame
p	Perifocal frame

p	Polar
r	Along position vector
R	Rotating planetocentric frame
s	Surface
T	Thrust
T	Trajectory frame, groundspeed based
V	Vehicle-centered horizontal frame
V	Velocity
x, y, z	Along X-, Y- and Z-axis
γ	Flight path angle
δ	Latitudinal direction
χ	Heading angle

Contents

1	Introduction	2
2	Moon Mission: scenarios and logistic aspects	6
2.1	Mission requirements	6
2.2	Mission scenario	7
2.3	Masses naming convention	9
2.4	Base and spaceport architecture	10
2.5	Launch capability	12
3	The dynamic system model	13
3.1	State-variable definitions	13
3.2	Reference frames	14
3.3	Transformations	18
3.4	Dynamic system model	24
3.5	Earth model	26
3.6	Aerodynamic forces	28
3.6.1	Drag	29
3.6.2	Lift	29
3.7	Propulsion system	30
3.8	Path constraints	32
3.8.1	Dynamic pressure	32
3.8.2	Bending load	33
3.8.3	Axial acceleration	34
3.8.4	Heat flux	34
3.8.5	Geographical constraints	35
4	Guidance programme	38
4.1	Initial conditions	39
4.2	Vertical Lift-off	39
4.3	Pitch turnover	40
4.4	Gravity turn	41
4.5	Bi-linear tangent law	41
4.6	Orbital coast phase and circularization burn	43
5	Optimization	45
5.1	The general optimization problem	45
5.2	Ascent trajectory optimization problem	46
5.3	Optimization techniques overview	46
5.4	Multi-objective optimization	48
5.5	Particle Swarm Optimization	48
5.6	Multi-objective optimizer	52
5.7	Setup of the optimizers	55
5.7.1	PSO	56

5.7.2	DG-MOPSO	56
5.8	Optimization of the launchers' parameters	57
6	Results	59
6.0.1	Final orbit	60
6.1	Vega launch for communication satellites	61
6.1.1	One-objective optimization results	61
6.1.2	Two-objectives optimization results	68
6.1.3	Three-objectives optimization results	70
6.1.4	Conclusions	72
6.2	Proton M	75
6.2.1	One-objective optimization results	75
6.2.2	Two-objective optimization results	78
6.2.3	Three-objective optimization results	79
6.2.4	Conclusions	89
6.3	Atlas V 552	90
6.3.1	One-objective optimization results	90
6.3.2	Two-objective optimization results	94
6.3.3	Three-objective optimization results	96
6.3.4	Conclusions	104
6.4	Ariane 5 ESC-A	104
6.4.1	One-objective optimization results	104
6.4.2	Two-objective optimization results	107
6.4.3	Three-objective optimization results	108
6.4.4	Conclusions	113
6.5	Delta IV Heavy: preliminary analysis	114
6.6	Atlas V HLV: preliminary analysis	117
6.7	Global overview	118
6.8	Launch schedule for the lunar base mission	122
7	Conclusions and Recommendations	125
7.1	Conclusions	125
7.2	Recommendations	128
	Bibliography	131
A	Aerodynamic data	136
A.1	The Near's <i>M3HAX</i> code	136
A.2	Drag: Ariane 5 and the Dnepr profile assumptions	137
A.3	Lift: USAF Missile DATCOM code	138
A.4	Sensitivity analysis	139
B	Launch vehicles data description and trajectory configuration settings	142
B.1	Vega	142
B.1.1	Property data	142
B.2	Proton M	142
B.2.1	Property data	142
B.3	Atlas V 552	143
B.3.1	Property data	143
B.4	Ariane 5 ESC-A	143
B.4.1	Property data	143
B.5	Delta IV Heavy	144
B.5.1	Property data	144
B.6	Atlas V HLV	144
B.6.1	Property data	144

C Detailed results	146
C.1 Proton M	146
C.1.1 Trajectories accuracy	146
C.1.2 Path constraints violations	147
C.1.3 Normalized path constraints violations	148
C.1.4 Three-objective optimization: 3D view	149
C.2 Atlas V 552	151
C.2.1 Trajectories accuracy	151
C.2.2 Path constraints violations	152
C.2.3 Normalized path constraints violations	153
C.2.4 Three-objective optimization: 3D view	156
C.3 Ariane 5 ESC-A	157
C.3.1 Trajectories accuracy	157
C.3.2 Path constraints violations	158
C.3.3 Normalized path constraints violations	160
C.3.4 Three-objective optimization: 3D view	161

List of Figures

2.1	Luna 16 orbit trajectory.	7
2.2	The International Space Station.	8
2.3	ATV-ISS rendezvous.	8
2.4	A mass breakdown for the crew expedition shows which elements are part of it, including the vehicle to return on Earth.	9
2.5	The cargo expeditions are the first to be flown to the Moon in order to place the material that will compose the base.	10
2.6	The supply expedition should provide goods for the living of the astronauts and tools and instruments, in case of damages and failures.	10
2.7	Configuration for the lunar base.	11
2.8	Spaceport configuration.	11
3.1	Orbital elements.	14
3.2	Cartesian and spherical components are depicted.	15
3.4	Perifocal reference frame [Hall, 2003].	15
3.3	Spherical components in a rotating frame [Mooij, 1997].	16
3.5	The inertial, rotating and vehicle-centered reference frame and the relation between each other is depicted [Mooij, 1997].	17
3.6	Euler transformation about the Z -axis of an angle α	18
3.7	Relation between the perifocal and the inertial Earth-centered frame [Shan, 2009].	19
3.8	Reference frames.	22
3.9	Orientation of the body frame with respect to the vehicle-centered horizontal frame.	23
3.10	Cartesian components.	26
3.11	Ariane 5 drag coefficient.	30
3.12	Solid propellant grain configuration.	31
3.13	Relation between the velocity vector and the body reference frame.	34
3.14	Importance of the radiative heat flux compared to the convective heat flux in the case of re-entry vehicles. Units are expressed in the Imperial system, [Anderson, 2001].	36
4.1	Pitch-over maneuver: the linear decrease and the following exponential decay is shown [Markl, 2001].	40
4.2	Pitch angle bi-linear tangent law.	42
5.1	Single and multi-peak functions.	47
5.2	Particle Swarm Optimization.	50
5.3	Example of double grid in a (two) objective space.	53
5.4	The flow chart depicts the multi-objective particle swarm optimizer on which the DG-MOPSO is based.	54
5.5	Comparison between different PSO inertia weight and confidence parameters during the evolution of the global best solution along the iterations.	55
5.6	Comparison between different PSO inertia weight and confidence parameters during the evolution of the constraint violations along the iterations.	56
5.7	Spiky pitch and yaw profile.	58

6.1	Possible types of trajectory to reach the Moon.	60
6.2	Final payload mass at 5.5° inclination.	65
6.3	Final payload mass for Vega launcher at different orbit inclinations resulting from the one-objective optimizations.	65
6.4	Vega: semimajor axis accuracies at three different final orbit inclinations.	69
6.5	Vega: eccentricity accuracies at three different final orbit inclinations.	70
6.6	Vega: effect of different aerodynamic configurations on the final eccentricity.	71
6.7	Vega: inclination accuracies at three different final orbit inclinations.	72
6.8	Vega: path constraints violations.	73
6.9	Vega: normalized path constraints. The normalization has been performed according to the different limits set per run.	74
6.10	Vega: two-objective optimization.	76
6.11	Vega: three-objective optimization, run 1.	77
6.12	Vega: three-objective optimization, run 2.	78
6.13	Vega: zoom of the 2D view of the Pareto surface shown in Fig. 6.12b. Solutions with a higher <i>RSS</i> of path constraints of the first group have a lower <i>RSS</i> of path constraints of the second group.	79
6.14	Vega: control history of the best solution found.	80
6.15	Vega: altitude-velocity plot for the best solution.	80
6.16	Proton M: optimal payload masses resulting from the runs.	83
6.17	Proton M: two-objective optimization runs. The plots show the Pareto fronts obtained for the four runs performed.	84
6.18	Proton M: three-objective optimization, run 1 Pareto front views.	86
6.19	Proton M: zoom of the 2D view of the Pareto surface shown in Fig. 6.18b. This detailed view shows that the solutions are not on the <i>x</i> -axis but very close to it.	86
6.20	Proton M: three-objective optimization, run 2 Pareto front views.	87
6.21	Proton M: three-objective optimization, run 3 Pareto front views.	87
6.22	Proton M: three-objective optimization, run 4 Pareto front views.	87
6.23	Proton M: three-objective optimization, run 5 Pareto front views.	88
6.24	Proton M: control history of the best solution found.	89
6.25	Proton M: altitude-velocity plot for the best solution.	90
6.26	Atlas V 552: real throttle profile for missions to LEO orbit, from [Lockheed Martin, 1999].	93
6.27	Atlas V 552: throttle profile from simulation.	93
6.28	Atlas V: summary of the payload masses obtained in the best trajectories from the one-objective optimization.	94
6.29	Atlas V: difference between optimal and non-optimal control parameter in the pitch over phase.	95
6.30	Pareto front of a constrained problem, [Deb et al., 2000].	96
6.31	Atlas V: results of the two-objective optimization, run 1 to 3. The second objective is the <i>RSS</i> of the orbital elements.	99
6.32	Atlas V: results of the two-objective optimization, run 4 and 5. The second objective is the <i>RSS</i> of path constraints violations.	100
6.33	Atlas V: three-objective optimization, run 1.	100
6.34	Atlas V: three-objective optimization, run 2.	101
6.35	Atlas V: three-objective optimization, run 3.	101
6.36	Atlas V: three-objective optimization, run 4.	101
6.37	Atlas V: three-objective optimization, run 5.	102
6.38	Atlas V: three-objective optimization, run 6.	103
6.39	Atlas V: three-objective optimization, run 7.	103
6.40	Atlas V 552: control history for the best solution.	104
6.41	Atlas V 552: altitude-velocity plot for the best solution.	105
6.42	Ariane 5, run 2. During the gravity turn, the launcher pitches up and then down.	106
6.43	Ariane 5: summary of the payload masses obtained from the one-objective optimization.	109
6.44	Ariane 5: Pareto fronts of the two-objective optimization runs.	111
6.45	Ariane 5: three-objective optimization, run 1.	112

6.46	Ariane 5: three-objective optimization, run 2.	113
6.47	Ariane 5: three-objective optimization, run 3.	113
6.48	Ariane 5: three-objective optimization, run 4.	114
6.49	Ariane 5: control history for the best trajectory.	114
6.50	Ariane 5: altitude-velocity plot for the best trajectory.	115
A.1	Drag coefficient versus Mach number profile computed using <i>M3HAX</i>	137
A.2	139
A.3	Comparison of the lift coefficient profiles. For the Ariane 5, it only concerns the central core. Attention has to be paid on the behaviour of the profiles.	141
C.1	Proton M: accuracy on the final semimajor axis.	146
C.2	Proton M: accuracy on the final eccentricity.	147
C.3	Proton M: accuracy on the final inclination.	147
C.4	Proton M: path constraint violations.	148
C.5	Proton M: normalized path constraint violations.	149
C.6	Proton M: three-objective optimization 3D view.	150
C.7	Atlas V 552: accuracy on the final semimajor axis.	151
C.8	Atlas V 552: accuracy on the final eccentricity.	151
C.9	Atlas V 552: accuracy on the final inclination.	152
C.10	Atlas V 552: path constraint violations.	153
C.11	Atlas V 552: normalized path constraint violations.	154
C.12	Atlas V 552: three-objective optimization 3D view.	156
C.13	Ariane 5: accuracy on the final semimajor axis.	157
C.14	Ariane 5: accuracy on the final eccentricity.	157
C.15	Ariane 5: accuracy on the final inclination.	158
C.16	Ariane 5: path constraint violations.	159
C.17	Ariane 5: normalized path constraint violations.	160
C.18	Ariane 5: three-objective optimization 3D view.	161

List of Tables

2.1	Mass breakdown for each module.	11
2.2	Total mass breakdown.	12
3.1	Reference surface.	30
3.2	Dynamic pressure.	33
3.3	Axial acceleration.	35
3.4	Nose cone radius.	36
3.5	Locations of launch sites.	37
4.1	Ascent trajectory guidance programme.	44
5.1	Number of nodes for throttle setting optimization.	57
5.2	Number of nodes for guidance optimization.	58
6.1	Number of runs performed for each launch vehicle.	59
6.2	Simulation plan considering the sensitivity analysis for the aerodynamic model of each launcher.	60
6.3	Vega: setup of the runs, launching into 5.5° inclination orbit.	62
6.4	Vega: a summary of the optimization runs is presented. The error on the final orbital elements are shown. Final orbit inclination is 5.5°	63
6.5	Vega: the setup of the runs, launching into 28.5° inclination orbit.	64
6.6	Vega: a summary of the optimization runs is presented. The error on the final orbital elements are shown. Final orbit inclination is 28.5°	66
6.7	Vega: the setup of the runs, launching into 51.6° inclination orbit.	67
6.8	Vega: a summary of the optimization runs is presented. The error on the final orbital elements are shown. Final orbit inclination is 51.6°	68
6.9	Vega: two-objectives optimization settings: final orbital elements and constraint limits.	71
6.10	Vega: payload masses for the best trajectories resulting from the two-objective optimizations. The green cells highlight the trajectories that satisfy the given tolerances on the final orbital elements according the criterion $RSS < 1$	75
6.11	Vega: three-objectives optimization settings: final orbital elements and constraints limits.	75
6.12	Vega: three-objective optimization. In run 1, only the best aerodynamic configuration manages to have a $RSS < 1$. Run 2 does not give any flyable trajectory.	79
6.13	Proton M: setup of the runs, launching into 51.6° inclination orbit. The final orbital elements, the relative tolerances and the path constraint limits are shown. Moreover, for each run, presence or coast arcs and circularization burn is indicated.	81
6.14	Proton M: results for the one-objective optimization.	82
6.15	Proton M: two-objectives optimization settings: final orbital elements and constraints limits.	83
6.16	Proton M: the results of the two-objective optimization runs are summarized.	85
6.17	Proton M: three-objectives optimization settings: final orbital elements and constraints limits.	85
6.18	Proton M: results of the three-objective optimization runs.	88
6.19	Atlas V: setup of the one-objective optimization runs.	91
6.20	Atlas V: results for the one-objective optimization.	92
6.21	Atlas V: Setup for two-objective optimization.	96

6.22	Atlas V: results of the two-objective optimization.	97
6.23	Atlas V: setup for the three-objective optimization runs. Orbital elements tolerances and path constraints are shown.	97
6.24	Atlas V: results of the three-objective optimization runs.	98
6.25	Ariane 5: setup of the single-objective optimization runs.	107
6.26	Ariane 5: results of the single-objective optimizations.	108
6.27	Ariane 5: setup of the two-objective optimization runs.	110
6.28	Ariane 5: results of the two-objective optimizations.	110
6.29	Ariane 5: setup of the three-objective optimization runs.	110
6.30	Ariane 5: results of the three-objective optimizations.	112
6.31	Delta IV Heavy: setup of the single-objective optimization runs for the lunar Hohmann transfer orbit.	115
6.32	Delta IV Heavy: results of the single-objective optimization runs for the lunar Hohmann transfer orbit.	116
6.33	Delta IV Heavy: setup of the single-objective optimization runs for the low Earth parking orbit.	116
6.34	Delta IV Heavy: setup of the single-objective optimization runs for the low Earth parking orbit.	117
6.35	Atlas V HLV: setup of the single-optimization runs for the lunar Hohmann transfer orbit.	118
6.36	Atlas V HLV: results of the single-optimization runs for the lunar Hohmann transfer orbit.	118
6.37	Atlas V HLV: setup of the single-optimization runs for the low Earth parking orbit.	119
6.38	Atlas V HLV: results of the single-optimization runs for the low Earth parking orbit.	119
6.39	Vega: best payload masses obtained at different orbit inclination. The solutions with an asterisk do not satisfy the path constraints or the orbital elements tolerances.	120
6.40	Best payload masses for the launchers. The solutions with an asterisk do not satisfy the path constraints or the orbital elements tolerances.	120
6.41	Vega: payload mass needed in LEO parking orbit for the Earth-Moon communication satellites [Zuccarelli, 2009].	120
6.42	ΔV budgets needed for each launcher according the transfer method used [Zuccarelli, 2009].	121
6.43	The propellant masses needed for each launcher are shown.	121
6.44	Vega: ΔV budgets and propellant masses needed for Earth-Moon transfer from each orbit inclination.	122
6.45	Payload masses available in low lunar orbit relative to Earth-Moon transfer method.	122
6.46	Launch schedule for the lunar mission to settle a permanent base on the South Pole of the Moon.	123
6.47	Schedule for the maintenance phase of the base.	124
7.1	Best payload masses for the launchers. The solutions with an asterisk do not satisfy the path constraints or the orbital elements tolerances.	125
7.2	Launch schedule for the lunar mission to settle a permanent base on the South Pole of the Moon.	127
7.3	Schedule for the maintenance phase of the base.	128
A.1	Launcher's components contribution to overall vehicle drag.	138
B.1	Vega characteristics.	142
B.2	Proton M characteristics.	143
B.3	Atlas V 552 characteristics.	143
B.4	Ariane 5 ESC-A characteristics.	144
B.5	Delta IV Heavy characteristics.	144
B.6	Atlas V HLV characteristics.	145

Chapter 1

Introduction

In the past few years, a new spirit for the exploration of the Solar System spread among the space community. A new race to the Moon started in which each space agency was running on its own.

Before proceeding, some reasons should be given about this renovated spirit of conquest. The official reason would be that, in order to be able to get to new planets, first we should be able to familiarize with a new way of living in a different environment and adapting to it and testing new technology.

On the other hand, one unofficial reason for which we should explore and colonize in the future other planets is that, at the rate we are consuming the terrestrial resources, we will soon run out of them. This will put us in front of a dramatic change in our life style. Moreover, it is not unlikely that an asteroid could impact the Earth, causing extinction for many species and difficulties to survive. Then, also for these unpredictable reasons, exploring and adapting to new planet environments is the goal for coming generations.

Besides these reasons about the revitalized push to explore new planets, this project exercise was addressed by [Ortega, 2008], from ESA-ESTEC, in order to improve the development of the open source software Space Trajectory Analysis (STA). In fact, the project resulted in a feasibility study to assess a lunar mission to build a permanent lunar base.

Moreover, after setting the base, the operational phase will start, that involves issues as maintenance, supply deliveries, etc.

The feasibility study is divided in three parts, that are, in execution order, the ascent of a launcher, the transfer from the Earth vicinity to the Moon and the lunar landing. In each phase, the focus is delivering the payload, that could either be cargo, crew or supplies, from the beginning of each phase to the end of it. The whole project is divided into three thesis works, which concern about Earth ascent Earth-Moon transfer and lunar landing. The current thesis will deal about the launching of the lunar payload into an orbit about the Earth. Therefore, the research question for this work is:

Is it possible, by means of existing launch vehicles, to set a permanent manned base on the South Pole of the Moon, before July 1, 2020?

To answer this question, the research will assess the available launchers in order to understand which are the most suitable, in terms of payload capabilities, to accomplish this mission. Since bringing material to the Moon and building a base requires a big effort in launcher capability terms, the focus will be on the maximization of the payload mass for each launcher.

The ascent trajectory problem originates from the fact that, in a launch, 97-98% of the total mass of the vehicle is structural and propellant mass. This means that only 2-3% can be used as payload and, at the same time, it is the reason for which we strive for gaining every single kilo. The larger the payload mass, the more efficient and the less expensive the launch (because the launcher cost is fixed).

In this thesis, the problem will be tackled by formulating it as an initial value problem (IVP), in which, given the launcher's initial conditions, the state vector is propagated by means of an integrator. During the flight, the vehicle will follow a guidance programme, expressed through mathematical laws whose parameters can be tuned. Moreover, the launcher will be subjected to constraints dictated by mechanical and thermal properties of the same. In order to find the trajectories with the largest payload mass, an optimization method will be applied. For this problem, finding the largest payload mass involves finding optimal parameters for

the control laws, satisfying the constraints and successfully achieving the target orbit. The optimization will be a global single and multi-objective one performed with the use of a particle swarm optimizer (PSO).

The particle swarm optimization method simulates the behaviour of a flock of birds looking for food. In such a model, each particle has certain characteristics that reflect the optimization variables. Each particle explores the search space and its motion is influenced by the best position where it found food and by the globally best position where food has been found. This model simulates the transmission of information between the particles in the flock and, as a consequence, performs optimization.

The current problem has been studied and analyzed by different authors since the '50s and '60s, when the Moon race started. Along the decades, it never lost the attention of engineers and scientists since every new idea, method of implementation or type of optimization could increase the performances of the launchers.

Most of the works found in literature formulate the ascent problem as a boundary value problem (BVP) where the initial and final conditions are given (e.g., the launch and the orbit injection points). In some researches NLP solvers or Newton's method are applied to solve the optimization problem (see [Gath, 1998, 2002]). These approaches rely on the computation of the gradient of the function to optimize. However, the most frequently used numerical methods to solve the boundary value problems are the shooting methods (direct or multiple shooting) found in [Jansch et al., 1990; Well, 2004; Lu et al., 2008; Park and Vadali, 1998]. The major issue of these methods is that an initial guess of the optimizable variables (with no physical meaning) is needed to solve the boundary value problem. As a consequence, deep knowledge of the problem is necessary to provide a good guess and reach convergence of the solution.

In the aforementioned method, the control is explicitly included in the equations of the boundary value problem without giving a direct physical insight of how the launcher is guided. However, a more clear way to include the control is to have the laws implicitly expressed as Euler angles that provide a clearer physical meaning. For an overview of the most used guidance laws, the reader is referred to [Perkins, 1966; Markl, 2001; Castellini, 2008a; Bruschi, 1976; Luke, 1993], from which the guidance implemented in this work has been taken.

Concerning the global optimization methods, genetic algorithms (GAs) have had large attention in the '90s and still nowadays. On the other hand, after the PSO was introduced, its development has run quite fast in the past years and has reached the level of maturity of GAs, in some cases outperforming them and yielding a faster convergence to the global solution. A wide description of the method and his features, for single objective, is given by [Kennedy and Eberhart, 1995; Nedjah and Mourelle, 2006], whereas, for multiple objectives, [Toscano Pulido and Coello Coello, 2004; Coello Coello et al., 2004; Coello Coello and Lechuga, 2002; Reyes-Sierra and Coello Coello, 2006; Nedjah, 2010] give an overview of the state of the art for the method.

About the multi-objective optimization applied to the ascent trajectory problem, nothing has been found in literature so far.

As mentioned before, the current study has to fit within the framework of a mission to the Moon for a permanent base settlement. Even though in the '60s and '70s the dream of the lunar conquest was quite alive, no projects or plans to build a lunar base were made because of shortage of money. On the other hand, in the past 4-5 years, after the *Vision for Space Exploration*¹ by the former U.S. president G. W. Bush, a new push has been given to space exploration. Therefore, as the first step was to get to the Moon to test new technology for further planets, several proposals about architecture, mobility, infrastructure etc. spread in the scientific community. Several works on the architecture, the launch strategy and astronauts work schedule are given by [Mosher and Kwong, 2004; Hofstetter et al., 2007; Paredes and Navarro, 2005; Chung and Weinstein, 2004; Hand, 2005; Kosmann and Bocam, 2006; Bodkin et al., 2006; Touns and Kennedy, 2008]. Besides the overview of the whole mission, also several in-depth studies about the communication system, the mobility on the Moon and the issue of storing solar power have been assessed. These works have been conducted by [Hill et al., 2006; Hamera et al., 2008; Bhasin et al., 2008; Malmstrom et al., 2006; Space Communication Architecture Working Group, 2004] on the communication methods, by [Woytach et al., 2005; Chun et al., 2006] for the mobility of the astronauts, by [Fincannon, 2008; Brandhorst et al., 2006] to assess the problem of achieving and storing power. In addition, other researches have been performed on the structure of the base itself, ranging from the spherical inflatable modules in [Roberts, 1988], to the rigid ones [Hoy et al., 1988], to prototypes of inflatable tents [ILCDOVER, 2008].

¹ http://www.nasa.gov/pdf/55583main_vision_space_exploration2.pdf

Ascent Module software

The current thesis work is mainly based on a simulation software to analyze and optimize ascent trajectories for launch vehicles. Fortunately, an existing software, namely STA Ascent Module (STA AM), that is a module that was meant to be part of the STA software², was already available. The AM software was developed by [Castellini, 2008a]. However, the software has been changed and developed further in order to be suited for the author's work, but accounting also the main broad scope it was intended for.

The AM software is coded in C++ language, but it does not make use yet of the object oriented programming typical of this language. All the simulations were performed on a MAC OS X 10.5 machine but the software has been tested also under Windows machines even though it resulted to be much slower. This issue might be due to the compiler used by Microsoft Visual C++, that is different from the GNU compiler used on the former operating system.

Launch vehicles

In [Pagano, 2008], the author has gathered all current heavy lift launch vehicles data, analyzed them and a preliminary choice about those to be investigated for this mission was made. The launchers left from this choice were Ariane 5, Proton, Ares I and V, and Atlas V. Two other launchers, namely the Delta IV Heavy and the Atlas V HLV, were prematurely discarded because their cost per flight was too high. Although this assumption is basically true, the author has performed some preliminary optimization analysis using also the Delta IV Heavy and the Atlas V HLV launcher. This is due to the fact that any carrier that might be useful to accomplish the mission to the Moon should be taken into account. However, as the dynamical model has not proved to be powerful enough, a more thorough study concerning these two launchers is left for future research.

Eventually, all the data of the aforementioned launch vehicles that are used in this work are summarized in Appendix B. It must be remarked that no aerodynamic data regarding drag and lift coefficients are present, but the method to compute and obtain them is described in Appendix A.

The Earth-Moon transfer analysis had been already performed before the results of this research were obtained. At that time (August-December 2009), NASA plans to build the two Ares rockets to bring the man on the Moon were still on going, although late on schedule. Therefore, the author of the Earth-Moon transfer (see [Zuccarelli, 2009]) systematically relied on the availability and use of Ares rockets. In fact, these two rockets have a theoretical capability much higher than the existing launchers (e.g., Ares V LEO payload would be 75 tons against 20-23 tons of existing launchers). Nevertheless, the Review of United States Human Space Flight Plans Committee, also called Augustine Commission, set by the U.S. Government in 2009, aimed to review the options available to human spaceflight programme after the retirement of the Space Shuttle programme, scheduled for late 2010. The committee reported that \$3 billion is needed by NASA for the next years in order to keep up with the Constellation programme. Considering this news and the fact that U.S. president Barack Obama is cutting on NASA funds ([Chang, 2010]), it is a quite fair and likely assumption that Ares rockets will never be built on time (base delivery before July 1, 2020) or at all (another rocket instead of the planned two might be built or commercial companies may provide "taxi service" to astronauts). Therefore, the author of this work has not considered the Ares launchers in this analysis.

In conclusion, the entire mission is based on existing launchers only and does not rely on any on-going vehicle development.

Final orbit

In the first place, the possible scenarios available for the ascent trajectory analysis include the direct ascent (DA) and the ascent to Low Earth Orbit (LEO). The former is used to inject the payload directly into an orbit to the Moon, whereas the latter can be used to perform a possible Earth Orbit rendezvous with other vehicle/capsule or simply to wait the right moment to perform the trans-lunar injection. Direct ascent here means that the launcher's thrust phase is then followed by a coasting phase that is part of an elliptical

² Actually, the Ascent Module will not be part of STA anymore due to some considerations about safety and security advanced by ESA.

transfer orbit. When the payload reaches the vicinity of the Moon, the coasting phase ends and an insertion maneuver (e.g., a lunar orbit injection, LOI) into a lunar orbit is performed.

This type of orbit has been thought only for the Delta IV Heavy and Atlas V HLV because, since they have not been included in Zuccarelli's work, the Earth-Moon transfer would be missing for them. For the other vehicles only an analysis to a LEO parking orbit is performed since the transfer phase has been studied in [Zuccarelli, 2009].

After all ascent trajectories, direct or into parking orbit, are performed, an analysis and comparison to evaluate which launchers perform better will be carried out. This analysis will help in the choice of the best launchers.

Layout of the thesis

To find an answer to the research question, first a general overview of different mission scenarios, base configuration and logistic aspects will be given in Chapter 2. The mathematical model used to assess the problem, ranging from equations of motion to reference frames and launcher representation, will be treated in Chapter 3. Chapter 4 will show the guidance programme that will be the reference of the flight profile for each launcher. A detailed presentation of the specific optimization method and the optimizers themselves will be given in Chapter 5. The evaluation of the optimization runs and the analysis of the results is offered in Chapter 6. Eventually, the conclusions that can be drawn and the recommendations for future research will be presented in Chapter 7.

Chapter 2

Moon Mission: scenarios and logistic aspects

In this chapter, several practical aspects related to a lunar mission and base settlement will be discussed:

- Mission requirements
- Mission scenario
- Mission definition
- Base and spaceport architectures

This chapter is written by the three authors (Antonio Pagano, [Zuccarelli, 2009] and [Boere, 2009]) that are designing this lunar mission for ESA. Some decisions were already made during the literature study and can be found in [Pagano, 2008].

2.1 Mission requirements

In this first section, all requirements imposed by ESA [Ortega, 2008], that have to be matched in this project, are listed:

- The exercise shall focus on trajectories and trajectory optimization with the aim of designing, building, and operating a permanent base on the South Pole of the Moon
- The mission base shall be in place and commissioned before 1 July 2020
- The entire mission shall be divided in two phases:
 - Building the base
 - Operating and maintaining the base (for 10 years)
- Permanent telescope of 1 meter diameter Newton type
- Communications equipment to reach 3 Earth ground stations separated by 120° each
- Human base shelter for a minimum of 3 astronauts
- Mobility means to displace a crew of 2 astronauts for 15 km around the base
- Spaceport for landings and launches

2.2 Mission scenario

There are several possible trajectories that can be used to travel from the Earth to the Moon. Many of these so-called mission scenarios were listed in [Pagano, 2008] and only four of them were selected for a successive study. These mission scenarios have to be considered in the design of a mission to build a base on the South Pole of the Moon. In this section, a brief overview of these scenarios is given. The final choice is based on a combination of the results obtained in this work, in [Zuccarelli, 2009] and in [Boere, 2009].

The fastest way to reach the Moon is by direct transfer. In contrast to the Apollo missions, there is no rendezvous with other spacecraft (S/C). Several lunar missions like Luna, shown in Fig. 2.1, and Surveyor have used this scenario.

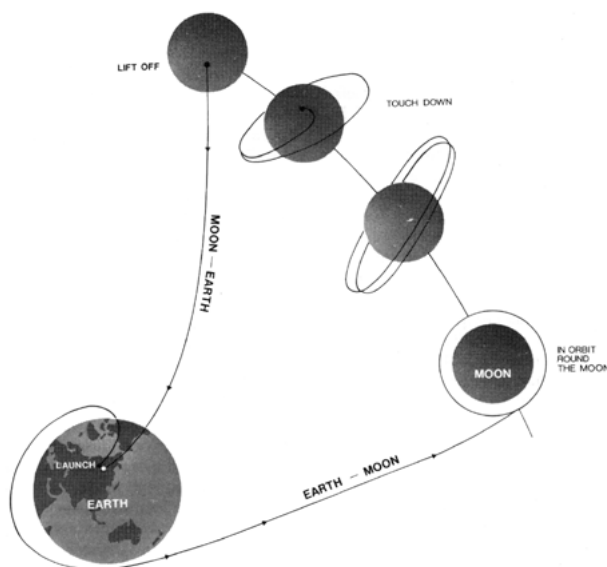


Figure 2.1: Luna 16 orbit trajectory.¹

Within the scenarios that make use of the International Space Station (ISS), many different options are available. It is possible to send cargo to the station and then assemble them, or it is possible to send astronauts to the ISS in order to guarantee a continuous link between the lunar base and the station. Moreover, it is possible to use a S/C to travel just between the station and the Moon (orbiting around it and dropping off the payload or landing on the Moon) and another (or many other) S/C that delivers payload from the Earth to the station and the other way around.

If multiple launchers are needed, the S/C can rendezvous in space. Earth orbit rendezvous allows the assembly of cargo in an orbit about the Earth. In addition, a transport S/C can pick up cargo in an Earth orbit and release it in an orbit about the Moon. Rendezvous in LEO has already been accomplished successfully in several missions, therefore it is a proven and consolidated technique.

The lunar orbit rendezvous is similar to the previous one, but rendezvous is accomplished in a lunar orbit.

Of these four mission scenarios, the ISS scenario seems to be the worst candidate for this mission, for many different reasons. First of all, the availability of the ISS cannot be guaranteed. The international regulations are quite strict and permission may be denied. Moreover, many missions visit the ISS causing the station itself to be unavailable at certain times². Besides these practical aspects, it also does not seem so attractive from an orbital point of view. Launchers deliver S/C and cargo into a low Earth orbit. In

¹ <http://www.lpi.usra.edu/lunar/missions/>

² http://www.russianspaceweb.com/iss_chronology_flights.html

order to reach the ISS, a high inclination and a raise of the altitude are needed. This is quite expensive. At the ISS, these cargo and S/C should be assembled and finally sent to the Moon. This entire scenario is much more expensive than, for instance, the Earth orbit rendezvous, because in this latter one no changes of inclination and altitude are required. Although the ISS offers infrastructure (e.g., mechanical arms, etc.) that can simplify the assembling phase, it does not seem to outweigh the disadvantages presented. Therefore, the ISS mission scenario has been discarded.



Figure 2.2: The International Space Station.³



Figure 2.3: ATV-ISS rendezvous.⁴

As mentioned before, three students are designing the lunar base mission. Unfortunately, the work is not carried out at the same time. Therefore it has been decided to split the final choice of the mission scenario over different studies. In this work, the pros and cons of the possible scenarios (DA and injection into parking orbit) will be presented. These results can then be used and compared with a lunar orbit rendezvous from the thesis work of [Boere, 2010], which is to describe the lunar phase of the mission. There, the fuel consumption of the mission scenarios will be compared and a final mission scenario will be selected.

³ http://www.jaxa.jp/projects/iss_human/iss/index_e.html

⁴ http://cadmos.cnes.fr/en/iss_microgravity.html

2.3 Masses naming convention

Before showing the base elements and starting the discussion about payloads and masses, some definitions are given here and they will be adopted through the entire thesis in order to clarify the nomenclature and simplify the life of the reader. The following schemes summarize the definitions adopted and gives a global overview of the mission definition.

A first breakdown is presented and it regards the type of mission to be flown during the different phases needed to settle and operate the lunar base. The possible missions are divided into crew, cargo and supply expedition. This breakdown gives a first insight on how such a big project can be simplified and executed.

Crew expedition

A crew expedition is a mission in which a group of astronauts (3-4) is sent to the Moon to assemble the several components of a module, and then the modules together. A crew is needed in order to put together the several pieces that make up the base and to locate payload and instruments inside each module and then to make them work. This type of mission is foreseen to last a week at most since a lander and a module able to host the astronauts for a period longer than this has never been designed. In addition, the crew expedition can be flown only when module components and structures have already been placed on the lunar soil.

Later on, during the lunar base operation phase, a crew expedition every about 6 months occurs in order to change the astronauts working in the base, as occurs with the crew on the ISS. A breakdown of the masses can be seen in Fig. 2.4.

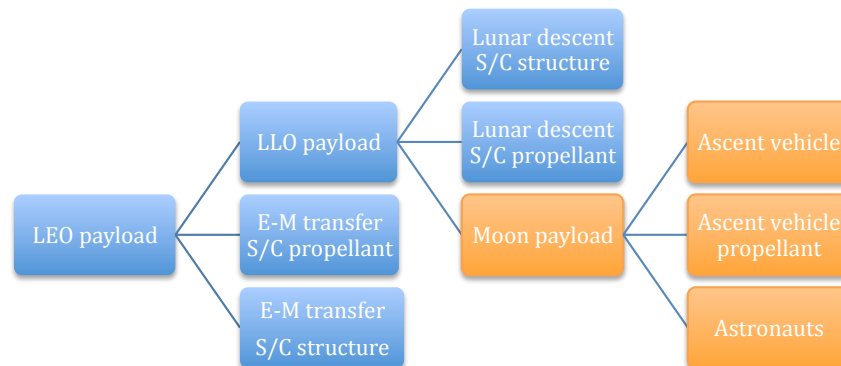


Figure 2.4: A mass breakdown for the crew expedition shows which elements are part of it, including the vehicle to return on Earth.

Because of the budget cuts, NASA put on hold and will, maybe, give up on the Constellation programme. This programme was the only one involving the design and test of a manned capsule and a lander to get to the Moon. Because of this, no other existing manned vehicles are available besides the Soyuz. However, this capsule, is not designed to get to and land on the Moon. For these reasons, and mainly because present technologies had to be used, the author has not included any studies about ascent trajectory for a manned launcher.

Cargo expedition

The cargo expedition consists in bringing to the Moon all the modules, instruments and devices that will be part of the base to make it fully operative. The rover and the telescope are also included in this type of mission. Usually several cargo expeditions should be flown before a crew can be sent in order to assemble the components. The cargo should be landed on the Moon by landing a S/C not too far from the base location. Fig. 2.5 shows the components part of a cargo mission type.

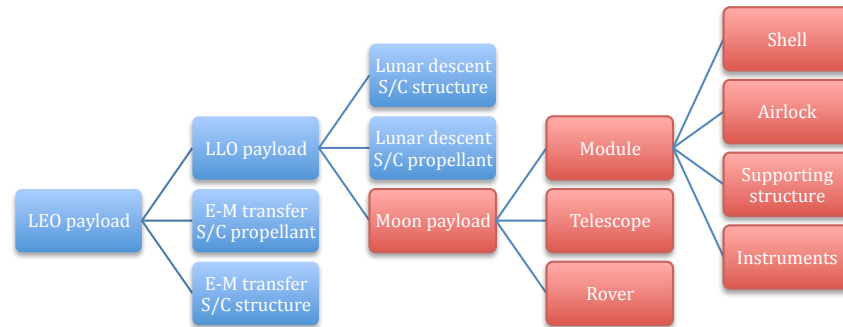


Figure 2.5: The cargo expeditions are the first to be flown to the Moon in order to place the material that will compose the base.

Supply expedition

As for the crew expedition needed to change the group of astronauts working in the base, the supply expedition is needed to provide the astronauts with food, water, oxygen and essential things to live in the base (see Fig. 2.6). Moreover, this type of mission includes also tools, devices and instruments to replace damaged ones or to fix and cope with problems arising during the operative phase of the base.

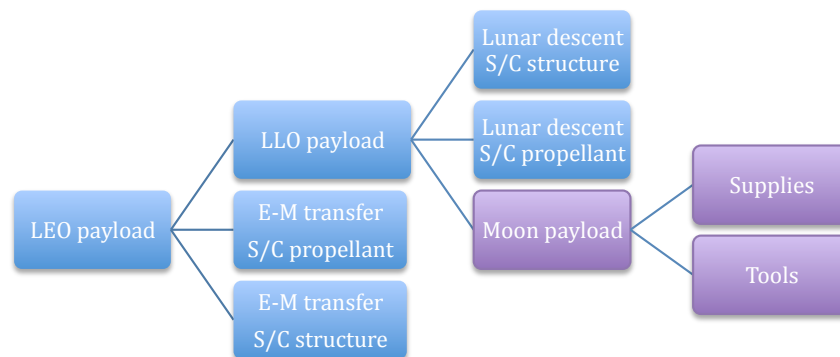


Figure 2.6: The supply expedition should provide goods for the living of the astronauts and tools and instruments, in case of damages and failures.

2.4 Base and spaceport architecture

The lunar base and spaceport architecture were presented in [Pagano, 2008]. A short summary will be given in this section. The requirements for the lunar base were set by ESA (see [Ortega, 2008]). For more details and design decisions the reader is encouraged to read [Pagano, 2008].

The lunar base consists of four modules, i.e., two habitation modules, one science module and one control module. These modules are connected with airlocks, providing access to the modules from the lunar environment. The modules are fixed, inflatable and made of Earth materials. The mass of one lunar base, emergency and spaceport module (Module mass) consists of 0.7 tons inflatable shell, 3 tons supporting structure, 5 tons airlock, 8 tons of payload mass for the base modules and 6.5 tons for the others (see Table 2.1). The payload mass can be divided into different parts, while shells, supporting structures and airlock for each module cannot be split into small pieces. The configuration of the lunar base can be seen in Fig. 2.7. This base is able to host a minimum of three astronauts, satisfying the mission requirements.

Eventually, a 1-m diameter Newton type permanent telescope will be placed near the lunar base. This lunar telescope is not obstructed by atmospheric pollution and will have a clear view when placed into a permanently shadowed crater.

Table 2.1: Mass breakdown for each module.

Module Type	Shell [tons]	Supporting structure [tons]	Airlock [tons]	Payload [tons]	Module mass [tons]
Base	0.7	3	5	8	16.7
Emergency	0.7	3	5	6.5	15.2
Spaceport	0.7	3	5	6.5	15.2

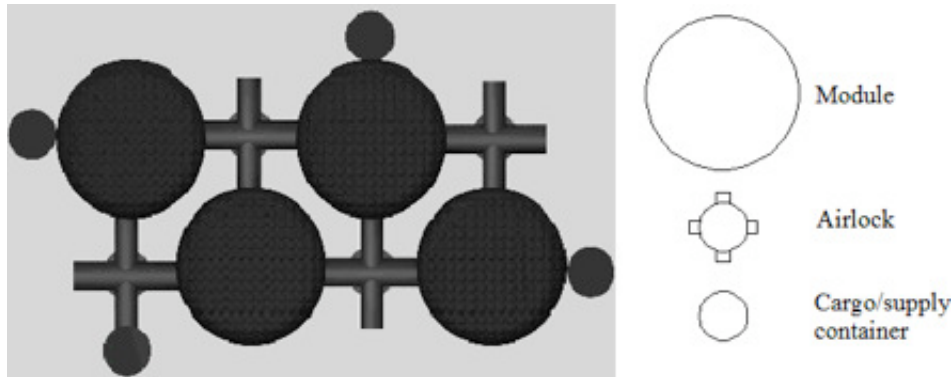


Figure 2.7: Configuration for the lunar base. The base consists of four modules and four airlocks. Containers are used to store fuel, food, water, etc. [Pagano, 2008]

In addition to the lunar base described above, one module with one airlock will serve as an emergency module for the astronauts. In case of an emergency in the lunar base, the astronauts can use this emergency site to communicate with the Earth. Only equipment will be installed that is absolutely necessary for emergency, like the communication system, food and water for some days, a thermal system, etc. If the base cannot be repaired, a spacecraft will be sent from Earth and the astronauts will leave the emergency module and go to the spaceport for their return to Earth.

The spaceport consists of two modules, i.e., the control module and the maintenance module. Its configuration can be seen in Fig. 2.8.

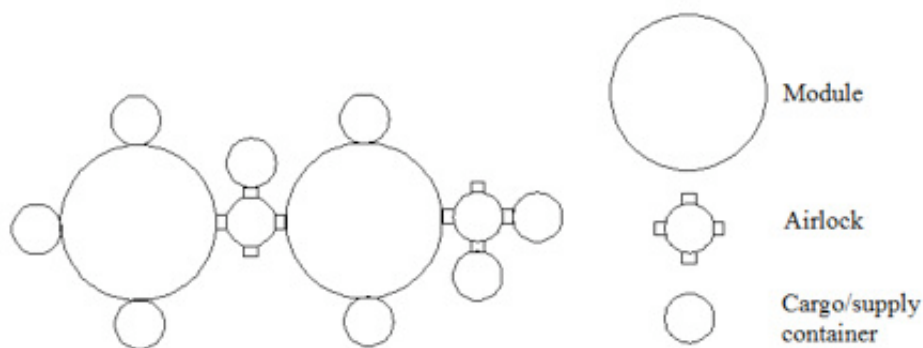


Figure 2.8: Spaceport configuration. The spaceport consists of two modules; one for communication (right module) and one for maintenance (left module). Containers are used to store fuel, water, etc. [Pagano, 2008]

For the emergency and spaceport modules less payload (6.5 tons) than that for the base is needed, [Pagano, 2008].

Both the lunar base and the spaceport have the ability to attach containers for supplies, e.g., water, air and food.

A link between the lunar base, the emergency base and the spaceport should be guaranteed by using

different rovers. In addition, mobility to displace a crew of two astronauts for 15 km around the base should be guaranteed. The following rovers will be brought on the lunar surface:

- Unpressurized manned rover, for short excursions;
- Pressurized manned rover, for long excursions (e.g., in the lunar craters);
- Cargo rover, to transport equipment and supplies.

Finally, a communication system has to be guaranteed between the Earth and the Moon. For this reason two satellites will be put into a Halo orbit around the Lagrangian point L_2 with a 7.5-days period, in order to continuously cover the entire South Pole. The satellites will be able to guarantee communications with three Earth ground stations separated by 120° each, [Pagano, 2008].

Determining the total mass that has to be brought to the lunar surface is the most important aspect of this phase. A mass breakdown is shown in table Table 2.2. The masses of the different parts were already determined in [Pagano, 2008]. From the mass breakdown it becomes apparent which parts can be launched together and whether some parts exceed the capability of the launcher.

Table 2.2: Total mass breakdown.

Lunar base		
Module mass Structure (4x)	8.7 tons (4x)	[Roberts, 1988] and [Pagano, 2008]
Module mass Payload (4x)	8 tons (4x)	[Roberts, 1988] and [Pagano, 2008]
Emergency module		
Module mass Structure	8.7 tons	[Roberts, 1988] and [Pagano, 2008]
Module mass Payload	6.5 tons	[Roberts, 1988] and [Pagano, 2008]
Spaceport		
Module mass Structure (2x)	8.7 tons (2x)	[Roberts, 1988] and [Pagano, 2008]
Module mass Payload (2x)	6.5 tons (2x)	[Roberts, 1988] and [Pagano, 2008]
Observatory		
Telescope mass	1.2 tons	[Sutherland et al., 2007]
Rover		
Unpressurized rover mass	0.2 tons	[Woytach et al., 2005]
Pressurized rover mass	6 tons	[Woytach et al., 2005]
Cargo rover mass	0.5 tons	[Volpe and Udomkesmalee, 2009]
Communication		
Satellite mass (2x)	0.4 tons (2x)	[Hamera et al., 2008]
Complete base total mass	121.1 tons	

2.5 Launch capability

Of course, at the beginning of the mission analysis one cannot know what might be the payload mass available on the Moon. This value is obtained once all the phases of the mission have been analyzed. Therefore, for this feasibility study we cannot foresee the payload mass we will have on the Moon. In [Zuccarelli, 2009], a minimum Moon payload mass of 5 tons was assumed because the heaviest unit in the base design was given by the airlock. It was stated that, if this requirement, would not be satisfied, the mission could be unfeasible. However, even though this consideration might be true, we cannot be so drastic and another solution would be that to design and manufacture a lighter airlock.

Chapter 3

The dynamic system model

This chapter will give a detailed overview of the dynamic formulation of the ascent trajectory problem. A definition of the state variables is given in section 3.1, all the reference frames useful to describe the motion and the dynamic of the system are given in section 3.2 and the transformations between them in section 3.3. In section 3.5, 3.6 and 3.7, a description of the forces involved is presented and finally the path constraints acting on the vehicle are introduced in section 3.8.

3.1 State-variable definitions

In this section, we are going to introduce the possible ways to express the position and the velocity of a rigid body that is moving around another one. The equations of motion are expressed in Cartesian components. This is due to the fact that these components do not produce singularities for some particular values of angles. Then, in the final results presented to the user, those coordinates are also converted into spherical components to give a better understanding of the problem. In this way, the problem concerning the singularities is overcome because during the conversion from Cartesian to spherical components they do not appear.

Orbital elements

These state variables are useful when describing the motion or the orbit of the body about a planet with respect to an inertial reference frame. They are depicted in Fig. 3.1 and are [Mooij, 1997]:

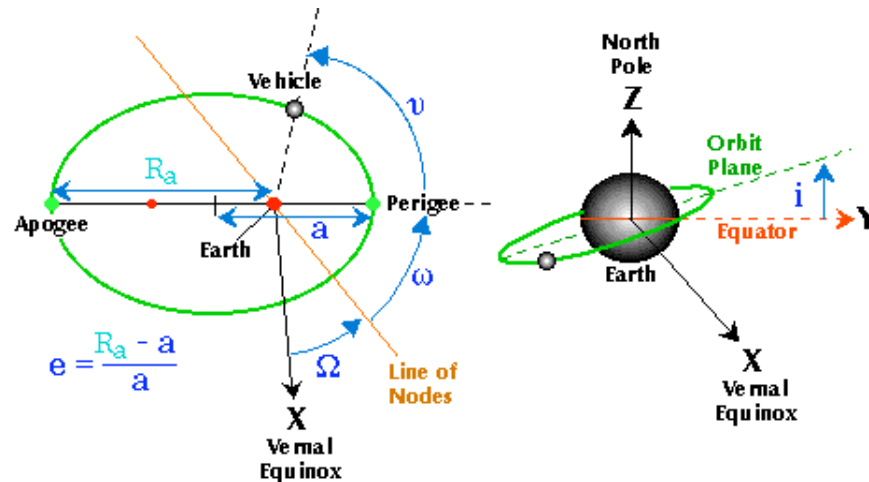
- e : the eccentricity ($e \geq 0$)
- a : the semimajor axis ($a > R_e$)
- i : the inclination ($0^\circ \leq i \leq 180^\circ$)
- ω : argument of pericentre ($0^\circ \leq \omega < 360^\circ$)
- Ω : the longitude of the ascending node ($0^\circ \leq \Omega < 360^\circ$)
- M : mean anomaly ($0^\circ \leq M < 360^\circ$)

Unlike true anomaly, the mean anomaly is an auxiliary angle. As mean anomaly is linearly increasing in time, it is easier to compute the time elapsed between two points of the orbit.

Cartesian components

The Cartesian components are used to describe the position and the velocity of the body with respect to an inertial or rotating frame. These components do not give a clear and direct insight in the physical problem of the trajectory of the motion about the Earth or a planet (see Fig. 3.2). However, they are very useful in the computation and in the integration of the equations of motion, because they avoid the singularities that occur when, for instance, the flight path angle γ is $\pm 90^\circ$.

Position: x, y, z

Figure 3.1: Orbital elements.¹

Velocity: $\dot{x}, \dot{y}, \dot{z}$

In case the velocity components are expressed with respect to a rotating frame, they can be expressed as x_R, y_R, z_R [Mooij, 1997].

Spherical components

The advantage given by the spherical components arise in the visualization of the motion of, in this case, a launch vehicle because they give the physical insight of the problem. We define them with respect to a rotating frame as shown in Fig. 3.3, [Mooij, 1997]:

Position: distance r , longitude τ , latitude δ

Velocity: V_G , flight path angle γ , heading angle χ

where G indicates groundspeed based velocity.

The longitude is measured positively to the east ($-180^\circ \leq \tau < 180^\circ$). The latitude is measured along the meridian from the equator and is positive in the north direction ($-90^\circ \leq \delta < 90^\circ$). The distance r is the distance of the launcher from the center of the planet. The velocity V_G is the modulus of the velocity vector \vec{V} , expressed in the rotating frame. The flight path angle is the angle between \vec{V} and the local horizontal plane ($-90^\circ \leq \gamma \leq 90^\circ$, it is negative when \vec{V} is below the horizon). The heading angle is the projection of \vec{V} in the local horizontal plane with respect to the local north ($-180^\circ \leq \chi \leq 180^\circ$, where $\chi = 90^\circ$ is due East).

3.2 Reference frames

In this section several reference frames will be introduced. The reason why not only one frame is used is due to the fact that some reference frames make the derivation of the equations of motion or the definition of forces easier than others. So one can describe a certain motion in a reference frame and then make a translation/rotation into another one in which the motion has to be derived.

Perifocal reference frame

The perifocal coordinate system ($Oeph$) is centered in one of the foci (i.e., the planet about which the orbit is centered) of the orbit. The e -axis is directed toward the periapsis of the orbit, in the direction of the

¹ http://science.nasa.gov/Realtime/rocket_sci/orbmech/state/class.html/

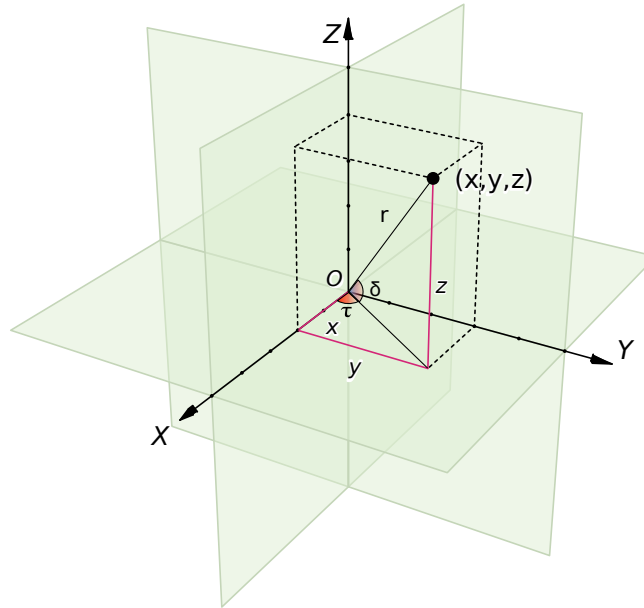


Figure 3.2: Cartesian and spherical components are depicted.

eccentricity vector. The h -axis is directed as the angular momentum (defined as $\vec{r} \times \vec{V}$) and the p -axis completes the right-handed system (see Fig. 3.4).

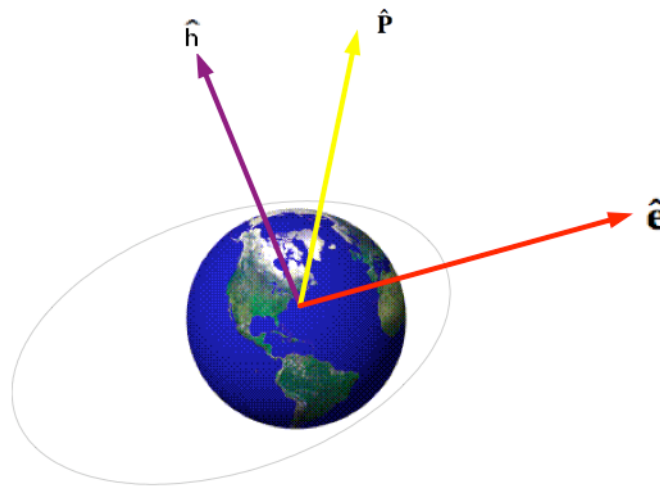


Figure 3.4: Perifocal reference frame [Hall, 2003].

$$E_p = \begin{bmatrix} e_e \\ e_p \\ e_h \end{bmatrix} \quad (3.1)$$

Inertial geocentric reference frame

This reference frame ($OX_I Y_I Z_I$) has its origin at the center of mass of the Earth. The Z_I -axis is pointing north along the spin axis of the Earth. The $OX_I Y_I$ plane is coincident with the equatorial plane and X_I -axis is directed to the vernal equinox or First Point of Aries. The Y_I -axis completes the right-handed system

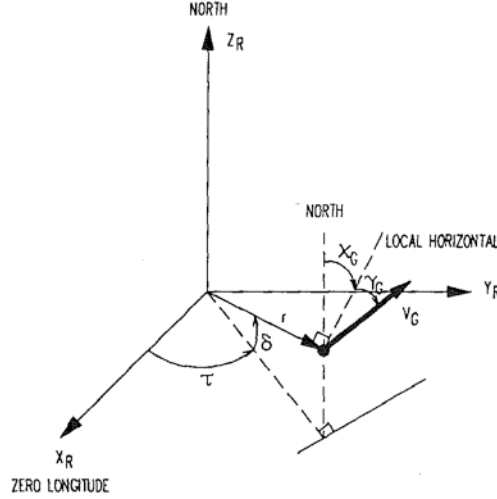


Figure 3.3: Spherical components in a rotating frame [Mooij, 1997].

[Cornelisse et al., 1979].

$$E_I = \begin{bmatrix} e_{X_I} \\ e_{Y_I} \\ e_{Z_I} \end{bmatrix} \quad (3.2)$$

Rotating geocentric reference frame

This reference frame ($OX_R Y_R Z_R$) is an Earth-fixed reference frame. It differs from the inertial frame since the X_R -axis points towards the Greenwich meridian. The Z_R -axis is pointing north but it rotates around the spin axis of the Earth that coincides with Z -axis. The Y_R -axis completes the right-handed system. Since the X_R -axis coincides with the Greenwich meridian, the rotating geocentric reference frame is fixed with the Earth and rotates with the Earth's angular velocity about the Z_R -axis [Cornelisse et al., 1979].

$$E_R = \begin{bmatrix} e_{X_R} \\ e_{Y_R} \\ e_{Z_R} \end{bmatrix} \quad (3.3)$$

Body reference frame

The body-fixed reference frame ($OX_B Y_B Z_B$) is fixed to the center of mass of the launch vehicle. The X_B -axis is in the plane of symmetry of the body and is directed (positive direction) towards the fairing. The Z_B -axis also lies in the plane of symmetry of the launcher, but is directed downward and the Y_B -axis completes the right-handed coordinate system [Cornelisse et al., 1979].

$$E_B = \begin{bmatrix} e_{X_B} \\ e_{Y_B} \\ e_{Z_B} \end{bmatrix} \quad (3.4)$$

Vehicle-centered horizontal reference frame

A reference frame ($OX_V Y_V Z_V$) with the origin in the center of mass of the vehicle is introduced. This reference frame is used to describe the orientation of the rocket and its velocity vector relative to the Earth's surface and it can be obtained from the rotating geocentric frame by two successive rotations and a translation. The first rotation of the rotating geocentric frame is about the Z_R -axis over an angle τ and the second is about the intermediate Y -axis over an angle of $-(\pi/2 + \delta)$, where τ is the geocentric longitude

and δ is the geocentric latitude of the vehicle. The Z_V -axis is pointing to the center of the Earth. The X_V -axis lies in the meridian plane pointing North and the Y_V -axis completes the right-handed system and is pointing East [Cornelisse et al., 1979]. The relation between this frame and the rotating and the inertial one can be seen in Fig. 3.5.

$$E_V = \begin{bmatrix} e_{X_V} \\ e_{Y_V} \\ e_{Z_V} \end{bmatrix} \quad (3.5)$$

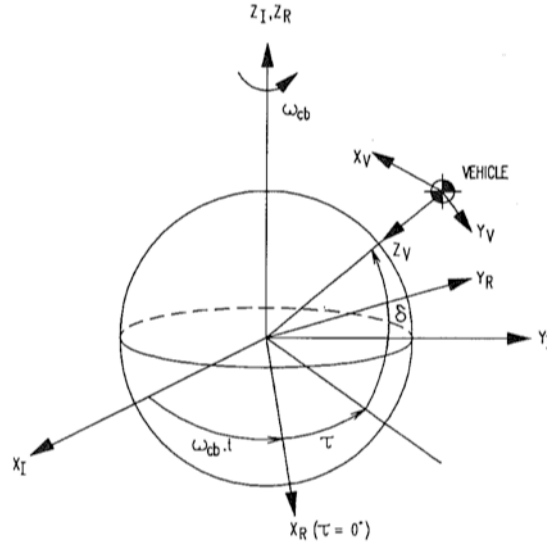


Figure 3.5: The inertial, rotating and vehicle-centered reference frame and the relation between each other is depicted [Mooij, 1997].

Trajectory reference frame

In this frame ($Ox_T Y_T Z_T$) the X_T -axis is aligned with the velocity vector, the Z_T -axis is pointing downward and is contained in the local vertical plane. The Y_T -axis is in the local horizontal plane and completes the right-handed system. If no wind is considered (which is the case), this reference system coincides with the air-path reference frame (described below).

$$E_T = \begin{bmatrix} e_{X_T} \\ e_{Y_T} \\ e_{Z_T} \end{bmatrix} \quad (3.6)$$

Air-path reference frame

The air-path (aerodynamic) reference frame ($Ox_A Y_A Z_A$) is coupled to the aerodynamic velocity (or air-path velocity) that is the velocity of the center of mass of the vehicle relative to the undisturbed air. X_A -axis is in the direction of the aerodynamic velocity, Z_A -axis is in the symmetry plane of the vehicle and Y_A -axis completes the right-handed system. The angle of attack α and the sideslip angle β determines the orientation of this reference frame with respect to the body system.

$$E_A = \begin{bmatrix} e_{X_A} \\ e_{Y_A} \\ e_{Z_A} \end{bmatrix} \quad (3.7)$$

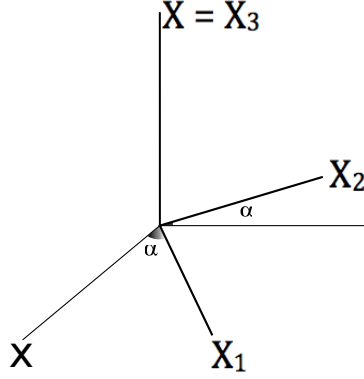


Figure 3.6: Euler transformation about the Z-axis of an angle α .

3.3 Transformations

In order to go from one reference frame to another, transformation matrix are needed. Unit axis transformations can help in this process. In fact, a rotation to go from one frame to the other can be decomposed into unit axis rotations. Then, according to about which axis we apply the rotation, we have:

$$C_1(\alpha) = \begin{bmatrix} 1 & 0 & 0 \\ 0 & \cos \alpha & \sin \alpha \\ 0 & -\sin \alpha & \cos \alpha \end{bmatrix} \quad (3.8)$$

$$C_2(\alpha) = \begin{bmatrix} \cos \alpha & 0 & -\sin \alpha \\ 0 & 1 & 0 \\ \sin \alpha & 0 & \cos \alpha \end{bmatrix} \quad (3.9)$$

$$C_3(\alpha) = \begin{bmatrix} \cos \alpha & \sin \alpha & 0 \\ -\sin \alpha & \cos \alpha & 0 \\ 0 & 0 & 1 \end{bmatrix} \quad (3.10)$$

where C_1 , C_2 and C_3 are orthonormal matrix and subscripts 1, 2 and 3 indicate rotations about x , y and z axis.

Earth centered rotating to Earth centered inertial frame, $C_{I,R}$

The transformation matrix to go from the rotating geocentric reference frame to the inertial geocentric reference frame is [Cornelisse et al., 1979]:

$$C_{I,R} = C_3(-\omega_E t) = \begin{bmatrix} \cos \omega_E t & -\sin \omega_E t & 0 \\ \sin \omega_E t & \cos \omega_E t & 0 \\ 0 & 0 & 1 \end{bmatrix} \quad (3.11)$$

where ω_E is the spin angular velocity of Earth about the polar axis in radians per second ($\omega_E = 7.292115090 \cdot 10^{-5}$ rad/s). The systems are related according to [Cornelisse et al., 1979]:

$$E_I = C_{I,R} E_R \quad (3.12)$$

If the initial position of the launch vehicle is given, for example, in spherical coordinates, then the initial values in the Cartesian coordinates (in an inertial reference frame) are given by the relation:

$$\begin{bmatrix} X \\ Y \\ Z \end{bmatrix} = C_{I,R} \begin{bmatrix} X_R \\ Y_R \\ Z_R \end{bmatrix} \quad (3.13)$$

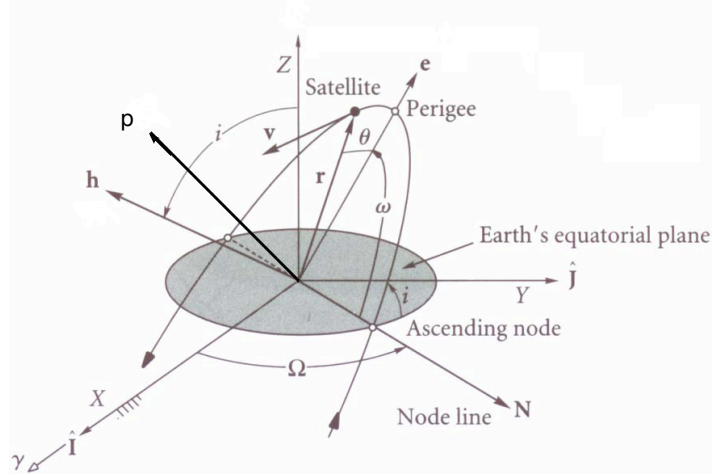


Figure 3.7: Relation between the perifocal and the inertial Earth-centered frame [Shan, 2009].

while, to derive the spherical components from the Cartesian ones in the rotating frame, we can use the following:

$$r = \sqrt{X_R^2 + Y_R^2 + Z_R^2} \quad (3.14)$$

$$\sin \delta = \frac{Z_R}{r} \quad (3.15)$$

with $-90^\circ < \delta < 90^\circ$,

$$\sin \lambda = \frac{Y_R}{\sqrt{X_R^2 + Y_R^2}} \quad (3.16)$$

$$\cos \lambda = \frac{X_R}{\sqrt{X_R^2 + Y_R^2}} \quad (3.17)$$

with $-180^\circ < \lambda \leq 180^\circ$.

Earth centered inertial to perifocal frame, $C_{p,I}$

Three rotations are needed to go from the inertial reference frame to the perifocal system (see Fig. 3.7). These rotations have to be done in the order:

$$C_{p,I} = C_3(\omega) C_1(i) C_3(\Omega) \quad (3.18)$$

according to the relation:

$$E_p = C_{p,I} E_I \quad (3.19)$$

where ω , the argument perigee (or periapsis) is the angle, in the orbital plane, between the ascending node and the periapsis. Ω is the right ascension of the ascending node (RAAN) and is the angle measured eastwards in the Earth's equatorial plane between the first point of Aries and the ascending node of the orbit. i is the inclination of the orbit measured with respect to the Earth's equatorial plane.

Moreover, one has to convert the spherical coordinates in orbital elements. Therefore, we can follow the step by step derivation done by [Wakker, 2007]:

$$a = \frac{r}{2 - \frac{rV^2}{\mu}} \quad (3.20)$$

$$e^2 = 1 - \frac{rV^2}{\mu} \left(2 - \frac{rV^2}{\mu} \right) \cos^2 \gamma \quad (3.21)$$

$$e = \sqrt{1 - \frac{rV^2}{\mu} \left(2 - \frac{rV^2}{\mu} \right) \cos^2 \gamma} \quad (3.22)$$

where a is the *semimajor axis* that describes the dimension of the orbit, e is the *eccentricity* of the same that can be seen as how much it deviates from a circular orbit and μ is the gravitational parameter of the planet.

$$E = \arctan \left[\sqrt{\left[\frac{a}{\mu} \right] \frac{rV \sin \gamma}{a - r}} \right] \quad (3.23)$$

where E is the *eccentric anomaly* that can be determined unambiguously using:

$$e \cos E = 1 - \frac{r}{a} \quad (3.24)$$

$$e \sin E = \frac{rV \sin \gamma}{\sqrt{\mu a}} \quad (3.25)$$

If it results that $e = 0$, then E and also ω are not defined (the time of the perigee passage is not defined as well).

The *true anomaly*, θ , follows from:

$$\tan \frac{\theta}{2} = \sqrt{\frac{1+e}{1-e}} \tan \frac{E}{2} \quad (3.26)$$

where $\frac{\theta}{2}$ and $\frac{E}{2}$ are located in the same quadrant. The *time of the perigee passage*, τ , follows from:

$$\tau = t - \sqrt{\frac{a^3}{\mu}} (E - e \sin E) \quad (3.27)$$

For the determination of the orbital elements i , Ω , ω , using the spherical geometry one can derive the following:

$$\cos(\omega + \theta) = \cos \delta \cos(\lambda - \Omega) \quad (3.28)$$

$$\sin(\omega + \theta) \cos i = \cos \delta \sin(\lambda - \Omega) \quad (3.29)$$

$$\sin(\omega + \theta) \cos \chi = \cos(\lambda - \Omega) \sin \delta \quad (3.30)$$

$$\sin \delta = \sin i \sin(\omega + \theta) \quad (3.31)$$

$$\sin(\lambda - \Omega) = \sin \chi \sin(\omega + \theta) \quad (3.32)$$

From these equations, the following relation follows:

$$\cos i = \cos \delta \sin \chi \quad (3.33)$$

with which is possible to compute the inclination. Then:

$$\begin{aligned}\cos(\lambda - \Omega) &= \frac{\cos \chi}{\sin i} \\ \sin(\lambda - \Omega) &= \tan \delta \cot i\end{aligned}\tag{3.34}$$

allow to compute Ω unambiguously, while ω can be derived from:

$$\begin{aligned}\sin(\omega + \theta) &= \frac{\sin \delta}{\sin i} \\ \cos(\omega + \theta) &= \cos \delta \frac{\cos \chi}{\sin i}\end{aligned}\tag{3.35}$$

In case $i = 0^\circ$, another set of equations could be used:

$$\mathbf{h} = \mathbf{r} \times \mathbf{V}\tag{3.36}$$

$$\mathbf{N} = \hat{\mathbf{z}} \times \frac{\mathbf{h}}{|\mathbf{h}|}\tag{3.37}$$

$$\mathbf{e} = \frac{\mathbf{V} \times \mathbf{h}}{\mu} - \frac{\mathbf{r}}{r}\tag{3.38}$$

$$\tan \Omega = \frac{N_y}{N_x}\tag{3.39}$$

$$\cos \omega = \hat{\mathbf{e}} \cdot \hat{\mathbf{N}}\tag{3.40}$$

$$\cos \theta = \hat{\mathbf{r}} \cdot \hat{\mathbf{e}}\tag{3.41}$$

where $\hat{\mathbf{z}}$ is a unit vector normal to the equatorial plane, \mathbf{h} is the angular momentum, \mathbf{r} is the radius vector, \mathbf{V} the velocity vector and \mathbf{e} the eccentricity vector.

Earth centered rotating to vehicle-centered horizontal frame, $C_{V,R}$

The transformation matrix to go from the rotating geocentric reference frame to the vehicle-centered horizontal reference frame is [Cornelisse et al., 1979]:

$$C_{V,R} = C_3(\tau) C_2\left(-\left(\frac{\pi}{2} + \delta\right)\right) = \begin{bmatrix} -\sin \delta \cos \tau & -\sin \delta \sin \tau & \cos \delta \\ -\sin \tau & \cos \tau & 0 \\ -\cos \delta \cos \tau & -\cos \delta \sin \tau & -\sin \delta \end{bmatrix}\tag{3.42}$$

where τ is the longitude and δ is the geocentric latitude of the vehicle. The systems are related according to [Cornelisse et al., 1979]:

$$E_V = C_{V,R} E_R\tag{3.43}$$

Vehicle-centered horizontal to trajectory frame, $C_{T,V}$

To go from the vehicle-centered horizontal reference frame to the trajectory reference frame, that are related according to the equation:

$$E_T = C_{T,V} E_V\tag{3.44}$$

the following transformation matrix has to be used:

$$C_{T,V} = C_2(\gamma) C_3(\chi) = \begin{bmatrix} \cos \gamma \cos \chi & \cos \gamma \sin \chi & -\sin \gamma \\ -\sin \chi & \cos \chi & 0 \\ \sin \gamma \cos \chi & \sin \gamma \sin \chi & \cos \gamma \end{bmatrix}\tag{3.45}$$

where γ is the flight path angle and χ is the heading angle.

Trajectory to body frame, $C_{B,T}$

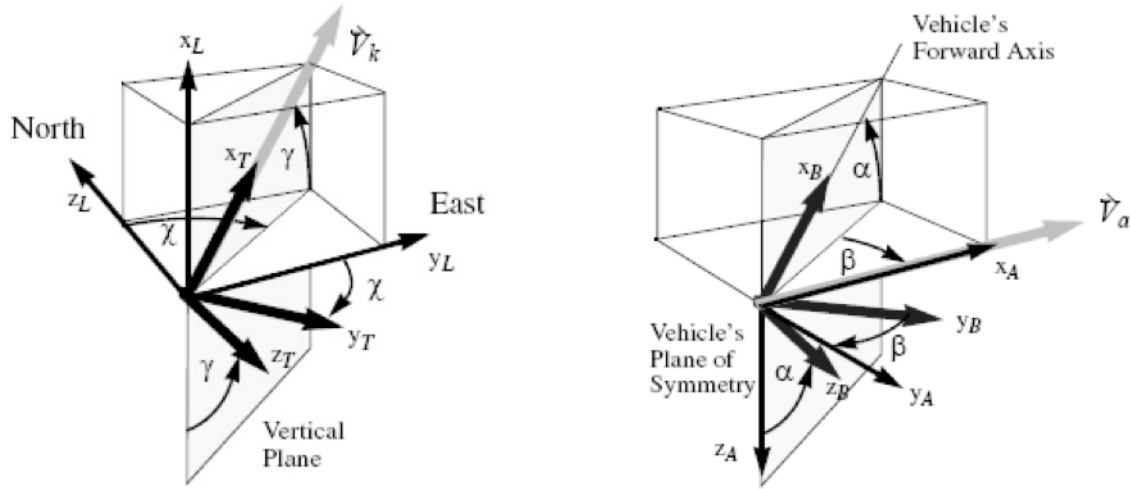
The relation that links the body reference frame with the trajectory reference frame (from trajectory to body system) is:

$$C_{B,T} = C_2(\alpha) C_3(-\beta) = \begin{bmatrix} \cos \alpha \cos \beta & -\cos \alpha \sin \beta & -\sin \alpha \\ \sin \beta & \cos \beta & 0 \\ \sin \alpha \cos \beta & -\sin \alpha \sin \beta & \cos \alpha \end{bmatrix} \quad (3.46)$$

using the relation:

$$E_B = C_{B,T} E_T \quad (3.47)$$

In the transformation matrix α is the angle of attack and β is the sideslip angle.



(a) The trajectory system is showed with respect to a local vertical system [Castellini, 2008a].

(b) The body system is defined with respect to the air-path reference frame, that is coincident with the trajectory reference frame because no wind is present [Castellini, 2008a].

Figure 3.8: Reference frames. The relation between trajectory frame and local vertical frame and between body frame and trajectory frame is shown.

Vehicle-centered horizontal to body frame, $C_{B,V}$

The transformation matrix to go from the vehicle-centered reference frame to the body reference frame (Fig. 3.9) is [Cornelisse et al., 1979]:

$$C_{B,V} = C_1(\varphi) C_2(\theta) C_3(\psi) = \begin{bmatrix} C\theta C\psi & C\theta S\psi & -S\theta \\ S\varphi S\theta C\psi - C\varphi S\psi & C\varphi C\psi + S\varphi S\theta S\psi & S\varphi C\theta \\ S\varphi S\psi + C\varphi S\theta C\psi & C\varphi S\theta S\psi - S\varphi C\psi & C\varphi C\theta \end{bmatrix} \quad (3.48)$$

where $C\theta = \cos \theta$, etc. and ψ , θ , φ are the Euler angles that link the orientation between the two systems. ψ is the angle between the vertical plane through the longitudinal axis of the rocket and the X_V -axis: the yaw angle; θ is the angle between the longitudinal axis and the local horizontal plane, the pitch angle; and φ is the angle between the z -axis and the vertical plane through the longitudinal axis, called the roll angle. The two systems are related according to [Cornelisse et al., 1979]:

$$E_B = C_{B,V} E_V \quad (3.49)$$

The Euler angles have one drawback that comes out when one of the angles, here the pitch angle, assumes the value $\pm 90^\circ$. In this case (vertical flight), the other two angles are undetermined. In order to avoid this

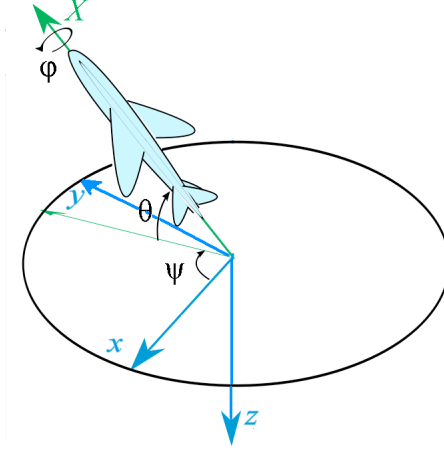


Figure 3.9: Orientation of the body frame with respect to the vehicle-centered horizontal frame.

problem and because the kinematics equations will describe the motion of the rocket in the inertial frame, one can use the *method of direction cosines*. This method focuses on the fact that by expressing the coordinates of the new reference frame with respect to the starting frame we can express the rotation.

The transformation matrix between the inertial geocentric reference frame and the body reference frame will be called $C_{B,I}$ and the relation is [Cornelisse et al., 1979]:

$$E_B = C_{B,I}E_I \quad (3.50)$$

After multiplying this equation by E_I^T , that is the transpose of E_I and, because $E_I \cdot E_I^T = I$ (because E_I is a orthonormal matrix), where I is the identity matrix, the following matrix is obtained [Cornelisse et al., 1979]:

$$C_{B,I} = E_B \cdot E_I^T = \begin{bmatrix} e_x \cdot e_X & e_x \cdot e_Y & e_x \cdot e_Z \\ e_y \cdot e_X & e_y \cdot e_Y & e_y \cdot e_Z \\ e_z \cdot e_X & e_z \cdot e_Y & e_z \cdot e_Z \end{bmatrix} \quad (3.51)$$

The elements of this matrix are the cosines of the angles between the axes of both systems. By defining [Cornelisse et al., 1979]:

$$c_{11} = \cos(x, X) = e_x \cdot e_X, \quad (3.52)$$

$$c_{12} = \cos(x, Y) = e_x \cdot e_Y,$$

etc., one can write

$$C_{B,I} = [c_{ij}] \quad i, j = 1, 2, 3. \quad (3.53)$$

The drawback of using the direction cosines is that you have to deal with 9 variables and not three as in the case of Euler angles. That means six more kinematics equations, but the nine elements of the previous matrix are not independent. Therefore multiplying Eq. 3.50 [Cornelisse et al., 1979]:

$$E_B \cdot E_B^T = C_{B,I}E_I \cdot E_B^T \quad (3.54)$$

Then, because $E_B \cdot E_B^T = I$ and according to Eq. 3.51, $E_I \cdot E_B^T = (E_B \cdot E_I^T)^T = C_{B,I}^T$, it follows from Eq. 3.54 that [Cornelisse et al., 1979]:

$$C_{B,I}C_{B,I}^T = I \quad (3.55)$$

Because of the fact that $C_{B,I}C_{B,I}^T$ is a symmetric matrix, Eq. 3.55 leads to six non-linear equations in the elements c_{ij} . So only three of the nine variables are independent and generally it is not possible to eliminate all six dependent direction cosines. From Eq. 3.55 it follows that the transpose of the matrix $C_{B,I}$, is also its inverse, then the matrix is orthogonal.

The transformation matrix $C_{B,I}$ can also be obtained by applying the transformation $C_{B,V}$, $C_{V,R}$ and $C_{R,I}$ in succession:

$$C_{B,I} = C_{B,V}C_{V,R}C_{R,I} \quad (3.56)$$

One has to notice that the order of the rotations should not be changed because of the fact that matrix multiplication is not commutative.

Quaternions

Quaternions are another way to express rotations and attitude motion in space just like Euler angles are. The advantage they present is that they are free from singularities but on the other side is more difficult to get a direct insight of the rotation itself, that is, it is not easy to understand the way the rotation are being performed. The set of quaternions is composed by 4 parameters of which, the first three are part of a vector while the fourth is not.

$$\mathbf{q} \doteq \begin{Bmatrix} \mathbf{q}_1 \\ q_2 \\ q_3 \end{Bmatrix} \quad (3.57)$$

Of course, transformation matrix between Euler angles and quaternions are provided. Then, given a rotation angle θ and an axis, $\mathbf{e} = [e_x \ e_y \ e_z]^T$, about which this rotation is performed, the 4 quaternions can be obtained using the following:

$$\begin{aligned} q_1 &= e_x \sin \frac{\theta}{2} \\ q_2 &= e_y \sin \frac{\theta}{2} \\ q_3 &= e_z \sin \frac{\theta}{2} \\ q_4 &= \cos \frac{\theta}{2} \end{aligned} \quad (3.58)$$

The 4 quaternions are normalized parameters and obey the equation:

$$q_1^2 + q_2^2 + q_3^2 + q_4^2 = 1 \quad (3.59)$$

If one has knowledge of quaternions' values, obtaining the rotation matrix starting from quaternions follows by using the matrix [Tewari, 2006]:

$$C = \begin{pmatrix} q_1^2 - q_2^2 - q_3^2 + q_4^2 & 2(q_1q_2 + q_3q_4) & 2(q_1q_3 - q_2q_4) \\ 2(q_1q_2 - q_3q_4) & -q_1^2 + q_2^2 - q_3^2 + q_4^2 & 2(q_2q_3 + q_1q_4) \\ 2(q_1q_3 + q_2q_4) & 2(q_2q_3 - q_1q_4) & -q_1^2 - q_2^2 + q_3^2 + q_4^2 \end{pmatrix} \quad (3.60)$$

and the relations between each quaternion and the components of c_{ij} of the rotation matrix are:

$$\begin{aligned} q_1 &= \frac{c_{23} - c_{32}}{4q_4} \\ q_2 &= \frac{c_{31} - c_{13}}{4q_4} \\ q_3 &= \frac{c_{12} - c_{21}}{4q_4} \end{aligned} \quad (3.61)$$

with

$$q_4 = \pm \frac{1}{2} \sqrt{1 + c_{11} + c_{22} + c_{33}} \quad (3.62)$$

3.4 Dynamic system model

In the analysis of the trajectory or trajectory simulation, one is interested in the motion of the center of mass of the vehicle more than its attitude motions. In considering the motion of the center of mass of the vehicle, it is assumed that the body is represented by a point. Therefore, a three degrees of freedom (3 DoF) study is performed. The motion of the vehicle, that could be a launcher or an aircraft, is governed by Newton's

second law². In writing the equations of motion, the aerodynamic, propulsive and gravitational forces have to be known.

The fastest and most robust way to express and integrate the equations of motion is to have them in an inertial Earth-fixed reference frame and expressed in Cartesian coordinates. As it has been said, spherical elements give problems because of singularities, for instance when the launch vehicle is on the launch pad its flight path angle is 90° . So, we have:

$$\mathbf{r}_{\mathbf{cm}} = (x_I, y_I, z_I)^T \quad (3.63)$$

$$\mathbf{V}_{\mathbf{I}} = (\dot{x}_I, \dot{y}_I, \dot{z}_I)^T \quad (3.64)$$

and the following dynamic and kinematic equations of motion:

$$\frac{d\mathbf{r}_{\mathbf{cm}}}{dt} = \begin{pmatrix} \dot{x}_I \\ \dot{y}_I \\ \dot{z}_I \end{pmatrix} \quad (3.65)$$

$$\frac{d\mathbf{V}_{\mathbf{I}}}{dt} = \begin{pmatrix} \ddot{x}_I \\ \ddot{y}_I \\ \ddot{z}_I \end{pmatrix} = \frac{1}{m} [\mathbf{F}_{A,I} + \mathbf{F}_{G,I} + \mathbf{F}_{T,I}] \quad (3.66)$$

where aerodynamic, gravitational and thrust force are expressed in the inertial reference frame [Mooij, 1997].

Since spherical coordinates are used as output coordinates because they give a better insight and understanding about what is happening and the way the vehicle is moving, they will be used to present results to the user.

Since initial conditions for the vehicle are expressed in spherical coordinates, first we need to get (Cartesian) coordinates in the vehicle-centered horizontal frame, then into rotating Earth-centered frame and eventually into the inertial frame. For the velocity vector $(u, v, w)^T$, we first need to derive the velocity vector in the vehicle reference frame and then transform it in the rotating frame. $\mathbf{V}_{\mathbf{v}} = (V_x, V_y, V_z)^T$ is the velocity vector in the vehicle frame and from [Mooij, 1997]:

$$V_x = V_G \cos \gamma \cos \chi \quad (3.67)$$

$$V_y = V_G \cos \gamma \sin \chi \quad (3.68)$$

$$V_z = -V_G \sin \gamma \quad (3.69)$$

Then, the velocity in the rotating frame is computed applying the inverse of transformation matrix 3.42 and then inertial coordinates are obtained applying Eq. 3.13.

For output results, in spherical coordinates, the modulus of the velocity vector can be computed as:

$$V_G = \sqrt{u^2 + v^2 + w^2} \quad (3.70)$$

while flight path angle and heading (azimuth) angle can be computed as [Mooij, 1997]:

$$\chi = \text{atan2}(V_y, V_x) \quad (3.71)$$

$$\gamma = -\arcsin\left(\frac{V_z}{V_G}\right) \quad (3.72)$$

² The net force F applied on a body of mass m produces an absolute acceleration a . This acceleration is measured in a reference frame that does not translate or rotate with respect to the fixed stars (inertial frame).

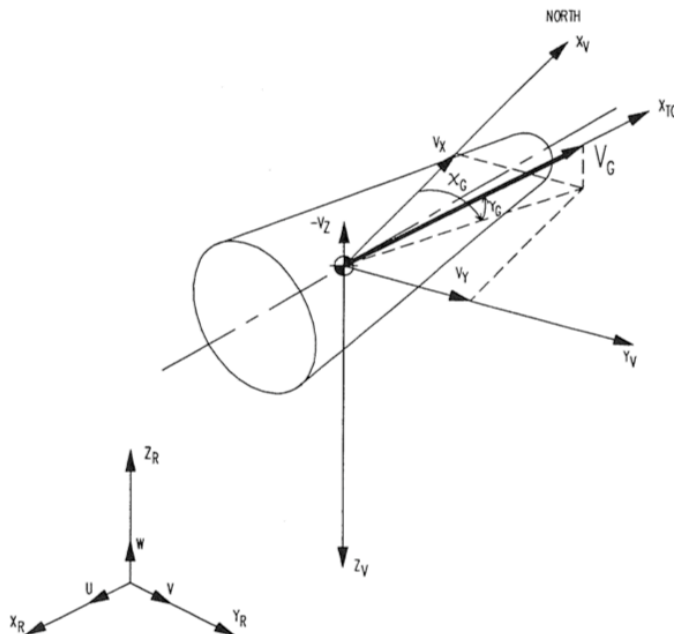


Figure 3.10: Cartesian components. For the computation of the Cartesian velocity $(u, v, w)^T$ in the rotating frame, the spherical velocity $(V, \gamma, \chi)^T$ is first transformed to a Cartesian velocity in the vehicle frame $(V_x, V_y, V_z)^T$ [Mooij, 1997].

Fig. 3.10 clearly depicts how the velocity in spherical coordinates is related to the velocity in the vehicle-centered frame.

3.5 Earth model

Atmosphere

The atmosphere of the Earth can be regarded as a thin layer around the planet. In order to make the analysis of the ascent trajectory more accurate, it is wise to develop a model that describes the properties (temperature, density and pressure) of each layer with a good approximation. The lowest part of the atmosphere (< 15 km) can be considered in thermal equilibrium³ and even though horizontal winds and the presence of vapours perturb it, all atmospheric models focus on vertical variations of thermodynamics variables and neglect those perturbations. Moreover, some models average out all spatial and temporal variations of the atmospheric variables so that one *standard atmosphere* can be provided. On the other hand, another model, namely *reference atmosphere*, takes into account the latitudinal, seasonal, geomagnetic and solar effects but it must be completed with another model at lower altitude (since it is defined for altitude between 90 and 2500 km).

All standard models consider the atmosphere to be divided into different strata: the troposphere (up to 11 km), the stratosphere ($11 \text{ km} < h < 47 \text{ km}$), mesosphere ($47 \text{ km} < h < 86 \text{ km}$) with which the assumption of thermal equilibrium ends, the thermosphere ($86 \text{ km} < h < 500 \text{ km}$) and the exosphere which is indefinite and where electromagnetic effects are predominant [COESA, 1976].

In this work, the 1976 US Standard Atmosphere, [COESA, 1976], has been used. The atmosphere model is divided, like the real atmosphere, into several layers and its structure and properties have been described thoroughly in Pagano [2008].

³ Only when the exchange of heat, between two system in contact, is over, the thermal equilibrium has been reached, [Mandl, 1988].

Earth gravity

Most studies on rocket and launcher trajectory that involve a model of the Earth assume it to be a sphere. Though this assumption does not correspond to reality, because the Earth is much closer to an oblate spheroid, which is the equilibrium shape of a rotating, fluid body, the spherical model is still a good approximation. Instead, for our study, the Earth will be modeled as an ellipsoid of revolution (i.e., an oblate spheroid). This choice is due to the fact that, for mission involving high inclination or polar orbits low Earth orbits, a maximum difference of about 21 km cannot be neglected if one strives for a reliable knowledge of the position of the payload. When considering the Earth as an ellipsoid, the difference of 21 km between the radius at the equator and the radius at the pole has to be pointed out and a parameter called *ellipticity*, that gives a feeling of how much the Earth differentiates from a sphere, is defined [Mooij, 1998]:

$$e = \frac{R_E - R_p}{R_E} = 1 - \frac{R_p}{R_E} \quad (3.73)$$

where:

$R_p = 6,356.752$ m, mean radius at the pole.

$R_E = 6,378.136$ m, mean radius at the equator.

The ellipticity can be used to derive an expression for the radius at an arbitrary point along the surface, R_s . The following expression can be found [Regan and Anandkrishnan, 1993]:

$$R_s = R_E \left[1 - \frac{e}{2} (1 - \cos 2\delta^*) + \frac{5}{16} e^2 (1 - \cos 4\delta^*) - \dots \right] \quad (3.74)$$

Here, δ^* is the geographic (or geodetic) latitude which is, for the ellipsoid, not the same as the geocentric latitude δ . However, since the difference is very small, it is justified to approximate δ^* by δ [Mooij, 1998]. Moreover, for a first-order analysis, one can approximate Eq. 3.74 by:

$$R_s \approx R_E \left[1 - \frac{e}{2} (1 - \cos 2\delta) \right] \quad (3.75)$$

Eq. 3.75 for R_s can be used to define the height above the planetary surface. The height h can be derived from:

$$h = r - R_s \approx r - R_E (1 - e \sin^2 \delta) \quad (3.76)$$

In the matter of the gravitational field, this is assumed to be directed to the centre of the Earth, varying with the latitude and the J_2 factor is included. This term has an important role in perturbing satellite's orbit at low altitudes and it has been included as it becomes more effective when no other major forces act on the system (e.g., orbital coast phase). The gravitational acceleration vector is defined, with respect to the Earth-centered rotating frame, as [Mooij, 1997]:

$$\mathbf{g} = (g_x, g_y, g_z)^T \quad (3.77)$$

where g_x , g_y and g_z are given by (from [Duhamel, 1989]):

$$g_x = -\frac{\mu}{r^3} x \left[1 + \frac{3}{2} J_2 \left(\frac{R_E}{r} \right)^2 \left(1 - 5 \frac{z^2}{r^2} \right) \right] \quad (3.78)$$

$$g_y = -\frac{\mu}{r^3} y \left[1 + \frac{3}{2} J_2 \left(\frac{R_E}{r} \right)^2 \left(1 - 5 \frac{z^2}{r^2} \right) \right] \quad (3.79)$$

$$g_z = -\frac{\mu}{r^3} z \left[1 + \frac{3}{2} J_2 \left(\frac{R_E}{r} \right)^2 \left(3 - 5 \frac{z^2}{r^2} \right) \right] \quad (3.80)$$

where:

$J_2 = 0.0010826$, oblateness parameter of the Earth, [Larson and Wertz, 1999].

r = distance of the launch vehicle from the centre of the Earth [m].

δ = geocentric latitude [rad].

$\mu_e = 398600.4415 \cdot 10^9 \text{ m}^3/\text{s}^2$, gravitational constant of the Earth, [NIMA, 1997].

x, y, z are the Cartesian components of the vehicle in the rotating, Earth-centered frame.

3.6 Aerodynamic forces

Usually, during its motion, a rocket does not maintain its body axis coincident with the velocity vector, which is tangent to the flown trajectory. The angle of attack α , between the launcher body axis and the velocity vector during a guided ascent is kept small ($\alpha < 6^\circ$) in order to avoid drag losses.

When a body moves through the air, it is subjected to a total aerodynamic force that can be broken down into components. The component parallel to the velocity vector, passing through the center of gravity of the body, but directed in the opposite direction is called drag. The perpendicular component is called lift. Obviously, if a rocket trajectory is parallel to its axis no lift is generated. Thus, in the vertical phase, the launch vehicle does not experience any lift, whereas during the turnover lift is generated and during a gravity turn one tries to keep it as low as possible to minimize transverse stress. In this latter case, one should take care that the bending moment given by the product between dynamic pressure and angle of attack does not become too high (e.g., 300 – 400 kPa · deg). Therefore, not only the angle of attack and the dynamic pressure should be kept small but also their product that can cause serious failure in the system.

In this description model no side forces have been considered, first because no wind (so no gusts) is considered and then because the drag and lift force are much larger than lateral forces. Therefore, the components of aerodynamic forces are only two and they are described in an air-path reference frame (coincident with the trajectory system) as:

$$\vec{F}_A = \vec{F}_T = \begin{bmatrix} -D \\ 0 \\ -L \end{bmatrix} \quad (3.81)$$

where the subscript A indicates the air-path reference frame, T the trajectory reference frame, D and L are the drag and lift force respectively.

In analyzing these two forces, the reference area S_{ref} has to be considered. In addition, the angle of attack has to be computed in order to find the correct value of drag or lift coefficient for the given Mach number and aerodynamic attitude. Therefore the following formula has been used (from [ASTOS, 2007]):

$$\alpha = \arctan \left(\frac{v_{T,z}}{v_{T,x}} \right) \quad (3.82)$$

that has been obtained by normalizing the groundspeed based velocity (that is directed along the x -axis in the trajectory frame). Therefore, the obtained unit vector is transformed into the body reference frame:

$$\begin{bmatrix} v_{T,x} \\ v_{T,y} \\ v_{T,z} \end{bmatrix}_B = C_{B,V} C_{V,T} \begin{bmatrix} 1 \\ 0 \\ 0 \end{bmatrix}_T \quad (3.83)$$

where $v_{T,i}$ are the body-fixed components of the unit vector.

As one can see, no sideslip angle has been included in this analysis. In fact, for a 3 DoF analysis, the sideslip angle is set to zero. This means that the launcher steers without sideslipping or that the yaw rate is infinite so that the velocity vector aligns instantaneously with the X_B -axis. In this way, the lift and drag forces are in the load factor plane. The load factor plane is given by $X_B - Z_B$ plane and includes the velocity vector with respect to Earth as well [Zipfel, 2007].

One of the issues of the ascent trajectory analysis problem is given by the fact that launch vehicles experience quite some drag and lift forces during the flight, that are due to the shape and the dimensions of the vehicles themselves, and that, since performances may vary according to the forces experienced, accurate data concerning the aerodynamics of the launchers are needed for a good analysis of the trajectories.

These aerodynamic data principally concern the drag and the lift coefficients, since drag and lift are two forces that, together with thrust and gravitation, are experienced by the vehicle during the ascent. Therefore, when we talk about aerodynamic data, we mean specifically those data.

Not having good and reliable aerodynamic data for the vehicles means that there is an uncertainty in the final results that might affect the characteristics of the whole mission. On the other hand, obtaining precise aerodynamic data of launchers is quite difficult if not almost impossible since, most of the times, these data are kept secret within the manufacturing company and not published nor released. Therefore, it happens that mission analysts have to use rough data or sometimes go through data available from other similar vehicles. However, if one wants to be very precise and full-bore, analysis with vehicles' mock-up in wind tunnels could be performed or, in another way, a computational fluid dynamic (CFD) analysis might be followed to get approximate data. The last two approaches have not been followed but future researches may be dedicated to them in order to understand in which measure the results they produce differ from the current approach.

3.6.1 Drag

The expression for drag is given by:

$$D = \frac{1}{2} \rho(h) S_{ref} C_D(M, \alpha) V^2 \quad (3.84)$$

In this equation, ρ is the air density and varies with the altitude, S_{ref} is the reference area of the vehicle that corresponds to the cross-sectional area of the body, C_D is the drag coefficient, is dependent on the velocity of the body expressed in Mach and on the angle of attack. Usually, tables for this coefficient show its behaviour as function of the two variables.

Values of C_D coefficients reach a maximum when approaching $M = 1$, that represents the transonic part of the flight and in which instabilities in the flow trajectory around the body arise.

For further details on the drag coefficient profiles for the launch vehicles the reader is invited to read Appendix A.

Data for the reference areas of the launchers before and after the jettison of the boosters, if applicable, are presented in Table 3.1.

3.6.2 Lift

In the same way as for drag, lift is expressed by:

$$L = \frac{1}{2} \rho(h) S_{ref} C_L(M, \alpha) V^2 \quad (3.85)$$

where C_L represents the lift coefficient that varies with the Mach number and the angle of attack.

For further details on the lift coefficient profiles for the launch vehicles the reader is invited to read Appendix A.

⁴ <http://www.astos.de>

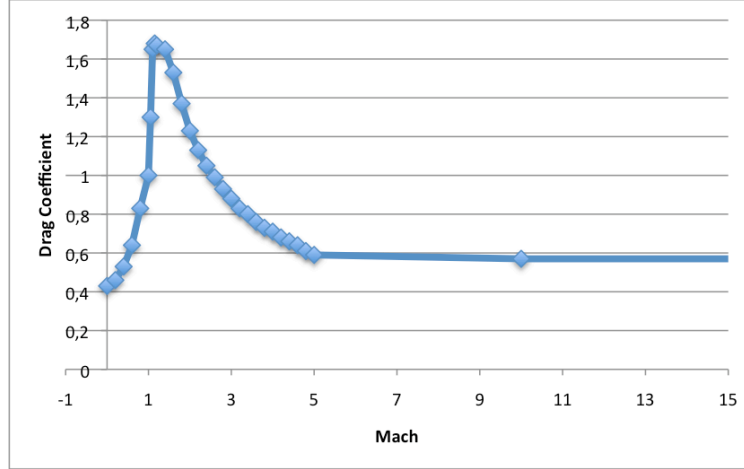


Figure 3.11: Ariane 5 drag coefficient. The data taken from *ASTOS*^{®4} have been interpolated linearly and the behaviour of drag coefficient as function of Mach number has been obtained.

Table 3.1: Reference surface. The reference area for each launcher taken from the user's guides are reported.

	S_{ref} at liftoff [m ²]	S_{ref} after booster separation [m ²]
Ariane 5	37.5	22.9
Vega	7.06	7.06
Proton	25.25	13.2
Atlas V 5 boosters version	25.4	22.9
Atlas HLV	37	22.9
Delta IV Heavy	58.8	19.6

3.7 Propulsion system

The propulsion system is the means that compensates the gravity force and drag, and lifts the entire launch vehicle and makes it fly through the atmosphere until the desired target orbit. Most of existing vehicles are lifted by more engines (a cluster of engines), boosters, and other stages.

The fact that only one stage could not bring a rocket into orbit can be derived from the Tsiolkovsky rocket equation (or ideal rocket equation) [Cornelisse et al., 1979]:

$$\Delta V = I_{sp} g_0 \ln \frac{m_i}{m_f} \quad (3.86)$$

where:

I_{sp} : is the specific impulse of the propellant used [s].

g_0 : is the gravity at sea level [m/s²].

m_i : is the total initial mass of the rocket [kg].

m_f : is the final mass of the stage after stage propellant has been burnt [kg].

If we consider, for instance, a two stage vehicle such as the Ares I (focusing the attention on the performance of the vehicle as imagined and not on the fact that it does not exist), and we use data from Pagano [2008], considering a payload mass of 20 tons, the first stage produces a $\Delta V \approx 4,490$ m/s that is unable to put the launcher in a permanent orbit about the Earth. In fact, the launcher would need a minimum ΔV of 9,300 - 10,000 m/s for an orbit at 200 km altitude (1,500 - 2,000 m/s needed to compensate gravity losses and drag losses, that are losses due to gravitational force and to the drag caused by the atmosphere).

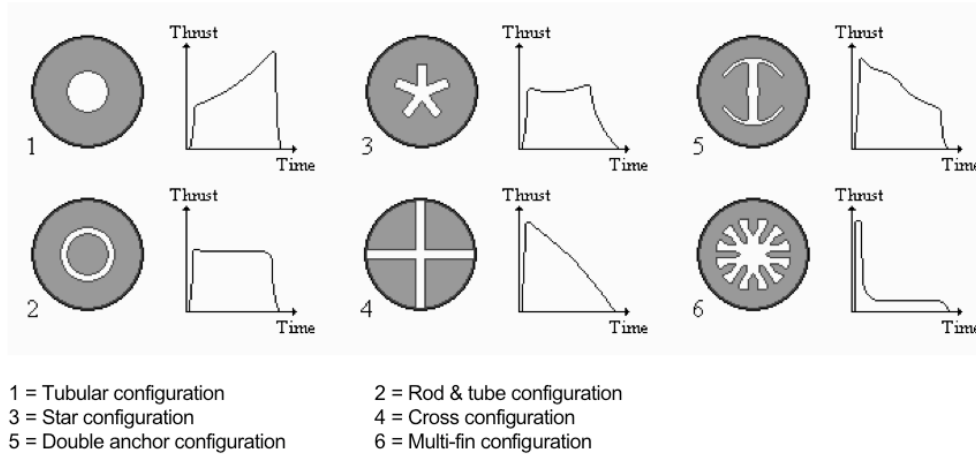


Figure 3.12: Solid propellant grain configuration. Some configurations for solid propellant grain are showed [Zandbergen, 2008].

Rocket motors are based on one principle: accelerate mass and expel it. Then, according to Newton's third law, a reaction force is generated which thrusts the rocket [Cornelisse et al., 1979]. The main problem with the rocket motor, with respect to air-breathing engines, is that they need to take along their propellants, whereas a jet-engine brings only fuel, that burns with atmospheric oxygen. This is due to the fact that rocket motors also have to operate outside the atmosphere, where no oxygen is available. Moreover, this makes them much heavier than jet-engines (because of piping etc.). Actually, at least 95% of the mass of the launch vehicle is made of engines, propellant tanks and structure, and among these, propellants take the lead. The propellants used by actual launch vehicles are mainly liquid or solid. Solid propellants are used mainly for boosters whereas cryogenic ones are used for main and upper stages.

Hereafter, we will not make a detailed description of how a rocket motor works or how we can compute its performance but we will try to model the propulsion system in a reliable and good way in order to make it, in the limits of this study, as closely as possible to reality.

With respect to the assumptions made, regarding the use of a thrust profile for the launch vehicles provided with boosters and the ability to be throttleable between the 60% and the 105% of the nominal thrust, some changes have been made following the way the software was structured. On this side, the boosters' thrust does not follow a thrust profile like the Ariane 5's one but, if it is throttleable it is optimized between the minimum throttle and a 100% nominal thrust. If the thrust is not throttleable, it is assumed to be the nominal thrust.

The thrust force should be throttleable for several reasons. One of these is that when the main or first stage, for instance, is coupled with boosters, the thrust cannot be too large in order to not exceed the load factor or the dynamic pressure and not to stress the structure too much. Thus, the thrust of the main engines has to be throttled to be under the limits and then can be throttled up when the boosters are jettisoned or when the maximum dynamic pressure phase is reached. Moreover, the thrust will be assumed to be aligned with the X_B -axis, that means no thrust misalignment and moments due to thrust vector control is present. Thrust vector control consists in deflecting the hot combusted gases in the wanted direction in order to control the direction of the launch vehicle and it permits also to optimize its performance.

The implementation of coasting phases can also be inserted during the burning of the main stages. On the other hand, this would be feasible for these stages or for those of them that can be restarted but it would seriously increase the risks of the mission. So, for safety and risk issues, this option is not included in this study and in the following analysis.

The thrust force is computed in the body reference frame as:

$$\vec{T}(h) = \begin{bmatrix} T_{vac} - A_e \cdot p_a \\ 0 \\ 0 \end{bmatrix} \quad (3.87)$$

where:

A_e : is the engine nozzle exit area.

p_a : is the atmospheric pressure, varying with the altitude.

T_{vac} : is the vacuum thrust, given for each engine from launch vehicle data.

The mass flow can be computed from:

$$\dot{m} = \frac{\delta_T T_{vac}}{I_{sp} g_0} \quad (3.88)$$

where:

I_{sp} : is the specific impulse in the vacuum and is defined as the impulse delivered per unit weight of propellant.

g_0 : is the gravity at sea level whose value is 9.80655 m/s.

δ_T : is the throttle level and holds $\delta_T \in [0.6; 1.05]$.

In the previous equation the throttle level is a variable that can be optimized in the analysis of the trajectory. Furthermore, from the knowledge of the propellant mass flow, the fuel consumption can be traced step by step.

3.8 Path constraints

In any phase of the flight, the payload is protected by the fairing from aerodynamic loads and from the external environment in general. Usually, the fairing is jettisoned when the heating rate is below an acceptable value that is determined by the launch vehicle owner. In this case the dynamic pressure or bending load do not play any role since their peak is usually reached earlier in the flight. Some of the loads affecting the fairing are a function of the total pressure (static and dynamic pressure) acting on the vehicle. These pressures depend on the altitude and the velocity of the launcher. Therefore, some limitations or constraints need to be set to satisfy the launch vehicle and payload integrity, or the crew safety in case of manned missions or yet the safety of people living close to the launch site area or in the areas covered by the footprint of the trajectory of launcher and/or boosters. This last constraint is necessary, because the stages of the vehicle should not fall on populated areas and not cause any risk.

3.8.1 Dynamic pressure

The dynamic pressure is the component of the pressure given by the fluid that represents the kinetic energy of the fluid (i.e., during the motion). The dynamic pressure is composed of a velocity term and a term that is characteristic of the atmospheric density, yielding the quantity q_{dyn} :

$$q_{dyn} = \frac{1}{2} \rho V^2 \quad (3.89)$$

represents the dynamic pressure where:

ρ : is the atmospheric density.

V : is the velocity of the vehicle with respect to the aerodynamic frame.

Dynamic pressure has two important properties. The quadratic dependence on velocity means that the lift and drag, and the disruptive forces on the rocket, increase very rapidly as the rocket accelerates. The effect of drag on first-stage acceleration is quite significant: the acceleration of the vehicle is often almost constant even though the mass is reducing. The dynamic pressure also depends on the atmospheric density, which decreases rapidly as the rocket gains altitude. Thus, with velocity increasing, and density decreasing, with time after launch, every launcher passes through a condition known as maximum dynamic pressure, or “*maximum q*”. This is the time when the atmospheric forces are at their maximum, and when the risk to the structural integrity of the rocket is greatest. To reduce the risk, if the vehicle’s structure is not tailored to support the loads it experiences during the flight, the engines are throttled down in order to reduce the forces acting on the vehicle. This approach is possible because the peak in dynamic pressure is so sharp, as a

direct result of the exponential reduction in atmospheric density with altitude and the quadratic dependence of the dynamic pressure on velocity [Turner, 2001]. The dynamic-pressure constraints for the launch vehicles selected can be found in Table 3.2.

Table 3.2: Dynamic pressure. The values of maximum dynamic pressure the existing launchers can withstand during the ascent are presented.

Launch vehicle	Maximum Dynamic pressure [Pa]	Source
Ariane 5	40000	Arianespace, <i>Ariane 5 User's manual</i> , Issue 5, Revision 0, July 2008
Delta IV Heavy	17200	Ulalaunch.com, <i>United Launch Alliance Successfully Completes First Operational Delta IV Heavy Launch</i> , DSP-23 Mission Booklet, November 2007
Atlas V 500 series	44000	Lockheed Martin Corporation, <i>Atlas Launch System Mission Planner's Guide</i> , <i>Atlas V Addendum</i> Revision 8, December 1999
Atlas V HLV	20600	Lockheed Martin Corporation, <i>Atlas Launch System Mission Planner's Guide</i> , Revision 10a, January 2007
Proton	40000	International Launch Services, <i>Proton Launch System Mission Planner's Guide</i> , December 2004
Vega	N/A	-

3.8.2 Bending load

Among the several path constraints that might be used when optimizing ascent trajectories, bending-moment constraints have a primary role since they are the most suitable to prevent serious mechanical damages to the launch vehicle. In fact, bending moments are basically the product between the dynamic pressure and the total angle of attack, with which the launcher is flying and is a measure of a structural load. This product is more important than both terms considered singularly, since the launcher can fly trajectories either with a low angle of attack and a high dynamic pressure value or with a relatively high angle of attack and low dynamic pressure value. In both cases the launch vehicle could undergo very high bending moments that might damage it seriously (e.g., the vehicle could break apart). The bending load is given by the formula:

$$n_{bending} = q \cdot \alpha_t \quad (3.90)$$

where α_t is the total angle of attack (see Fig. 3.13) and is computed using the formula ([ASTOS, 2007]):

$$\alpha_t = \arccos(\cos \alpha \cdot \cos \beta) \quad (3.91)$$

where α is the angle of attack and β is the sideslip angle (that in this analysis is zero as mentioned in section 3.6). Therefore, for this research it results:

$$\alpha_t = \alpha \quad (3.92)$$

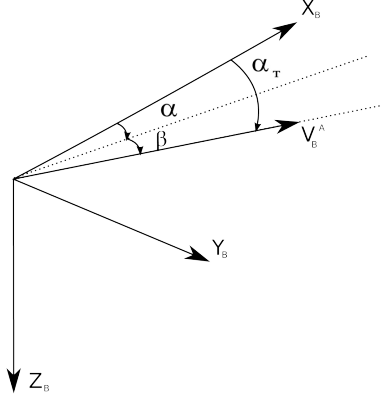


Figure 3.13: Relation between the velocity vector and the body reference frame.

3.8.3 Axial acceleration

During any launch, the payload is protected by the fairing which is the top part of a launch vehicle. The fairing protects the payload from the propulsive loads that, together with dynamic pressure and bending load, are usually called *load factors* and can be measured in terms of g levels. The fuel of a launcher is typically a large percentage of the total mass at launch time. When the fuel of a stage is being depleted while the thrust is kept constant, the acceleration of the vehicle is continuously increasing. At some point the thrust must be reduced, to prevent critical failures for the launcher or the payload [Markl, 2001]:

$$a_x = \frac{T(t) - D(t)}{m(t)g_0} \leq a_{x_{max}} \quad (3.93)$$

where a_x is directed along the longitudinal axis of the vehicle, with $g_0 = 9.80665 \text{ m/s}^2$.

Mainly, this constraint is dictated by the structural properties of the launcher and, in case of manned flights, by safety conditions for the astronauts. The critical values for the actual launchers can be found in Table 3.3. No lateral loads have been analyzed here mainly because the side force has been considered null; however, it might be interesting to take it into account in a more complete model for future research.

3.8.4 Heat flux

In the analysis of constraints, we should take into account the thermal environment. By analyzing it, it is possible to know when the fairing can be jettisoned; the flux is calculated as a free molecular flow acting on a plane surface perpendicular to the velocity direction, and based on the atmospheric model used. Thus, the calculated heat rate is a measure for the amount of energy that the ambient medium will dissipate to the vehicle per unit of time.

The peak heat flux is experienced by the launcher at the stagnation point on the nose. The total heat flux is given only by the convective heat flux. The radiative heat flux has been neglected since for launch vehicles trajectories it is less important because it has very low values with respect to the convective one. As Fig. 3.14 shows, the importance of the radiative heat flux arises at velocities larger than 11 km/s, where for nose radius of about 4.5 m, at 66 km altitude, a heat flux of 1.13 MW/m^2 is generated. At lower speed ($< 7.5 \text{ km/s}$) and with smaller radius of the nose the heat generated is almost null. Therefore:

$$\dot{Q}_{TOT} = \dot{Q}_c \quad (3.94)$$

The convective heat flux [W/m^2] is calculated at the stagnation according to Chapman [1959]:

$$\dot{Q}_c = C \left(\frac{\rho}{\rho_0} \right)^n \left(\frac{V}{V_{circ}} \right)^m \frac{1}{\sqrt{R_N}} \quad (3.95)$$

Table 3.3: Axial acceleration. The maximum axial acceleration for each launcher is showed; these values are taken from launchers' user manual.

Launch vehicle	Maximum axial acceleration	Source
Ariane 5	4.55	Arianespace, <i>Ariane 5 User's manual</i> , Issue 5/ Revision 0, July 2008
Delta IV Heavy	5.55	United Launch Alliance, <i>Delta IV Payload Planners Guide</i> , September 2007
Atlas V 500 series	4.6	Lockheed Martin Corporation, <i>Atlas Launch System Mission Planner's Guide</i> , Revision 10a, January 2007
Atlas V HLV	5	Lockheed Martin Corporation, <i>Atlas Launch System Mission Planner's Guide</i> , Revision 10a, January 2007
Proton	4	International Launch Services, <i>Proton Launch System Mission Planner's Guide</i> , Revision 7, July 2009
Vega	5.5	Arianespace, <i>Vega User's manual</i> , Issue 3/ Revision 0, March 2006

where for the free stream:

$$C = 1.1097 \cdot 10^8 \text{ W/m}^{3/2};$$

$$n = 0.5;$$

$$m = 3.0;$$

$$V_{circ} = 7,905 \text{ m/s};$$

$$\rho_0 = 1.225 \text{ kg/m}^3;$$

R_N is the nose radius of the launcher and several data can be found in Table 3.4.

For all the launch vehicles the maximum free molecular heating rate is equal to or less than $1,135 \text{ W/m}^2$. However, this value is the value after which the fairing can be jettisoned. To avoid exposing the fairing of the launch vehicle to very high values of heat flux that can damage or degrade its properties, a constraint is usually imposed during the trajectory. Finding heat flux limits for the launch vehicles is not easy since this information is secret within the companies that manufacture the vehicles. Therefore, some first order considerations have to be made. In Fischer [2005], some trajectory analysis plots show that, for Ariane 4, the maximum heat flux value is about 80 kW/m^2 . It is not unrealistic to think that, since this launch vehicle has been developed in the '80s and updated in the '90s, the new Ariane 5 or other heavy launch vehicles, that are meant to carry heavier payload, have a higher heat flux limits. Therefore, based on this assumption, we will assume peak heat flux limits as $100 - 120 \text{ kW/m}^2$.

Anyway, the aforementioned method is not the only one approach available. The material properties of the fairing, among which the maximum temperature is the most important, can be assessed. Then, the convective heat flux can be evaluated using Fay-Riddell and Boltzmann formulas, [ASTOS, 2007].

3.8.5 Geographical constraints

Geographical constraints are represented by the launch and flight azimuth that a launcher can be given. The flight azimuths are limited by available stage and fairing impact areas along the flight trajectory. The impact areas have to satisfy conditions on safety of populations living nearby. Actually, each launch site has its own azimuth range into which is possible to launch. Moreover, these ranges are also restricted by the

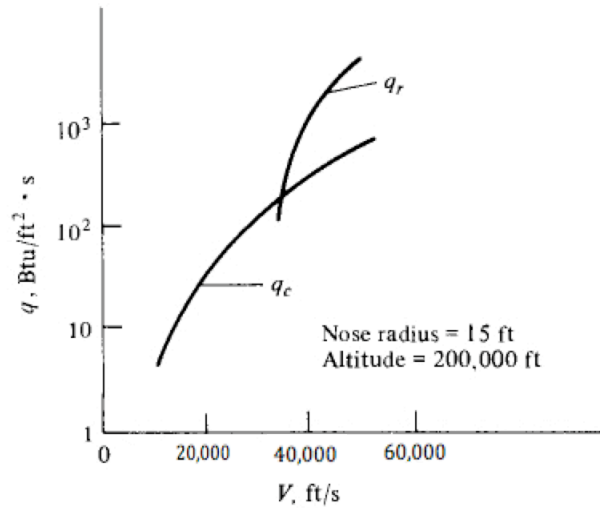


Figure 3.14: Importance of the radiative heat flux compared to the convective heat flux in the case of re-entry vehicles. Units are expressed in the Imperial system, [Anderson, 2001].

Table 3.4: Nose cone radius. The nose cone radius of the launch vehicles and the corresponding material are shown. All data are taken from launch systems user's guides.

Launch Vehicle	Nose cone radius [mm]	Remarks
Ariane 5	506	composite
Delta IV Heavy	661/724	661 for composite / 724 for metallic fairing
Atlas V 500 series	723.9	composite
Atlas V HLV	723.9	composite
Proton	164.5	composite
Vega	290	composite

availability of tracking stations. However, since the azimuth for vertical take-off is undefined it cannot be imposed on the first few seconds of flight time. A list of permitted azimuth ranges for each launch site can be found in Table 3.5.

Table 3.5: Locations of launch sites. Inclination, azimuth and launchers available for each launch site are presented (based on [Vallado, 2001]).

Site	Latitude	Azimuth Min	Azimuth Max	Min Incl.	Max Incl.	Available launchers
Kourou	5.2° N	349.5°	93.5°	5°	100°	Ariane 5, Vega
Baikonur ⁵	45.6° N	22.5°	61.3°	49°	99°	Proton
Cape Canaveral	28.5° N	0°	112°	28°	57°	Atlas V series and Delta IV Heavy

⁵ Only three corridors for the azimuth are available: 22.5°, 35°, 61.3°.

Chapter 4

Guidance programme

During its ascent, the launch vehicle performs a series of maneuvers in order to reach the desired final orbit. These maneuvers are executed, optimally, to minimize the fuel consumption and maximize the final payload mass. A general, widely accepted, guidance scheme involves four main sections. At the launch pad, the vehicle is accelerated vertically until the launch tower is cleared. Then, a pitch-over maneuver is executed to achieve a well defined interface with the subsequent gravity turn. Eventually, the vehicle is aimed to reach the target orbit conditions [Markl, 2001].

In the following section, the reference guidance programme followed by the majority of the launch vehicles is described. The programme can also be seen as a way to divide the ascent trajectory into phases for which, depending on the specific guidance law, a set of optimizable parameters can be defined. By means of the integration process, i.e., propagation of the state of the vehicle, the continuity of the state variables is ensured. Roll (in the particular case of non axial-symmetric launcher), pitch and yaw are typical guidance variables of a launch vehicle. In this work, as all the launchers considered are axial-symmetric, the roll angle does not have any meaning but it is assumed to be null to avoid problems during frame transformations, [Castellini, 2008a].

The division of phases, on the basis of boosters and stages jettison, is done according to the configuration and architecture of each launch vehicle. Besides the optimization of the parameters typical of the yaw and pitch guidance laws, for engines the throttle setting is optimized as well. In this study, the reference guidance programme adopted will be the same used in [Castellini, 2008a], in turn taken from [Markl, 2001]. It is used in many ascent trajectory optimization problems (see [Well, 2004] and [Brusch, 1976]). The following guidance laws will be described hereafter:

- Vertical lift-off
- Pitch turnover
- Gravity turn
- Bi-linear tangent law
- Orbital coast phase and circularization

The task of the optimizer is to determine the evolution of the guidance achieving the optimal parameters or control values. Depending on the type of control law, the optimizer finds better values of the parameters typical of the guidance law or finds the values of the pitch and yaw in the neighborhood of a reference value (e.g., for the yaw control or during the gravity turn phase) that gives the best fitness of the problem.

Even if the aforementioned approach will be used, a new method that is worth future research and investigation is mentioned. As the described guidance laws will require a large number of optimization variables (between 10 and 20), a method that decreases the optimization variables and improves speed computation would be desirable. This alternative method express the pitch, yaw and throttle function as polynomials:

$$\theta(t) = a_0 + a_1t + a_2t^2 + a_3t^3 \quad (4.1)$$

With this method, only a_n coefficients need to be optimized, and in this case they are only 4 (but lower or higher order can be considered). If we take also 4 for yaw and thrust profile, we need to optimize 12 variables. Moreover, a further condition can be applied. The derivative of the control function and a relative constraint on this can be taken. This can be used to guarantee the smoothness of the control profile, mainly for yaw and pitch angles, and avoid the bang-bang problems or instantaneous variations of the control angles.

For instance, for pitch history we would have:

$$\dot{\theta}(t) = a_1 + 2a_2t + 3a_3t^2 \quad (4.2)$$

with a possible constraint:

$$\left| \dot{\theta}(t) \right| \leq 5 \text{ deg/s} \quad (4.3)$$

4.1 Initial conditions

When writing the model that describes the entire trajectory optimization problem, one has to provide the initial conditions of the launch system. From this point on (i.e., the launch pad), the integrator will numerically propagate the equations of motion step by step. In this work, the initial conditions are given by the mass of the launcher at lift-off including a reference payload mass, the position on Earth given by latitude, longitude and altitude of the launch site, initial velocity (0 m/s at lift-off), and flight path angle γ approximately equal to 90° , because the first part is a vertical ascent. The heading angle is not defined in the vertical phase but, since this initial set will be converted to a Cartesian set, the heading angle has been set to 90° or to a value consistent with the permitted launch-site azimuth range. This value has been chosen in order to facilitate the successive pitch over phase to be directed towards this particular azimuth that, according to Eq. 3.33, gives the lowest inclination reachable from a given latitude (that theoretically gives the largest payload mass). Of course, if azimuth constraints apply, the heading angle should be constrained in the permitted range.

The aforementioned set of variables gives the position of the launcher in the rotating reference frame. Usually the point mass describing the vehicle is not attached in the exact position mentioned before, but it is located some meters higher, and it is found in the center of mass, or barycenter, of the vehicle. This reflects the fact that the barycenter of a launcher is some 10 meters high from the bottom of the launcher itself. Initial conditions are given in spherical coordinates but, before the propagation starts, they are converted into Cartesian coordinates:

$$\begin{aligned} r &= r_{LS} + 10 \text{ m} \\ \tau &= \tau_{LS} \\ \delta &= \delta_{LS} \\ V &= 0 \text{ m/s} \\ \gamma &= 90 \text{ deg} \\ \chi &= 90 \text{ deg} \end{aligned} \quad (4.4)$$

where the variables with the subscript LS refer to the launch site¹.

4.2 Vertical Lift-off

Since on the launch ramp the rocket is standing in a vertical position, the natural way to lift-off is to fly a vertical trajectory. The vertical lift-off consists of flying with a pitch angle of 90° . Since it is a high-gravity loss phase, the launcher flies with this attitude for a very short time after which it is kicked in order to start the pitch over phase. The trajectory is propagated over the time span $\mathbf{0} < \mathbf{t} < \mathbf{t}_{F1}$ using this guidance law.

In this phase there are no optimizable parameters for the guidance law. The pitch and yaw values are:

$$\theta = \frac{\pi}{2} \quad (4.5)$$

¹ In the case of r_{LS} , this can be taken as the distance of a point on the surface that varies with the latitude using Eq. 3.75.

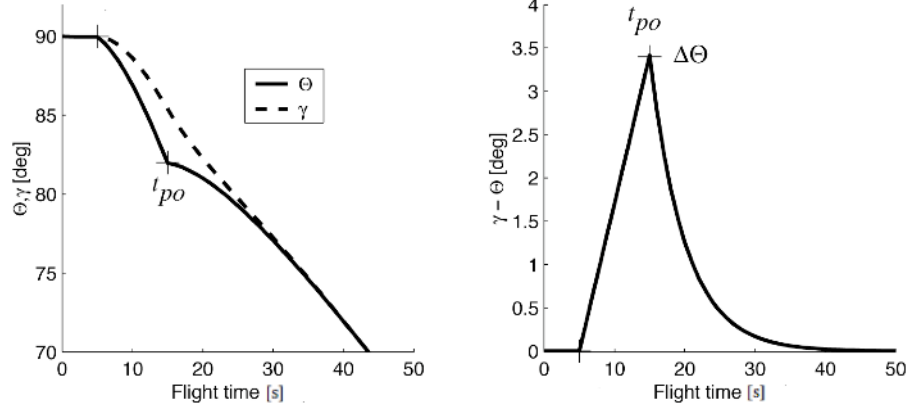


Figure 4.1: Pitch-over maneuver: the linear decrease and the following exponential decay is shown [Markl, 2001].

$$\psi = \psi_0 \quad (4.6)$$

where ψ_0 is given by the target inclination law given in Eq. 4.8. Since the flown phase is vertical, the yaw angle does not influence the attitude of the rocket, but it is needed to go from one frame to the other during the propagation of the trajectory.

4.3 Pitch turnover

Right after lift-off, the launch-vehicle attitude needs to be inclined in order to avoid further gravity losses and, later, to be ready to fly the gravity turn phase. This very phase that prepares the vehicle to achieve the previous mentioned condition is the pitch turnover flown over the time span $\mathbf{t}_{F1} < t < \mathbf{t}_{F2}$. First, a linear pitch over decrease and later an exponential decay of the pitch, to connect this phase to the successive gravity turn, are used, following Castellini [2008a]. While the linear pitch-over maneuver moves the launcher off the 90° pitch attitude, the exponential decay is needed to bring the pitch value close to the flight path angle value to start the gravity turn. If this does not occur, there might be a jump in the values of the pitch and flight path angle at the connection of the two phases (pitch over and gravity turn). In addition, the exponential decay should decrease the possible angle of attack that might generate when the gravity turn starts and keep the bending load low. Fig. 4.1 might make the idea more clear.

$$\begin{cases} \theta = \gamma - \frac{t-t_{F1}}{\Delta t_{TO}} \Delta\theta & \text{for } t_{F1} < t < t_{F1} + \Delta t_{TO} \\ \theta = \gamma - \Delta\theta \exp\left(-\frac{t-t_{TO}}{t_c}\right) & \text{for } t_{F1} + \Delta t_{TO} < t < t_{F2} \end{cases} \quad (4.7)$$

where Δt_{TO} is the duration of the linear pitch over, t_c is a parameter of the rotational dynamics of the launcher and $\mathbf{t}_{F2} = \mathbf{t}_{F1} + \Delta t_{TO} + 3t_c$. The optimizable variable is given by $\Delta\theta$ and the range in which the optimizer looks for it is $1^\circ \leq \Delta\theta \leq 10^\circ$.

Concerning the yaw, we have:

$$\begin{cases} \psi_{ref} = \arcsin\left(\frac{\cos i_T}{\cos \delta}\right) & \text{if } -1 < \frac{\cos i_T}{\cos \delta} < 1 \\ \psi_{ref} = \frac{\pi}{2} & \text{if } \frac{\cos i_T}{\cos \delta} > 1 \\ \psi_{ref} = -\frac{\pi}{2} & \text{if } \frac{\cos i_T}{\cos \delta} < -1 \end{cases} \quad (4.8)$$

where i_T is the inclination of the final orbit and δ is the latitude of the vehicle.

In this case the optimizer looks for the best yaw values around the reference value given by Eq. 4.8. The range in which the optimizer looks is $-20^\circ \leq \psi_{ref} \leq +20^\circ$.

4.4 Gravity turn

The third maneuver, called gravity turn, is flown to reduce the aerodynamic loads on the vehicle by keeping the angle of attack close to zero degrees. This maneuver is flown by the launcher first in its initial configuration and then in the configuration after the boosters' jettison (if included), staging and payload fairing jettison. It consists of an optimized pitch in the neighbourhood of a gravity-turn maneuver, and of an optimized yaw in the neighbourhood of a target inclination law.

The initial conditions are those at the end of the previous phase and the complete equations of motion are integrated over a time span $t_{F2} < t < t_{F3}$, where t_{F3} is the burn-out instant of the last stage before the upper one. No modifications to the guidance law occur due to boosters and/or payload-fairing jettison. This phase is repeated for the number of lower stages of a launch vehicle, for instance if the launcher has three stages and four boosters, the gravity turn is repeated for the first stage with boosters, the first stage after boosters jettison and second stage. Moreover, in between the stage separation, coasting phases can be included. This solution does not change anything except that there is no thrust and the coasting time has to be optimized. In this case, i.e., for launch vehicles with more stages, this time interval can be divided into more intervals according to the number of booster and stages and coasting arcs. This means that, in the case of the launcher with boosters and three stages, we will have 5 intervals, respectively:

1. interval with first stage plus boosters burning;
2. interval with first stage only (after boosters jettison; in fact, usually, the first stage thrusting together with boosters lasts longer);
3. interval of coasting arc between first and second stage;
4. interval with the second stage thrusting;
5. interval of coasting arc between the second stage and the upper stage.

This follows an empirical law in which the number of time intervals is given by:

$$N_{coast} = 2 \cdot N_{stages} - 1 \quad (4.9)$$

where the time intervals can be included in the global time span from t_{F2} to t_{F3} and their duration can be optimized in a range given by the user.

The gravity turn condition corresponds to:

$$\theta = \gamma \quad (4.10)$$

where γ is the flight path angle.

This control law permits to fly with a zero angle of attack, minimizing the drag losses, although this produces gravity losses. In order to minimize also these losses, it is used as a reference around which an optimal value has to be found. The range in which the optimizer will work is given by $\gamma - 10^\circ \leq \theta_i \leq \gamma + 10^\circ$, where θ_i is the value of the of the pitch angle at the specific node.

The same holds for the yaw control. Eq. 4.8 and the same range applies here as well.

4.5 Bi-linear tangent law

The fourth phase of the modelled launch is performed by the launcher's upper stage and consists of a bi-linear tangent law for pitch and an optimized yaw in the neighbourhood of a target inclination law for yaw. As it has been shown in [Markl, 2001], in place of the optimized pitch control, use of the bi-linear tangent law can be made. The results given by the two control laws are nearly identical², but the bi-linear tangent has only three design variables, making the optimization process more efficient.

² This is valid under specific conditions as flat planet, constant gravitational field and negligible atmospheric drag. It has to be remarked that this type of guidance is only used during the exoatmospheric phase and, in this case, drag can be neglected. In addition, the bi-linear tangent law has been proved to be the optimal solution for spherical Earth as the optimal pitch control is for the flat model, [Perkins, 1966].

Initial conditions for integration of equations of motion are those coming from the last phase over a time span $t_{F4} < t < t_{F5}$, where t_{F5} is either the burn-out of the last stage or its shut down before the ballistic orbital arc preceding the circularization burn.

Actually, the bi-linear tangent law is the solution of a control problem called “the maximum velocity transfer to rectilinear path” (see [Bryson and Ho, 1979]):

Consider a particle of mass m , acted upon by a force of magnitude ma . We assume planar motion and use an inertial coordinate system x, y to locate the particle; the velocity components of the particle are u, v . The thrust-direction angle $\beta(t)$ is the control variable of the system.

...

We wish to transfer the particle to a path parallel to the x -axis, a distance h away, in a given time T with the maximum value of $u(t)$.

Although this law is valid only under certain conditions, it can be used with good results also for the guidance of rockets. The control β is replaced by the pitch angle θ and the distance h by the perigee altitude of the target orbit.

The bi-linear tangent law, obtained from [Markl, 2001], is:

$$\tan \theta = \frac{a^\xi \tan \theta_0 + (\tan \theta_f - a^\xi \tan \theta_0) \hat{t}}{a^\xi + (1 - a^\xi) \hat{t}} \quad \text{with} \quad \hat{t} = \frac{t - t_{F4}}{t_{F5} - t_{F4}} \quad (4.11)$$

where $a > 1$ is an arbitrary constant, θ_0 and θ_f are the initial and final values of the pitch angle and $\xi \in [-1; 1]$ is a measure of the curvature of $\tan \theta$ profile. The previous three parameters are the optimizable ones with the boundaries given by:

- $\theta(t_{F4}) - 20^\circ \leq \theta_0 \leq \theta(t_{F4}) + 20^\circ$;
- $-90^\circ \leq \theta_f \leq +90^\circ$;
- $-1 \leq \xi \leq 1$.

The parameter a has been fixed to 100 because with this value and a ξ in the aforementioned range, the pitch can assume a wider range of values (as seen in Fig. 4.2). However, for further investigations, also the parameter a can be included in the optimization.

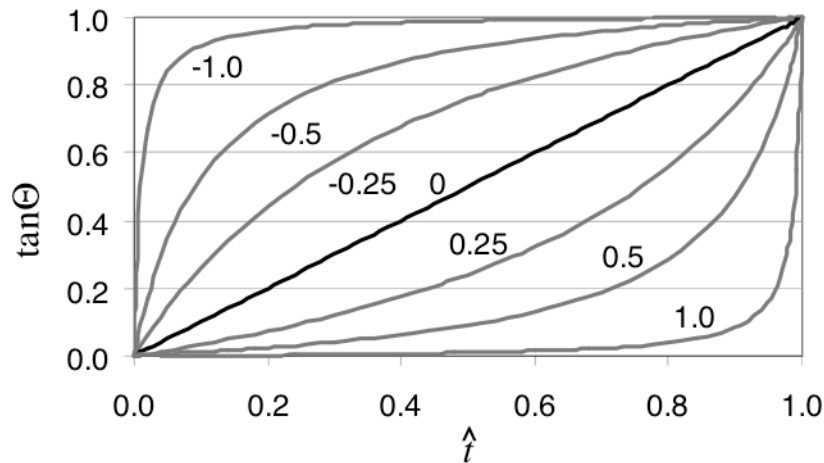


Figure 4.2: Pitch angle bi-linear tangent law. The effect of the curvature parameter is shown, for that covers a wide range of curvatures. The end value are $\tan \theta_0=0$ and $\tan \theta_f=1$, respectively, [Markl, 2001].

As yaw control law Eq. 4.8 holds and the same range for the search.

4.6 Orbital coast phase and circularization burn

As it has been done in [Castellini, 2008a], a circularization is needed to reach a circular orbit (especially those higher than 250-300 km) and this can be more efficient by using two burns of the upper stage. In fact, if the launcher tries to reach the final orbit with a direct ascent, it has to thrust all the way to the apocenter of the orbit. A more efficient approach involves the launcher thrusting up till the pericenter of a transfer orbit, with the apocenter equal to the final altitude of the circular orbit, is reached. From there, a orbital coast, in which only gravitation is active, is flown till the apocenter is reached where a burn is given to circularize the trajectory. The method is more efficient in terms of fuel consumption since the launcher does not have to thrust (and consume propellant) for a long period as in the case of the direct ascent. The motion is propagated until a true anomaly equals to $180^\circ + \Delta\theta^*$ is reached.

At this point, another guidance variable is used to fix the time of ignition of the engines for the final burn that lasts until the target semimajor axis has been reached. The remaining propellant cannot be converted into added mass for payload, because the payload mission will continue (it has to arrive at the Moon).

The optimizable variable here is $-10^\circ \leq \Delta\theta^* \leq +10^\circ$.

A summary of the described guidance laws can be seen in Table 4.1.

Table 4.1: Ascent trajectory guidance programme. A complete summary of the guidance program is reported (time intervals, fixed parameters and optimization variables are summarized for the different phases of the flight).

Phase	Time interval	Pitch guidance law	Yaw guidance law	Guidance fixed parameters	Guidance optimization variables	Guidance variables boundaries
1	$0 < t < t_{F1}$	Constant pitch 90°	none	$H_{\text{clear}} = 50 \text{ m}$ $\Theta = 90^\circ$	none	none
2	$t_{F1} < t < t_{F2}$	Pitch turnover	Constant $\Psi = \chi = \Psi_0$	$\Delta t_{TO} = 10 \text{ s}$ $t_c = 3 \text{ s}$	$\Delta\Theta, \Psi_0$	$1^\circ < \Delta\Theta < 10^\circ$ $\tilde{\Psi} - 20^\circ < \Psi_0 < \tilde{\Psi} + 20^\circ$
3	$t_{F2} < t < t_{F3}$	Optimized gravity turn	Optimized target inclination	none	Θ_i, Ψ_i $i = 1, \dots, N_p$	$\gamma - 10^\circ < \Theta_i < \gamma + 10^\circ$ $\Psi_{ref} - 20^\circ < \Psi_i < \Psi_{ref} + 20^\circ$
4	$t_{F3} < t < t_{F4}$	Bi-linear tangent law	Optimized target inclination	none	$\Theta_0, \Theta_f, \xi, \Psi_i$ $i = 1, \dots, N_p$	$\Theta(t_{F3}) - 20^\circ < \Theta_0 < \Theta(t_{F3}) + 20^\circ$ $-90^\circ < \Theta_f < 90^\circ$ $-1 < \xi < 1$ $\Psi_{ref} - 20^\circ < \Psi_i < \Psi_{ref} + 20^\circ$
5	$t_{F4} < t < t_{F5}$	none	none	Circularization option	$\Delta\theta^*$ (Keplerian EOM)	$-10^\circ < \Delta\theta^* < 10^\circ$

Chapter 5

Optimization

A thorough overview and survey of the most known optimization methods and techniques has been carried out in [Pagano, 2008]. It will not be repeated here again, but the formulation of the optimization problem will be given together with a presentation of the difference between a global and a local optimization. In addition, the general formulation of the optimization problem will be applied to the ascent trajectory optimization problem.

5.1 The general optimization problem

The general optimization problem is to find a set of parameters or design variables \bar{x} , which minimize or maximize a system characteristic that is dependent on \bar{x} . The vector \bar{x} is defined as:

$$\bar{x} = (x_1, x_2, \dots, x_n)^T \quad (5.1)$$

The objective, or cost function $f(\bar{x})$, to be optimized might be subject to constraints (equality and inequality). These constraints limit the solution space and determine the feasible solution space \mathbf{X} .

The optimization problem has the following form:

$$\min f(\bar{x}) \quad (5.2)$$

subjected to respectively the equality and the inequality constraints:

$$g_i(\bar{x}) = 0 \quad \text{for } i = 1, 2, \dots, j \quad (5.3)$$

$$g_i(\bar{x}) \geq 0 \quad \text{for } i = j + 1, \dots, m \quad (5.4)$$

where j is the number of equality constraints and $m-j$ is the number of inequality constraints. The number of equality constraints is generally smaller than the number of parameters x_i , otherwise the solution would be already determined.

There is no fundamental difference between minimization and maximization. A maximum of a function can be determined by a minimization operation using [Visser, 2007]:

$$\max f(\bar{x}) = -\min [-f(\bar{x})] \quad (5.5)$$

A difference is made between a static and dynamic optimization problem. Static optimization is frequently referred to as parameter optimization. In contrast to dynamic optimization, the system variables \bar{x} of a static optimization problem are not time varying [Visser, 2007].

Except for simple problems which can be solved analytically, the solution to more complex problems can only be obtained by using a numerical method. The problem of an optimal ascent trajectory is a complex problem so numerical optimization techniques will be used.

5.2 Ascent trajectory optimization problem

The problem of trajectory optimization is a nonlinear¹ problem which is described by ordinary differential equations. The *state equation* is given by the following equation [Visser, 2007]:

$$\dot{\bar{x}} = \bar{f}[\bar{x}(t), \bar{u}(t), t] \quad (5.6)$$

where $\bar{x}(t)$ contains the state variables and $\bar{u}(t)$ contains the control variables.

Both the state variables and the control variables may be subjected to certain physical constraints. These constraints are called *path constraints* that can be written in the form:

$$\bar{g}(\bar{x}, \bar{u}, t) \geq 0 \quad (5.7)$$

A control history which satisfies the control constraints is called an *admissible control* and a state trajectory which satisfies the state variable constraints is called an *admissible trajectory* [Visser, 2007].

Also *boundary constraints* are present. They specify the initial conditions and the required final conditions of the problem and can be expressed as:

$$\psi_0(\bar{x}_0, t_0) \geq 0 \quad (5.8)$$

$$\psi_f(\bar{x}_f, t_f) \geq 0 \quad (5.9)$$

The general performance criterion, performance index or *objective function* is defined as [Visser, 2007]:

$$J = \phi[\bar{x}(t_f), t_f] + \int_{t_0}^{t_f} L[\bar{x}(t), \bar{u}(t), t] \quad (5.10)$$

where ϕ and L are scalar functions. The end cost term ϕ only depends on the final state while the second term can be seen as an accumulated cost term. If an optimization problem has a performance index as given in Eq. 5.10, the problem is known as the Bolza problem. If ϕ or L is equal to zero, the problem is a Lagrange problem or a Mayer problem, respectively.

Starting from the initial state and applying a control $\bar{u}(t)$ causes the system to follow some trajectory and the performance criterion J assigns a unique real number to each trajectory of the system.

The tasks to be performed take the form of initial and terminal boundary conditions and the trajectory optimization problem or optimal-control problem can be stated as follow [Visser, 2007]:

From among all admissible control functions \bar{u} , find the one which minimizes J subject to the dynamic constraints of Eq. 5.6 and all initial and terminal boundary conditions that may be specified.

The particular control function $\bar{u}^*(t)$ that minimizes J is called an optimal control and the corresponding state history $\bar{x}^*(t)$ is called an optimal trajectory.

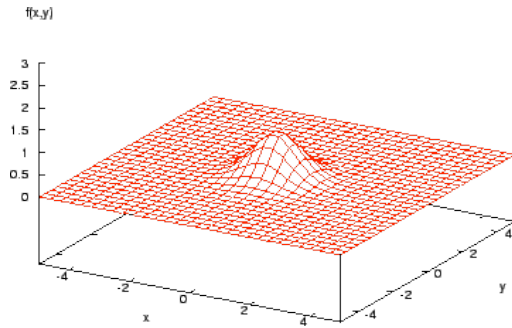
In an optimization scheme, the design variables (here the control functions) are usually the input to the state equations which describe the dynamics of the system. After an evaluation of these equations, the objective function can be evaluated to judge the acceptability of the set of proposed design variables.

5.3 Optimization techniques overview

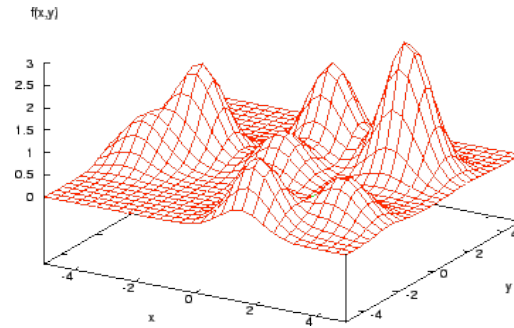
The numerical optimization techniques can be split into two major classes: local and global optimization techniques. The difference between local and global optimization can be explained using Fig. 5.1a and 5.1b. A local optimizer will have no problem in finding the optimum of the function as shown in Fig. 5.1a. For more complex functions as the one in Fig. 5.1b a local optimizer may miss the target, the highest peak, when the search algorithm starts in the neighbourhood of a lower peak. Global optimizers do not have this problem and could find, but that is not always guaranteed², the global optimum.

¹ A nonlinear problem arises when a linear combination of independent components of the variables of the problem cannot be written down.

² Only global optimization methods that use interval analysis provide rigorous guarantees that a global optimum is found, for more information see <http://www.cs.sandia.gov/opt/survey/interval.html> or [Moore, 1966].



(a) This peak is easy to be found with a local optimizer [Kemp, 2008].



(b) The highest peak is easy to be found with a global optimizer [Kemp, 2008].

Figure 5.1: Single and multi-peak functions.

Moreover, a local optimizer would need an initial guess from which it can start looking for the optimum. This aspect requires a minimum knowledge of and insight in the problem to analyze which might not always be the case. On the other hand, global optimizers do not need an initial guess, because the initial guess or population is created randomly in the search space. This property of this type of optimizer makes them attractive to be used by people who do not have a deep insight of the problem.

Both local and global optimization techniques can be classified further into different methods, based on [Noomen, 2008]:

- Local optimization techniques
 - Calculus based (gradient based) methods
 - * Nonlinear programming
 - * Steepest Descent
 - * Newton's method
 - Numerical methods
 - * Direct shooting
 - * Multiple shooting
 - * Collocation
- Global optimization techniques
 - Enumerative methods
 - * Dynamic Programming
 - * Genetic Algorithms
 - * Simulated Annealing
 - * Particle Swarm Optimization
 - * Differential Evolution
 - * Interval analysis
 - Random methods
 - * Monte Carlo

For a further review of the local and global methods listed here, the reader is referred to [Pagano, 2008].

5.4 Multi-objective optimization

Usually practical problems involve several criteria of optimality. For instance, in the Earth-Moon transfer we might be interested in minimizing the propellant consumption, but the same mission could involve the presence of human beings and therefore the time of flight has to be also minimized for safety reason. The problem, set in this way, consists of at least two parameters equally important in defining the best solution. Combining these two objectives functions defines a multi-objective optimization problem [Goldberg, 1989], [Chung and Alonso, 2004].

One approach to handle multiple objective optimization problems is to combine the objective functions into a single scalar objective F by averaging each objective function f_i and then weighing their influence to the overall objective function through weighting factors w_i [Goldberg, 1989], [Chung and Alonso, 2004]. On the other hand, this solution introduces new parameters in the form of weighting factors, to which the individual solution is very sensitive. The determination of the correct weighting factors can, therefore, become an optimization process on its own. Moreover, the user could be interested in a set of optimal solutions trading between different objectives rather than a single value. It therefore becomes desirable to develop a more robust, multi-objective algorithm, able to identify the relationships between objective functions and to produce complete sets of optimal solutions. In the case of minimization of D objectives, the problem can be expressed as

$$\min \bar{f}(\bar{x}) = [f_1(\bar{x}), f_2(\bar{x}), \dots, f_D(\bar{x})] \quad (5.11)$$

subject to j equality constraints and $m - j$ inequality constraints:

$$\bar{g}(\bar{x}) = [g_1(\bar{x}), g_2(\bar{x}), \dots, g_i(\bar{x})] = 0 \quad \text{for } i = 1, 2, \dots, j \quad (5.12)$$

$$\bar{g}(\bar{x}) = [g_1(\bar{x}), g_2(\bar{x}), \dots, g_i(\bar{x})] \geq 0 \quad \text{for } i = j + 1, \dots, m \quad (5.13)$$

Such a problem finds solutions in the theory of Pareto optimization, named after the Italian sociologist and economist Vilfredo Pareto (1848-1923). The Pareto-optimal set is a family of points, which is optimal in the sense that no improvement can be achieved in any objective function without degradation in one or more of the other ones.

Following [Fieldsend, 2004], the concept of Pareto optimality will be made clearer by using the notion of *dominance*. A decision vector \mathbf{u} is said to *strictly dominate* another decision vector \mathbf{v} (denoted $u \prec v$) if

$$\begin{aligned} f_i(u) &\leq f_i(v) \quad \forall i = 1, \dots, D \quad \text{and} \\ f_i(u) &< f_i(v) \quad \text{for at least one } i \end{aligned} \quad (5.14)$$

Less stringently, \mathbf{u} *weakly dominates* \mathbf{v} (denoted $u \preceq v$) if

$$f_i(u) \leq f_i(v) \quad \forall i = 1, \dots, D \quad (5.15)$$

A set of M decisions vectors $\{w_i\}$ is said to be a *non-dominated set* (an estimated Pareto front ε) if no member of the set is dominated by any other member:

$$w_i \not\prec w_j \quad \forall i, j = 1, \dots, M \quad (5.16)$$

5.5 Particle Swarm Optimization

It is useful to give a general overview of the Particle Swarm Optimization method since it is implemented in the AM software. The PSO is used for single and multi-objective optimization, where, for the one-objective run, the function to be maximized is the final payload mass that a launcher can put into the final orbit. The PSO is an evolutionary algorithm for exploring the solution space of a problem and to achieve (if possible) the global best solution of the same. Hereafter an introduction to PSO, several methods to

handle constraints and some remarks about solving trajectory-optimization problems using this method will be given. Further and more detailed information on PSOs can be found at the Particle Swarm Central, <http://www.particleswarm.info>.

A theoretical description of PSO is given rather easily: the solution is represented by particles, which have a position in the solution space. These particles also have a speed so that they move and can be attracted by special places: in the original algorithm, these two special places are the global best place, and the individual's best place. "Best" in this context then is the position where the best fitness value is reached (the minimum or the maximum, depending on the formulation of the problem).

The algorithm originates from the social behaviour of a flock of birds or a herd of sheep. Naturally, groups of animals move from place to place in their habitat looking for food. The location where food is found can be seen as an optimum in the search space and the location where the largest amount of food is can be compared to the maximum of the entire search space.

Basic algorithm

Mathematically, the PSO can be described as follows: suppose a solution can be described by a position vector x_i (with real-valued elements), then for valid position vectors, a fitness f_i can be calculated. Each solution also has an associated velocity vector v_i (again, with real-valued elements). The last element of knowledge an individual remembers is the position vector and fitness of the best position it has visited, and a global best position is kept available. In Fig. 5.2 the flow through a simple PSO algorithm is depicted. At each iteration, the velocity of each individual is determined by the following formula:

$$v_{i,new} = v_i + c_1 rand(0, 1) \cdot (x_i^* - x_i) + c_2 rand(0, 1) \cdot (x_G^* - x_i) \quad (5.17)$$

and the new position is determined using:

$$x_{i,new} = x_i + v_i \quad (5.18)$$

in which $rand(0, 1)$ is a random number generator with output between 0 and 1, and c_1 and c_2 are constants, called particle and swarm confidence parameter, (usually with recommended values of 2 [Kennedy and Eberhart, 1995] or 1.494 [Eberhart and Shi, 2000], but it depends on the problem), x_i^* is the individual's best (archived) position, and x_G^* is the global best (archived) position. If the particles' new positions are outside their search space boundaries, they are constrained to be on the boundary that they violated (lower or upper). Then, the velocity that brought the particle in that situation is given the opposite value so that it can bounce back in the search space at the next iteration. As the results of the optimization process are tuning-dependent and the tuning depends on the type of problem, it might be useful to have these parameters optimized together with the variables of the problem. However, this approach has not been investigated but it might be in future works.

The effect of this is that particles are attracted by their own best historic position, and the population's best position. If this process is repeated for each individual solution, those solutions tend to swarm, and reach the best solution.

Inertia weight

In [Shi and Eberhart, 1998], a small change to Eq. 5.17 is proposed, which improves the performance of the algorithm:

$$v_{i,new} = w \cdot v_i + c_1 rand(0, 1) \cdot (x_i^* - x_i) + c_2 rand(0, 1) \cdot (x_G^* - x_i) \quad (5.19)$$

The term w is coined as inertia weight. The effect of it is that when $w < 0.8$, the search is slowed down, and the flock tends to get stuck in a local optimum, but it does not take a lot of time to converge to this optimum; if $w > 1.2$, the search is more explorative, but tends to take more steps to converge. The advice given is to set $w = 1.4$ and gradually decrease it to 0 over the complete search. This is the approach (i.e., the linearly decreasing inertia weight) used in the single-objective PSO present in the AM software. In [Toscano Pulido and Coello Coello, 2004], though, a different range for the inertia weight is used: w taking a value randomly generated within the range [0.1, 0.5] is used, together with c_1 and c_2 randomly picked from the range [1.5, 2.5]. These values are then kept constant during the search.

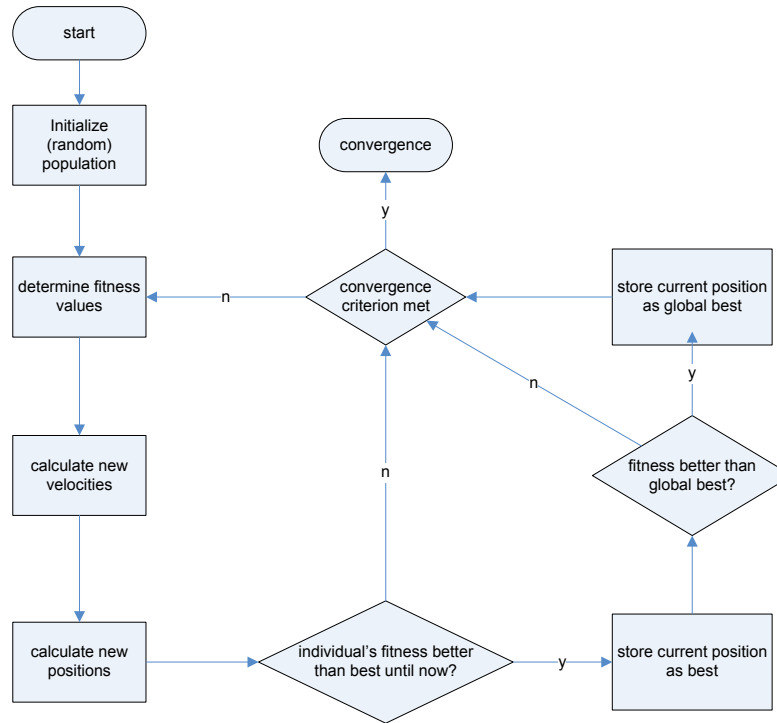


Figure 5.2: Particle Swarm Optimization. Flowchart of a simple Particle Swarm Optimization algorithm.

As stated above, the PSO optimizer used for this work implements a linear decreasing inertia weight of the form:

$$w = w_i + \frac{(w_f - w_i)}{n_{Max\ iter}} k_i \quad (5.20)$$

where w_i and w_f are the initial and final inertia weight, $n_{Max\ iter}$ is the maximum number of iteration to perform during the optimization process and k_i is the current iteration in the process.

It is clear that the inertia weight decreases linearly as the number of iterations increases. This very approach drives the process to a global exploration of the space in the initial phase because the inertia weight is larger. As the optimization continues, the inertia weight decreases, permitting a more local exploration, refining the search in a local area for better results. This very implementation of the inertia weight tries to gather the global and local approach of an optimizer.

With other words, if the velocity term is not considered in the first part of Eq. 5.19, and the particle and swarm confidence parameter are given a value of 2, as in [Kennedy and Eberhart, 1995], the particles statistically contract the swarm towards the actual best position until a new global best is found. This is due to the fact the particle and swarm confidence parameter get an average value of 1. Therefore, it resembles a kind of local search algorithm that statistically shrinks through iterations, [Shi and Eberhart, 1998]. Moreover, it is likely to find a global optimum only if the initial population covers the space where it actually is. In conclusion, the inertia weight is important because it expands the search space and permits to the particles to explore it.

Mutation

A mutation is also implemented in the PSO optimizer in the AM software. This characteristic acts through a randomly generated number: in case this number is lower than a value set arbitrarily to 0.01 then all the optimizable variables are generated again randomly in the range $[0, 1]$.

Constraints handling

For each particle, a vector containing the constraint violations is created. After that, all these constraints are normalized and summed up into a “penalty” variable, which is added to the objective value. If one or more constraints have been violated during the simulation, they are normalized, given a negative value and summed up together. This latter value, namely the penalty, is first multiplied by a huge constant, as shown in Eq. 5.22, (i.e., $1 \cdot 10^{10}$) and is then subtracted from the objective function worsening its value. Since the maximization of the objective function (i.e., the payload mass in this very case) consists of the minimization of the negative value of the mass, by subtracting the penalty to the objective, the latter becomes less negative and, from an optimal point of view, is worsened.

The constraints of the ascent trajectory problem, also called path constraints, are mainly dictated by the mechanical and thermal limits that a vehicle can withstand. The way these constraints are treated is shown here:

$$\text{ConstraintViolation}_i = \begin{cases} 0 & \text{if } x_i < C_i \\ \frac{(x_i - C_i)}{C_i} & \text{if } x_i > C_i \end{cases} \quad (5.21)$$

where C_i is the constraint the launcher can withstand and x_i is the violation value. All path constraints are meant to find single event violations and they are not integrated over time. The profile of the dynamic pressure or bending load, for instance, presents an increasing behaviour, a peak and then a sharp decreasing, lasting 80-100 seconds at most. Unless holes or damages are present in the structure, that would be quite clear before the flight, there are no reasons for considering an integrated value of them. On the other hand, concerning the heat flux, large amount of heat for long period of time might weaken the structure without evident proof.

$$\text{Penalty} = \left(\sum_{i=1}^n \text{ConstraintViolation}_i \right) \cdot 10^{10} \quad (5.22)$$

Equation 5.21 shows that the constraints are normalized and treated in a linear way. Other ways to handle the constraints include the logarithmic, the exponential and the quadratic penalty function. Even though the linear penalty function performed quite well for this kind of problem, in the future, it might be useful to investigate the performance given by a logarithmic penalty, that has been proved to perform better than the linear and quadratic one in the knapsack problem (see [Michalewicz and Arabas, 1994]).

We have mentioned also boundary constraints in an optimization problem. In the ascent trajectory problem, the boundary constraints can be the orbital elements of the target orbit that we want to reach. In the one-objective PSO the following formula is used to reach the accuracy, set by the user:

$$E_i = \frac{(x_i - x_{TARGET,i})}{\text{tol}_i} \quad (5.23)$$

where x_i is the orbital element, $x_{TARGET,i}$ is the target value of the orbital element, tol_i is the tolerance set by the user on that particular orbital element. If a particular final orbital element is within the set tolerance it is not included in the penalty function. Otherwise, the error on the orbital elements outside of the tolerances are summed up in a penalty function as was the case of the constraints:

$$\text{Penalty} = \sum_{i=1}^n E_i^2 \quad (5.24)$$

The main difference with respect to the constraints evaluated with a linear function is that boundary constraints are evaluated by using a quadratic penalty function. In this case, this approach is used because the vehicle can miss, for instance, the final semimajor axis by more or less than 5 km and still be within the predefined tolerance. Therefore there is need to penalize in both direction the missed target.

In the multi-objective optimization, the boundary constraints represented by the orbital elements are gathered in a single function, the root sum square (*RSS*), that becomes an objective function. The *RSS* of the final orbital elements represents the accuracy achieved by the trajectory. It means that by using the *RSS* as an objective function we strive for a good accuracy (at least within the predefined tolerances). However, since this objective will be optimized together with other objectives, a Pareto front will be created, meaning

that there will be, for instance, trajectories with a low accuracy on the final orbital elements, but with a very high payload mass or trajectories with a good accuracy and a lower payload mass. In case the RSS is set as an objective, the optimizer tries to minimize it. This is the same as minimizing the error on the orbital elements:

$$RSS_{orb_elem} = \sqrt{\sum_{i=1}^n E_i^2} \quad (5.25)$$

Another use of the RSS is made when it is chosen as objective, but computed from the path constraints. In this case, it does not have the same meaning as explained above. In fact, this RSS is computed by taking the squared constrained violations as shown in Eq. 5.26. This is done because the path constraints do not have tolerances but only limit values. Therefore, the order of magnitude of the RSS of the path constraints may be smaller than that of the orbital elements since each term is divided by the limit that is larger (in terms of magnitude) than a tolerance.

$$RSS_{path_constr} = \sqrt{\sum_{i=1}^n \text{ConstraintViolation}_i^2} \quad (5.26)$$

5.6 Multi-objective optimizer

The Ascent Module software includes two multi-objective optimizers, the NSGA-II and the DG-MOPSO. Only the latter will be described and used for the optimization runs. From [Castellini, 2008b], DG-MOPSO outperforms the NSGA-II algorithm and for this reason it has been chosen as the only multi-objective optimizer for this analysis.

DG-MOPSO

The DG-MOPSO optimizer, developed by Castellini (see [Castellini, 2008a]), is mainly based on the standard MOPSO proposed by [Coello Coello et al., 2004] and includes the gridded search space feature taken from the Pareto Archived Evolution Strategy (PAES, see [Knowles and Corne, 1999, 2000]).

The DG-MOPSO algorithm is described below:

1. Randomly initialize the swarm particles and initialize velocities to null value;
2. Evaluate the fitness of each particle;
3. Store the non-dominated solution in the archive;

This step is performed applying the concept of Pareto dominance explained in Section 5.4.

4. Define the initial grid boundaries and positions of the particles in the outer and inner grid;

This feature consists of a double grid (see Fig. 5.3) generated in the objectives space to keep track of the least and the most crowded areas. The double grid is composed of outer grids which are divided in inner grids. These inner grids are meant to move the individuals to the less crowded ones in order to have a uniform distribution of solutions. This is done by assigning, in an outer grid, to each particle a leader positioned in the least crowded inner grid. Once the archive of the best solutions is full, it is pruned by deleting the solutions in the most crowded grids of the objective space. A double grid is shown in Fig. 5.3. The objective space has been bisected twice ($N_{out} = 2$) for the outer grids and each outer grid has been bisected once ($N_{in} = 1$).

5. Define fitness for each particle (to be used in selection of the leader of the swarm);

According to the number of particles present in each outer and inner grid, a fitness is given to each solution. The fitness is computed according:

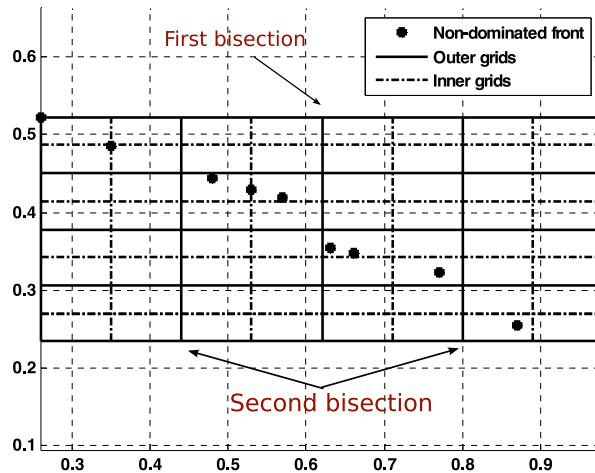


Figure 5.3: Example of double grid in a (two) objective space.

$$fitness_{out/in} = \frac{10}{N_{sol_out/in}} \quad (5.27)$$

This formula permits to chose the leader within the less crowded grid.

6. FOR each iteration

- (a) find the grid where it is located and choose the leader for it;

The leader assigned to each member of the swarm varies from particle to particle. First the outer grid, in which the particle is located, is found. Then, if there is no archive solution in that outer grid, *roulette wheel selection*, based on Eq. 5.27, is performed using the non-empty outer grids. If there are more than one solution, one is randomly chosen. On the other hand, if there are solution in the outer grid where the particle is, the inner grid with the highest fitness is selected (randomly selected if grids have the same numbers of solutions). This means that the less crowded grid is chosen.

- (b) update velocities of the particles and compute new positions;
(c) apply mutation operator;
(d) check that particles' positions are within the boundaries;
(e) evaluate fitnesses of the particles;
(f) update best for each particle;

The update of the best for each particle is based on Pareto dominance. Moreover, in case the two solutions that are compared are both non-dominated, update is based on the highest fitness of the outer grids where the particles are. If these "outer" fitnesses are equal, update is based on the fitness of the inner grids.

- (g) update the archive and delete the dominated solutions;
(h) prune the archive;

Once the archive has been filled, the solutions in the most crowded inner grids are deleted.

7. END FOR

The MOPSO algorithm is showed in Fig. 5.4, and if the number of objectives is larger than 2, then the grid becomes an hypercube.

Handling of the constraint is achieved through a penalty function that is the sum of the constraints violations. This penalty is multiplied by a huge constant (i.e., $1 \cdot 10^{10}$) and then summed to each objective.

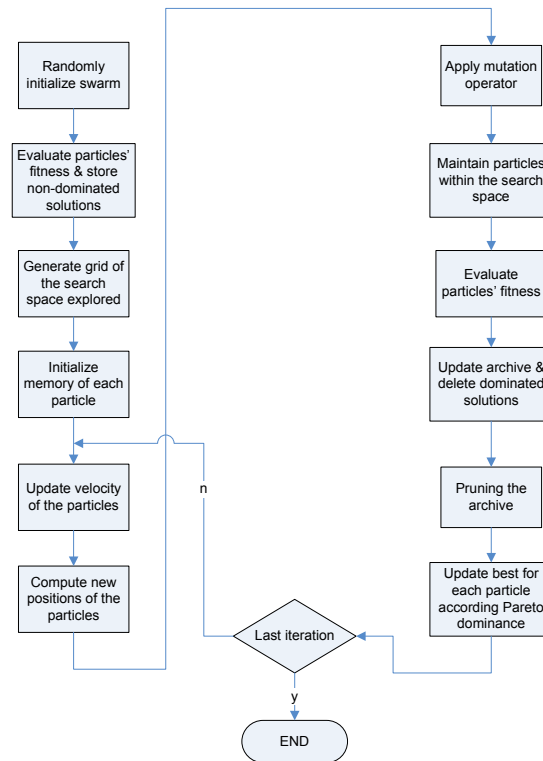


Figure 5.4: The flow chart depicts the multi-objective particle swarm optimizer on which the DG-MOPSO is based.

Therefore, the solutions that violate the constraints will get very bad fitness values and will be dominated as soon as solutions with no violations occur.

For further information and a thorough description of the algorithm the reader is referred to [Castellini, 2008a].

Diversification of objectives and constraints

An implementation embedded in the AM software is the diversification of the choice between objectives, or cost functions. The original version of the AM had, for the three optimization modes, the following objectives:

- one-objective optimization:
 - final payload mass.
- two-objectives optimization:
 - final payload mass;
 - root sum square (RSS) of the final orbital elements (a_f , e_f , i_f and, if optimized, Ω_f and ω_f).
- three-objectives optimization:
 - final payload mass;
 - root sum square (RSS) of the a_f , e_f and i_f ;
 - root sum square (RSS) of Ω_f and ω_f .

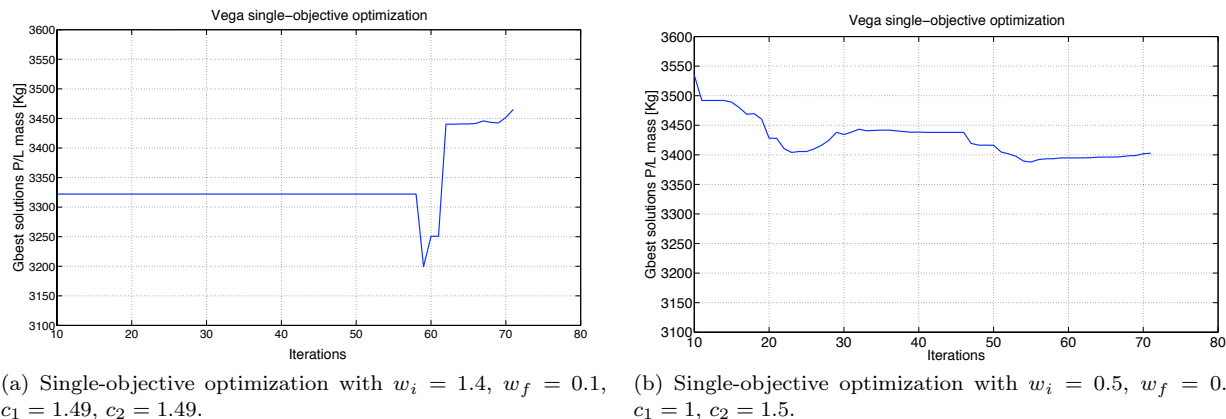


Figure 5.5: Comparison between different PSO inertia weight and confidence parameters during the evolution of the global best solution along the iterations.

The new sets of objectives that can be selected in the two and three-objectives optimizations are:

- two-objectives optimization (final orbital elements used as optimization constraints):
 - final payload mass;
 - root sum square (RSS) of path constraints.
- three-objectives optimization:
 - Set 1 (no constraints are used in the penalty function):
 - * final payload mass;
 - * root sum square (RSS) of the final orbital elements (a_f , e_f , i_f and, if optimized, Ω_f and ω_f);
 - * root sum square (RSS) of path constraints.
 - Set 2 (final orbital elements used as optimization constraints):
 - * final payload mass;
 - * root sum square (RSS) of a first chosen set of path constraints;
 - * root sum square (RSS) of a second chosen set of path constraints.

5.7 Setup of the optimizers

In this section, the setup of the characteristic parameters of the two optimizers used will be presented. The parameters set have not been changed as they gave good results during the verification and validation of the AM module from [Castellini, 2008b]. Moreover, some simulations have shown that the parameters suggested in [Kennedy and Eberhart, 1995] or [Eberhart and Shi, 2000] are not the most suitable for this kind of problem. In Fig. 5.5 and 5.6, it is shown the difference in the global best and constraint violations given by the suggested parameters and those used for this research and presented hereafter. The launcher simulated is a Vega, aiming at 185 km altitude circular orbit, 5.5° inclination. It is evident that, in Fig. 5.5a and 5.6a, the particles found solutions with lower constraint violations only after iteration 58 (out of 70 total iterations), where the inertia weight is equal to 0.34 (value which is included in the inertia weight range used for second case). Both runs have been performed using the same random seed.

The role of the population size is crucial in problems where a high number of variables (e.g., more than 10-15) is present. For the optimization runs performed, the population size has been set to 100 that should be a good trade-off between the computational time and the coverage of the search space. However, future investigation can be addressed to see if a larger population size improves the objective fitness and, if so, in which measure.

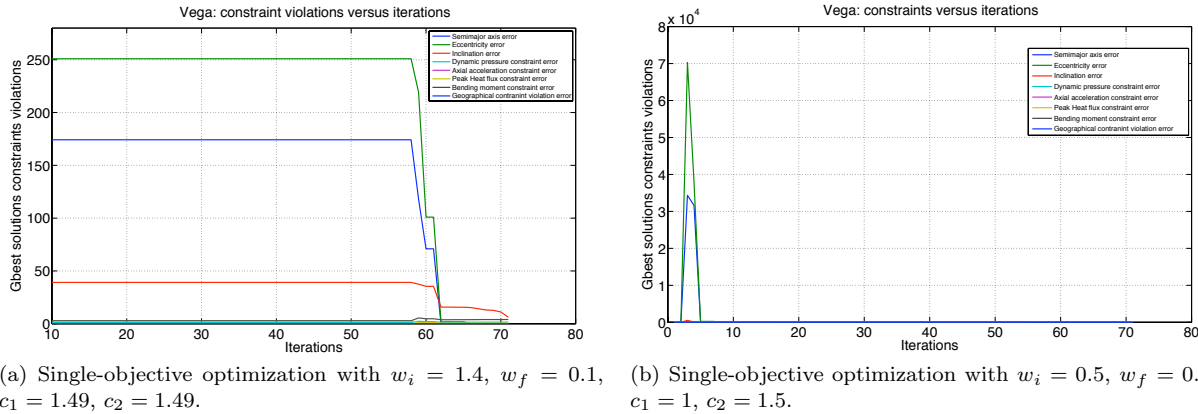


Figure 5.6: Comparison between different PSO inertia weight and confidence parameters during the evolution of the constraint violations along the iterations.

The random seed influences the population created. If the same seed is used for different simulations, the same population is created. This is useful to compare how the particles evolve during the optimization when different aerodynamic configurations of the launcher are used.

5.7.1 PSO

Parameter settings:

- Swarm population: 100;
- Iterations: 100;
- Initial inertia weight: $w_i = 0.5$;
- Final inertia weight: $w_f = 0.2$;
- Self confidence parameter: $c_1 = 1$;
- Swarm confidence parameter: $c_2 = 1.5$;
- Mutation probability: $p_{mut} = 0.01$.

5.7.2 DG-MOPSO

Parameter settings:

- Swarm population: 100;
- Iterations: 100;
- Number outer grid bisections: $N_{out} = 4$, then, the number of outer grids is given by $2^{N_{out} \cdot N_{obj}}$;
- Number inner grid bisections (for each outer grid): $N_{in} = 1$, then, the number of inner grid per outer grid is given by $2^{N_{in} \cdot N_{obj}}$;
- Initial inertia weight: $w_i = 0.5$;
- Final inertia weight: $w_f = 0.2$;
- Self confidence parameter: $c_1 = 1$;
- Swarm confidence parameter: $c_2 = 1.5$;

- Initial mutation distribution (see [Deb et al., 2000]): 0;
- Final mutation distribution (see [Deb et al., 2000]): 5;
- Mutation probability: $p_{mut} = 0.01$.

5.8 Optimization of the launchers' parameters

Besides the constraints, the final orbital elements and their relative tolerances there are other variables concerning the characteristics of the launchers that are optimized. These variables, or nodes, are typical of the guidance and thrust settings of a launcher.

Nodes for throttle setting

In order to simulate the throttleable engines of a launch vehicle, if applicable, the thrusting period of each stage can be divided in at least 2 nodes and at most 10. The thrust profile is then obtained by linearly interpolating the throttle between each node and multiplying the value needed at a specific time by the nominal thrust.

For each launcher, except for those without throttleable engines, the number of nodes selected has been derived mainly by observation of the thrust or axial acceleration profiles found in the user's manuals. The nodes are reported in Table 5.1.

Table 5.1: Number of nodes for throttle setting optimization.

Launcher	No. nodes
Vega	5/5/5 ³
Atlas V 552	8
Atlas V HLV	4 – 10
Delta IV Heavy	8

Nodes for guidance optimization

As it has been said in Chapter 4, especially concerning the gravity turn and the bi-linear tangent law phase, the trajectory is optimized in the neighborhood of a reference guidance profile. The same approach applied for the throttle level optimization, using nodes, is exploited here. The pitch and yaw control in the gravity turn phase and the yaw control in the upper stage phase have been divided by means of nodes (from 2 to 10). Then, the optimizer finds the optimal values of the displacements from the reference pitch and yaw at the nodes. Successively, the optimized displacements are linearly interpolated between the nodes and, along the trajectory, the linear displacement, function of the time, is added to the reference guidance control.

A good tuning of the number of nodes is critical for the guidance laws. Many nodes can generate a spiky profile that might not be flown in reality as shown in Fig. 5.7. Therefore, in order to avoid guidance profiles far from reality a number between 3 and 5 has been chosen for each launcher. In Table 5.2, the number of nodes per each launcher can be found.

Besides the nodes to model the pitch and yaw control in the gravity turn and bi-linear tangent law, the parameters characteristic of the other control laws are optimized to adapt the control profile to satisfy the path constraints and reach terminal boundaries.

³ For Vega, the first three stages are not throttleable since they fueled with solid propellant. However, the grains are tailored in order to avoid high accelerations and constraint violations. As no thrust or mass flow profile was found in literature, the author decided to let the optimizer find the optimal throttle settings.

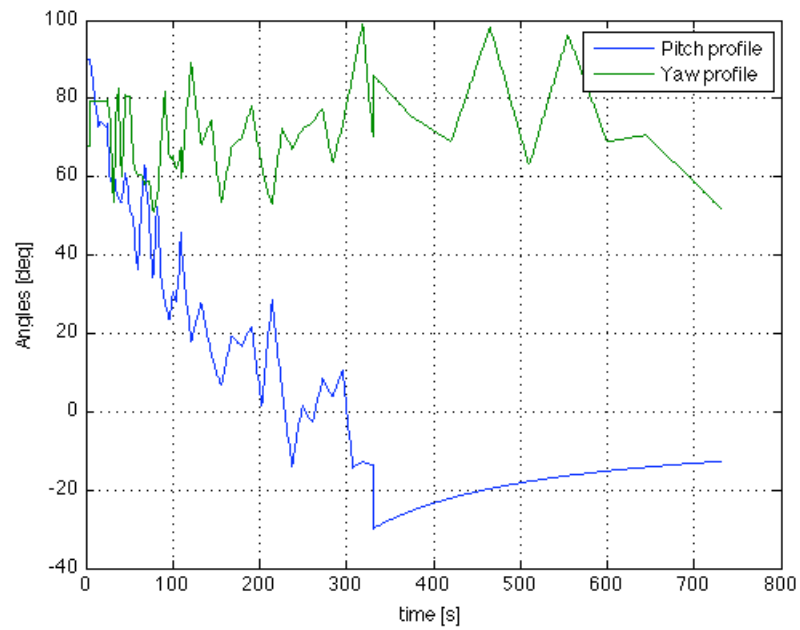


Figure 5.7: Spiky pitch and yaw profile.

Table 5.2: Number of nodes for guidance optimization.

Launcher	No. nodes
Vega	3
Ariane 5	2 – 5
Proton	3 – 5
Atlas V 552	3
Atlas V HLV	3
Delta IV Heavy	3

Chapter 6

Results

In the following chapter, the results obtained from the optimization process will be presented for each launcher. The complete set of results, include the orbital elements achieved, path constraint values achieved and normalized path constraints and Pareto fronts or surfaces for multi-objective optimizations, will be shown only for Vega. For the other vehicles, the final orbital elements achieved from the trajectories and the normalized path constraints vale are included in Appendix C. For the Delta IV Heavy and the Atlas V HLV, only a short set of results from single-objective optimizations will be presented. Qualitatively, these results are not comparable to those of the other launchers, because the software model did not allow for a better reproduction of the real throttle profiles.

The settings used for the optimizer have been reported in section 5.7 and will not be repeated here, whereas the setup of each launcher’s runs is reported hereafter for each vehicle.

For each launcher, a number of runs between 10 and 15 has been performed. This number varies from launcher to launcher depending on convergence of calibration results. In fact, calibration runs (between 3-6) have been performed prior to the runs presented here in order to get a feeling with the settings of each launcher. If in the calibration there was convergence, in the sense that the vehicle was able to satisfy easily the constraint and fly a smooth control profile, then less runs were successively performed. The reason is that less variations of tolerances on the final orbital elements and path constraints were needed in order to explore the possible trajectories of the launcher and achieve optimal results. In Table 6.1, the number of runs per launcher and type of optimization (single, two and three-objective) are reported. For Delta IV Heavy and Atlas V HLV no multi-objective optimization runs were performed since a huge computational effort was needed for the single-objective ones and it was found out that the available model was not able to cope with the real configuration of the two vehicles.

Moreover, in order to take into account possible errors or imprecisions in the computed aerodynamic model of the launchers, an assessment of the software has been performed. This assessment aims at getting a better understanding about how the software can cope with a variation in the input data and, specifically, with the aerodynamic ones.

The logic behind this analysis is better explained in section A.4. Therefore, the same simulations are executed using the varied aerodynamic configurations. In order to cover the widest variation of the aerodynamic properties, the best and the worst aerodynamic configuration that deviate from the reference one are considered, as shown in Table 6.2.

However, in this research, it was not possible to use the same random seed for the same simulation performed with the three different configurations. Several simulations were performed using the same seed,

Table 6.1: Number of runs performed for each launch vehicle.

	Vega	Proton M	Atlas V 552	Ariane 5	Delta IV Heavy	Atlas V HLV
1-D runs	18	14	16	9	5/5	5/5
2-D runs	4	4	5	4	-	-
3-D runs	2	5	7	4	-	-

Table 6.2: Simulation plan considering the sensitivity analysis for the aerodynamic model of each launcher.

	Worst case	Reference case	Best case
Launcher simulations	Reference $C_L - 10\%$ Reference $C_D + 10\%$	Aerodynamic data obtained as described in Appendix A.	Reference $C_L + 10\%$ Reference $C_D - 10\%$

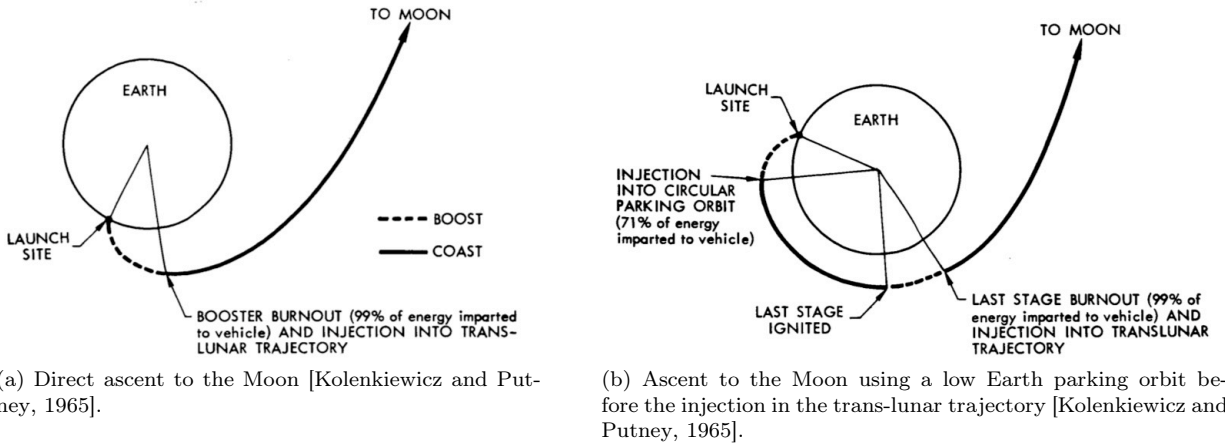


Figure 6.1: Possible types of trajectory to reach the Moon.

but in some cases, during the integration process, the requested accuracy on the state vector elements caused problems and the optimization suddenly terminated. According to the authors of the integrator (a Runge-Kutta-Fehlberg of order 4-5), [Shampine et al., 1976], when this error occurs, the solution is changing rapidly or a singularity may be present. For this reason, a fixed seed could not be used for the three configuration of each run. For future work and improvements in the software, the cause of this error should be investigated.

6.0.1 Final orbit

Depending on the mission requirements, a direct ascent can be less efficient than an ascent into a LEO parking orbit followed by a burn to reach the Moon or vice versa. Some aspects that should be considered in this analysis are:

- the use of cryogenic propellants;
- attitude control of the launcher;
- tracking from ground stations;
- booster recovery.

Usually, for orbits below 300 km a direct ascent might be more convenient, but it is not always the case. Moreover, a parking orbit permits to achieve the final orbit with a better accuracy and to perform a check of the system of the payload.

However, a very rough comparison is performed in order to understand how different the strategy is. The results achieved from the analysis of the direct ascent should not be considered reliable since they originate from a first, rough analysis in which some weaknesses of the used mathematical model arise. Anyway, they are a starting point for future research.

Low Earth parking orbit

Concerning the case of a final LEO parking orbit, all launchers' payload masses will be optimized by using final orbital elements as boundary constraints:

semimajor-axis: $a = 6563.137$ km

eccentricity: $e = 0$

inclination: $i = i_{LS}$

where i_{LS} is the minimum inclination reachable from a launch site. This assumption is done since the maximum payload mass for a launcher is given for inclinations that equal the latitude of the launch sites from which they depart.

The aforementioned type of parking orbit corresponds to a circular parking orbit at 185 km altitude (100 nautical miles).

Lunar Hohmann transfer orbit

The direct ascent involves the injection of the launcher into a transfer orbit to the Moon. The optimal transfer orbit, from the propellant mass consumption point of view, is a Hohmann transfer where the vehicle ends its injection at the pericenter of the orbit and approaches the Moon at the apocenter of the same transfer orbit, with the Moon being there at the same time. Since this is a first order analysis of capabilities of the launchers, a mean distance of the Moon from the Earth can be considered, that is 384,400 km. We assume the injection occurring ideally at the pericenter at 185 km altitude. Therefore, the final orbital elements of the transfer orbit to achieve are:

semimajor-axis: $a = 195481$ km

eccentricity: $e = 0.966426$

inclination: $i = i_{LS}$

Initially, this type of orbit was only thought for the Delta IV Heavy and Atlas V HLV because, since they have not been included in Zuccarelli's work, the Earth-Moon transfer would be missing for them. However, as reaching this orbit is not easy, a preliminary analysis is performed for these launchers injected in a low Earth parking orbit as well.

6.1 Vega launch for communication satellites

The first step of the entire mission is to provide permanent communication between the astronauts on the Moon and the operation center on Earth. As stated in Chapter 2 and in [Hamera et al., 2008], two communication satellites in a Halo orbit around the Lagrangian point L_2 of the Earth-Moon system permits to have a complete coverage of the South Pole. In this way, the satellites are always visible from the Earth and can communicate with the Deep Space Network (DSN), satisfying the requirement of permanent communication.

In [Zuccarelli, 2009], an analysis to find the cheapest (in terms of ΔV cost) initial parking orbit, from which the spacecraft can depart towards the Moon, has been performed. Concerning the departure parking orbit, the analysis involved also the search of the inclination that gives the lowest ΔV to reach the target orbit.

The launch site for the Vega launch vehicle is Kourou, at 5.2358° N and -52.7747° W, in French Guiana. The optimization analysis performed on the Vega trajectory aims at reaching a circular orbit at 185 km altitude, while the inclination is varied between 5.5° , 28.5° and 51.6° . Vega is a four stage vehicle and only the maximum axial acceleration is known, that is 5.5 g, from [Arianespace, 2006].

6.1.1 One-objective optimization results

In this section, the results obtained from the one-objective optimization runs are shown. The runs performed are organized by final orbit inclinations (5.5° , 28.5° and 51.6°). For each orbit inclination, first the setup of the runs is presented, showing the tolerance set on the orbital elements and the path constraint limits. In addition, in the setup table, the use of the circularization burn and of the coast arcs between the stages is specified.

Right after the setup, a table with the results is shown. This table summarizes, for each run and for each aerodynamic configuration (worst, reference and best), the error on each orbital element tolerance. Besides that, if in a particular run, the vehicle has violated the constraints, the violation for each constraint is reported. Then, the value reported is the exceeding value with respect to the limit presented in the setup table. Eventually the final payload masses are reported.

Circular orbit @ 185 km altitude, 5.5° inclination

In this section the results for a final orbit inclination equal to the latitude of the Kourou launch site are presented. The payload mass ranges between 2050 kg and 3600 kg, but the largest part of the runs gives a payload mass higher than 2900 kg. As can be seen from Table 6.3, runs 2 to 4 have a higher final semimajor axis (200 km altitude, circular orbit). In this case, the simulations aimed at analyzing how different it would have been to achieve a higher orbit, any constraint violations and the relative performances that could justify the use of a higher orbit. Differences between the runs comprise constraints and orbital elements accuracy satisfaction. However, as can be seen from Table 6.4, the tolerance on the final inclination is often not respected, producing errors. In addition, several violations, mostly in the peak heat flux, axial acceleration and geographical constraints are present.

It has to be stressed the the geographical constraint is something related to the permitted launch site azimuth range and it is active until the rocket reaches 100 km altitude. This is done to prevent any jettisoned stage or part of the vehicle from falling on inhabited areas.

The first run is the only one that does not violate any constraints and respects all tolerances. But, as can be noted from Table 6.3, the tolerance on the final eccentricity is one order of magnitude higher than all the other cases, showing that the tolerance on this orbital element might have a predominant role in driving the optimization process to a good or bad (in terms of constraints and payload mass) ascent of the launcher. However, even though no constraints or tolerances are violated, the resulting orbit has a pericenter and apocenter that differ by 40 km. This cannot be accepted in LEO since the orbit has to be circular and match with the work of Zuccarelli in order to accomplish the mission [Zuccarelli, 2009].

Taking a particular look at run 8, in which the circularization burn is used to achieve the circular orbit, the tolerance on the eccentricity is not satisfied in the reference aerodynamic configuration and as a consequence it gives a higher payload mass with respect to the other cases.

Table 6.3: Vega: setup of the runs, launching into 5.5° inclination orbit.

Parameter	Simulation 1	Simulation 2	Simulation 3	Simulation 4	Simulation 5	Simulation 6	Simulation 8	Simulation 17	Simulation 18
a [km]	6563.137	6578.137	6578.137	6578.137	6563.137	6563.137	6563.137	6563.137	6563.137
e [-]	0	0	0	0	0	0	0	0	0
i [deg]	5.5	5.5	5.5	5.5	5.5	5.5	5.5	5.5	5.5
Tolerance a [km]	2	2	2	2	2	2	3	2	2
Tolerance e [-]	0.003	0.0001	0.0001	0.0001	0.0001	0.0001	0.0005	0.0001	0.0001
Tolerance i [deg]	0.1	0.1	0.1	0.1	0.1	0.1	0.1	0.1	0.1
Dynamic pressure [kPa]	≤ 55	≤ 50	≤ 50	≤ 50	≤ 50	≤ 50	≤ 50	≤ 57	≤ 57
Peak heat flux [kW/m ²]	≤ 120	≤ 120	≤ 120	≤ 120	≤ 120	≤ 120	≤ 120	≤ 120	≤ 120
Axial acceleration [g]	≤ 5.5	≤ 5.5	≤ 5.5	≤ 5.5	≤ 5.5	≤ 5.5	≤ 5.5	≤ 5.5	≤ 5.5
Bending load [kPa*deg]	≤ 280	≤ 260	≤ 260	≤ 280	≤ 280	≤ 280	≤ 300	≤ 300	≤ 300
Circularization burn	No	No	No	No	No	No	Yes	No	No
Coast arcs	No	No	Yes	Yes	Yes	Yes	No	No	Yes

One curious observation is that most of the runs involving the best aerodynamic configuration tend to violate the bending load, the axial acceleration, the peak heat flux and the dynamic pressure. This behaviour might be explained by considering the velocity of the vehicle. With a better aerodynamic configuration, i.e., lower C_D and higher C_L , the drag experienced by the launcher is lower giving as result a higher velocity that is involved in the dynamic pressure and peak heat flux (and consequently in the bending load). Regarding the axial acceleration, this is simply higher since the drag is lower.

In Table 6.4, concerning the eccentricity, the error is an offset with respect to the target value (circular orbit, $e = 0$). About the path constraints' violations, only the excess from the limit is shown.

Table 6.4: Vega: a summary of the optimization runs is presented. The error on the final orbital elements are shown. Final orbit inclination is 5.5° .

Parameter		Simulation 1	Simulation 2	Simulation 3	Simulation 4	Simulation 5	Simulation 6	Simulation 8	Simulation 17	Simulation 18
Error a	W	-	-	-	-	-	-	-	-	-
	R	-	-	-	-	-	-	-	-	0.43%
	B	-	-	-	-	-	-	-	-	-
Error e	W	-	-	-	-	-	-	-	-	-
	R	-	-	0.000249	-	-	0.087	0.0014	-	0.0044
	B	-	0.000196	-	0.000463	-	-	-	-	0.000389
Error i	W	-	-	15.90%	-	-	-	-	-	-
	R	-	-	-	3.70%	-	8.45%	-	-	11%
	B	-	7.56%	-	6.58%	-	-	-	-	-
Dynamic pressure violation [kPa]	W	-	-	-	-	-	-	-	-	19.6
	R	-	-	-	-	-	-	-	-	-
	B	-	290.0	-	-	13.4	-	-	-	2.1
Peak heat flux violation [kW/m ²]	W	-	49.2	51.6	-	-	-	-	-	343.2
	R	-	21.6	-	44.5	-	0.3	-	-	15.7
	B	-	2209.9	-	-	80.8	-	0.1	16.2	146.9
Axial acceleration violation [g]	W	-	-	0.2	0.0	-	1.3	0.7	-	1.0
	R	-	0.0	-	-	-	0.4	-	0.2	-
	B	-	0.8	-	0.6	-	0.2	0.2	-	0.4
Bending moment violation [kPa*deg]	W	-	-	-	-	-	-	-	-	240.3
	R	-	-	-	-	-	-	-	-	-
	B	-	4091.7	-	-	307.5	-	-	-	93.7
Geographical violation [deg]	W	-	-	5.2	-	-	-	-	-	2.0
	R	-	0.0	1.8	0.2	-	-	-	-	5.6
	B	-	-	0.5	-	4.4	1.7	0.7	-	-
Final payload mass [kg]	W	3,364	3,481	2,988	3,385	3,261	2,984	3,175	3,052	3,534
	R	3,295	3,585	3,441	3,476	3,453	2,399	3,518	2,985	2,385
	B	2,726	2,050	2,926	3,043	3,579	3,268	3,343	3,113	2,969

W = worst aerodynamic configuration

R = reference aerodynamic configuration

B = best aerodynamic configuration

- = no violation

■ = trajectory without path constraint

and orbital element tolerance violations

By analyzing Table 6.4 together with Fig. 6.2, it is quite evident that the best aerodynamic configuration does not always produce the highest payload mass. This is due to the fact that path constraints and tolerances are violated more often, yielding to higher penalties in the objective function that might steer the optimization in non-optimal areas of the search space.

Circular orbit @ 185 km altitude, 28.5° inclination

This section presents the results for the runs having a 28.5° orbit inclination as target. As it can immediately be seen in Table 6.6, those runs involving the best aerodynamic configuration (all but run 16) violate the tolerance on the final eccentricity. Therefore, all the resulting trajectories cannot be taken into account for the mission since a strong requirement is satisfying the final orbit characteristics in order to match the work developed in [Zuccarelli, 2009] and to provide a reliable study. In addition, the reason the best aerodynamic configuration behaves so badly with respect to the others has been reported for the 5.5° orbit inclination case.

However, going on with the analysis of the table, it results that at this final inclination the azimuth range constraint is never violated (except in run 1, violated by only 0.25°). The first run has the hardest constraints and the vehicle manages to violate the dynamic pressure by only 2 kPa at maximum in the reference configuration. On the other hand, the heat flux is violated by about 70 kW/m^2 .

Eventually, the best case, run 16, presents no violations for all the configurations. Even though a circularization burn has been included in the setup, the optimal trajectories do not use it. Therefore, this run has the same setup as run 4 but it differs completely in the results. This might be due to the randomness of the initial population in the search space that might cover different areas of the space itself.

Table 6.5: Vega: the setup of the runs, launching into 28.5° inclination orbit.

Parameter	Simulation 7	Simulation 9	Simulation 10	Simulation 11	Simulation 12	Simulation 15	Simulation 16
a [km]	6563.137	6563.137	6563.137	6563.137	6563.137	6563.137	6563.137
e [-]	0	0	0	0	0	0	0
i [deg]	28.5	28.5	28.5	28.5	28.5	28.5	28.5
Tolerance a [km]	2	3	3	3	3	3	3
Tolerance e [-]	0.0001	0.0005	0.0005	0.0005	0.0005	0.0005	0.0005
Tolerance i [deg]	0.1	0.1	0.1	0.1	0.1	0.1	0.1
Dynamic pressure [kPa]	≤ 45	≤ 50	≤ 57	≤ 50	≤ 50	≤ 50	≤ 50
Peak heat flux [kW/m ²]	≤ 100	≤ 120	≤ 180	≤ 120	≤ 120	≤ 160	≤ 120
Axial acceleration [g]	≤ 5.5	≤ 5.5	≤ 5.5	≤ 5.5	≤ 5.5	≤ 5.5	≤ 5.5
Bending load [kPa*deg]	≤ 200	≤ 280	≤ 300	≤ 300	≤ 300	≤ 300	≤ 300
Circularization burn	No	No	No	No	No	No	Yes
Coast arcs	No	No	No	No	Yes	No	Yes

Circular orbit @ 185 km altitude, 51.6° inclination

The results achieved for trajectories with 51.6° as final orbit inclination are presented here. In this case since only two runs have been performed, differences are quite clear from Table 6.8. Both the trajectories include the option for coast arcs but only one of them include the option for the circularization burn. However, also in this case the trajectories flown do not make use of it. In this sense, then, the main differences between the two cases can be due to the fact that the initial populations, created by the optimizer, cover different areas of the search space.

However, by comparing the final mass of the different aerodynamic configurations, it can be noticed that there is no clear relation between the aerodynamics and the final payload mass. For instance, the values in the worst configuration are higher than those in the reference one. This is a very strange result and it might only be addressed to the fact the same random seed was not used for the same simulation because of errors arisen during the integration for certain configurations (the error was not dependent on a certain configuration). Therefore, the variety of masses obtained has to be addressed to the different initial population generated. In addition, concerning the orbital elements and the path constraints, the violations occur only in the worst and reference configurations.

In run 13, the errors on the final orbital elements point out that the found control profile is not the optimal for both the yaw and the pitch. Then, this results in an error in the final inclination mainly due to the yaw profile, and an error in the final eccentricity due to the pitch profile. The violations in the axial acceleration indicate that, depending of the initial populations, the optimal values at the nodes for the throttle setting were not always found. The solution might be either to have simulations with lower minimum throttle level or with the real thrust profile of the stages (since they are solid propellant fueled and with a tailored thrust).

On the other hand, the violation of the peak heat flux and of the bending load is due to the longer time spent in the atmosphere. This is due to the fact that the launcher arrives into a wrong orbit with a lower altitude.

In Tables 6.2, 6.3a and 6.3b, it can be noticed that, in some simulations, one of the configurations has a payload mass much smaller than the other two. In some cases, as run 7 and 18, one aerodynamic configurations have small violations compared to the other two. This is due to the optimizer that is able to find a solution with a smaller payload that does not violate the constraints. In other cases, as run 2, 6, 13 and 15, the solutions found are not optimal and large constraint violations occur, whereas in the optimal solutions there are no violations.

Trajectories accuracy

In the Tables presented in this section, the solid grey line indicates the target orbital element and the dashed black one indicates the boundaries given by the tolerances around the target value. Concerning the eccentricity, since the target value is 0, for a circular orbit, there is no lower bound as a negative eccentricity does not exist.

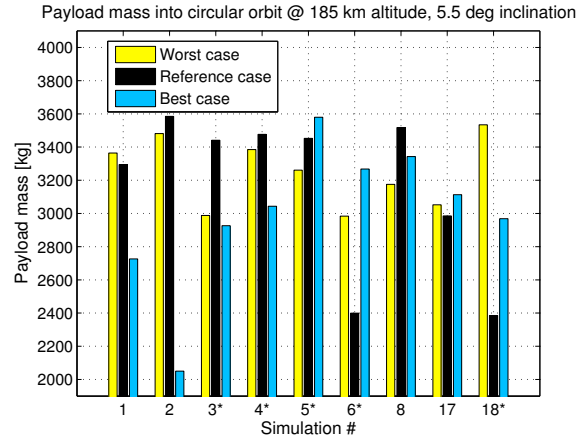
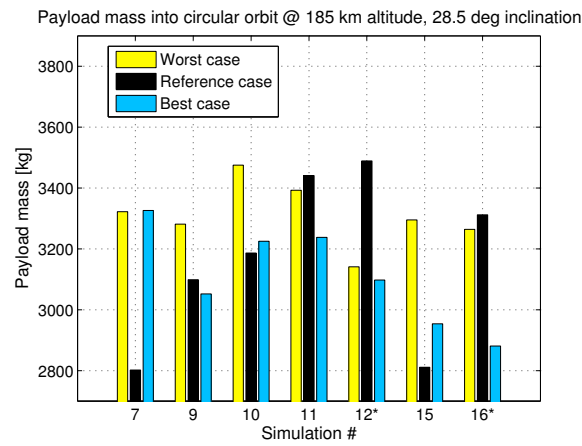
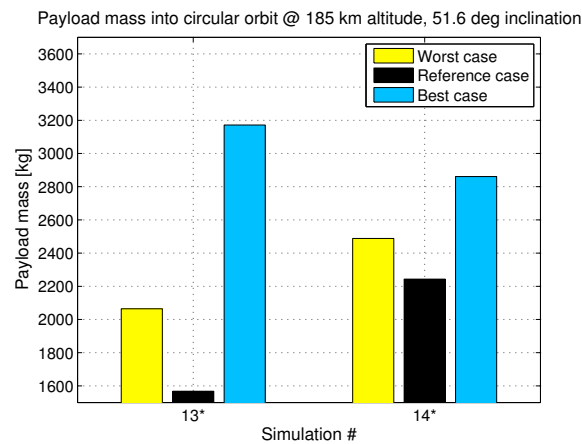


Figure 6.2: Final payload mass at 5.5° inclination.



(a) Final payload mass at 28.5° inclination.



(b) Final payload mass at 51.6° inclination.

* = trajectory with coast arcs

Figure 6.3: Final payload mass for Vega launcher at different orbit inclinations resulting from the one-objective optimizations.

Table 6.6: Vega: a summary of the optimization runs is presented. The error on the final orbital elements are shown. Final orbit inclination is 28.5°.

Parameter		Simulation 7	Simulation 9	Simulation 10	Simulation 11	Simulation 12	Simulation 15	Simulation 16
Error a	W	-	-	-	-	-	-	-
	R	-	-	-	-	-	-	-
	B	-	-	-	-	-	-	-
Error e	W	-	0.000542	-	-	0.000547	-	-
	R	-	-	-	-	-	0.000949	-
	B	0.00015	0.000735	0.000545	0.000649	0.000531	0.000727	-
Error i	W	-	-	-	-	0.40%	-	-
	R	-	-	-	-	-	-	-
	B	3.32%	-	0.86%	-	-	-	-
Dynamic pressure violation [kPa]	W	1.3	-	-	-	-	0.9	-
	R	2.7	-	-	-	-	-	-
	B	0.9	-	-	13.0	-	-	-
Peak heat flux violation [kW/m ²]	W	73.4	-	-	25.6	-	-	-
	R	-	37.0	46.7	30.8	99.1	-	-
	B	76.5	-	-	58.6	136.9	-	-
Axial acceleration violation [g]	W	0.9	-	-	0.9	0.0	0.5	-
	R	-	-	-	-	-	-	-
	B	-	0.2	-	1.2	-	-	-
Bending moment violation [kPa*deg]	W	133.8	-	-	-	-	27.7	-
	R	-	-	-	8.4	-	227.0	-
	B	-	-	-	265.3	-	-	-
Geographical violation [deg]	W	-	-	-	-	-	-	-
	R	0.3	-	-	-	-	-	-
	B	-	-	-	-	-	-	-
Final payload mass [kg]	W	3,322	3,281	3,475	3,393	3,141	3,295	3,264
	R	2,802	3,099	3,186	3,441	3,489	2,811	3,312
	B	3,326	3,052	3,225	3,238	3,098	2,954	2,881

W = worst aerodynamic configuration

R = reference aerodynamic configuration

B = best aerodynamic configuration

- = no violation

■ = trajectory without path constraint

■ = orbital element tolerance violations

Semimajor axis accuracy

Figures 6.4a and 6.4c show that the only case in which the semimajor axis tolerance is violated occurs in run 13 and 18, in the reference aerodynamic configuration. It can be seen that in both cases together with this violation also the other two orbital-element tolerances are not satisfied. This might be due to the fact that, while trying to reach the tolerance set on the eccentricity, there is a point at which the set semimajor axis tolerance is satisfied, but not the one of eccentricity. Then the vehicle keeps flying, in order to satisfy the eccentricity tolerance, but then the semimajor axis is already out of its bounds. At this point the trajectory simulation is stopped giving an error on both elements. Of course this explanation has also to take into account that the optimizable parameters might not be the optimal ones.

The problem about the optimizer not finding the optimal control angles depends on the initial population. If the particles flying in the search space are “stuck” in areas where violations of constraints occur, as the optimization goes on, this situation cannot change because the linearly decreasing inertia weight makes the search more exploitative than explorative.

Eccentricity accuracy

The tolerance on the eccentricity is the most violated amongst the orbital elements because a circular orbit is difficult to achieve with a direct launch. Moreover, the violations occur in those trajectories, which tolerance is 0.0001 or for vehicles with the best configuration. The reason may be that having a higher velocity (due to lower drag, with the best configuration), the launcher reaches about 170 km in a shorter time and has less time to curve towards a circular orbit, at 185 km. In this way it misses slightly (or heavily in some cases) the set tolerance. A drawback of this trajectory is that, by spending a longer time in the denser layers of the atmosphere, the vehicle violates slightly the dynamic pressure, the bending load and the peak heat flux.

This theoretical explanation can be proved by Fig. 6.6a and 6.6b regarding run 15, where Fig. 6.6a is the optimal trajectory flown with the best configuration and Fig. 6.6b is the optimal trajectory flown with

Table 6.7: Vega: the setup of the runs, launching into 51.6° inclination orbit.

Parameter	Simulation 13	Simulation 14
a [km]	6563.137	6563.137
e [-]	0	0
i [deg]	51.6	51.6
Tolerance a [km]	3	3
Tolerance e [-]	0.0005	0.0005
Tolerance i [deg]	0.1	0.1
Dynamic pressure [kPa]	≤ 50	≤ 50
Peak heat flux [kW/m ²]	≤ 120	≤ 120
Axial acceleration [g]	≤ 5.5	≤ 5.5
Bending load [kPa*deg]	≤ 300	≤ 300
Circularization burn	No	Yes
Coast arcs	Yes	Yes

the worst configuration (where no violation occurs). The launcher with the best aerodynamic configuration, reaches 170 km after about 300 s, with a steeper trajectory and it flies for a longer time trying to reach the given eccentricity. This may be caused by the worst attitude profile found. On the other hand, the launcher with the worst aerodynamic configuration, flies a less steep trajectory with a smoother attitude profile that makes it reach the final eccentricity within the tolerance.

Inclination accuracy

Hereafter, Fig. 6.7 shows the final inclination reached by several runs. It might be strange that an orbit with a lower inclination than the launch site latitude can be reached. This is formulated from the following geometric formula:

$$\cos i = \frac{\cos \delta_0}{\sin \psi_0} \quad (6.1)$$

where i is the inclination of the orbit, δ_0 is the latitude of the launch site and ψ_0 is the launch azimuth (or heading angle). From here, we can derive that the minimum inclination that can be reached from a launch site is by launching with $\psi_0 = 90^\circ$ (due east) for which an inclination equal to the latitude of the launch site is achieved.

However, the lower inclinations reached in some cases (runs 2, 4, 7, 10, 13 and 18) are possible because during the trajectories there are several plane changes achieved by means of attitude control. The yaw angle is mainly responsible for this event that steers the launcher towards the desired inclined plane. Of course this change of plane has some cost in terms of propellant that penalize the final payload mass.

Path constraints

The plots reported in Fig. 6.8 offer a graphical view of what has already been summarized in Table 6.4, 6.6 and 6.8. Moreover, normalized version of these plots can be found in Fig. 6.9. By normalizing the mechanical and thermal results to their path constraints, it becomes possible to appreciate those that have a major influence on the behaviour of the trajectory.

For the Vega as for other launchers, the peak heat flux limit is not know and neither the bending load limit. Therefore from the assumed limits, the major violations occur in the bending load and peak heat flux. These two characteristics are very important during the ascent and they should be satisfied as much as possible. Moreover, the fact that the bending load is often violated is due to the fact the angle of attack can get to 10° quite easily. Normally, during flown trajectories it is kept below this value, and if possible below 5° .

Furthermore, this analysis shows that the optimizer is not able to find control parameters at the nodes that result in lower angles of attack. However, in order to solve this issue, for future research, the effect of a constraint on the angle of attack should be investigated. Actually, only a constraint on the dynamic pressure

Table 6.8: Vega: a summary of the optimization runs is presented. The error on the final orbital elements are shown. Final orbit inclination is 51.6° .

Parameter		Simulation 13	Simulation 14
Error a	W	-	-
	R	0.07%	-
	B	-	-
Error e	W	0.00292	-
	R	0.0059	-
	B	-	-
Error i	W	0.27%	-
	R	0.30%	-
	B	-	-
Dynamic pressure violation [kPa]	W	-	-
	R	-	-
	B	-	-
Peak heat flux violation [kW/m ²]	W	-	-
	R	42.7	-
	B	-	-
Axial acceleration violation [g]	W	1.3	-
	R	-	0.7
	B	-	-
Bending moment violation [kPa*deg]	W	-	-
	R	70.1	-
	B	-	-
Geographical violation [deg]	W	-	-
	R	-	-
	B	-	-
Final payload mass [kg]	W	2,065	2,488
	R	1,568	2,243
	B	3,172	2,861

W = worst aerodynamic configuration

R = reference aerodynamic configuration

B = best aerodynamic configuration

- = no violation

■ = trajectory without path constraint

and orbital element tolerance violations

and the bending load is present and a constraint on the angle of attack might also help to satisfy better the bending load.

6.1.2 Two-objectives optimization results

Regarding the two-objective optimization, 4 runs have been performed for Vega. Table 6.9 shows the final orbital elements, relative tolerances and constraint limit sets.

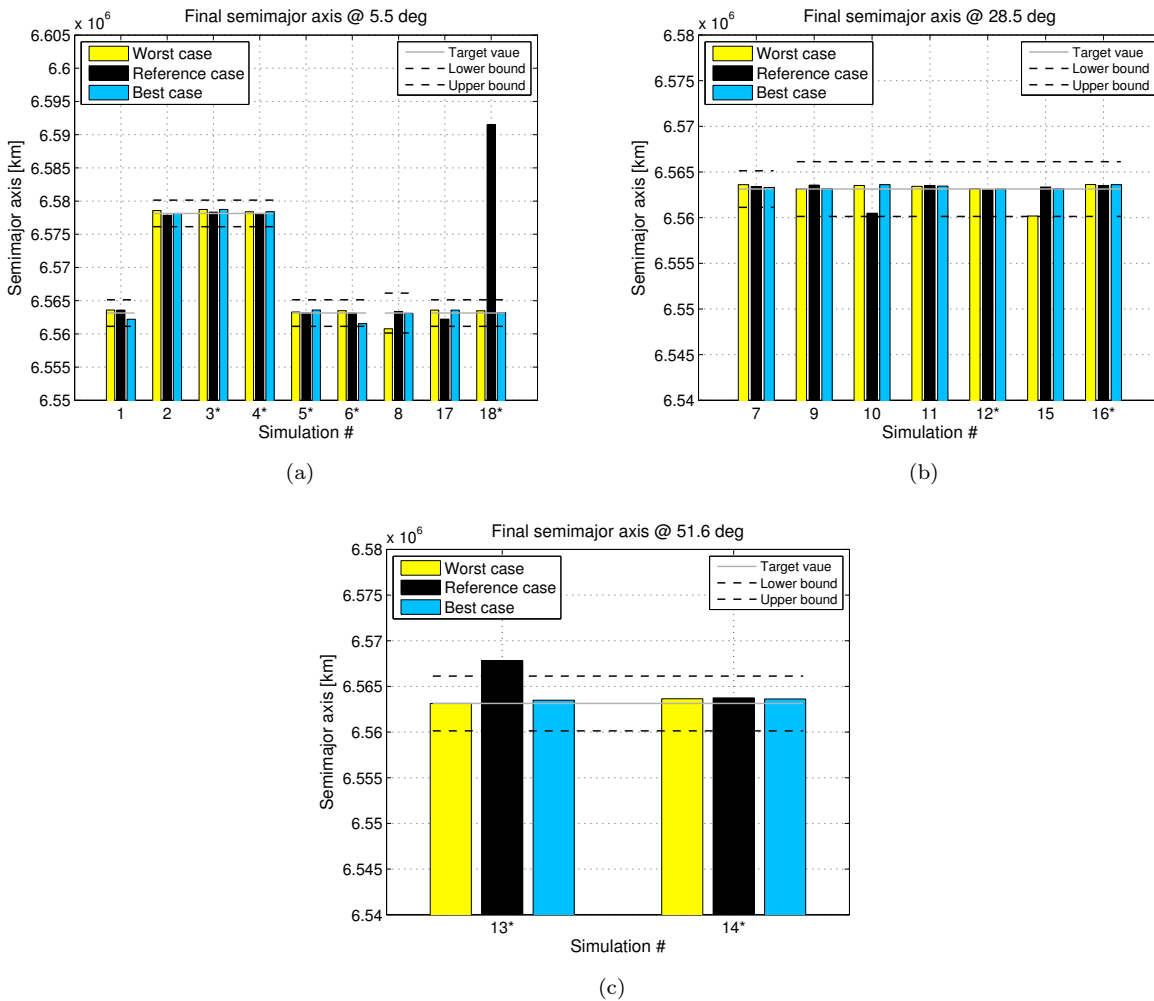
In this kind of optimization, there is one run for each final inclination, except for a 28.5° inclination for which two runs have been performed.

The main difference between the four runs is in the bending load limit and in the peak heat flux that is higher for the trajectory reaching 51.6° . In addition, for this final condition, the circularization burn may be used if necessary.

First thing to say about this multi-objective optimization is that the RSS of the final orbital elements is a measure of the accuracy achieved in the trajectory. If the RSS is smaller than 1 ($RSS < 1$), it means that the final orbital elements of the relative trajectory satisfy all the tolerances set.

In the analysis of the Pareto front obtained by the four runs the attention shall be focused on those trajectories that present a $RSS \leq 1$ or, if none, as close as possible to 1. The reason for this choice is that a LEO parking orbit is a low orbit for which apocentre and pericentre might decrease quite rapidly due to atmospheric drag. Furthermore, since this ascent analysis has to match the initial condition used in [Zuccarelli, 2009], the highest accuracy has to be striven.

However, concerning the orbital elements, this assumption does not exclude that a trajectory with a $RSS > 1$ might still satisfy all the tolerances. This is because each single term in the RSS formula (see Eq. 5.25) represents the measure of satisfaction of the single tolerance. Each single term can be still lower than 1 but when they are added together, their sum can get up to 3 (in case semimajor axis, eccentricity and inclination tolerances only are considered). By taking the root square of the term we have a maximum value of 1.73. Therefore, if we say that the RSS has to be smaller than 1, we are assuming that the point



* = trajectory with coast arcs

Figure 6.4: Vega: semimajor axis accuracies at three different final orbit inclinations.

in space that represents the target orbital elements (three in this very case) has a spherical space around it in which the actual trajectory can satisfy all the tolerances.

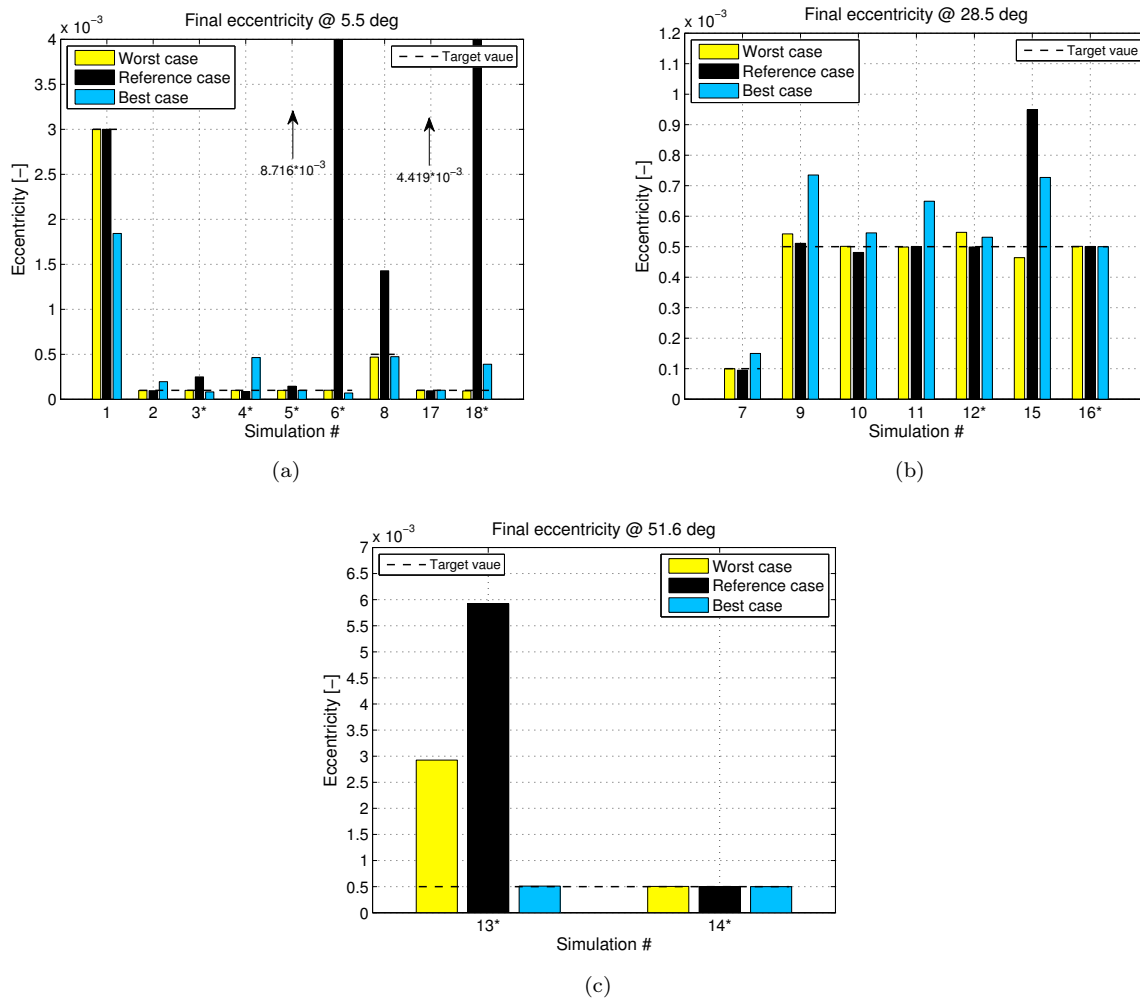
On the other hand, if we consider that the RSS has to be smaller than 1.73, we are considering a cubic space around the target point. The spherical space tells us that the tolerances are satisfied for sure, whereas the cubic space does not imply that all the tolerances are satisfied, but there could be at least two that might violate them.

A solution to this problem has not been found and the disadvantage of the RSS appears. The only thing that can be done would be the use of a flag for each tolerance, which record if the single orbital element is smaller or higher than 1. In this way the user has an insight, when looking at the RSS , on whether tolerances violations occur at all.

What has been said so far does not apply to the RSS of the path constraints since the formula used for this case is different from the one used for the orbital elements.

From the closest view of Fig. 6.10a, it results that the trajectories with an RSS following the aforementioned requirements are listed in Table 6.10.

It must be said that the trajectories present in Table 6.10 do not violate the path constraints (dynamic pressure, peak heat flux, bending moment and axial acceleration) at all.



* = trajectory with coast arcs

Figure 6.5: Vega: eccentricity accuracies at three different final orbit inclinations.

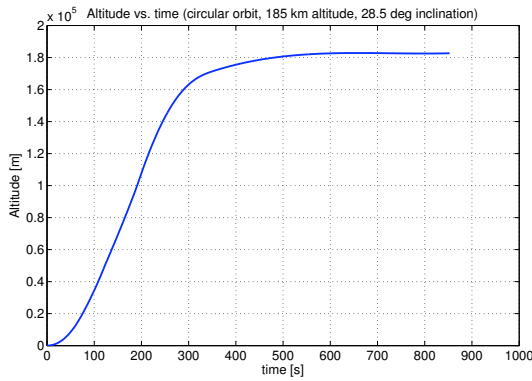
6.1.3 Three-objectives optimization results

Regarding the three-objective optimization, 2 runs have been performed. Table 6.11 shows the final orbital elements, relative tolerances and constraint limits set.

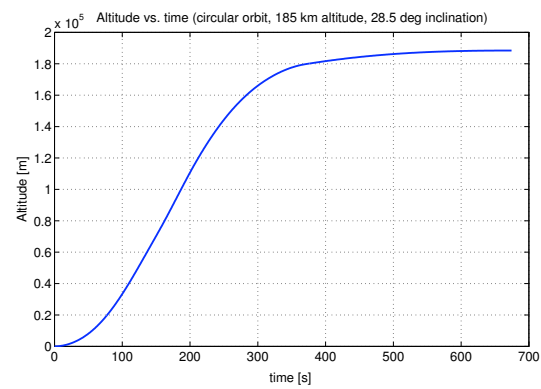
In the first run, in Fig. 6.11, the first 2D view shows that the solutions form a kind of Pareto front (but not a real one). The second 2D view shows that most of the found solutions have an *RSS* of the path constraints close to 0. This latter observation helps in explaining the behaviour in the first view similar to a Pareto front. It is clear that all the solutions of the Pareto surface can be used according one's criteria of design of the mission. If final orbit element did not have to be satisfied with high accuracy and slight violations in the path constraints were permitted, then a solution giving a higher payload mass would be available. This kind of analysis is very useful especially when no maiden flight has occurred yet and the effects that it might cause are to investigated. Eventually, the 3D view in Fig. 6.11c gives a global view of the Pareto surface from which the solutions might be chosen more easily.

In this multi-objective optimization, for one run (i.e., run 2), an experiment has been performed including *RSS* of two groups of path constraints. In this case the orbital elements are used as constraints. This kind of optimization was aimed at analyzing how the optimizer would perform with different type of objectives.

For the specific case, the first group of constraints is composed by dynamic pressure and axial acceleration



(a) Vega with the best aerodynamic configuration.



(b) Vega with the worst aerodynamic configuration.

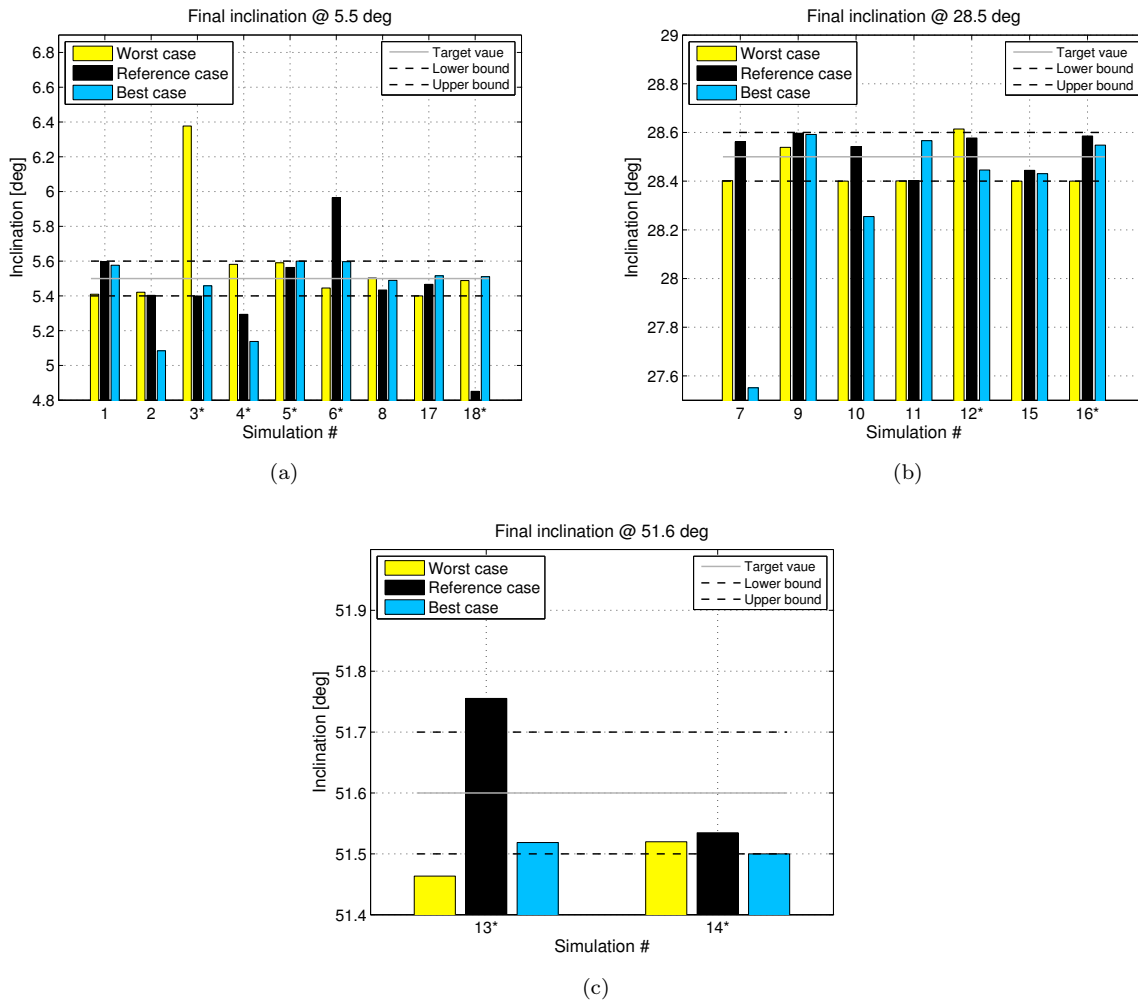
Figure 6.6: Vega: effect of different aerodynamic configurations on the final eccentricity.

Table 6.9: Vega: two-objectives optimization settings: final orbital elements and constraint limits.

Parameter	Simulation 1	Simulation 2	Simulation 3	Simulation 4
a [km]	6563.137	6563.137	6563.137	6563.137
e [-]	0	0	0	0
i [deg]	5.5	28.5	28.5	51.6
Tolerance a [km]	3	3	3	3
Tolerance e [-]	0.0005	0.0005	0.0005	0.0005
Tolerance i [deg]	0.1	0.1	0.1	0.1
Dynamic pressure [kPa]	≤ 50	≤ 50	≤ 50	≤ 50
Peak heat flux [kW/m ²]	≤ 120	≤ 120	≤ 120	≤ 160
Axial acceleration [g]	≤ 5.5	≤ 5.5	≤ 5.5	≤ 5.5
Bending load [kPa*deg]	≤ 300	≤ 280	≤ 280	≤ 300
Circularization burn	No	No	No	Yes
Coast arcs	No	No	Yes	No

constraints. The second group is made by peak heat flux, bending load and geographical constraints. The objectives are the *RSS* of the constraints themselves. Moreover, one has to be careful to create the groups by balancing the type of constraints included, e.g., by splitting the dynamic pressure and bending load. This trick should give a balance in the importance of the constraints as the bending load is composed by the dynamic pressure term. Therefore, if a violation occurs in the dynamic pressure, it might also occur in the bending load and vice versa. About the dynamic pressure and bending load constraint, the angle of attack should be introduced in the constraint set, as suggested in the previous sections, to investigate the influence on the objective in which is inserted and on the overall simulation. It has to be stressed that still the bending load constraint should be present since dynamic pressure and angle of attack are important for the integrity of the structure also when the product of them is considered.

The meaning of a *RSS* of the path constraints is not the same as in the case of the orbital elements. In this case the *RSS* gives a measure of the total violation of the constraints. From Fig. 6.12a, 6.12b and 6.12c, the reader might think that less solutions are found by the optimizer. This is not the case because from a closer look, in Fig. 6.13, it is evident that there are as many solutions as for the other configurations but they are more close to each other. Specifically, the first group of constraints is made up by dynamic pressure and axial acceleration whereas the second group is made up by peak heat flux, bending load and geographical constraints. In Fig. 6.13, the user should not try to find a Pareto front as this is only a closer look of Fig. 6.12a and it should be noticed that solutions with a higher *RSS* of the path constraints of the first group have a lower *RSS* of path constraints of the second group (which is the criterion of Pareto dominance to find the solutions on the Pareto surface). It is also apparent that solutions of the reference aerodynamic case have a



* = trajectory with coast arcs

Figure 6.7: Vega: inclination accuracies at three different final orbit inclinations.

much higher RSS along both groups and a lower payload mass, that means the optimizer completely missed the right area where better solutions were (that might be addressed to the initial population).

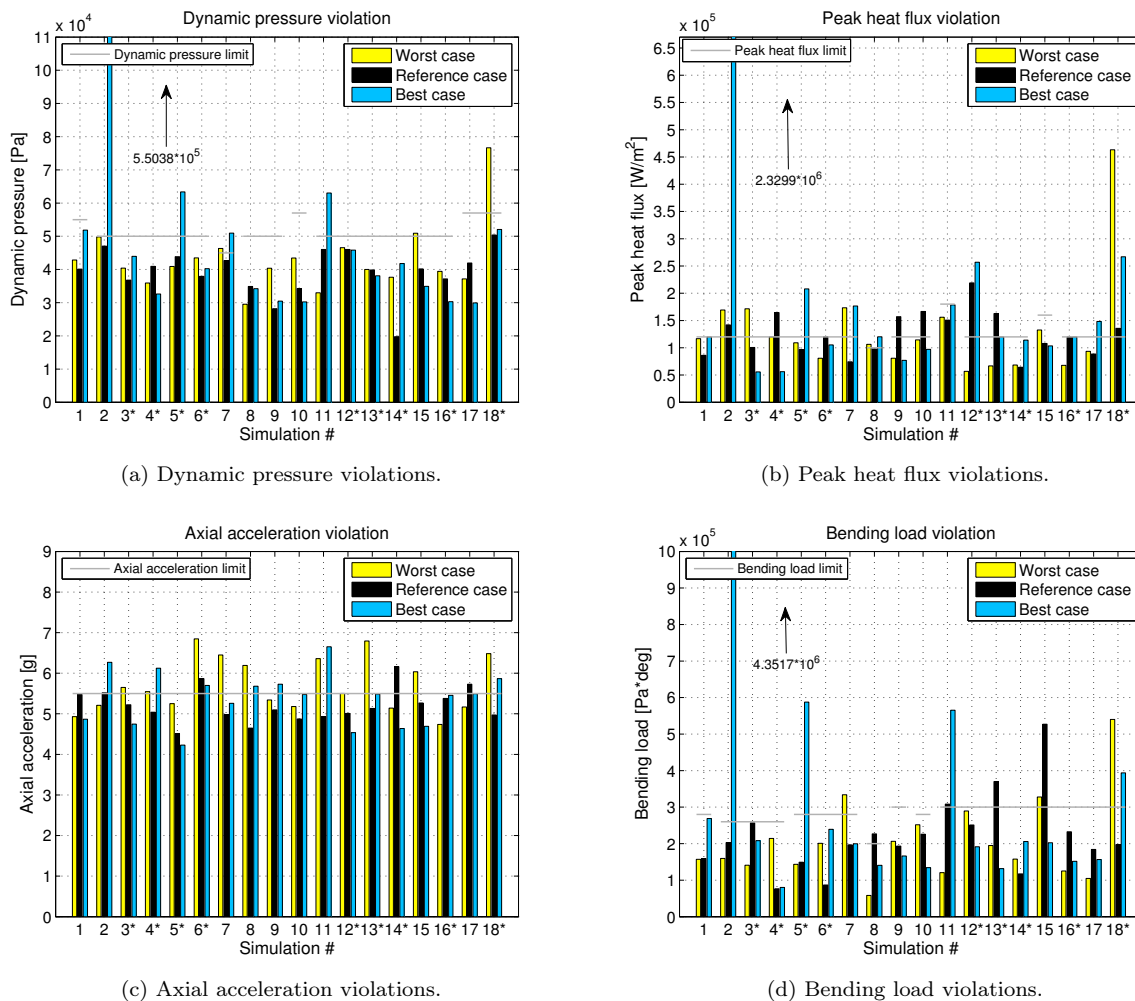
Moreover, by using this type of objective, it is more likely that trajectories with constraint violations will result in order to form the Pareto surface. If a trajectory, where no violations occur, is found the whole Pareto surface would reduce to one point (if no other trajectories without violations are found). This would be a good trajectory for the launcher but would alter the purpose of the multi-objective optimization.

Eventually, from Table 6.12, applying the criterion for which a trajectory is selected if it satisfies the constraints, we can apply a second criterion according to which the trajectory has to satisfy the tolerances on the orbital elements. Therefore, in this case, the optimal solution is given by the highlighted green cells, yielding a final payload mass of 3,046 kg.

On the other hand, for run 2, none of the depicted trajectories can be selected since they all violate at least one group of constraints.

6.1.4 Conclusions

In conclusion, for Vega, all the found optimal trajectories do not make use of any orbital coast phase, even though the option of circularization is available. The launcher burns its stages till reaching the final orbit



* = trajectory with coast arcs

Figure 6.8: Vega: path constraints violations.

because the burnout of the stage before the upper one occurs at about 160 km altitude. At that altitude it is not convenient to use a coast phase anymore since the final orbit is 25 km higher.

Moreover, the coast arcs between the stages, when active, are in the 2-8 seconds range. However, no advantages seem to derive from the use of coasting periods for the configuration and the trajectories flown by this launcher.

Then, in Fig. 6.14, the control history for best solution is presented where the nodes can be clearly seen during the gravity turn (pitch and yaw) and the bi-linear tangent law (yaw). The profile refers to the solutions found in run 10 in the worst aerodynamic configuration that yields a final payload mass of 3,475 kg. Still, the yaw presents some sharp changes in the control profile and it has to be verified if the vehicle can fly this kind of profile. In Fig. 6.15, the altitude-velocity plot is depicted and the main events occurring during the flight are shown (e.g., stages burnout and fairing jettison).

It is clear that the 4th stage is not needed to increase the launcher velocity since it has a thrust lower than that of the other stages. A lower thrust is necessary since the atmospheric influence is much weaker whereas a higher thrust of the previous stages is necessary to escape the gravitational attraction.

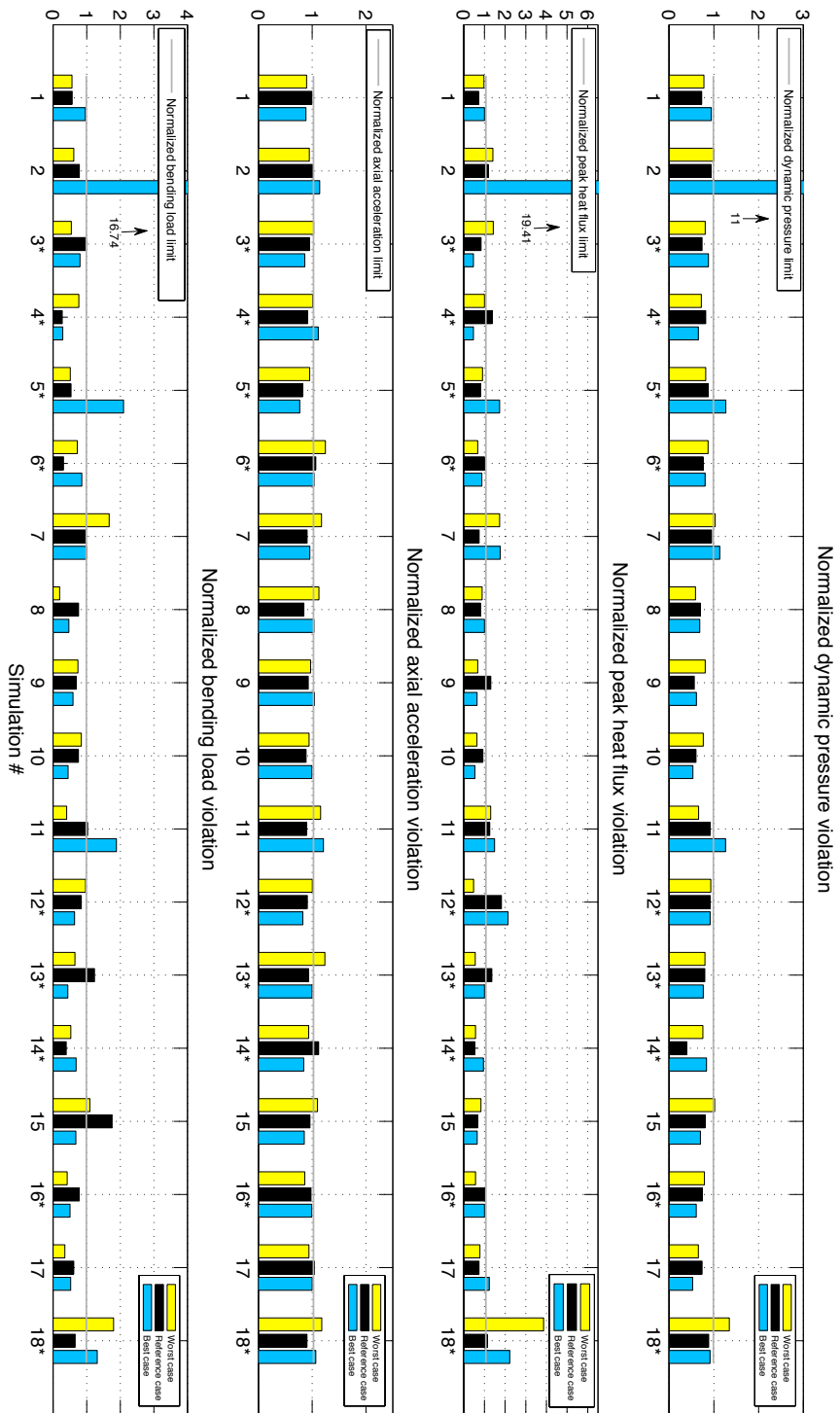


Figure 6.9: Vega: normalized path constraints. The normalization has been performed according to the different limits set per run.

Table 6.10: Vega: payload masses for the best trajectories resulting from the two-objective optimizations. The green cells highlight the trajectories that satisfy the given tolerances on the final orbital elements according the criterion $RSS < 1$.

	Run 1		Run 2		Run 3		Run 4	
	Payload mass [kg]	RSS orbital elements						
Worst	3,441	1.077	3,268	0.9695	3,307	0.9352	3,169	1.229
	3,454	1.082	3,269	0.9977	3,402	1.069	3,173	1.549
	3,522	1.269			3,404	1.078		
Reference	3,282.50	2.763	3,419	2.006	3,447	1.801	3,034	1.674
	32,832.80	2.789	3,421	2.172	3,453	2,325	3,043	1.994
Best	3,391	0.8965	2,607	2.58	3,484	1.882	3,263	1.066
	3,392	0.9345	2,609	2.609	3,491	3.291	3,269	1.235
	3,393	0.9725						
	3,405	0.9942						

■ = trajectory without path constraint
and orbital element tolerance violations

Table 6.11: Vega: three-objectives optimization settings: final orbital elements and constraints limits.

Parameter	Simulation 1	Simulation 2
a [km]	6563.137	6563.137
e [-]	0	0
i [deg]	5.5	5.5
Tolerance a [km]	3	3
Tolerance e [-]	0.0005	0.0005
Tolerance i [deg]	0.1	0.1
Dynamic pressure [kPa]	≤ 50	≤ 50
Peak heat flux [kW/m ²]	≤ 120	≤ 120
Axial acceleration [g]	≤ 5.5	≤ 5.5
Bending load [kPa*deg]	≤ 300	≤ 300
Circularization burn	Yes	Yes
Coast arcs	Yes	Yes

6.2 Proton M

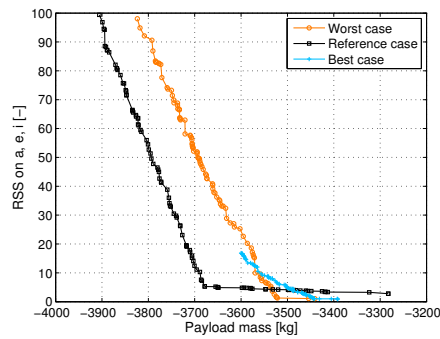
From this point on, the analyzed launchers are used to bring payload to the Moon or supplies once the base has been built. The Proton M is a three-stage launcher without boosters, launched from Baikonur. The axial acceleration limit is 4 g and the maximum dynamic pressure that the launcher can withstand is 40,000 Pa, from [ILS, 2009].

6.2.1 One-objective optimization results

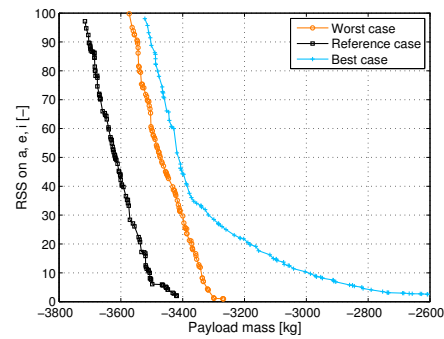
Concerning the launches to bring material to the Moon to build the base, the first launcher to be analyzed is the Proton, that is launched from Baikonur towards a circular orbit at 185 km altitude and 51.6° inclination. For all the runs performed, no circularization burn option has been included in the setup.

From the analysis of Table 6.13 and 6.14, it is evident that all optimal trajectories violate by some degrees the range azimuth imposed. In fact, for launches from Baikonur, there are very narrow corridors in which the vehicle has to fly since it passes over inhabited areas. This safety constraint is due to the jettisoned stages falling on the land. As a consequence, it results in very strict geographical constraints that in this case are not satisfied. This does not mean that the launcher flies all the time outside the given corridor but that it does so in some part of the trajectory.

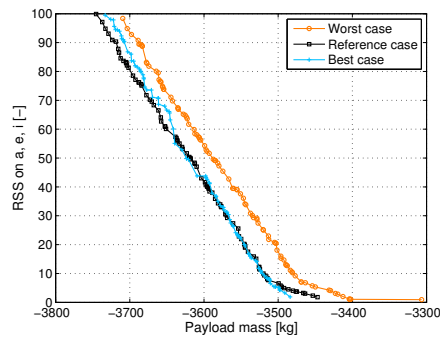
Another peculiar fact is that a strict tolerance (i.e., 0.0001, in runs 7 to 9) on the final eccentricity produces more effect on the final inclination, violating it, than on the eccentricity itself (see Fig. C.3). This behaviour is strange since the inclination is influenced only by the azimuth and the latitude and it should



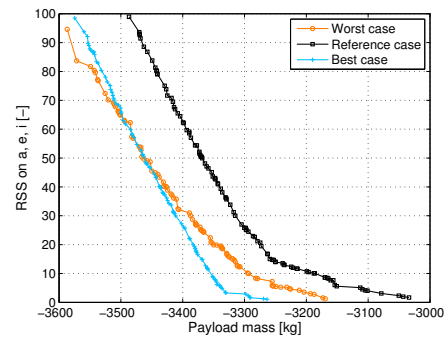
(a) Run 1. Final orbit inclination is 5.5° . It might be apparent that, for the best aerodynamic configuration, the particles found by the optimizer are less than the other two case. This is not the case but it is due to the fact that all the solutions composing the Pareto (that are as many as in the other cases) have a RSS lower than 20.



(b) Run 2. Final orbit inclination 28.5° .



(c) Run 3. Final orbit inclination 28.5° .



(d) Run 4. Final orbit inclination 51.6° .

Figure 6.10: Vega: two-objective optimization.

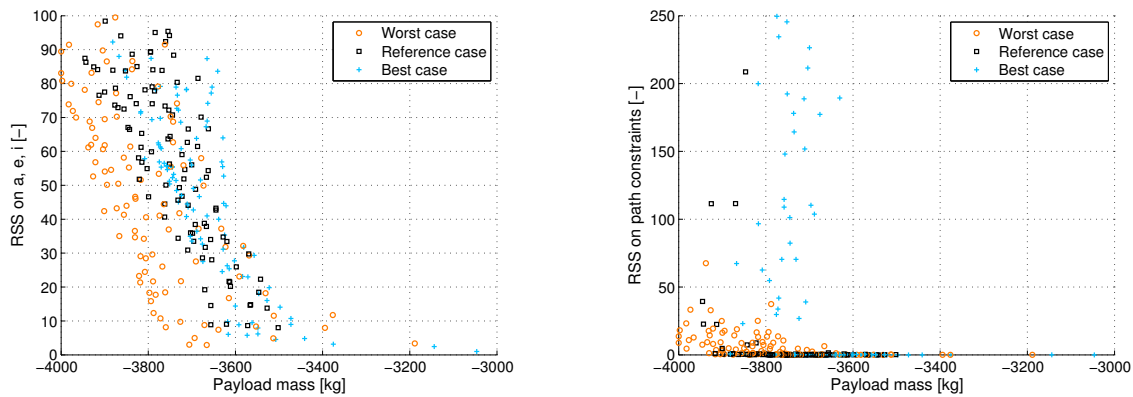
not have a correlation with the eccentricity. Anyway, an hypothesis is that the optimizer does not converge since it is not able to find solutions that satisfy the given tolerances but this has to be investigated further. Moreover, in the same runs a violation of the bending load occurred consistently (except in two cases, in run 7).

The peak heat flux and the axial acceleration limits are never exceeded and the dynamic pressure limit is violated only twice by a maximum of 900 Pa. On the other hand, the bending load is violated several times: in some runs it might be related to the stricter tolerance on the eccentricity, but in the other cases it can be addressed only to non-optimal values of the pitch angles in the gravity turn phase.

One issue that is recursive also for this launch vehicle is that, with the best aerodynamic configuration, the eccentricity is violated more often than with other configurations. The reason for this to happen has already been explained for the Vega and holds also for the Proton. Moreover, as has been said for Vega, there is a correlation between the semimajor axis and eccentricity tolerance violation, which has been explained in section 6.1.1, where the *Semimajor axis accuracy* is discussed.

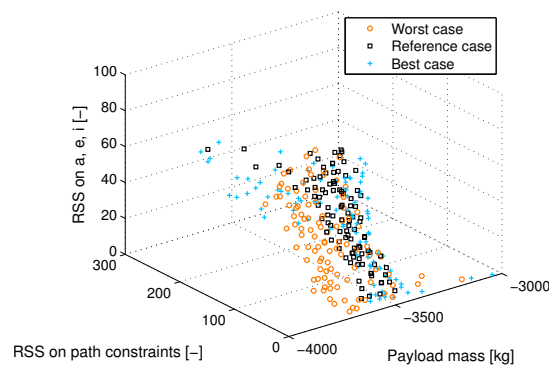
In Appendix C, the complete set of results are presented for each launcher. There, the orbital elements for each run and aerodynamic configuration and path constraints, normalized and not, are given. Therefore, from now on, those results can be found there.

The most difficult path constraint to fulfill is the bending load as it can be seen from Fig. C.5. All other path constraints are easily satisfied. Since the dynamic pressure is always within the limit of the launcher, the violation is due to high angles of attack that originate from the fact that the pitch angle is optimized in



(a) 2D view of the Pareto surface with payload mass on x -axis and RSS of final orbital elements on z -axis.

(b) 2D view of the Pareto surface with payload mass on x -axis and RSS of path constraints violations on y -axis.



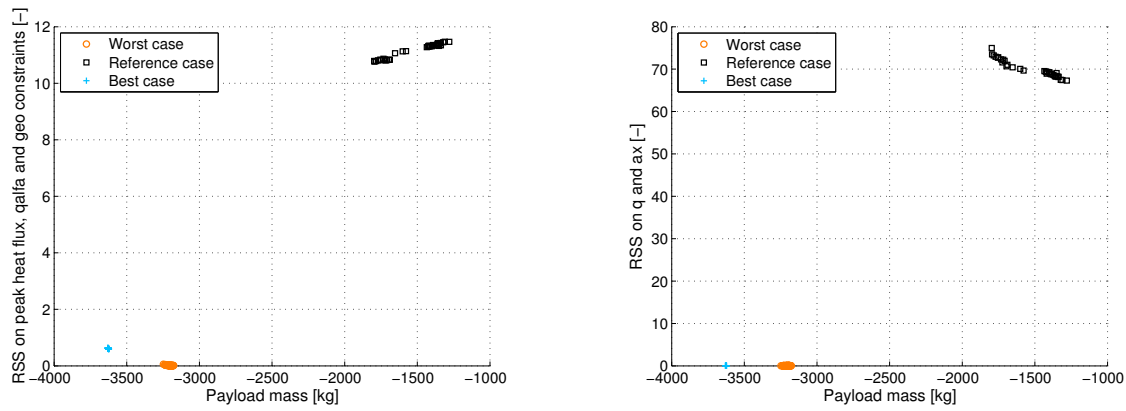
(c) 3D view of the Pareto surface obtained.

Figure 6.11: Vega: three-objective optimization, run 1.

the neighbourhood of the flight-path angle and differences between the two arise quite easily. This should be due to the optimizer that does not prove to work very well but that might be solved through the reduction of the range around the flight path angle in which the pitch angle is optimized, or the introduction of an angle-of-attack constraint.

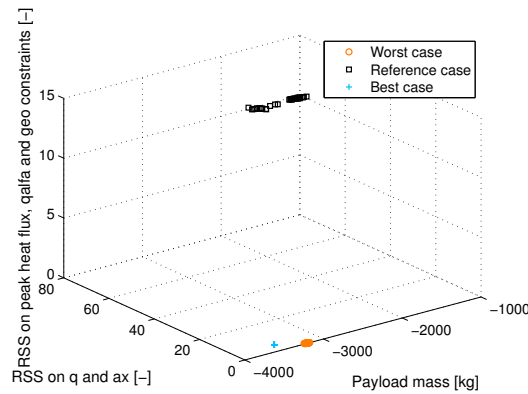
Eventually, as the best trajectory or trajectories have to be chosen, the driving factor would be, besides constraints satisfaction, the azimuth range satisfaction. Since none of the trajectories fully respect this constraint, those that violate it by the smallest amount are picked. Therefore, the resulting best trajectory is highlighted in green in Table 6.14. The azimuth violation for this trajectory is about 2.2° and the payload mass is 23,091 kg. The payload masses have values between 19,500 kg and 24,000 kg (see Fig. 6.16). Besides the trajectories with the strictest eccentricity tolerances (i.e., runs 7 to 9, in the reference configuration), the highest payload mass is usually given by the best aerodynamic configuration, even though their final eccentricities are always out of bounds.

Concerning the worst aerodynamic configuration, in the first 11 runs, it gives payload masses lower than those given by the reference configuration. This means that the worst configuration, for this launcher, presents disadvantages, namely higher drag and consequently more propellant to reach the final orbit. On the other hand, the best aerodynamic configuration performs better or slightly better than the reference configuration, as it might be expected, but in some runs it is difficult to match the orbital elements required. The explanation might be found in the optimizer that is not always to cope with all the path and boundaries constraints in a good way.



(a) 2D view of the Pareto surface with payload mass on x -axis and RSS on the second group of path constraints on z -axis. The second group gathers peak heat flux, bending load and geographical constraints.

(b) 2D view of the Pareto surface with payload mass on x -axis and RSS on the first group of path constraints on y -axis. The first group includes dynamic pressure and axial acceleration constraints.



(c) 3D view of the Pareto surface obtained.

Figure 6.12: Vega: three-objective optimization, run 2.

6.2.2 Two-objective optimization results

For the Proton, 4 two-objectives optimizations have been performed. Table 6.15 summarizes the settings for this vehicle. All the runs performed involve as a second objective the RSS of the path constraints.

From the analysis of Fig. 6.17 and Table 6.16, it results that this type of optimization, involving the RSS of the path constraints as second objective, aims at finding trajectories that have a low RSS for the constraint violations. The fact that there are not many particles in some of the Pareto fronts means that, even though all the trajectories satisfy the tolerances on the orbital elements (constraints in this case), the improvement for a lower RSS is much harder than when use of RSS of orbital elements is made.

In Fig. 6.17, it can be seen that the lower plots, for run 3 and 4, that have a higher dynamic pressure and peak heat flux constraints, have larger Pareto fronts. This might be due to the fact that two constraints are larger and they may not be violated, producing a lower RSS . In all the configurations and runs that present a very small Pareto front, it has to be pointed out that the number of solutions is the same as the other configurations and runs, but the front is more concentrated in a smaller area. It may be that the more strict the constraints are (since the tolerances are not varied), the smaller is the Pareto front, meaning that solutions on the front are more likely to be only slightly improved or worsened.

From the results obtained, shown in Table 6.16, the lowest RSS have been obtained in the runs in which higher constraints on the dynamic pressure and peak heat flux have been set up. However, this might be due to the fact that the terms in the RSS formula have a larger denominator or that this more relaxed

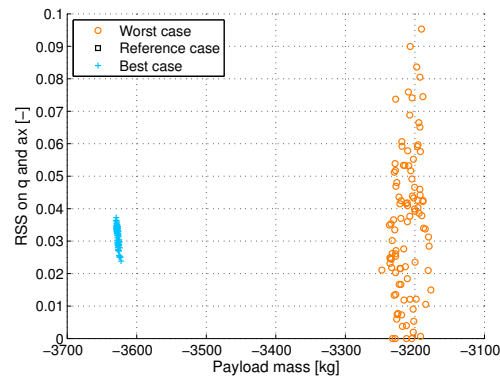


Figure 6.13: Vega: zoom of the 2D view of the Pareto surface shown in Fig. 6.12b. Solutions with a higher RSS of path constraints of the first group have a lower RSS of path constraints of the second group.

Table 6.12: Vega: three-objective optimization. In run 1, only the best aerodynamic configuration manages to have a $RSS < 1$. Run 2 does not give any flyable trajectory.

	Run 1			Run 2		
	Payload mass [kg]	RSS path constraints	RSS orbital elements	Payload mass [kg]	RSS path constraints (group 1)	RSS path constraints (group 2)
Worst	3,666	6.4	2.9	3,190	0.095	0
	3,706	3.628	2.989	3,188	0.0744	0.00046
				3,193	0.0804	0.00062
Reference	3,502	0.211	8.019	1,795	73.48	10.7
				1,783	73.23	10.78
Best	3,046	0	0.985	3,624	0.0279	0.591
				3,623	0.025	0.595

■ = trajectory without path constraint
and orbital element tolerance violations

constraints are not violated.

Comparing run 1 and 2, it results that the use of coast arcs produces higher violations of the constraints that is due to the change in pitch value from a value around the flight path angle (through linearization of the control) to the flight path angle itself. However, with larger constraints, in run 3 and 4, the coast arcs used in run 4 produce lower violations with respect to the case in which they are not used.

This type of optimization, involving this type of RSS , is a new approach in the multi-objective optimization. However, for the final goal of this thesis, that regards a feasibility study for a mission to the Moon, the launchers have to be able to fly the optimal trajectories without constraint violations, as the launch systems might not be able to withstand values higher than those given in their user's manuals. Moreover, from the RSS of the path constraints, one can get less information with respect to the one of orbital elements, unless one has no knowledge of the mechanical and thermal limits of a vehicle. In this latter case, this kind of analysis help in assessing the launch system and its capabilities.

6.2.3 Three-objective optimization results

For the Proton, 5 three-objectives optimizations have been performed. Table 6.17 summarizes the settings for this vehicle. The first four runs have been performed using the final payload mass, the RSS of the path constraints and the RSS of the orbital elements as objectives (no constraints), while the fifth run has been performed using the final payload mass and the RSS of two groups of path constraints as objectives (first objective with dynamic pressure and axial acceleration, second objective with peak heat flux, bending load and geographical constraint whereas the tolerances of the orbital elements are used as constraints). The resulting Pareto surface views are shown in Fig. 6.18 to Fig. 6.23.

From Table 6.18, it is evident that in all the first four runs the RSS of the path constraints is low except

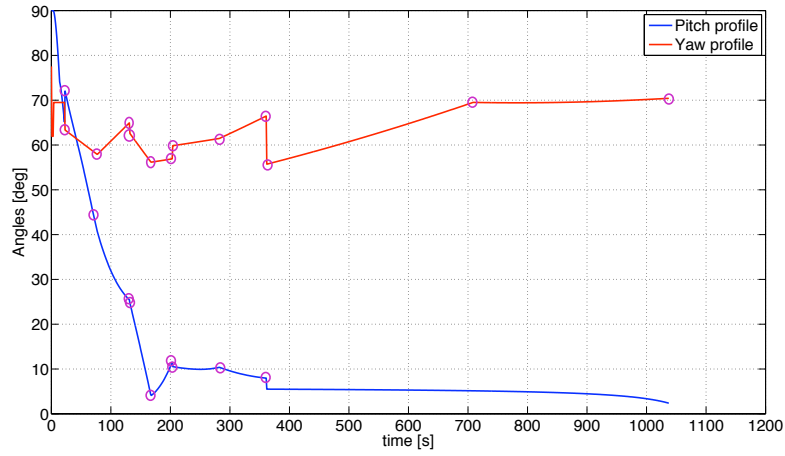


Figure 6.14: Vega: control history of the best solution found.

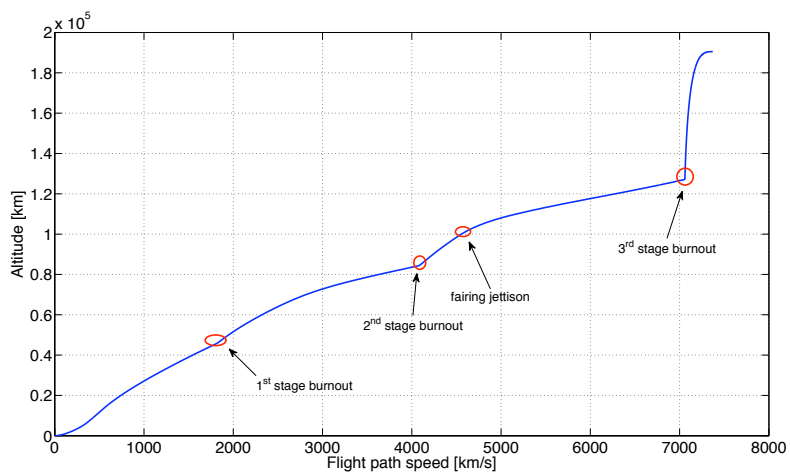


Figure 6.15: Vega: altitude-velocity plot for the best solution.

Table 6.13: Proton M: setup of the runs, launching into 51.6° inclination orbit. The final orbital elements, the relative tolerances and the path constraint limits are shown. Moreover, for each run, presence of coast arcs and circularization burn is indicated.

Parameter	Simulation 1	Simulation 2	Simulation 3	Simulation 4	Simulation 5	Simulation 6	Simulation 7	Simulation 8	Simulation 9	Simulation 10	Simulation 11	Simulation 12	Simulation 13	Simulation 14
a [km]	6563.137	6563.137	6563.137	6563.137	6563.137	6563.137	6563.137	6563.137	6563.137	6563.137	6563.137	6563.137	6563.137	6563.137
e [-]	0	0	0	0	0	0	0	0	0	0	0	0	0	0
i [deg]	51.6	51.6	51.6	51.6	51.6	51.6	51.6	51.6	51.6	51.6	51.6	51.6	51.6	51.6
Tolerance a [km]	3	3	3	3	3	3	2	3	3	3	3	3	3	3
Tolerance e [-]	0.0005	0.0005	0.0005	0.0005	0.0005	0.0005	0.0001	0.0001	0.0001	0.0005	0.0005	0.0005	0.0005	0.0005
Tolerance i [deg]	0.1	0.1	0.1	0.1	0.1	0.1	0.1	0.1	0.1	0.1	0.1	0.1	0.1	0.1
Dynamic pressure [kPa]	≤ 40	≤ 40	≤ 40	≤ 40	≤ 40	≤ 40	≤ 40	≤ 40	≤ 40	≤ 40	≤ 40	≤ 40	≤ 45	≤ 40
Peak heat flux [kW/m ²]	≤ 120	≤ 120	≤ 120	≤ 120	≤ 120	≤ 120	≤ 120	≤ 120	≤ 120	≤ 100	≤ 100	≤ 120	≤ 120	≤ 100
Axial acceleration [g]	≤ 4	≤ 4	≤ 4	≤ 4	≤ 4	≤ 4	≤ 4	≤ 4	≤ 4	≤ 4	≤ 4	≤ 4	≤ 4	≤ 4
Bending load [kPa*deg]	≤ 100	≤ 150	≤ 200	≤ 200	≤ 100	≤ 100	≤ 100	≤ 100	≤ 100	≤ 80	≤ 100	≤ 120	≤ 120	≤ 100
Circularization burn	No	No	No	No	No									
Coast arcs	No	No	No	Yes	No	No	No	No	No	No	No	No	Yes	No

Table 6.14: Proton M: results for the one-objective optimization.

Parameter	Simulation 1	Simulation 2	Simulation 3	Simulation 4	Simulation 5	Simulation 6	Simulation 7	Simulation 8	Simulation 9	Simulation 10	Simulation 11	Simulation 12	Simulation 13	Simulation 14
Error a	W	0.18%	-	0.21%	-	0.21%	-	-	0.16%	-	-	0.08%	-	0.30%
	R	0.13%	-	-	-	0.08%	-	0.05%	-	-	-	-	-	-
Error e	W	0.0011	0.17%	0.05%	-	-	-	-	0.0033	0.0023	-	-	0.00077	0.10%
	R	0.0021	-	0.0022	0.002	-	0.0014	0.00026	-	-	-	-	0.00055	0.0012
Error i	W	-	0.0014	0.0016	0.00052	0.00096	0.00053	-	0.0006	0.00096	0.00096	-	0.0014	0.0017
	R	-	1.23%	-	-	-	0.35%	1.15%	1.28%	1.72%	-	0.28%	-	-
Dynamic pressure violation [kPa]	W	-	-	-	-	-	-	0.04	-	-	-	-	-	-
	R	-	-	-	-	-	-	0.9	-	-	-	-	-	-
Peak heat flux violation [kW/m2]	W	-	-	-	-	-	-	-	-	-	-	-	-	-
	R	-	-	-	-	-	-	-	-	-	-	-	-	-
Axial acceleration violation [g]	W	-	-	-	-	-	-	-	-	-	-	-	-	-
	R	-	-	-	-	-	-	-	-	-	-	-	-	-
Bending load violation [kPa*deg]	W	120.3	23.7	-	-	122.2	-	0.9	83.8	13.0	23.7	-	130.6	133.8
	R	-	23.2	-	-	171.1	-	209.7	77.4	-	-	-	177.2	92.1
Geographical violation [deg]	W	69.7	2.5	0.7	31.6	-	79.6	296.0	176.8	-	-	-	42.0	159.1
	R	2.3	2.5	4.3	3.7	4.5	3	4.8	4.3	5.4	4.5	4.6	2.6	3.4
Final payload mass [kg]	W	19,683	20,153	20,072	20,166	21,707	22,055	20,537	21,425	21,557	21,706	23,488	21,785	22,098
	R	23,806	22,535	22,514	23,050	22,284	23,688	23,100	22,322	22,284	22,284	19,663	19,995	22,850
	B	-	-	23,671	23,050	22,801	19,876	21,896	19,705	22,801	22,801	23,091	20,093	20,972

W = worst aerodynamic configuration

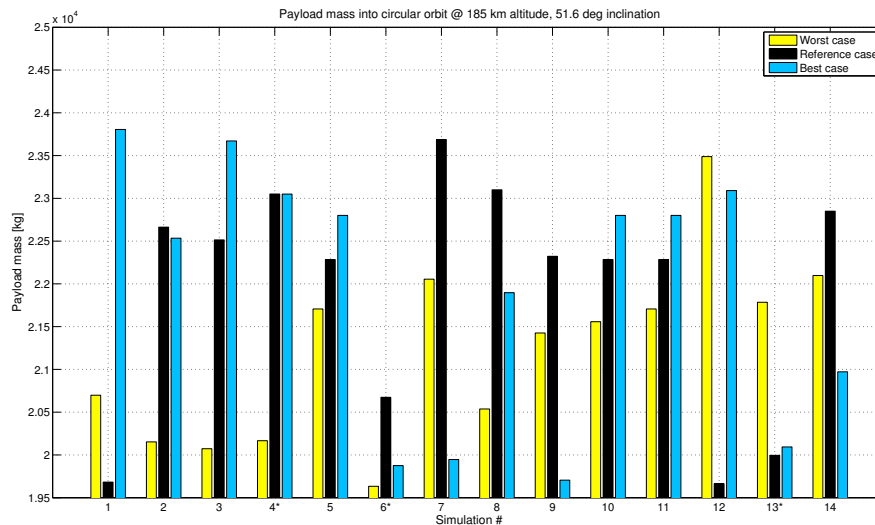
R = reference aerodynamic configuration

B = best aerodynamic configuration

- = no violation

■ = trajectory without path constraint

■ = and orbital element tolerance violations



* = trajectory with coast arcs

Figure 6.16: Proton M: optimal payload masses resulting from the runs.

Table 6.15: Proton M: two-objectives optimization settings: final orbital elements and constraints limits.

Parameter	Simulation 1	Simulation 2	Simulation 3	Simulation 4
a [km]	6563.137	6563.137	6563.137	6563.137
e [-]	0	0	0	0
i [deg]	51.6	51.6	51.6	51.6
Tolerance a [km]	3	3	3	3
Tolerance e [-]	0.0005	0.0005	0.0005	0.0005
Tolerance i [deg]	0.1	0.1	0.1	0.1
Dynamic pressure [kPa]	≤ 40	≤ 40	≤ 45	≤ 45
Peak heat flux [kW/m ²]	≤ 100	≤ 100	≤ 120	≤ 120
Axial acceleration [g]	≤ 4	≤ 4	≤ 4	≤ 4
Bending load [kPa*deg]	≤ 100	≤ 100	≤ 120	≤ 120
Circularization burn	No	No	No	Yes
Coast arcs	No	Yes	No	Yes

in some cases (i.e., run 3 with the worst configuration). No trajectory has a RSS of the orbital elements smaller than 1 and the smallest is 1.22, that means that the tolerances on the orbital elements might be violated. This solution has an RSS of the path constraints equal to 0.081 and yields a payload mass of 20,548 kg. Anyway, it cannot be flown for launch system requirements (i.e., dynamic pressure, peak heat flux, bending load and axial acceleration).

A curious thing can be seen in the fifth run, in Table 6.18 and in Fig. 6.23b, where the RSS of the first group of path constraints (dynamic pressure and axial acceleration) is 0. That means that no violation occurred for those constraints. From this result, it might also be derived that the RSS values in the two-objective optimizations are mainly given by the violation of the second group of constraints. However, from the one-objective optimization, it has been seen that the peak heat flux has never been violated. Therefore, the main contributions to the RSS , in the two-objective and in the group 2 of the three-objective optimization, is given by the bending load and azimuth range constraints.

Once again, it is confirmed that the bending load is the most difficult constraint to satisfy and that a constraint on the angle of attack is needed. In addition, in the case of the Proton M, it is necessary to satisfy the azimuth constraint for safety reason (i.e., lower stages falling over inhabited areas). As the range

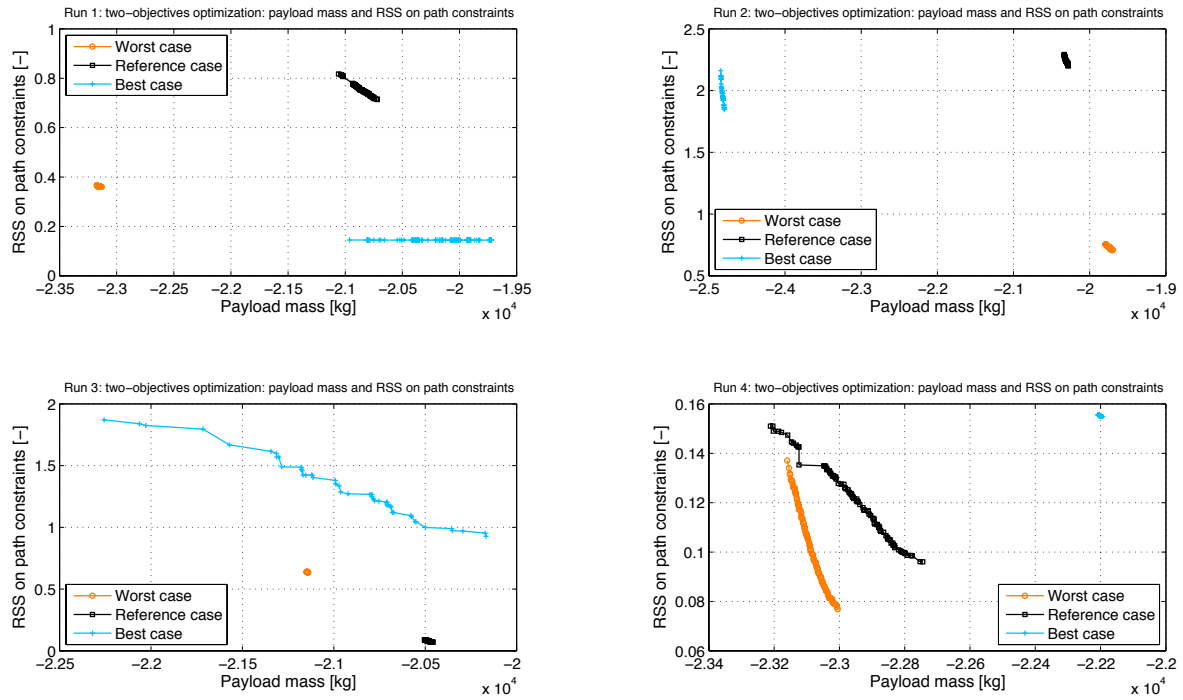


Figure 6.17: Proton M: two-objective optimization runs. The plots show the Pareto fronts obtained for the four runs performed.

in which the optimizer was searching gave trajectories with violations, it might be useful to try to narrow the range and see if it could be satisfied.

Table 6.16: Proton M: the results of the two-objective optimization runs are summarized.

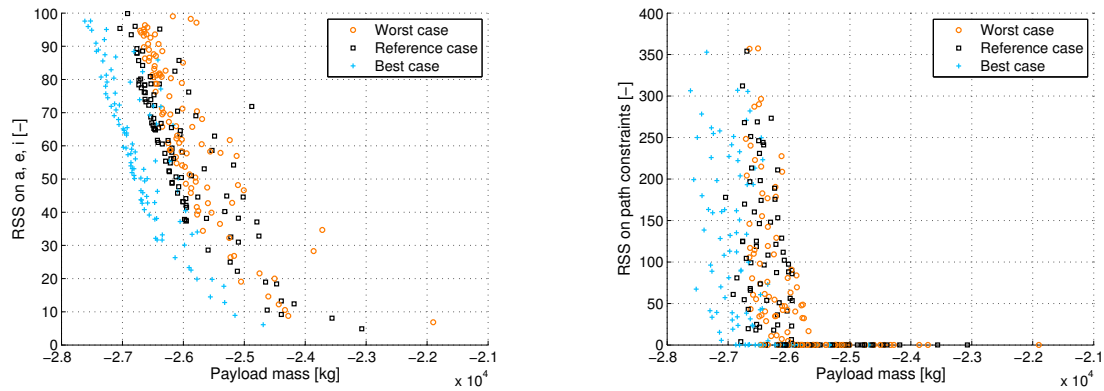
	Run 1		Run 2		Run 3		Run 4	
	Payload mass [kg]	RSS path constraints						
Worst	23,130	0.3601	19,700	0.7075	21,140	0.635	23,005	0.0768
	23,138	0.3602	19,701	0.7086	21,140	0.6352	23,008	0.0777
	23,139	0.3604	19,702	0.7129	21,140	0.6353	23,010	0.0786
Reference	20,720	0.7136	20,281	2.202	20,460	0.0696	22,745	0.096
	20,722	0.7153	20,283	2.202	20,460	0.078	22,753	0.0961
	20,743	0.7169	20,284	2.204	20,460	0.0716	22,777	0.0985
Best	19,721	0.1443	24,796	1.846	20,168	0.9272	22,193	0.1549
	19,723	0.1443	24,797	1.863	20,170	0.9537	22,196	0.1549
	19,730	0.1443	24,800	1.864	20,294	0.97	22,196	0.1549

■ = trajectory without path constraint

and orbital element tolerance violations

Table 6.17: Proton M: three-objectives optimization settings: final orbital elements and constraints limits.

Parameter	Simulation 1	Simulation 2	Simulation 3	Simulation 4	Simulation 5
a [km]	6563.137	6563.137	6563.137	6563.137	6563.137
e [-]	0	0	0	0	0
i [deg]	51.6	51.6	51.6	51.6	51.6
Tolerance a [km]	3	3	3	3	3
Tolerance e [-]	0.0005	0.0005	0.0005	0.0005	0.0005
Tolerance i [deg]	0.1	0.1	0.1	0.1	0.1
Dynamic pressure [kPa]	≤ 40	≤ 40	≤ 40	≤ 40	≤ 40
Peak heat flux [kW/m ²]	≤ 120	≤ 100	≤ 100	≤ 100	≤ 100
Axial acceleration [g]	≤ 4	≤ 4	≤ 4	≤ 4	≤ 4
Bending load [kPa*deg]	≤ 100	≤ 100	≤ 100	≤ 100	≤ 100
Circularization burn	No	No	No	No	No
Coast arcs	No	Yes	No	Yes	No



(a) 2D view of the Pareto surface with payload mass on x -axis and RSS on final orbital elements on z -axis.

(b) 2D view of the Pareto surface with payload mass on x -axis and RSS on path constraints violations on y -axis.

Figure 6.18: Proton M: three-objective optimization, run 1 Pareto front views.

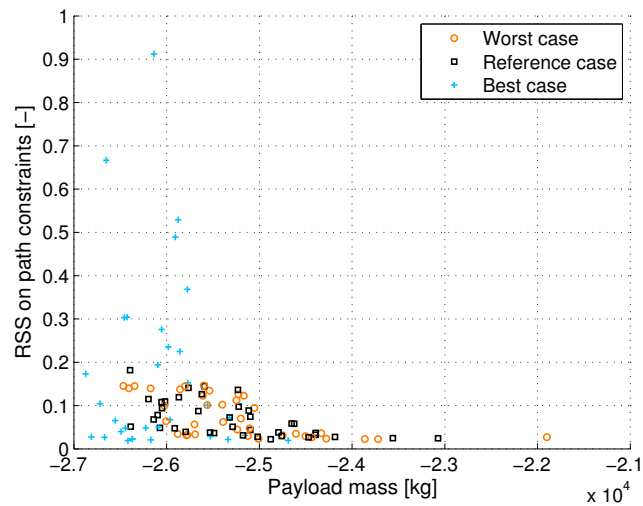
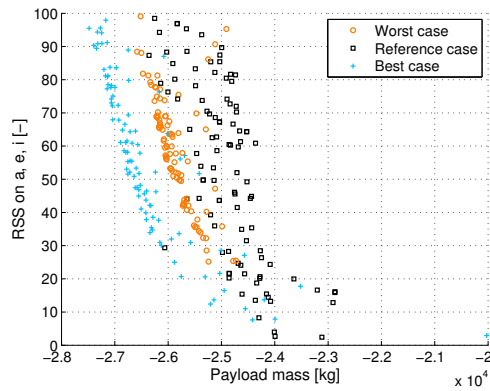


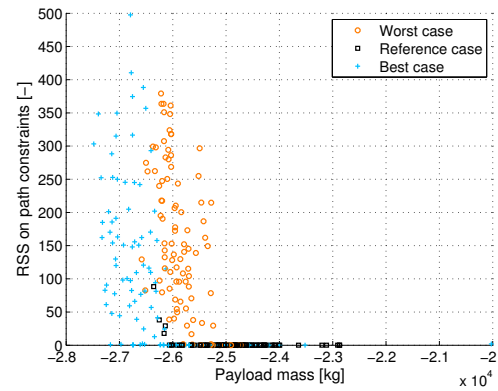
Figure 6.19: Proton M: zoom of the 2D view of the Pareto surface shown in Fig. 6.18b. This detailed view shows that the solutions are not on the x -axis but very close to it.

From Fig. 6.18, 6.20 and 6.21, the best aerodynamic configuration gives higher payload mass for the same accuracy of the orbital elements whereas the reference and the worst configuration give about the same results. Concerning the RSS of the path constraints, it is apparent that there are several solutions with values around 1, that still it is not a good value from the launch system point of view, because may produce failures and damages, but is the lower threshold achieved.

In Fig. 6.23, the run with the path constraints used as objectives is illustrated. It is clear that the number of solutions here is much smaller than the other cases. Actually, for the worst and reference aerodynamic configurations, the number of solutions found is 6 and 7, respectively. For the best configuration, the archive has been filled (total number of solutions for the archive of the Pareto front is 100). In this case, it might be that the initial population could not permit to find more solutions; then, simulations with a higher number of particles might solve any doubts.

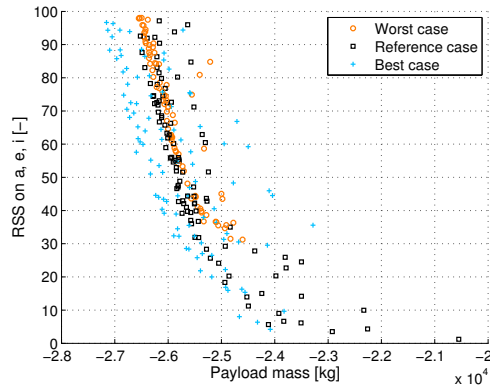


(a) 2D view of the Pareto surface with payload mass on x -axis and RSS on final orbital elements on z -axis.

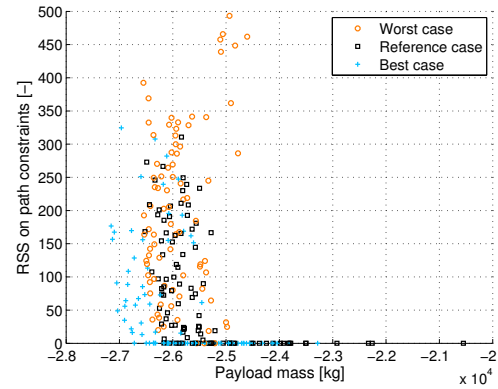


(b) 2D view of the Pareto surface with payload mass on x -axis and RSS on path constraints violations on y -axis.

Figure 6.20: Proton M: three-objective optimization, run 2 Pareto front views.

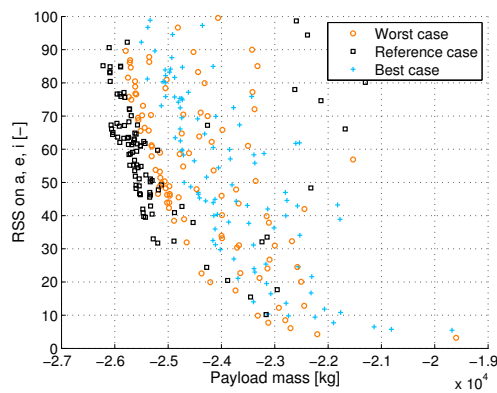


(a) 2D view of the Pareto surface with payload mass on x -axis and RSS on final orbital elements on z -axis.

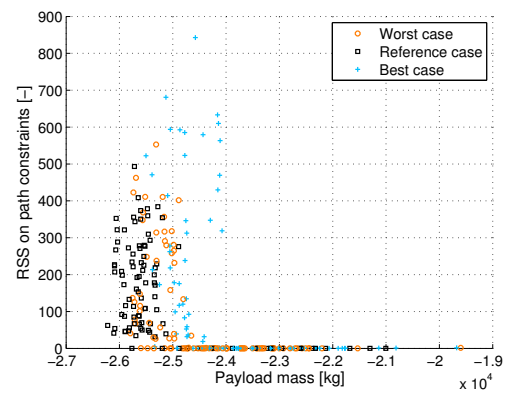


(b) 2D view of the Pareto surface with payload mass on x -axis and RSS on path constraints violations on y -axis.

Figure 6.21: Proton M: three-objective optimization, run 3 Pareto front views.

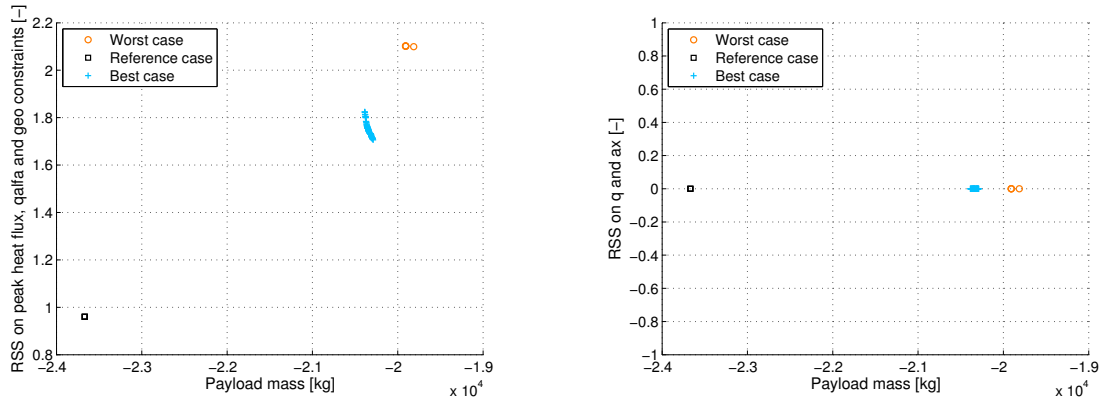


(a) 2D view of the Pareto surface with payload mass on x -axis and RSS on final orbital elements on z -axis.



(b) 2D view of the Pareto surface with payload mass on x -axis and RSS on path constraints violations on y -axis.

Figure 6.22: Proton M: three-objective optimization, run 4 Pareto front views.



(a) 2D view of the Pareto surface with payload mass on x -axis and RSS of the second group of path constraints on z -axis. The second group gathers peak heat flux, bending load and geographical constraints.

(b) 2D view of the Pareto surface with payload mass on x -axis and RSS of the first group of path constraints on y -axis. The first group includes dynamic pressure and axial acceleration constraints.

Figure 6.23: Proton M: three-objective optimization, run 5 Pareto front views.

Table 6.18: Proton M: results of the three-objective optimization runs.

	Run 1			Run 2			Run 3			Run 4			Run 5		
	Payload mass [kg]	RSS path constraints	RSS orbital elements	Payload mass [kg]	RSS path constraints	RSS orbital elements	Payload mass [kg]	RSS path constraints	RSS orbital elements	Payload mass [kg]	RSS path constraints	RSS orbital elements	Payload mass [kg]	RSS path constraints (group 1)	RSS path constraints (group 2)
Worst	21,899	0.027	6.84	24,241	29.56	25.17	24,603	461.9	31.24	19,600	1.55	3.19	19,813	0	2.099
	24,278	0.0234	8.77	24,780	0.216	25.37	24,830	448.4	31.5	22,201	0.106	4.26	19,906	0	2.101
	24,331	0.0362	10.55	24,726	0.197	25.47	24,935	493.2	34.66	22,794	0.038	6.07	19,907	0	2.101
Reference	23,073	0.024	4.89	23,116	0.027	2.42	20,548	0.081	1.22	23,163	0.048	10.18	23,667	0	0.959
	23,560	0.025	8.08	23,116	0.027	2.43	22,919	0.025	3.52	23,454	0.054	15.47	23,667	0	0.959
	24,392	0.036	9.19	23,993	0.023	2.65	22,258	0.02	4.33	22,954	0.048	17.69	23,668	0	0.959
Best	24,689	0.019	6.09	20,026	1.9	2.92	24,084	0.024	4.18	19,676	1.62	5.47	20,289	0	1.706
	25,152	0.31	8.9	24,418	0.026	7.62	24,324	0.037	6.36	20,813	1.01	5.73	20,293	0	1.709
	25,321	0.71	12.8	23,994	0.017	7.87	24,664	0.1	8.03	21,113	0.9	6.48	20,294	0	1.71

= trajectory without path constraint and orbital element tolerance violations

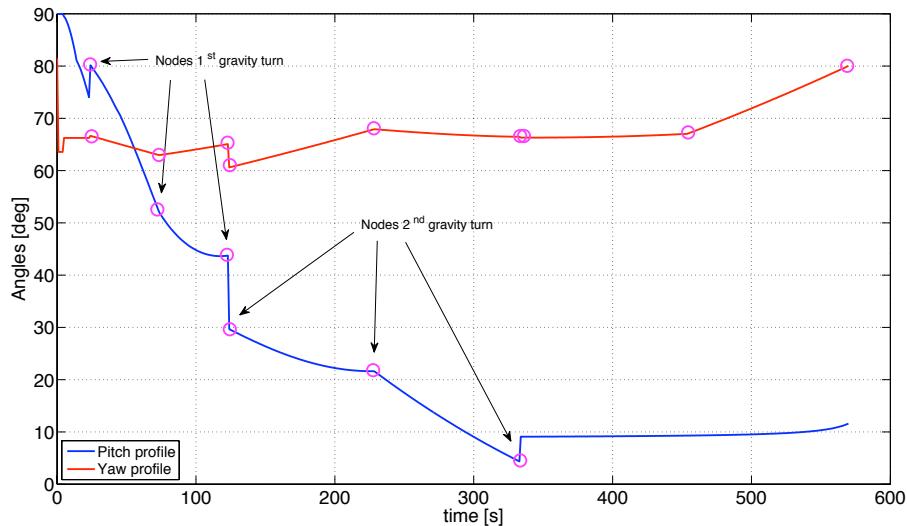


Figure 6.24: Proton M: control history of the best solution found.

6.2.4 Conclusions

In the single-objective optimization, the Proton is able to satisfy quite easily the dynamic-pressure, peak-heat-flux and axial-acceleration constraints. A more demanding constraint, the bending load, is violated in some cases, but the main factor that drives the violation is always the angle of attack. Also in the two and three-objective optimizations, the constraints violated more often are the bending load and azimuth range.

It is recommended to either narrow the range in which the yaw is optimized or use a higher penalty for those trajectories that do not satisfy the azimuth constraint.

In Fig. 6.24 and 6.25, it is possible to see the control history and the altitude-velocity plot for the best solution found that yields a payload mass of 23,091 kg. Concerning the control history, it is possible to see three jumps in the pitch profile and two in the yaw profile. The jumps occur at the connection between the phases: the first at the connection between the pitch-over maneuver and the gravity turn flown by the first stage, the second at the connection between the gravity turn flown by the first stage and the one flown by the second stage, whereas the third jump occurs at the connection between the gravity turn of the second stage and the bi-linear tangent law of the upper stage.

These jumps should be avoided because they lead to high angles of attack and are unlikely to be flown by a launcher since it cannot rotate its attitude instantaneously. In order to avoid them, one solution could be to:

- include a penalty on the rotation rates of the vehicle;
- have constraints that would force the end and the beginning of two connected phase to have equal values;
- make the difference between the control values at the connected phase as small as possible.

For the yaw profile, the same might be applied, but the optimal profile shows less jumps.

Concerning the altitude-velocity plot, in the 1st stage there is a linear relation between the velocity gained and the altitude reached by the launcher. In the 2nd stage, the vehicle first aims at reaching a high altitude (about 150-160 km) in which it is adjusting its attitude to fly perpendicularly to the radius vector and then the thrust is used only to increase its velocity. In Fig. 6.25 there is a part of the trajectory in which the launcher goes to an altitude higher than the final. By flying that part, the launcher first increases its potential energy and then converts it into kinetic energy; moreover, it occurs also to give time to the control law to adjust the attitude of the rocket.

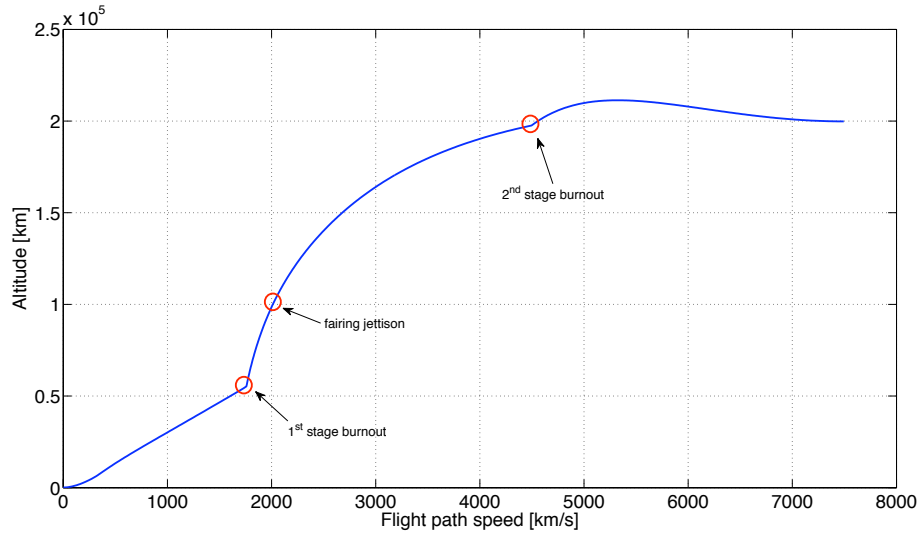


Figure 6.25: Proton M: altitude-velocity plot for the best solution.

6.3 Atlas V 552

The second launcher analyzed for the cargo/supply mission to the Moon is the Atlas V in the version 552, launched from Cape Canaveral. In the 500 series, this version is the most powerful since it is provided with 5 boosters thrusting at lift-off together with the central core. The upper stage, the Centaur, is provided with two engines (namely Dual Engine Centaur, DEC). The Atlas V is a two-stage launcher with boosters. The Atlas V 500 series has an axial acceleration limit of 4.6 g and a dynamic pressure limit of 44,000 Pa, from [Lockheed Martin, 2007, 1999].

6.3.1 One-objective optimization results

As it can be seen from the setup Table 6.19, the dynamic pressure limit along the runs has been varied from the nominal maximum limit given in [Lockheed Martin, 2007]. This is due to the fact that the mentioned limit, that was the only value for the 500 series, refers to the 521 version (only two booster and Single Engine Centaur) and it is 33,600 Pa, that has been set as limit in several runs. Only recently, during the optimization runs, an addendum, [Lockheed Martin, 1999], was found, in which the aforementioned limit was set to 44,000 Pa for the 552 version. Therefore, even though violations occur in those trajectories with a lower dynamic pressure constraints, still these can be considered as optimal results if they do not violate the latter limit.

From the analysis of Table 6.19 and 6.20, it can be seen that no violation in the peak heat flux (below 90 kW/m²) and azimuth range occur. A better look and understanding shows that all the optimal trajectories that violate the eccentricity tolerance have also a violation in the dynamic pressure and bending load. This affects all configurations.

In most of the optimal trajectories, both violations of dynamic pressure and bending load occur. This behaviour can be due either to the too high dynamic pressure only or, when this is not violated, to the high angles of attack. The origin of higher angles of attack is due to the optimizer that is not able to find optimal control parameter for the pitch over phase. When this happens, the transition to the gravity turn is not smooth and high angles of attack (of about 10-15°) arise. The reason for which the optimizer does not find optimal parameter in the control can be due to the position of the particles in the initial population, due to the randomness. A higher number of particles is suggested in order to cover larger areas in the search space. A comparison between the case in which optimal control parameters and non-optimal ones are found can be seen in Fig. 6.29. There, it can be seen that when the optimizer finds optimal parameters for the pitch-over phase, the transition between this phase and the successive gravity turn is much smoother. This prevents high angles of attack while keeping the bending load within limits.

Table 6.19: Atlas V: setup of the one-objective optimization runs.

Parameter	Simulation 1	Simulation 2	Simulation 3	Simulation 4	Simulation 5	Simulation 6	Simulation 7	Simulation 8	Simulation 9	Simulation 10	Simulation 11	Simulation 12	Simulation 13	Simulation 14	Simulation 15	Simulation 16
a [km]	6563.137	6563.137	6563.137	6563.137	6563.137	6563.137	6563.137	6563.137	6563.137	6563.137	6563.137	6563.137	6563.137	6563.137	6563.137	6563.137
e [-]	0	0	0	0	0	0	0	0	0	0	0	0	0	0	0	0
i [deg]	28.7	28.7	28.7	28.7	28.7	28.7	28.7	28.7	28.7	28.7	28.7	28.7	28.7	28.7	28.7	28.7
Tolerance a [km]	5	3	3	3	3	3	3	3	3	3	3	3	3	3	3	3
Tolerance e [-]	0.001	0.005	0.0005	0.0005	0.0005	0.0005	0.0005	0.0005	0.0005	0.0005	0.0005	0.0005	0.0005	0.0005	0.0005	0.0005
Tolerance i [deg]	0.1	0.1	0.1	0.1	0.1	0.1	0.1	0.1	0.1	0.1	0.1	0.1	0.1	0.1	0.1	0.1
Dynamic pressure [kPa]	≤ 33.6	≤ 33.6	≤ 40	≤ 40	≤ 40	≤ 35	≤ 35	≤ 35	≤ 35	≤ 33.6	≤ 50	≤ 50	≤ 25	≤ 60	≤ 33.6	≤ 44
Peak heat flux [kW/m ²]	≤ 120	≤ 120	≤ 120	≤ 120	≤ 120	≤ 120	≤ 120	≤ 120	≤ 120	≤ 120	≤ 120	≤ 120	≤ 120	≤ 120	≤ 100	≤ 100
Axial acceleration [g]	≤ 4.6	≤ 4.6	≤ 4.6	≤ 4.6	≤ 4.6	≤ 4.6	≤ 4.6	≤ 4.6	≤ 4.6	≤ 4.6	≤ 4.6	≤ 4.6	≤ 4.6	≤ 4.6	≤ 4.6	≤ 4.6
Bending load [kPa·deg]	≤ 100	≤ 100	≤ 100	≤ 150	≤ 150	≤ 200	≤ 150	≤ 150	≤ 150	≤ 150	≤ 150	≤ 150	≤ 150	≤ 150	≤ 120	≤ 150
Circularization burn	No	No	No	No	Yes	Yes	Yes									
Coast arcs	No	Yes	No	No	No	Yes	No	No	No	No						

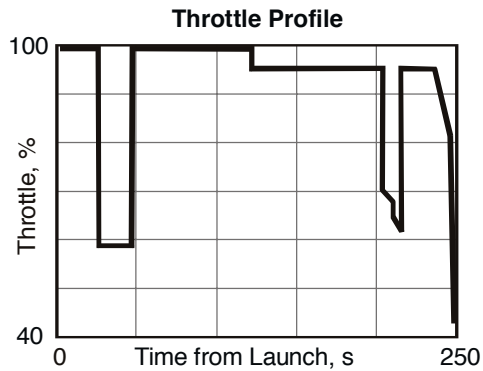


Figure 6.26: Atlas V 552: real throttle profile for missions to LEO orbit, from [Lockheed Martin, 1999].

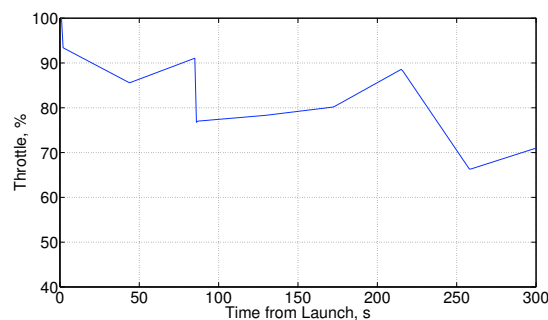


Figure 6.27: Atlas V 552: throttle profile from simulation.

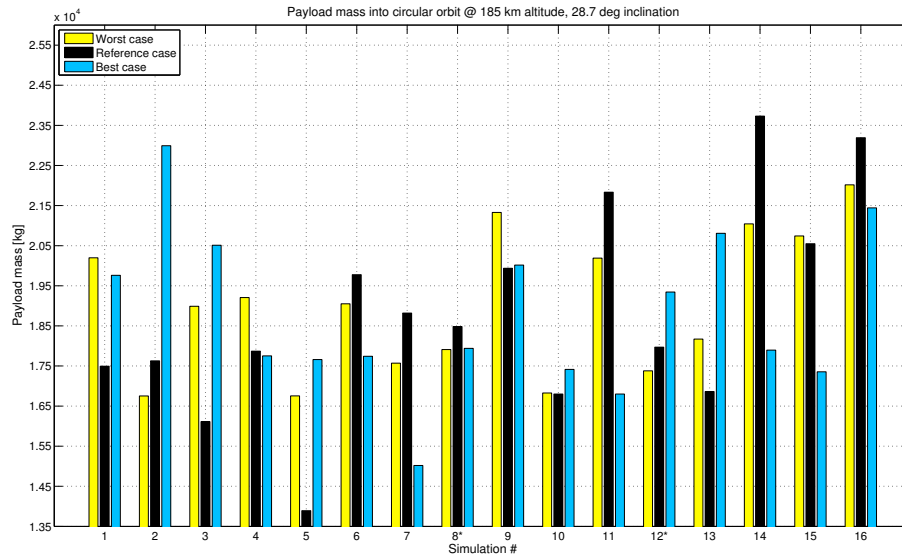
In addition, when the bending load is violated, the eccentricity tolerance is more likely violated.

Another point that can be stressed out, but that has been mentioned before, is that in 75% of the cases in which the eccentricity tolerance is not respected, also the semimajor axis tolerance is not. This can be due to the fact that, while trying to reach the tolerance set on the eccentricity, at some point the set semimajor axis tolerance is satisfied, but not the one of eccentricity. Then, in order to satisfy the eccentricity tolerance, the vehicle keeps flying, but the semimajor axis is already out of its bounds. When this occur, the trajectory simulation is stopped giving an error on both elements.

Regarding the axial acceleration violation, this occurs in half of all the simulations performed. The Atlas V has throttleable engines and even though the throttle option was included in the setup, the optimizer has not always been able to find the optimal throttle settings. However, also in this case the addendum to the user manual that was lately found cleared that, for the 552 version of the Atlas V, the maximum axial acceleration is set to 5 g. Therefore, for those simulations in which a maximum violation of the axial acceleration of 0.4 g is produced, this limit can be still accepted since they are still within the 5-g limit. Besides this new maximum limit of the vehicle, still the model is not able to cope with sharp and instantaneously variations of the throttle setting. An example of a typical throttle profile is shown in Fig. 6.26 whereas in Fig. 6.27 a typical profile achievable with the current model is presented. In the current model, only optimal values of the throttle at the nodes are found and then linearization of the profile is performed. With this methodology instantaneous throttle variations cannot be modeled.

As it can be seen, with the model currently used in AM, it is not possible to have sharp variations of the throttle and, therefore, of the thrust. It is advisable to implement this kind of approach for future version to have a more complete software.

From Fig. 6.28 it results that there is a wide range in the optimal payload masses, from about 13,800 kg to 23,700 kg. Moreover, there is a variety of results for which is not easy to find a common factor. On average most of the payload mass lie in the range of 16,500 kg and 18,500 kg, that is lower than the 20,500 kg reference value found in [Lockheed Martin, 2007]. Then, these results are heavily penalized by the constraints violations that somehow steer the optimization process in non optimal search spaces. For this



* = trajectory with coast arcs

Figure 6.28: Atlas V: summary of the payload masses obtained in the best trajectories from the one-objective optimization.

problem, for future research, it might be useful to investigate other kinds of penalty functions. Moreover, it is evident that the method implemented in the software is not always able to cope with throttleable rockets.

At first glance, the optimal trajectories, that do not violate any setup constraints, are only two, run 2 and 3. A third trajectory does not violate any constraints, giving a payload mass of 23,731 kg. Anyway, its dynamic pressure constraint was set higher than 44,000 Pa, that is the real constraints and the maximum value achieved in the trajectory is about 48,000 Pa. Therefore this trajectory cannot be taken into account.

Besides those optimal results, we can consider those trajectories for which the sum of the dynamic pressure constraint and the violation is below the real limit. In addition, we can consider those trajectories that have an axial acceleration violation smaller than 0.4.

With this assumption, 7 more trajectories can be considered optimal. The largest payload mass resulting from these trajectories is 22,993 kg. This is given by the best aerodynamic configuration and the dynamic pressure is kept lower than the real limit. Among the optimal solutions without violations, half of them occur in the best aerodynamic configuration and yield a payload mass higher than the other configurations. This might be expected because, if all constraints are satisfied, less drag is experienced by the launcher, that means less propellant is used and a higher payload mass can be delivered.

6.3.2 Two-objective optimization results

Five two-objective optimization runs have been performed for the Atlas V 552: 3 runs use the *RSS* of the orbital elements and 2 runs use the *RSS* of the path constraints as second objective.

By comparing results from Table 6.22 and Fig. 6.31 and 6.32, it can be seen that the two-objective optimization performs almost like the single-objective one. The largest payload mass, between the trajectories that satisfy the tolerance on the orbital elements, is 22,726 kg against 22,992 kg obtained before. Moreover, also two solutions, with the reference aerodynamic configuration, yield an *RSS* > 1 for the orbital elements' tolerances but are still good solutions as, from an analysis of the output files of the orbit achieved, they satisfy the set tolerances.

It results that when the dynamic pressure limit is more strict, the best aerodynamic configuration performs worse, violating the tolerances, with respect to the other two. On the other side, when this constraints are less strict, it performs better and satisfies the tolerances. In the first case it might be that the launcher,

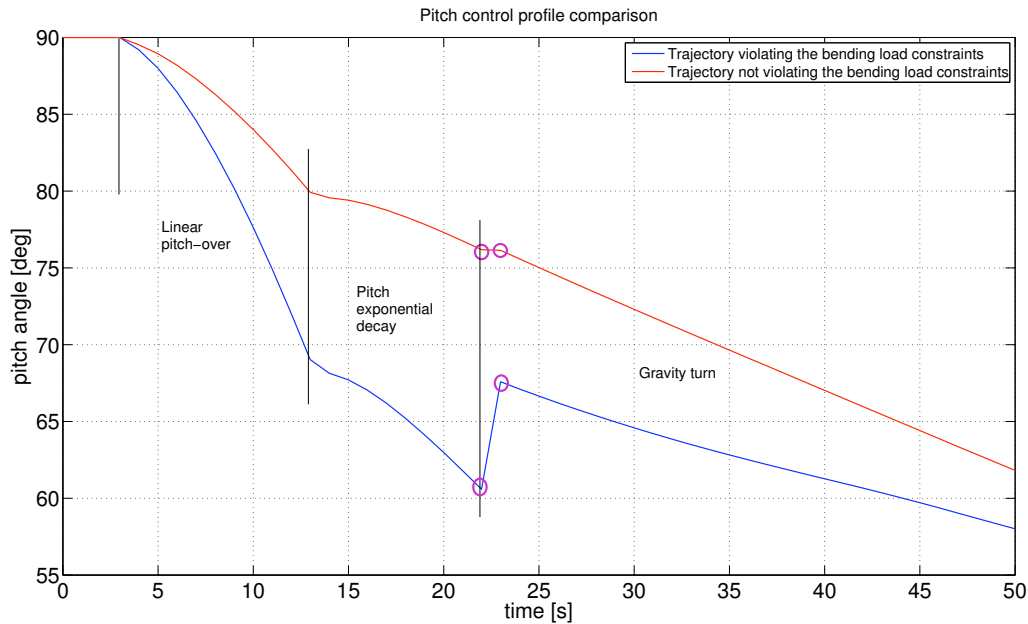


Figure 6.29: Atlas V: difference between optimal and non-optimal control parameter in the pitch over phase.

with a higher velocity due to the best aerodynamic configuration, has to fly a steeper trajectory not to violate the dynamic pressure. Therefore it reaches a certain altitude in a shorter time and has less time to control the attitude to meet the eccentricity tolerance. This fact has been shown already for the Vega launcher. However when the constraint is relaxed, it can spend more time in the atmosphere, flying a less steep trajectory and having more time to adjust the attitude and meet the tolerances.

It is also evident that the shape of the Pareto fronts, in Fig. 6.31, is not perfectly convex or non-convex, but it has a linear behaviour on the left side. Actually, a perfectly convex Pareto front, as shown from the solid line closest to the y -axis in Fig. 6.30, is more typical of non constrained problems.

However, in Fig. 6.30, a constrained Pareto front can be seen as well. The found solutions lie on the boundary of one constraint, in the left part of the Pareto front and the shaded area represents the space of feasible solutions. The same occurs for the ascent problem. Since it is a highly constrained problem, the solutions of the Pareto front do not form a perfectly convex front, but an almost linear one. Therefore, the particular shape is given by the constraints that force the optimizer not to look in the unfeasible regions (or to look but then getting a penalty). Then, for instance, by looking at the first plot in Fig. 6.30, no feasible solutions exist, for the reference configuration, with a payload mass larger than 24,500 kg and an accuracy lower than 20.

By analyzing Fig. 6.32 and Table 6.22, it can be seen that what has been said regarding a singular point representing the Pareto front, in the case of the RSS of path constraints, has occurred. That is, in run 4 and especially in run 5, one single solution per configuration, representing the Pareto front, has been found and is depicted.

The singular point, also called utopia point since the components give the best value for every single objective, is present also in populated Pareto fronts. However, the definition of utopia point is arguable because a user can apply his own design criteria to select the best solution.

However, in this case one single solution was found because no other solutions were found that could improve one or the other objective. In fact, all found solutions have either a RSS (of the path constraints) equals to zero but a lower payload mass or a higher RSS and still a lower payload mass. The best results obtained, by assuming the lower RSS of the path constraints, is obtained in run 5, by the best aerodynamic configuration, that gives 19,903 kg without violating the constraints. In order to avoid this kind of critical cases, a solution might be to have a larger initial population.

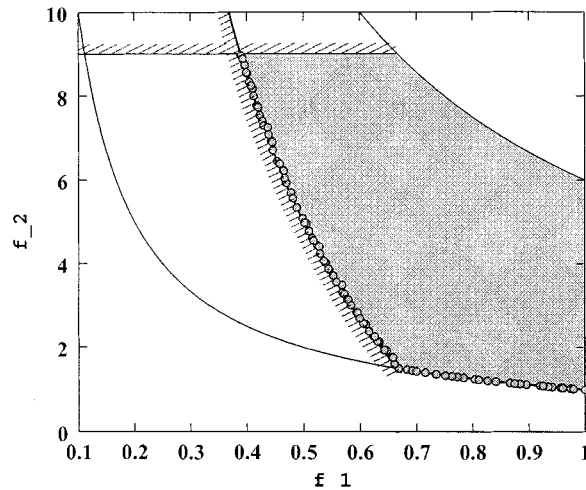


Figure 6.30: Pareto front of a constrained problem, [Deb et al., 2000].

Table 6.21: Atlas V: Setup for two-objective optimization.

Parameter	Simulation 1	Simulation 2	Simulation 3	Simulation 4	Simulation 5
a [km]	6563.137	6563.137	6563.137	6563.137	6563.137
e [-]	0	0	0	0	0
i [deg]	28.7	28.7	28.7	28.7	28.7
Tolerance a [km]	3	3	3	3	3
Tolerance e [-]	0.0005	0.0005	0.0005	0.0005	0.0005
Tolerance i [deg]	0.1	0.1	0.1	0.1	0.1
Dynamic pressure [kPa]	≤ 33.6	≤ 40	≤ 40	≤ 33.6	≤ 45
Peak heat flux [kW/m ²]	≤ 120	≤ 120	≤ 120	≤ 120	≤ 120
Axial acceleration [g]	≤ 4.6	≤ 4.6	≤ 4.6	≤ 4.6	≤ 4.6
Bending load [kPa*deg]	≤ 200	≤ 150	≤ 150	≤ 100	≤ 100
Circularization burn	Yes	Yes	Yes	No	No
Coast arcs	No	No	Yes	No	No

6.3.3 Three-objective optimization results

Seven three-objective optimization runs have been performed for Atlas V. Five of these runs have as objectives the payload mass, the *RSS* of the path constraints and that of the final orbital elements. The other two runs have, besides the payload mass, the *RSS* of two groups of path constraints.

From Fig. 6.33 to Fig. 6.37, it is quite clear, from the 2D view on the right of each figure, that the path constraints, in most of the solutions on the Pareto surface, are satisfied. This concerns not only the first type of optimization (runs 1 to 5) but also the second type. The verification is evident in Table 6.24.

Also for the Atlas V, in the first five runs, the first filter that has been applied to data in Table 6.24 regards the *RSS* of the path constraints. Since there are several solutions in all the five runs that do not violate the constraints, a second filter has been applied to rank these solutions: the lower the *RSS* of the orbital elements, the higher the position in the table, for the relative aerodynamic configuration. Once this criterion is applied, it resulted that, for run 1, 2 and 4, the accuracy of the best trajectories is very low, ranging from 4 to 94. Looking at Table 6.23, it can be noted that for those runs the setup involved strict constraints on the dynamic pressure and a lower constraint on the bending load. This means that in order to satisfy the higher (i.e., the more strict) constraints, the reached final orbits do not satisfy the tolerances on the orbital elements. Therefore, this approach reduces the accuracy of the trajectory and the behaviour of the optimization is different from the single-objective one. In that case, the path constraints were used as constraints and not as objectives, and the optimizer first tries to satisfy the accuracies and the constraints.

Table 6.22: Atlas V: results of the two-objective optimization.

	Run 1		Run 2		Run 3		Run 4		Run 5	
	Payload mass [kg]	RSS orbital elements	Payload mass [kg]	RSS orbital elements	Payload mass [kg]	RSS orbital elements	Payload mass [kg]	RSS path constraints	Payload mass [kg]	RSS path constraints
Worst	22,613	1.00	23,373	10.36	22,577	2.42	21,385	0.25	20,987	0.23
	22,675	2.04	23,591	10.41	22,594	2.53	21,391	0.25		
	22,699	2.56	23,597	11.17	22,675	2.82	21,399	0.25		
Reference	20,673	0.63	22,485	4.69	22,387	1.07	23,452	0.3	17,244	1.34
	20,679	0.91	22,519	4.72	22,517	1.81	23,459	0.3		
	20,715	1.06	22,603	4.79	22,547	2.04	23,459	0.3		
Best	20,686	12.66	21,787	0.38	22,588	0.32	16,507	0.69	19,903	0
	20,775	14.15	21,787	0.39	22,726	0.43				
	20,777	14.25	22,159	0.89	23,432	2.29				

= trajectory without path constraint
and orbital element tolerance violations

That is due to the fact that, in the single-objective optimizer, the trajectories with high errors on the orbital elements are severely penalized.

In the multi-objective optimization one cannot make use of the fact that, applying a more strict constraint, solutions with violations may still be chosen.

Table 6.23: Atlas V: setup for the three-objective optimization runs. Orbital elements tolerances and path constraints are shown.

Parameter	Simulation 1	Simulation 2	Simulation 3	Simulation 4	Simulation 5	Simulation 6	Simulation 7
a [km]	6563.137	6563.137	6563.137	6563.137	6563.137	6563.137	6563.137
e [-]	0	0	0	0	0	0	0
i [deg]	28.7	28.7	28.7	28.7	28.7	28.7	28.7
Tolerance a [km]	3	3	3	3	3	3	3
Tolerance e [-]	0.0005	0.0005	0.0005	0.0005	0.0005	0.0005	0.0005
Tolerance i [deg]	0.1	0.1	0.1	0.1	0.1	0.1	0.1
Dynamic pressure [kPa]	≤ 33.6	≤ 33.6	≤ 45	≤ 35	≤ 45	≤ 45	≤ 33.6
Peak heat flux							
k[W/m ²]	≤ 120	≤ 120	≤ 120	≤ 120	≤ 120	≤ 120	≤ 100
Axial acceleration [g]	≤ 4.6	≤ 4.6	≤ 4.6	≤ 4.6	≤ 4.6	≤ 4.6	≤ 4.6
Bending load [kPa*deg]	≤ 100	≤ 100	≤ 120	≤ 100	≤ 120	≤ 120	≤ 100
Circularization burn	No	No	No	No	Yes	Yes	Yes
Coast arcs	No						

By analyzing the runs 3 and 5, that have less strict constraints on dynamic pressure and bending load, the results show a better performance on the accuracy achieved. This is accomplished by satisfying the constraints as in the other runs. Now that the constraints are lower (i.e., less strict) it is possible for the trajectories to satisfy the given tolerances. However, a difference in the *RSS* of orbital elements still arise between run 3 and 5. This can be reported to the use of the circularization burn thanks to which a circular orbit can be reached with higher accuracy.

In addition, the differences between runs 1, 2 and 4 and runs 3 and 5, can also be seen from Fig. 6.33 to Fig. 6.37. For runs 3 and 5, the 2D view of payload mass versus *RSS* of the orbital elements looks more like the Pareto front achieved in the two-objective optimization. On the other hand, for runs 1, 2 and 4, the 2D view is less uniform, showing a larger variety due to the more strict condition of the constraints.

The difference in the shape of the Pareto front between these five runs is evident. As it has been explained for the two-objective optimization, the linear shape on the left part of the 2D view, with payload mass and *RSS* of the orbital elements, that can be seen in runs 3 and 5, is due to the solutions that lie on the boundary of the constraints. This means that the optimization process converged and found solutions on the border between the feasible and unfeasible area (lying in the feasible space). On the other hand, in runs 1, 2 and 4, the process did not produce good results, as seen from Table 6.24, and the solutions are spread in the central part of the feasible region.

In run 1 and 2, the solutions shown in the 2D view, with the payload mass and the *RSS* of the path

Table 6.24: Atlas V: results of the three-objective optimization runs.

	Run 1			Run 2			Run 3			Run 4			Run 5			Run 6			Run 7		
	Payload mass [kg]	RSS path constraints	RSS orbital elements	Payload mass [kg]	RSS path constraints	RSS orbital elements	Payload mass [kg]	RSS path constraints	RSS orbital elements	Payload mass [kg]	RSS path constraints	RSS orbital elements	Payload mass [kg]	RSS path constraints	RSS orbital elements	Payload mass [kg]	RSS path constraints (group 1)	RSS path constraints (group 2)	Payload mass [kg]	RSS path constraints (group 1)	RSS path constraints (group 2)
	21,813	0	17.21	21,199	0	21.03	18,784	0	2.21	22,885	0	41.51	24,443	0	0.83	23,513	0	0	17,225	0.59	0
	21,908	0	17.34	21,309	0	24.86	19,708	0	3.63	22,850	0	5.62	24,153	0	1.14	23,513	0	0	17,204	0.59	1.86
Worst	22,773	0	22.72	21,374	0	33.04	20,801	0	9.14	23,553	0.0003	94.51	24,648	0	2.22	23,513	0	0	17,193	0.6	1.84
	21,111	0	3.71	20,112	0	10.16	23,735	0	4.28	21,712	0	10.45	23,703	0	0.38	23,913	0	0	21,531	0.0011	0
Reference	22,716	0	9.06	21,767	0	22.42	23,872	0	9.35	22,447	0	22.25	24,186	0	2.59	23,913	0.000027	0	21,555	0.0016	0
	23,145	0	29.45	21,871	0	4.11	23,873	0	10.32	22,522	0	25.7	24,571	0	3.28	23,938	0.002	0	21,588	0.03	0
	22,254	0	12.66	22,691	0	4.11	23,148	0	1.39	22,147	0	13.13	20,201	0	0.53	20,432	0.04	0	21,385	0.03	0
	22,774	0	19.37	23,781	0	6.26	22,151	0	1.4	22,147	0	13.13	21,645	0	0.73	20,437	0.05	0	21,416	0.03	0
Best	22,185	0	24.49	23,994	0	17.73	23,636	0	5.02	22,179	0	15.27	21,572	0	0.78	20,461	0.06	0	21,419	0.03	0

■ = trajectory without path constraint and orbital element tolerance violations

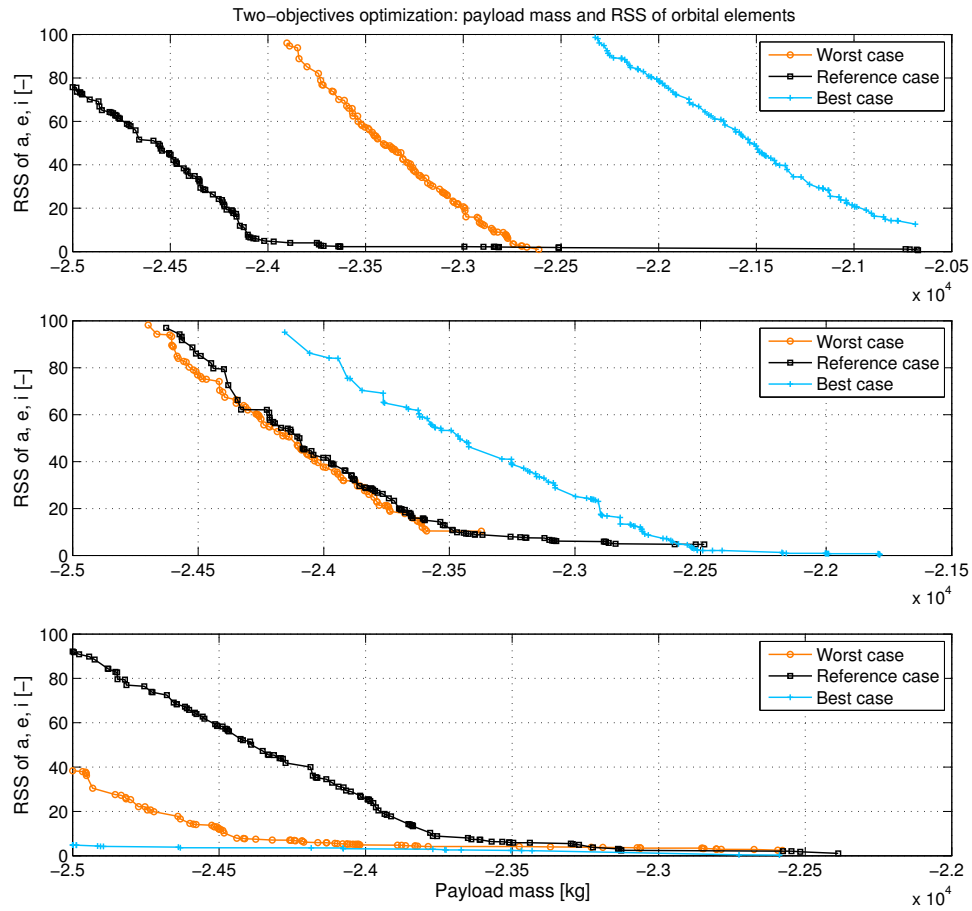


Figure 6.31: Atlas V: results of the two-objective optimization, run 1 to 3. The second objective is the *RSS* of the orbital elements.

constraints, might seem not to be part of the Pareto front. However, they are part of it since this is a three-objective optimization and those solutions are not dominated by any other (considering all the three objectives at the same time).

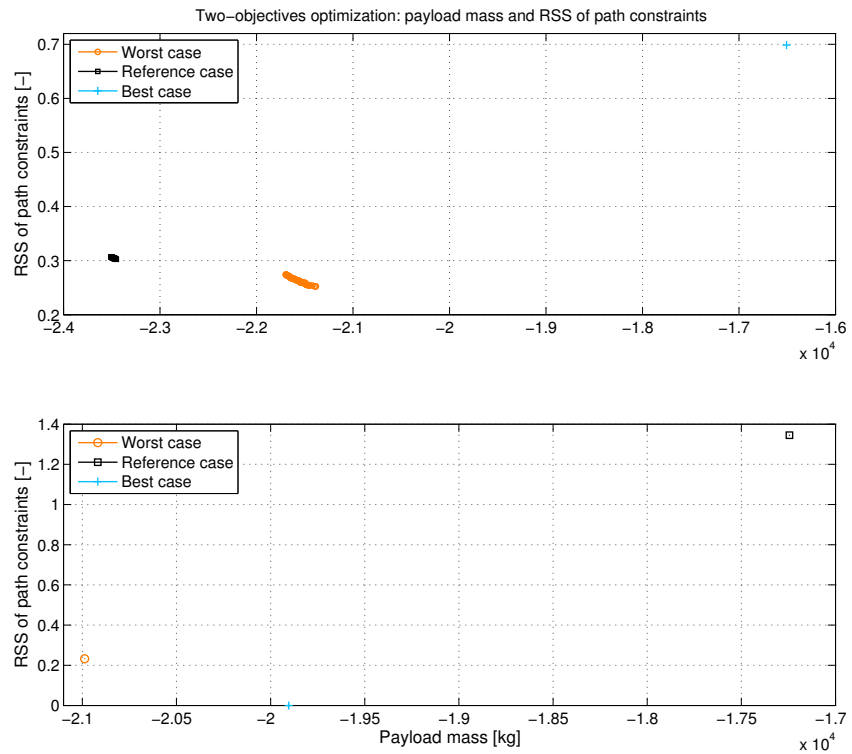
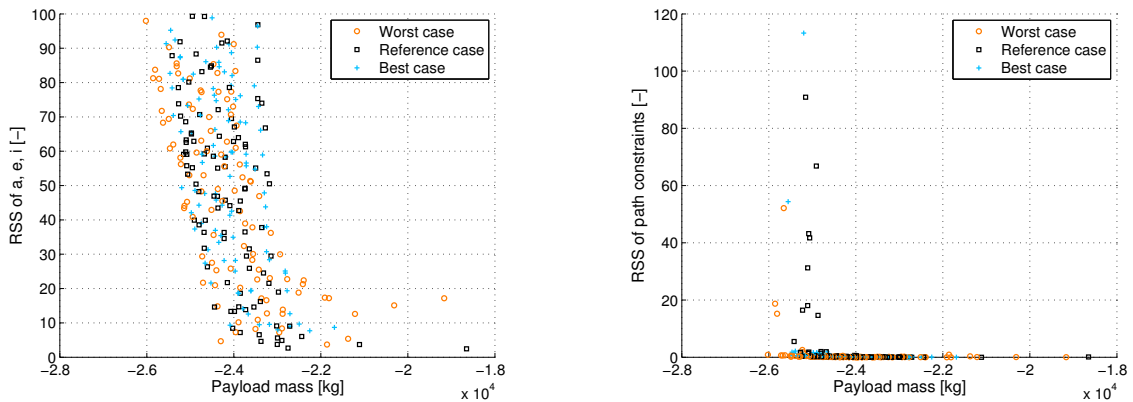


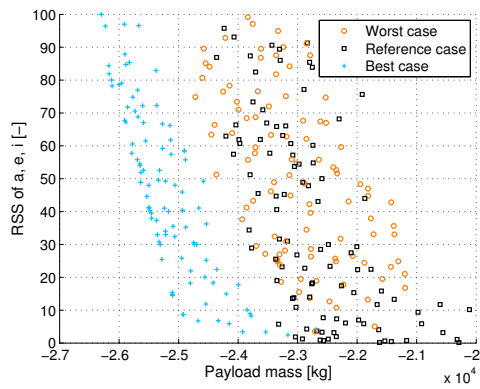
Figure 6.32: Atlas V: results of the two-objective optimization, run 4 and 5. The second objective is the *RSS* of path constraints violations.



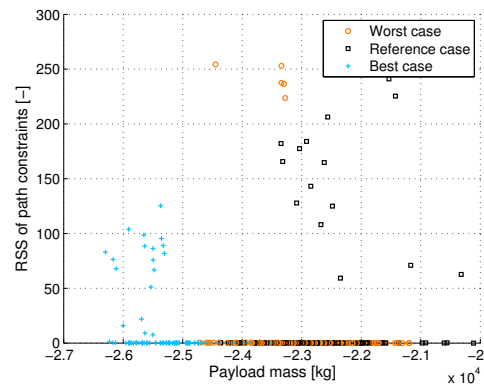
(a) 2D view of the Pareto surface with payload mass on *x*-axis and *RSS* of final orbital elements on *z*-axis.

(b) 2D view of the Pareto surface with payload mass on *x*-axis and *RSS* of path constraints violations on *y*-axis.

Figure 6.33: Atlas V: three-objective optimization, run 1.

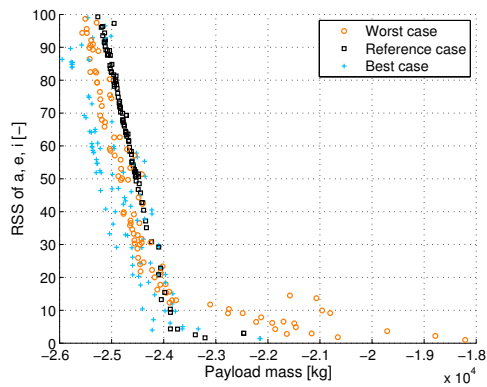


(a) 2D view of the Pareto surface with payload mass on x -axis and RSS of final orbital elements on z -axis.

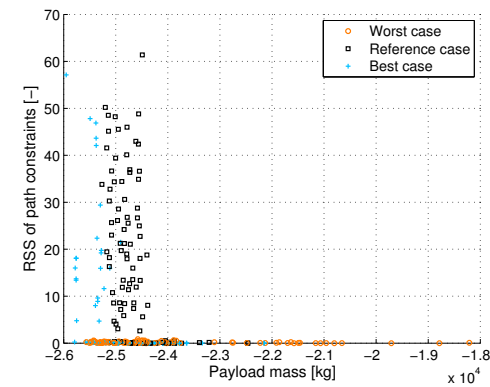


(b) 2D view of the Pareto surface with payload mass on x -axis and RSS of path constraints violations on y -axis.

Figure 6.34: Atlas V: three-objective optimization, run 2.

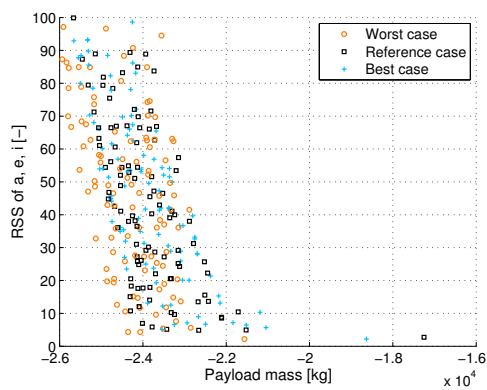


(a) 2D view of the Pareto surface with payload mass on x -axis and RSS of final orbital elements on z -axis.

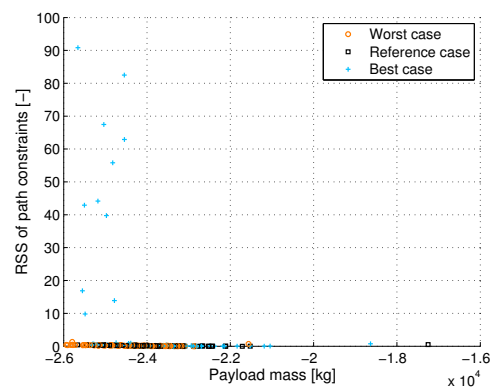


(b) 2D view of the Pareto surface with payload mass on x -axis and RSS of path constraints violations on y -axis.

Figure 6.35: Atlas V: three-objective optimization, run 3.

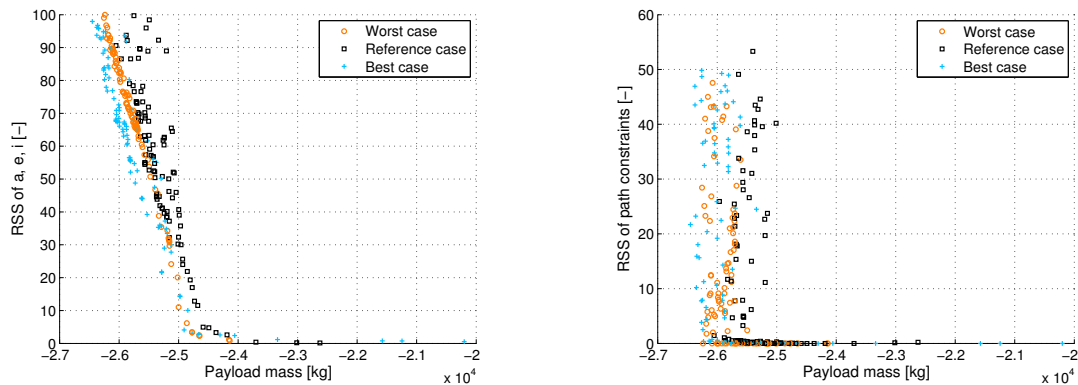


(a) 2D view of the Pareto surface with payload mass on x -axis and RSS of final orbital elements on z -axis.



(b) 2D view of the Pareto surface with payload mass on x -axis and RSS of path constraints violations on y -axis.

Figure 6.36: Atlas V: three-objective optimization, run 4.



(a) 2D view of the Pareto surface with payload mass on x -axis and RSS of final orbital elements on z -axis. (b) 2D view of the Pareto surface with payload mass on x -axis and RSS of path constraints violations on y -axis.

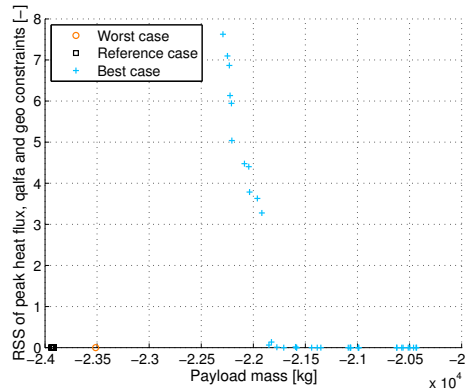
Figure 6.37: Atlas V: three-objective optimization, run 5.

Regarding the other type of objective used in this multi-objective optimization, from Fig. 6.38 and 6.39, the first difference that stands out is that, in run 6, there are more solutions lying on the axis, meaning that both groups of constraints are satisfied, and yielding RSS s closer to 0. A particular solution is found in the worst aerodynamic configuration, in run 6: it is the only one, shrinking the Pareto surface to a point. In this particular case, the optimizer is not able to find other possible solutions (with higher payload mass and lower RSS s) and it is advisable to increase the population size.

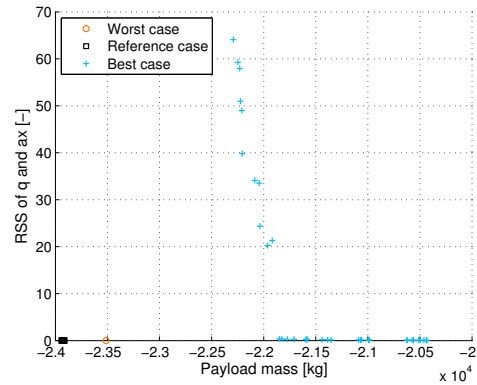
Run 7, on the other hand, having more strict constraints, presents a wider Pareto surface, and it is evident that the highest violations occur in the first group (with dynamic pressure and axial acceleration). This result might be expected since the launcher is more likely to violate those constraints (especially the axial acceleration) also in the one-objective optimization analysis.

Concerning the aerodynamic configurations, when the RSS of the path constraints and of the orbital elements are used, the best configuration gives a higher accuracy. When the RSS s of the two groups of path constraints are used, with more strict constraints, the best configuration performs worse because it produces higher accelerations. On the other hand, with less strict constraints (on dynamic pressure and bending load), it gives less violations and then more feasible solutions.

The best solution, then, found by this optimization runs is given in run 5 and yields a payload mass of 24,141 kg. A good solution is also given by run 6 (in which circularization burn is used), where the new type of objectives is used, and the resulting payload mass is 23,913 kg.

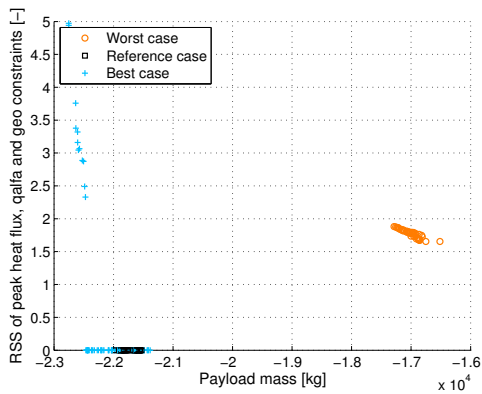


(a) 2D view of the Pareto surface with payload mass on x -axis and RSS of the second group of path constraints (peak heat flux, bending load and azimuth range) on z -axis.

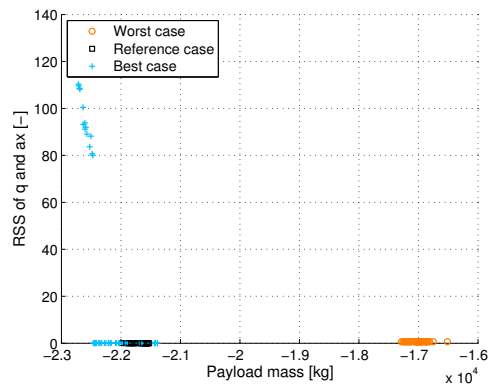


(b) 2D view of the Pareto surface with payload mass on x -axis and RSS of the first group of path constraints violations (dynamic pressure and axial acceleration) on y -axis.

Figure 6.38: Atlas V: three-objective optimization, run 6.



(a) 2D view of the Pareto surface with payload mass on x -axis and RSS of the second group of path constraints (peak heat flux, bending load and azimuth range) on z -axis.



(b) 2D view of the Pareto surface with payload mass on x -axis and RSS of the first group of path constraints violations (dynamic pressure and axial acceleration) on y -axis.

Figure 6.39: Atlas V: three-objective optimization, run 7.

6.3.4 Conclusions

Simulations for the Atlas V 552 yield a payload mass higher than the user manual reference one (i.e., 20,500 kg). The largest payload mass achieved is 24,141 kg in the worst aerodynamic configuration, found from the three-objective optimizations.

The typical throttled thrust profile of this launcher highlighted the difficulties of the software model to cope with instantaneous variations of the throttle. In order to have more control on the configuration of a rocket, such a feature should be implemented. In Fig. 6.40, the control history for pitch and yaw is shown. It is apparent that the best solution makes use of an orbital coast phase and a successive burn to circularize the orbit.

The launcher starts the orbital coast phase at the perigee of a transfer elliptical trajectory, at about 150 km altitude. At the apogee of the transfer trajectory, at 185 km altitude, the orbit is circularized. In this way, the vehicle reaches the perigee of the transfer orbit and it coasts until it reaches the apogee, corresponding to the final orbit altitude, saving the thrusting time that would have been necessary with a direct ascent.

Furthermore, during the coast phase, the pitch angle is equal to the flight path angle that is almost 0. In the meanwhile the yaw angle oscillates as, by following the target inclination law (see Eq. 4.8), the latitude of the launcher varies along the orbit (as it is not equatorial) and therefore the yaw does vary as well.

In Fig. 6.41, in the altitude-velocity plot, this phase of the trajectory can be seen.

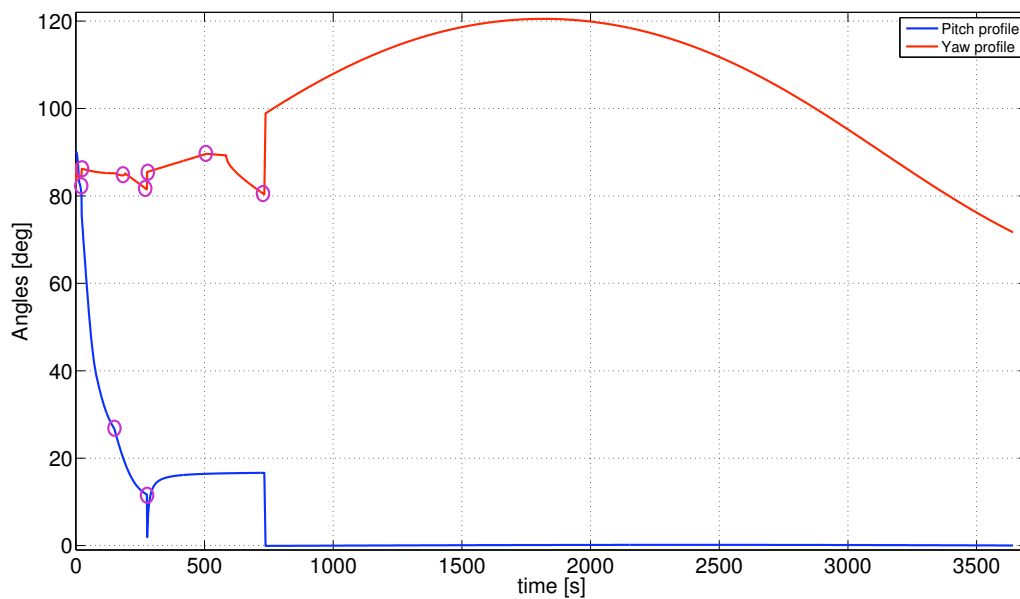


Figure 6.40: Atlas V 552: control history for the best solution.

6.4 Ariane 5 ESC-A

The last launcher analyzed for this feasibility study is the Ariane 5, launched from Kourou. The Ariane 5 is a two-stage vehicle provided with two boosters. The maximum endurable dynamic pressure is 40000 Pa, while the maximum axial acceleration is 4.55 g, taken from [Arianespace, 2008].

6.4.1 One-objective optimization results

For the Ariane 5, as Table 6.26 shows, no violations of peak heat flux, axial acceleration, semimajor axis and inclination (except in one case) occur. Concerning the axial acceleration, this launcher has two solid

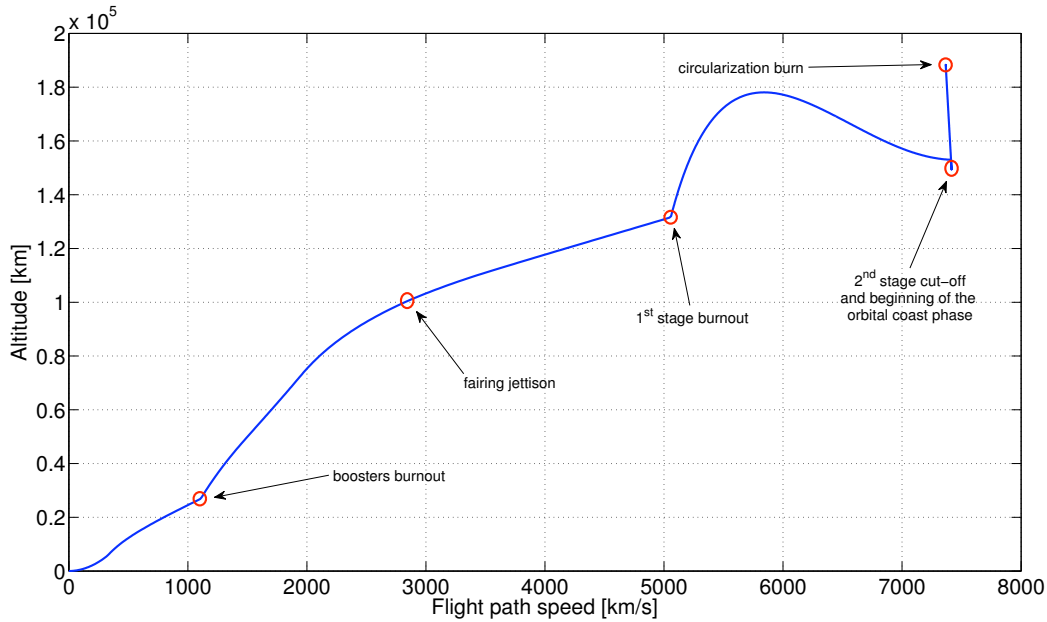


Figure 6.41: Atlas V 552: altitude-velocity plot for the best solution.

propellant boosters with a thrust profile tailored not to violate it. Therefore, the option to include the thrust profile for boosters has been implemented and no violations for this constraint occurred. In the case of Atlas V this was not needed since only its central core was throttled and the throttle level is optimized in order not to exceed the dynamic pressure and axial acceleration limits.

Between the three aerodynamic configurations, the best one, violates more often the bending load constraint. That is related to the higher velocity, less drag and the fact that, maybe, non-optimal parameters for the pitch-over phase have been found. These three factors generate high dynamic pressure and high angles of attack that result in bending load violations. The range azimuth is also violated sometimes and mostly in those trajectories with bending load violations.

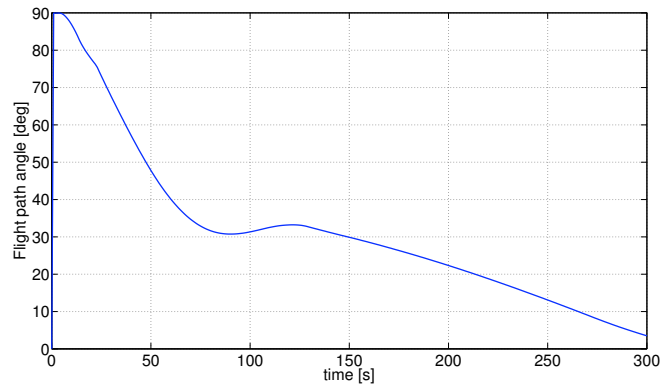
Concerning the bending load, in run 7, it might be violated also because of the more strict tolerance on the eccentricity. This orbital elements sometimes can be coupled to the bending load constraint as, to reach a better accuracy, usually a less steep trajectory has to be flown. The vehicle, then, spends more time in the denser layers of the atmosphere, with higher chances to violate dynamic pressure and bending load.

On the other hand, run 3 shows that also a more strict bending load constraint may produce errors in the eccentricity.

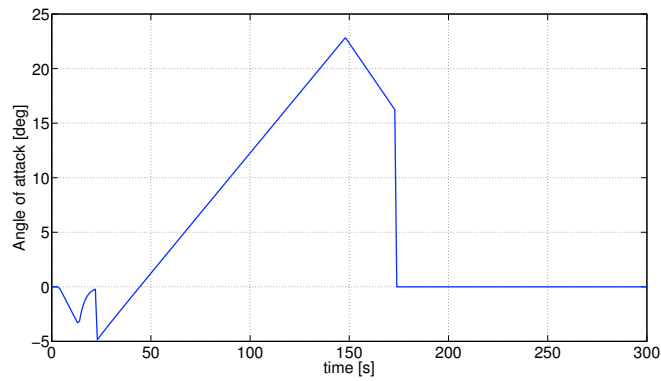
For all the runs, the payload masses range between 16,890 kg and 24,000 kg. However, besides some trajectories, it is difficult for the Ariane 5 to achieve payload mass of about 20-21 tons in this problem, as reported in its user manual [Arianespace, 2008]. Problems arose during the calibration runs because the launcher, during the gravity turn flown by the boosters and the first stage, was first going up with the pitch decreasing, then the pitch goes up and then down again, following its reference guidance (see Fig. 6.42c). For this reason, the number of nodes in the first stage has been reduced to 2 in the runs 4, 6, 8 and 9. In more detail, this strange behaviour occurred sometime before the boosters jettison (i.e., 80-120 seconds after launch). This behaviour might derive from the combination of high angle of attack, lift and thrust force.

Actually, from the equations of motion in spherical coordinates, an explanation can be drawn by analyzing the following, [Mooij, 1997]:

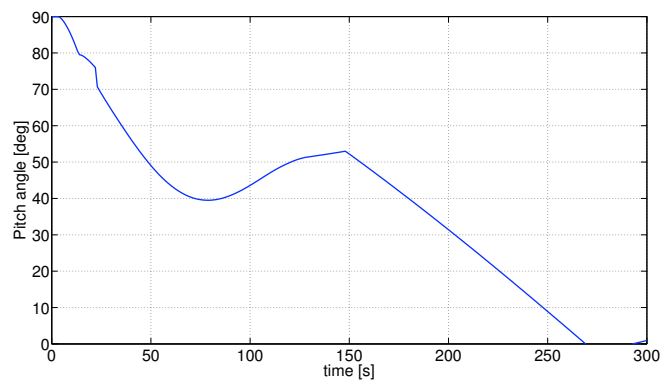
$$\begin{aligned} \dot{\gamma} = & \frac{(L + T \sin \alpha - m g_r \cos \gamma + m g_\delta \sin \gamma \cos \chi)}{m V} + 2 \omega \cos \delta \sin \chi \\ & + \frac{V}{r} \cos \gamma + \omega^2 \frac{r}{V} \cos \delta (\cos \delta \cos \gamma + \sin \delta \sin \gamma \cos \chi) \end{aligned} \quad (6.2)$$



(a) Flight path angle profile. The derivative of the flight path angle versus time is positive between 80 and 120 seconds.



(b) Angle of attack profile. After 180 seconds, the angle is zero because the launcher is above 100 km altitude, when the density is so low that it can be neglected.



(c) Pitch profile generated as consequence of the high lift, angle of attack and flight path angle.

Figure 6.42: Ariane 5, run 2. During the gravity turn, the launcher pitches up and then down.

where L is the lift, T is the thrust, α is the angle of attack, m is the mass, g_r is the component of the gravity along the radius vector, g_δ is the third component of the gravity in a vehicle based frame (that lies in the local horizontal plane), γ is the flight path angle, χ is the heading angle, V is the velocity in the Earth-centered rotating frame, r is the distance of the vehicle from the center of the Earth, ω is the Earth's rotational rate, δ is the latitude.

During the gravity turn, the derivative of the flight path angle with respect to time is negative as the flight path initially is 90° and reaches 0° to get tangentially into the final orbit. However, as can be seen in Fig. 6.42a, its derivative is positive. The profiles shown in Fig. 6.42a, 6.42b and 6.42c, refer to the best configuration from run 2. In Eq. 6.2, the main term that drives the sign of the derivative of the flight path angle is the first one, in which the lift and thrust forces are present. The reason for that behaviour to occur is due to the high lift. In the first term of Eq. 6.2, in the numerator, the term $mg_\delta \sin \gamma \cos \chi$ is smaller with respect to the others because of the gravity component and the heading angle (close to 90°).

In this case, the contribution of the angle of attack and the lift, which derives from the C_L and the angle of attack itself, make the term positive, yielding a flight path angle increasing along time. This fact reflects in the pitch profile that, since it is optimized in the neighborhood of a gravity turn (around the flight path angle), has the same behaviour, driving the launcher down (pitching up) and then up (pitching down). As a consequence, the launcher spends longer time in the atmosphere with higher chances to violate dynamic pressure, peak heat flux and bending load constraints.

This trajectory presents a high angle of attack (about 10°) that is quite high and that make the thrust term larger; therefore, it is highly advisable to implement an angle-of-attack constraint that should solve this problem.

Also for the Ariane 5, the most critical constraint is the bending load and this is due to the difficulty of the optimizer to find optimal parameters for the control laws that can keep the angles of attack low.

Table 6.25: Ariane 5: setup of the single-objective optimization runs.

Parameter	Simulation 1	Simulation 2	Simulation 3	Simulation 4	Simulation 5	Simulation 6	Simulation 7	Simulation 8	Simulation 9
a [km]	6563.137	6563.137	6563.137	6563.137	6563.137	6563.137	6563.137	6563.137	6563.137
e [-]	0	0	0	0	0	0	0	0	0
i [deg]	5.5	5.5	5.5	5.5	5.5	5.5	5.5	5.5	5.5
Tolerance a [km]	3	3	3	3	3	3	3	3	3
Tolerance e [-]	0.0005	0.0005	0.0005	0.0005	0.0005	0.0005	0.0001	0.0005	0.0005
Tolerance i [deg]	0.1	0.1	0.1	0.1	0.1	0.1	0.1	0.1	0.1
Dynamic pressure [kPa]	≤ 40	≤ 45	≤ 40	≤ 40	≤ 40				
Peak heat flux [kW/m ²]	≤ 120	≤ 100	≤ 120	≤ 100					
Axial acceleration [g]	≤ 4.55								
Bending load [kPa*deg]	≤ 300	≤ 150	≤ 100	≤ 120	≤ 100	≤ 120	≤ 150	≤ 150	≤ 150
Circularization burn	Yes	Yes	Yes	No	No	No	Yes	No	Yes
Coast arcs	No	No	No	No	Yes	Yes	No	No	No

6.4.2 Two-objective optimization results

For the two-objective optimization, 4 runs have been performed for Ariane 5. Two of these runs have the payload mass and the RSS of the orbital elements as objectives while the other two runs have payload mass and RSS of the path constraints.

Concerning the first two runs, from Table 6.28 it is evident that the reference aerodynamic configuration performs better than the others. In the first run, where the bending load constraint is higher with respect to the second, the reference configuration outperforms the other. As explanation one can think that with the best configuration, the launcher has too high velocity and, in order not to violate the bending load, flies a steeper trajectory with some problems in reaching the set accuracy on the eccentricity. With the worst configuration, the opposite effect might occur: that the launcher experiences high drag and has more difficulties in reaching the final eccentricity. Moreover, about the worst configuration, in run 1, the Pareto front on the left side is not perfectly linear as in the reference configuration. This might mean that the

Table 6.26: Ariane 5: results of the single-objective optimizations.

Parameter		Simulation 1	Simulation 2	Simulation 3	Simulation 4	Simulation 5	Simulation 6	Simulation 7	Simulation 8	Simulation 9
Error a	W	-	-	-	-	-	-	-	-	-
	R	-	-	-	-	-	-	-	-	-
	B	-	-	-	-	-	-	-	-	-
Error e	W	-	-	0.00101	0.001008	-	-	0.000163	-	0.001004
	R	-	-	-	-	-	-	-	-	-
	B	-	-	-	-	-	-	-	-	-
Error i	W	-	-	1.83%	-	-	-	-	-	-
	R	-	-	-	-	-	-	-	-	-
	B	-	-	-	-	-	-	-	-	-
Dynamic pressure violation [kPa]	W	-	-	-	-	-	-	-	-	-
	R	-	-	3.7	-	-	-	-	-	-
	B	-	-	-	-	-	-	12.7	4.4	-
Peak heat flux violation [kW/m ²]	W	-	-	-	-	-	-	-	-	-
	R	-	-	-	-	-	-	-	-	-
	B	-	-	-	-	-	-	-	-	-
Axial acceleration violation [g]	W	-	-	-	-	-	-	-	-	-
	R	-	-	-	-	-	-	-	-	-
	B	-	-	-	-	-	-	-	-	-
Bending load violation [kPa*deg]	W	6.7	-	198.8	-	-	-	225.1	-	-
	R	-	-	260.3	-	7.7	138.1	94.2	-	-
	B	14.6	101.6	71.5	40.3	94.9	-	346.0	249.3	-
Geographical violation [deg]	W	-	-	-	-	0.05	1	1.5	-	-
	R	-	0.8	-	0.3	-	1.5	1	-	-
	B	0.8	-	-	-	0.2	-	1.4	3	-
Final payload mass [kg]	W	17,367	20,144	23,321	19,365	20,228	21,143	19,855	21,296	21,691
	R	21,613	20,455	20,503	18,341	19,229	21,335	19,665	21,036	23,671
	B	16,890	20,783	19,600	18,019	19,930	24,000	20,377	22,813	21,558

W = worst aerodynamic configuration

R = reference aerodynamic configuration

B = best aerodynamic configuration

- = no violation

■ = trajectory without path constraint

and orbital element tolerance violations

optimization did not fully converge and that, as constrained problem, there might be other feasible solutions that yield higher payload masses at the same level of accuracy.

The worst configuration, in run 2, has few solutions in the lower part of the front, from which is difficult to understand if other solutions might have a better accuracy. To solve this problem a run should have been performed with a higher number of particles in the initial population. On the other hand, in run 1, it seems that this configuration is not able to achieve an accuracy better than the lower found and this can be seen from the lower part of the front.

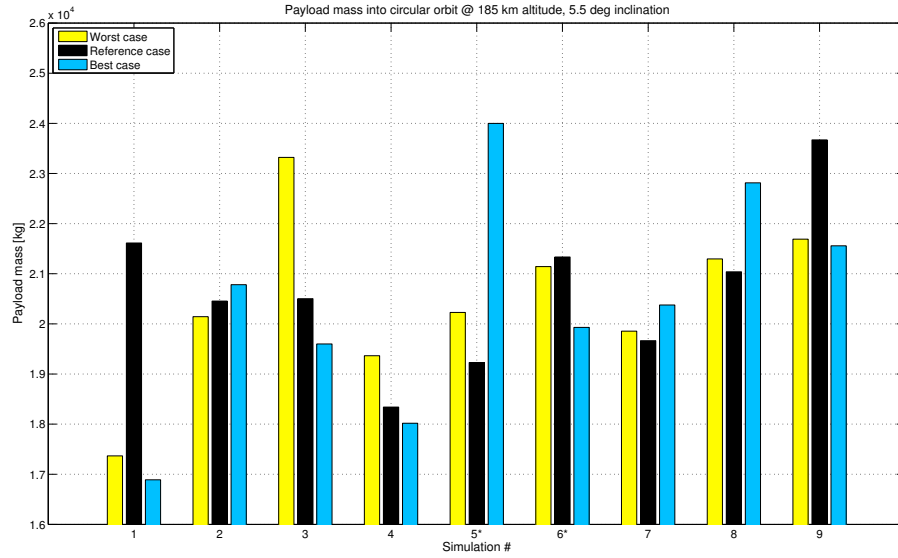
From a payload mass point of view, a quite high value is obtained, in the aforementioned run and configuration, equals to 25,420 kg. In run 2, however, a lower payload mass has been achieved due to the more strict bending load constraint.

For the optimization runs involving the *RSS* of the path constraints, no solutions without violations have been found. This confirms the results from the single-objective optimization, in which in several runs and configurations, violations occurred, especially in the bending load. And the bending load is the main factor that drives the variety of the Pareto front since in the run where it is more strict a less wide front is found (as shown in Fig. 6.44d).

For the worst configuration, in run 4, only one solution has been found. That means no other solutions, with a higher accuracy and a lower payload mass or vice versa have been found. To avoid this kind of problem, the advice for future work is to have a larger initial population from which more solutions can be found and also a larger search space can be covered. The same holds for the reference configuration, in run 3, where the front is made up by only 5 solutions.

6.4.3 Three-objective optimization results

Also for the three-objective optimization, for the Ariane 5, four runs have been performed. Three out of four runs use payload mass, *RSS* of the path constraints and *RSS* of the orbital elements as objectives. The fourth run uses payload mass and *RSS* of two groups of path constraints as objectives. The two groups of



* = trajectory with coast arcs

Figure 6.43: Ariane 5: summary of the payload masses obtained from the one-objective optimization.

constraints, for the fourth run, are made by dynamic pressure and axial acceleration on one side and peak heat flux, bending load and azimuth range on the other.

Table 6.27: Ariane 5: setup of the two-objective optimization runs.

Parameter	Simulation 1	Simulation 2	Simulation 3	Simulation 4
a [km]	6563.137	6563.137	6563.137	6563.137
e [-]	0	0	0	0
i [deg]	5.5	5.5	5.5	5.5
Tolerance a [km]	3	3	3	3
Tolerance e [-]	0.0005	0.0005	0.0005	0.0005
Tolerance i [deg]	0.1	0.1	0.1	0.1
Dynamic pressure [kPa]	≤ 40	≤ 40	≤ 40	≤ 40
Peak heat flux [kW/m ²]	≤ 100	≤ 100	≤ 100	≤ 100
Axial acceleration [g]	≤ 4.55	≤ 4.55	≤ 4.55	≤ 4.55
Bending load [kPa*deg]	≤ 150	≤ 120	≤ 120	≤ 100
Circularization burn	No	Yes	Yes	No
Coast arcs	No	Yes	No	No

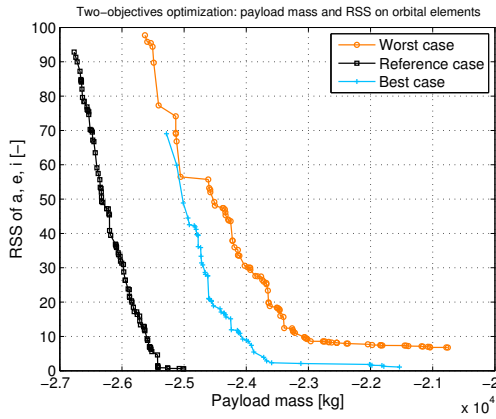
Table 6.28: Ariane 5: results of the two-objective optimizations.

	Run 1		Run 2		Run 3		Run 4	
	Payload mass [kg]	RSS orbital elements	Payload mass [kg]	RSS orbital elements	Payload mass [kg]	RSS path constraints	Payload mass [kg]	RSS path constraints
Worst	20,757	6.78	20,624	5.05	19,814	0.67	18,751	35.46
	20,782	6.79	20,805	5.06	19,998	0.7		
	21,042	6.81	20,806	5.26	20,412	0.85		
Reference	25,265	0.82	21,571	0.57	21,312	1.18	19,452	15.71
	25,266	0.83	21,590	0.83	21,321	1.18	19,468	15.75
	25,420	0.90	22,142	0.96	21,322	1	19,489	15.76
Best	21,534	1.07	23,298	2.48	22,265	2.59	21,533	1.76
	21,786	1.29	23,323	2.56	22,229	2.59	21,545	1.76
	21,817	1.53	23,550	2.92	22,239	2.59	21,546	1.77

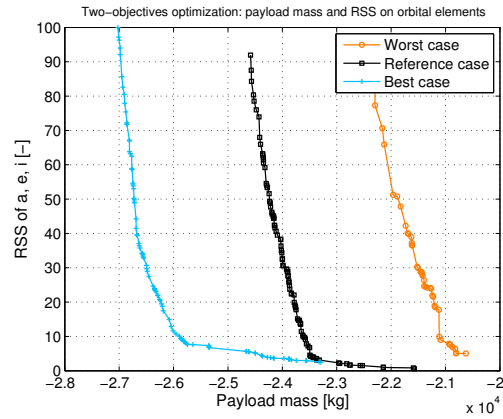
■ = trajectory without path constraint
 and orbital element tolerance violations

Table 6.29: Ariane 5: setup of the three-objective optimization runs.

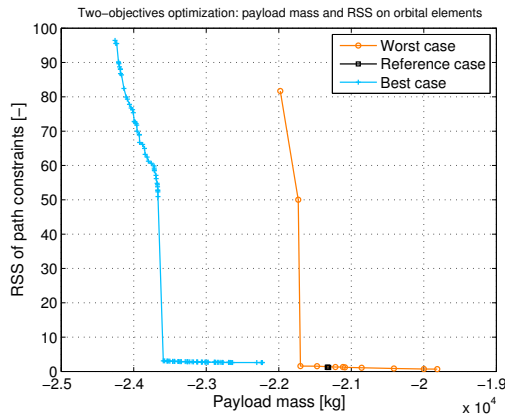
Parameter	Simulation 1	Simulation 2	Simulation 3	Simulation 4
a [km]	6563.137	6563.137	6563.137	6563.137
e [-]	0	0	0	0
i [deg]	5.5	5.5	5.5	5.5
Tolerance a [km]	3	3	3	3
Tolerance e [-]	0.0005	0.0005	0.0005	0.0005
Tolerance i [deg]	0.1	0.1	0.1	0.1
Dynamic pressure [kPa]	≤ 40	≤ 40	≤ 40	≤ 40
Peak heat flux [kW/m ²]	≤ 100	≤ 100	≤ 100	≤ 100
Axial acceleration [g]	≤ 4.55	≤ 4.55	≤ 4.55	≤ 4.55
Bending load [kPa*deg]	≤ 150	≤ 120	≤ 120	≤ 100
Circularization burn	No	Yes	Yes	No
Coast arcs	No	Yes	No	No



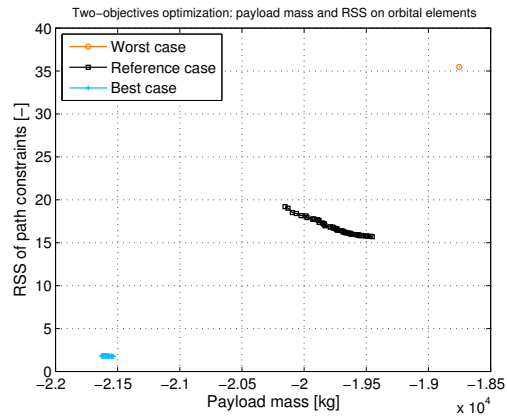
(a) Run 1. The second objective is the *RSS* of the orbital elements.



(b) Run 2. The second objective is the *RSS* of the orbital elements.



(c) Run 3. The second objective is the *RSS* of the path constraints.



(d) Run 4. The second objective is the *RSS* of the path constraints.

Figure 6.44: Ariane 5: Pareto fronts of the two-objective optimization runs.

Table 6.30: Ariane 5: results of the three-objective optimizations.

	Run 1			Run 2			Run 3			Run 4		
	Payload mass [kg]	RSS path constraints	RSS orbital elements	Payload mass [kg]	RSS path constraints	RSS orbital elements	Payload mass [kg]	RSS path constraints	RSS orbital elements	Payload mass [kg]	RSS path constraints (group 1)	RSS path constraints (group 2)
Worst	19,621	0	69.17	20,616	0	25.44	19,150	0	2.24	23,195	37.94	5.88
	20,019	0	70.84	20,756	0	36.46	20,308	0	4.16	23,247	37.97	5.84
	21,605	0	84.9	21,318	0	41.5	23,294	0	13.02	23,253	38.31	5.79
Reference	23,685	0	6.16	19,999	0	12.62	21,624	0	6.51	20,740	15.91	4.42
	23,791	0	9.81	21,254	0	15.14	22,754	0	16.4	20,739	15.95	4.41
	23,903	0	10.17	22,033	0	15.74	23,209	0	25.74	20,735	16.2	4.36
Best	24,406	0	12.03	23,617	0	13.64	23,704	0	19.34	20,244	0.11	2.2
	24,406	0	12.04	24,231	0	13.85	23,741	0	24.34	20,283	0.11	2.21
	24,413	0	12.19	24,264	0	15.91	23,915	0	37.42	20,263	0.11	2.21

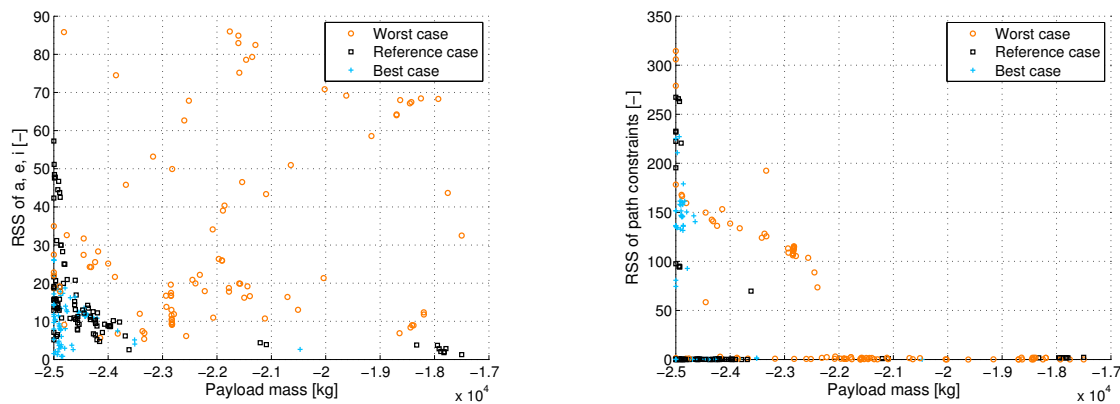
In Table 6.30 the solutions have been sorted out first for path constraints violation. Therefore, it is evident that there are, in the first three runs, solutions that do not violate any constraints. Secondly, those solutions were sorted according to the lower *RSS* of the orbital elements. When this criterion is applied, it is clear that all the solutions that do not violate the constraints reach a low accurate orbit. Also in the three-objective optimization, more than in the other two kinds of optimization, it is evident how difficult it is to find a good solution for this launcher. One recommendation is to increase the initial population size together with an angle-of-attack constraint.

The fact that several constraints are violated, and sometimes quite heavily, is shown also in run 4, from Table 6.30.

Analyzing Fig. 6.45, the best aerodynamic configuration gives higher payload mass and a better accuracy. A good accuracy is also given by the reference configuration. On the other hand, the worst configuration is more capable of satisfying the constraints but yielding a lower payload mass. Also run 2 presents similar results (see Fig. 6.46) for the best configuration, however the reference one satisfies the constraints better with respect to the other two. Moreover, for same values of *RSS* of path constraints, the best configuration gives higher payload.

Different is the analysis resulting from Fig. 6.47, where the worst configuration outperforms the other two in payload and accuracy, whereas the best configuration satisfies the constraints better.

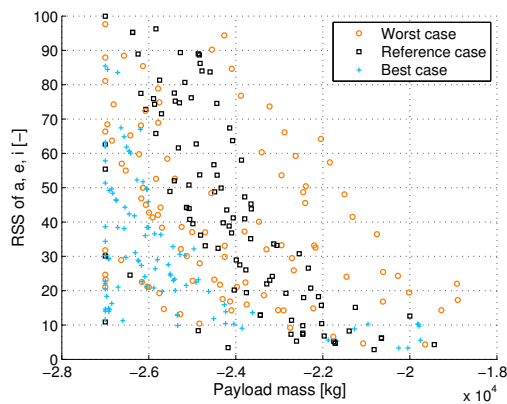
By analyzing Fig. 6.48, it can be said which group of constraints is better satisfied. It results that the best aerodynamic configuration satisfies the dynamic pressure better (since the axial acceleration is controlled by the fact of having a tailored boosters' thrust profile), but also the second group (peak heat flux, bending load and azimuth range).



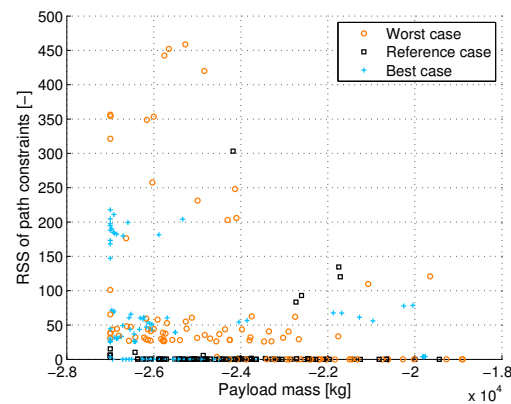
(a) Run 1. The second objective is the *RSS* of the orbital elements.

(b) Run 2. The second objective is the *RSS* of the orbital elements.

Figure 6.45: Ariane 5: three-objective optimization, run 1.

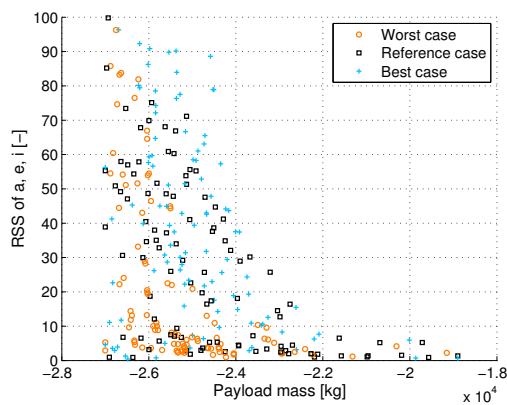


(a) Run 1. The second objective is the *RSS* of the orbital elements.

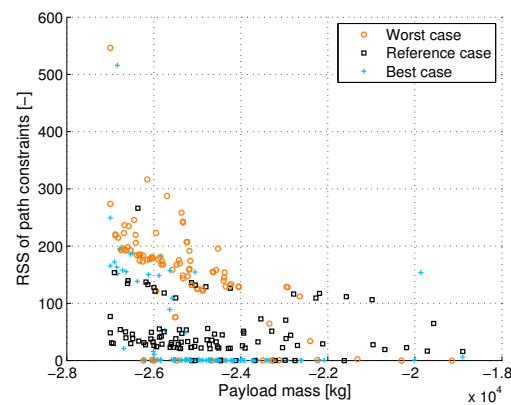


(b) Run 2. The second objective is the *RSS* of the orbital elements.

Figure 6.46: Ariane 5: three-objective optimization, run 2.



(a) Run 1. The second objective is the *RSS* of the orbital elements.



(b) Run 2. The second objective is the *RSS* of the orbital elements.

Figure 6.47: Ariane 5: three-objective optimization, run 3.

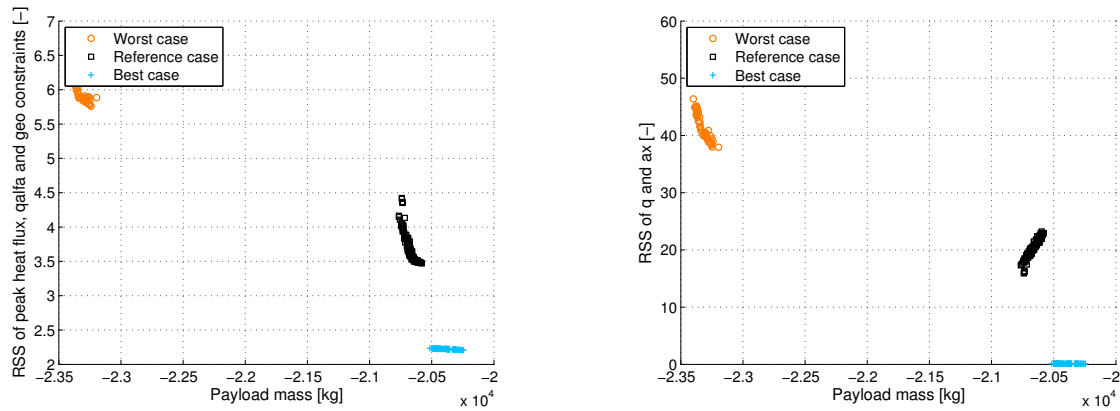
6.4.4 Conclusions

With the Ariane 5, it has been highlighted what the effect of not having an angle-of-attack constraint can be on the trajectory. Besides this consideration, the vehicle with the reference aerodynamic configuration yielded the largest payload mass of 25,420 kg, from the two-objective optimization in run 1.

The circularization burn has not helped to find better solutions and, on average, the runs that do not include it give a slightly higher payload mass.

In Fig. 6.49, the control history for the the best solutions can be observed. It is clear that the gravity turn is quite long as it is flown along all the burning phase of the core stage.

When the boosters are thrusting, the altitude and the velocity are almost linearly related. On the other hand, when the booster are jettisoned, the launcher is still flying a gravity turn that brings the vehicle in a quasi-tangential attitude. However, when the upper stage is started, the launcher increases its altitude and slightly its velocity. From Fig. 6.50, the altitude goes beyond 230 km. Even though this control profile brings the vehicle at a much higher altitude than the needed one, still it is optimum as the potential energy gained is then converted in kinetic energy to achieve the orbital velocity for the target orbit.



(a) Run 1. The second objective is the *RSS* of the orbital elements.

(b) Run 2. The second objective is the *RSS* of the orbital elements.

Figure 6.48: Ariane 5: three-objective optimization, run 4.

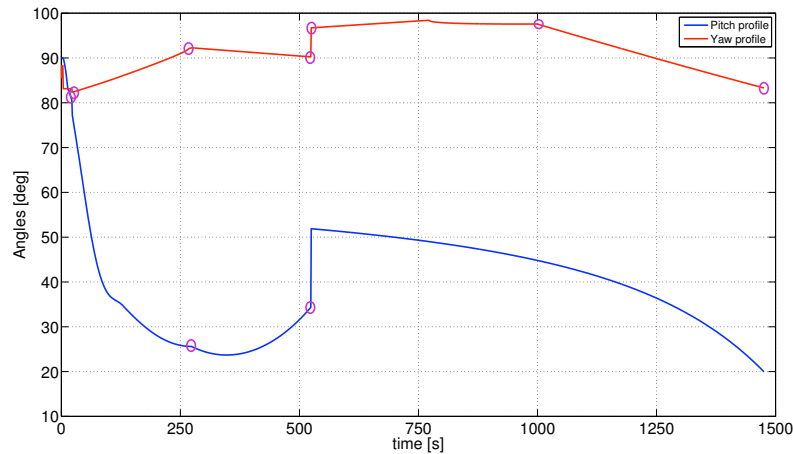


Figure 6.49: Ariane 5: control history for the best trajectory.

6.5 Delta IV Heavy: preliminary analysis

Initially, the Delta IV Heavy was intended to be optimized only for the lunar Hohmann transfer orbit. Because of shortage of time and enormous computational effort, only single-objective optimization in the reference aerodynamic configuration has been performed for this launcher. The only data that will be given are about the optimization runs setup and the relative results. In addition, as the results were not in line with the user manual reference values (they are much worse) also a few runs for insertion in a LEO parking orbit were performed.

The maximum axial acceleration for this launcher is 5.55 g while for the dynamic pressure a maximum value of 17,200 Pa can be withstood, taken from [ULA, 2007]. However, a higher dynamic pressure limit was set as the given was not satisfied, with the hope that a relaxation of this constraints could help in the optimization process to find better solutions.

Lunar Hohmann transfer orbit

Only 5 runs per final orbit were performed and the setup and the results are shown in Table 6.31 and 6.32.

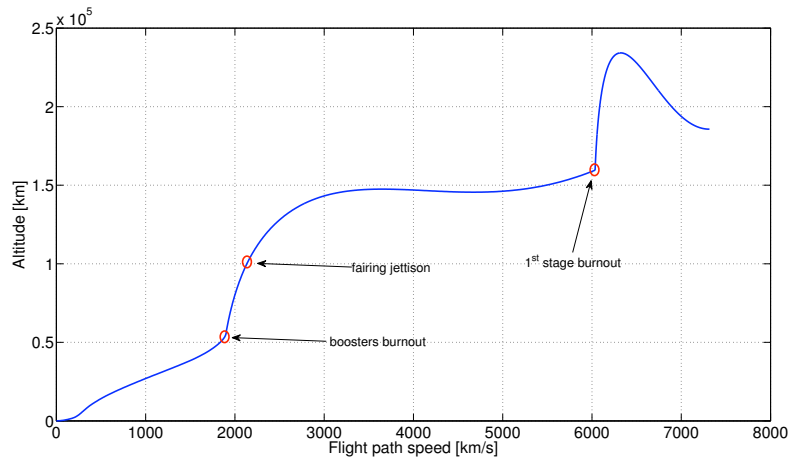


Figure 6.50: Ariane 5: altitude-velocity plot for the best trajectory.

Table 6.31: Delta IV Heavy: setup of the single-objective optimization runs for the lunar Hohmann transfer orbit.

Parameter	Simulation 1	Simulation 2	Simulation 3	Simulation 4	Simulation 5
a [km]	195481	195481	195481	195481	195481
e [-]	0.966426	0.966426	0.966426	0.966426	0.966426
i [deg]	12.122	28.5	28.5	28.5	28.5
Tolerance a [km]	3	3	3	3	3
Tolerance e [-]	0.0005	0.0005	0.0005	0.0005	0.0005
Tolerance i [deg]	0.1	0.1	0.1	0.1	0.1
Dynamic pressure [kPa]	≤ 60	≤ 60	≤ 60	≤ 60	≤ 60
Peak heat flux [kW/m ²]	≤ 300	≤ 300	≤ 300	≤ 300	≤ 300
Axial acceleration [g]	≤ 6	≤ 5.5	≤ 5.5	≤ 5.5	≤ 5.5
Bending load [kPa*deg]	≤ 300	≤ 300	≤ 300	≤ 300	≤ 300
Circularization burn	No	No	No	No	No
Coast arcs	No	No	No	No	No

As the results show, from Table 6.32, the path constraints are satisfied in all the optimal solutions but one (the axial acceleration, in run 2). However, in almost all the runs, the tolerances on the orbital elements are not respected. This should be due to the fact that the tolerances have been set quite strict for such an orbit. The tolerances set are more suited for ascent trajectories to LEO orbit than high elliptical orbit. In fact, for these type of orbits, less strict tolerances are set and correction maneuvers can be performed during the orbital coast phase to adjust for better precision.

Concerning the dynamic pressure, even though the constraint was never violated, the value got to 25,000 Pa on average, violating the original value.

The average payload mass is about 7.8 tons with a maximum of 7,876 kg. As said before, the results are not in line with the Launch Energy capability C_3 of the launcher, that is a measure of the energy of the orbit to be achieved. For this value, that is characteristics of the particular orbit at certain moment (in this case, at injection in the lunar transfer orbit), launchers' manufacturing companies publicly release the payload mass that can be delivered.

The C_3 value (that is two times the orbital energy) can be also regarded as the maximum orbital energy that can be achieved by the launcher with a certain payload mass. Assuming that injection occurs at pericenter, the energy needed to reach the Moon through a Hohmann transfer orbit is about $-2.064 \text{ km}^2/\text{s}^2$, that, in [ULA, 2007], would give about 10,500 kg, that is the reason why the software cannot cope with such extreme trajectory.

Table 6.32: Delta IV Heavy: results of the single-objective optimization runs for the lunar Hohmann transfer orbit.

Parameter		Simulation 1	Simulation 2	Simulation 3	Simulation 4	Simulation 5
Error a	R	0.01%	0.43%	-	0.04%	-
Error e	R	1.10%	0.36%	0.16%	0.06%	0.06%
Error i	R	90.0%	16.2%	28.6%	32.8%	32.8%
Dynamic pressure violation [kPa]	R	-	-	-	-	-
Peak heat flux violation [kW/m ²]	R	-	-	-	-	-
Axial acceleration violation [g]	R	-	0.2	-	-	-
Bending load violation [kPa*deg]	R	-	-	-	-	-
Geographical violation [deg]	R	-	-	-	-	-
Final payload mass [kg]	R	7,698	7,001	7,876	7,861	7,857

LEO parking orbit

For this type of orbit 5 runs have been performed as well. From some runs performed to calibrate the setup configuration for the launcher, it resulted that the Delta IV Heavy is not able to achieve a circular orbit at 185 km altitude by means of the Ascent Module software. The issue was related to the always violated axial acceleration constraint, that in reality the launcher can cope with by throttling down the central core. It is apparent that the Ascent Module has a lot of difficulties in doing that, at least when a launcher heavily relies on this capability. For the coming versions of the module, this feature is strongly recommended and it should not be very difficult to implement.

Moreover, as no reference payload was found at this altitude in [ULA, 2007] and as the minimum payload was reported for a circular orbit at 400 km altitude, five runs have been performed with this target.

Table 6.33: Delta IV Heavy: setup of the single-objective optimization runs for the low Earth parking orbit.

Parameter	Simulation 1	Simulation 2	Simulation 3	Simulation 4	Simulation 5
a [km]	6778.137	6778.137	6778.137	6778.137	6778.137
e [-]	0	0	0	0	0
i [deg]	28.5	28.5	28.5	28.5	28.5
Tolerance a [km]	3	3	3	3	3
Tolerance e [-]	0.0005	0.0005	0.0005	0.0005	0.0005
Tolerance i [deg]	0.1	0.1	0.1	0.1	0.1
Dynamic pressure [kPa]	≤ 50	≤ 50	≤ 50	≤ 50	≤ 30
Peak heat flux [kW/m ²]	≤ 150	≤ 150	≤ 150	≤ 150	≤ 200
Axial acceleration [g]	≤ 5	≤ 5	≤ 5	≤ 5	≤ 5.6
Bending load [kPa*deg]	≤ 200	≤ 200	≤ 200	≤ 200	≤ 250
Circularization burn	No	No	No	No	No
Coast arcs	No	No	No	No	No

In this case, from Table 6.34, the launcher still has troubles to perform according its capabilities (it can deliver 23 tons at the aforementioned orbit). This is the main reason for which further investigations and improvements in the software have to be made, mostly related to throttle capability and thrust profiles.

Table 6.34: Delta IV Heavy: setup of the single-objective optimization runs for the low Earth parking orbit.

Parameter		Simulation 1	Simulation 2	Simulation 3	Simulation 4	Simulation 5
Error a	R	-	-	-	-	-
Error e	R	-	-	0.001	-	-
Error i	R	-	1.10%	2.81%	8.01%	-
Dynamic pressure violation [kPa]	R	-	-	-	-	-
Peak heat flux violation [kW/m ²]	R	-	-	-	-	-
Axial acceleration violation [g]	R	-	0.6	0.8	-	-
Bending load violation [kPa*deg]	R	-	-	-	6.9	50.8
Geographical violation [deg]	R	-	-	-	-	-
Final payload mass [kg]	R	18,292	16,807	19,561	19,200	16,275

6.6 Atlas V HLV: preliminary analysis

The same thing said about the Delta IV Heavy holds for the heavy version of the Atlas V, namely HLV. Main goal of this optimization analysis was to reach the lunar Hohmann transfer orbit, but also in this case problems arose due to the throttle ability of the launcher and the issues of the Ascent Module to cope with it. The maximum dynamic pressure and axial acceleration are 20,600 Pa and 5 g, from [Lockheed Martin, 2007].

Lunar Hohmann transfer orbit

For this elliptical orbit, five runs were performed whose results are shown in Table 6.36. As mentioned before, the launcher is penalized by the high axial acceleration and bending load violations. These, moreover, lead also to heavy violations in the final orbital elements. It has to be noted that, with respect to the Delta IV Heavy for which strict tolerances were set, the tolerances are less strict. Maybe even the semimajor axis tolerance can be set to a higher value.

The found solutions yield a payload that range between 4,852 kg and 6,027 kg. The violations of the axial acceleration are too high and this leads to the fact that the software has difficulties in achieving the right throttle level by means of the current model and optimization. These optimal solutions would never be flown because the launcher would never make it through the ascent. It was not possible to compare the obtained results with any reference values as, in [Lockheed Martin, 2007], no payload mass as function of the C_3 energy were reported.

However, it seems quite impossible, for a launcher able to deliver 28,660 kg in LEO orbit at 185 km altitude, not to reach at least 10 tons in a transfer orbit to the Moon.

LEO parking orbit

The Atlas V HLV is able to deliver the highest payload mass, namely 28,600 kg, as is stated by its user manual report. But what Table 6.38 shows, seems to be quite far from those results.

First, the launcher is far from its reference payload mass and secondly all the path constraints are violated (except for the range azimuth). Even though its maximum dynamic pressure is lower, this constraint has been relaxed to check for possible better performance. Actually, by relaxing the path constraints sometimes helps the optimizer to evolve towards the most natural solution, that turns out not to violate the constraints. However, this was not the case.

The bending load and axial accelerations are heavily violated, that means the launcher would be completely destroyed if it flew. Furthermore, the payload masses vary considerably from 8,189 kg to 21,000 kg, which reflects the unreliability of the results.

Table 6.35: Atlas V HLV: setup of the single-optimization runs for the lunar Hohmann transfer orbit.

Parameter	Simulation 1	Simulation 2	Simulation 3	Simulation 4	Simulation 5
a [km]	195481	195481	195481	195481	195481
e [-]	0.966426	0.966426	0.966426	0.966426	0.966426
i [deg]	28.7	28.7	28.7	28.7	28.7
Tolerance a [km]	5	5	5	5	5
Tolerance e [-]	0.001	0.001	0.001	0.001	0.001
Tolerance i [deg]	0.1	0.1	0.1	0.1	0.1
Dynamic pressure [kPa]	≤ 20.6	≤ 25	≤ 25	≤ 25	≤ 25
Peak heat flux [kW/m ²]	≤ 120	≤ 120	≤ 120	≤ 120	≤ 120
Axial acceleration [g]	≤ 5	≤ 5	≤ 5	≤ 5	≤ 5
Bending load [kPa*deg]	≤ 200	≤ 200	≤ 200	≤ 200	≤ 200
Circularization burn	No	No	No	No	No
Coast arcs	No	No	No	No	No

Table 6.36: Atlas V HLV: results of the single-optimization runs for the lunar Hohmann transfer orbit.

Parameter		Simulation 1	Simulation 2	Simulation 3	Simulation 4	Simulation 5
Error a	R	0.01%	0.43%	-	0.04%	-
Error e	R	1.10%	0.36%	0.16%	0.06%	0.06%
Error i	R	90.0%	16.2%	28.6%	32.8%	32.8%
Dynamic pressure violation [kPa]	R	29.9	17.4	62.7	13.8	112.3
Peak heat flux violation [kW/m ²]	R	-	-	-	-	-
Axial acceleration violation [g]	R	2.8	2.9	3.6	2.4	7.4
Bending load violation [kPa*deg]	R	1293.5	1172.7	657.7	187.2	1138.6
Geographical violation [deg]	R	-	-	-	-	-
Final payload mass [kg]	R	6,027	5,608	4,880	4,901	4,852

Still, the explanation for such results is to be found in the inability of the software to cope with the throttle setting used for this launcher.

6.7 Global overview

A summary of the results presented in the previous sections is given here. This overview aims at showing the largest payload masses that can be achieved by the single launchers. From this comparison, the most suitable launchers can be selected for the lunar base mission. Then, the analysis of the other mission phases can follow.

The results are summarized by optimization type. Moreover, from the two and three-objective optimizations, only the solutions that gives the largest payload are included in Table 6.39 and 6.40. However, those that violate the path constraints or do not satisfy the given accuracies on the orbital elements have an asterisk.

From [Zuccarelli, 2009], it resulted that the payload masses in Table 6.41 are needed in order to put the communication satellites in the right orbit around the second Lagrangian point L_2 of the Earth-Moon system. From the results obtained for Vega, it is evident that it is not recommended to inject into an orbit with 5° inclination. This is due to the fact that, the largest payload mass available is 3,453 kg but the needed payload mass is 3,491 kg. A miscommunication between the author of this work and Zuccarelli occurred and

Table 6.37: Atlas V HLV: setup of the single-optimization runs for the low Earth parking orbit.

Parameter	Simulation 1	Simulation 2	Simulation 3	Simulation 4	Simulation 5
a [km]	6563.137	6563.137	6563.137	6563.137	6563.137
e [-]	0	0	0	0	0
i [deg]	28.7	28.7	28.7	28.7	28.7
Tolerance a [km]	5	5	5	5	5
Tolerance e [-]	0.001	0.0005	0.0005	0.0005	0.0005
Tolerance i [deg]	0.1	0.1	0.1	0.1	0.1
Dynamic pressure [kPa]	≤ 40	≤ 40	≤ 40	≤ 40	≤ 40
Peak heat flux [kW/m ²]	≤ 120	≤ 120	≤ 120	≤ 120	≤ 120
Axial acceleration [g]	≤ 5	≤ 5	≤ 5	≤ 5	≤ 5
Bending load [kPa*deg]	≤ 200	≤ 200	≤ 200	≤ 200	≤ 200
Circularization burn	No	No	No	Yes	Yes
Coast arcs	No	No	No	No	No

Table 6.38: Atlas V HLV: results of the single-optimization runs for the low Earth parking orbit.

Parameter		Simulation 1	Simulation 2	Simulation 3	Simulation 4	Simulation 5
Error a	R	-	-	-	-	-
Error e	R	-	-	-	-	-
Error i	R	2.1%	-	-	-	-
Dynamic pressure violation [kPa]	R	2.3	55.6	6.9	6.0	54.8
Peak heat flux violation [kW/m ²]	R	-	62.6	11.4	-	48.9
Axial acceleration violation [g]	R	4.3	1.8	5.4	1.2	1.9
Bending load violation [kPa*deg]	R	216.4	755.5	265.4	258.9	747.6
Geographical violation [deg]	R	-	-	-	-	-
Final payload mass [kg]	R	8,189	19,955	11,758	11,205	21,000

a mismatch of 0.5° in the final inclination orbit occurred.

The other two inclinations analyzed are more suitable for this launcher even if some plane changes occur in the ascent flight. Therefore, a final orbit inclination of 28.5° is chosen because the payload mass obtained is the highest with 3,475 kg and because the plane change maneuver is less expensive than that needed to reach a 51.6° orbit inclination. This orbit is also chosen since it offers also a safety margin about the mass involved.

Concerning the three launchers needed for the building phase of the lunar base, it is evident that Ariane 5 ESC-A delivers the largest payload mass with 25 tons. The Atlas V 552 and Proton M follow with about 24 and 23 tons. The choice will not be unilateral, meaning that choosing only one vehicle might not be a wise decision. Actually, to build the lunar base, which is time consuming, it is advisable to use more than one launcher in order to keep a high rate of launching. In fact, a launch campaign may keep a launch site and pad busy for more or less 3 months. This would lead to a launch rate of 4 per year, whereas if two or three launchers are used, the rate can be up to 12 per year. Moreover, it is wiser to perform such a mission in an international cooperation. This is also the best choice if one wants to build the base in a limited time period.

A particular note has to be mentioned about the Delta IV Heavy and the Atlas V HLV. The preliminary analysis made for these two launchers, even if very superficial, showed the deficiency of the Ascent Module software and the particular deficiency to cope with several throttle strategies. Moreover, not much can be said from the results obtained from the optimizations of these two launchers since the process was not

Table 6.39: Vega: best payload masses obtained at different orbit inclination. The solutions with an asterisk do not satisfy the path constraints or the orbital elements tolerances.

Optimization type	Vega		
	5.5°	28.5°	51.6°
1D optimization	3,453	3,475	3,172
2D optimization	3,405	3,269	3,263*
3D optimization	3,046	N/A	N/A

Table 6.40: Best payload masses for the launchers. The solutions with an asterisk do not satisfy the path constraints or the orbital elements tolerances.

Optimization type	Proton M	Atlas V 552	Ariane 5 ESC-A
1D optimization	23,091	22,993	24,000
2D optimization	23,005	22,726	25,420
3D optimization	23,073*	24,141	19,150*

successful.

By comparing the performances of the three types of optimizations, it results that the multi-objective optimizer DG-MOPSO equals or slightly outperforms the single-objective PSO. This might be due to the double grid implemented that is able to give a uniform distribution of the solutions in the objective space. However, in order to have high performances, it is advisable to have a large population size.

Interface with Earth-Moon transfer orbit

From Zuccarelli's work, we can present the ΔV budgets computed for the Ariane 5, Proton M, Atlas V and Vega. From these results, a first order analysis of the propellant mass that might be used for each payload launched can be extracted. This analysis assumes a high thrust engine,¹ the RD-0126E. This is a Russian concept for a cryogenic engine for upper stages. This is a design concept, but it is expected to fly soon. It should be included in the improved version of the Soyuz launcher, called Onega. The engine has a $I_{sp} = 472$ s.

The following propellant mass is computed by means of the Tsiolkovsky equation (see Eq. 3.86). The ΔV budgets are presented in Table 6.42 and the computed propellant masses, for each launcher, are given in Table 6.43. Regarding the Vega, the ΔV budgets for each orbit inclination and the relative propellant masses needed are given in Table 6.44.

From the tables presented, it can be seen that the Vega can reach the final orbit around the Lagrangian point from all the LEO parking orbit inclinations analyzed. The payload mass in the parking orbit obtained from this study is able to account for the propellant mass needed for the transfer.

Concerning the other three launchers, the payload masses that arrive in low lunar orbit are shown in Table 6.45.

¹ <http://www.astronautix.com/engines/rd0126.htm>

Table 6.41: Vega: payload mass needed in LEO parking orbit for the Earth-Moon communication satellites [Zuccarelli, 2009].

Inclination [deg]	LEO payload mass
5	3,491
28.5	2,154
51.6	2,203

Table 6.42: ΔV budgets needed for each launcher according the transfer method used [Zuccarelli, 2009].

	High thrust transfer	Low-thrust transfer	3 body transfer
Launcher	ΔV [m/s]	ΔV [m/s]	ΔV [m/s]
Ariane 5	4,698	3,352	4,775
Proton M	7,057	3,352	3,927
Atlas V 552	4,484	3,352	4,252

Table 6.43: The propellant masses needed for each launcher are shown.

	High thrust transfer propellant mass	Low-thrust transfer propellant mass ($I_{sp} = 1000$ s)	Low-thrust transfer propellant mass ($I_{sp} = 1500$ s)	3 body transfer propellant mass
Launcher	[kg]	[kg]	[kg]	[kg]
Ariane 5	15,302	6,948	4,890	15,409
Proton M	18,064	6,685	4,705	13,206
Atlas V 552	14,978	6,989	4,919	14,507

It is evident that the largest payload mass available are given by the low thrust transfer that has a higher transfer time in the order of months (depending on the engine selected) as drawback. On the other hand, the high thrust transfer and the transfer by means of weak stability boundaries, give about 8.5 – 10 tons of payload mass in low lunar orbit. With a first-order analysis, propellant mass, to insert the payload in the low lunar orbit, will be needed plus the propellant mass for the landing phase. Moreover, additional mass has to be accounted for the structural mass of the transfer S/C and landing device. Roughly, at least 4 tons would be needed if one accounts for 2000 m/s of ΔV and I_{sp} of about 350 s (Apollo lander's engines had a $I_{sp} = 311$ s). Therefore, the payload mass on the Moon might be about 4-5 tons.

We can compare the results obtained so far with the payload mass available in a low lunar orbit (100 km altitude) given by a direct ascent by a Delta IV Heavy. As we need to insert the payload in the orbit about the Moon, an impulsive maneuver can be considered at the apogee of the trajectory. As this is a first order analysis and the solution is derived from the 2-body problem, the achieved results are not very accurate. Actually, to achieve a higher accuracy, a patched conic method should be used to combine the part of the trajectory in the sphere of influence of the Earth (but outside that of the Moon) and that inside the sphere of influence of the Moon.

However, from basic orbital mechanics, the velocity at the apogee of the lunar Hohmann transfer orbit is about 34 m/s (in the Earth inertial frame) whereas the velocity needed in a circular orbit at 100 km altitude around the Moon is about 1600 m/s (in the Moon inertial frame). Therefore, the spacecraft is in a hyperbolic trajectory in the Moon inertial frame and a burn is needed to have a lunar orbit insertion. The ΔV needed is about 1570 m/s. This leads to a propellant mass of about 2200 kg if an I_{sp} of about 472 s is considered. In addition, propellant mass for a plane change has to be accounted for since the arrival orbit about the Moon will not be a polar orbit that has been used for the other transfer methods. Therefore, the payload mass in LLO would be about 3.5-4 tons. This result, obtained with a direct ascent into a lunar Hohmann transfer, is lower than the payload achieved with other transfer methods analyzed in [Zuccarelli, 2009] and proves that the direct ascent is less efficient than a strategy involving the use of a parking orbit about the Earth.

Eventually, the results obtained in this work can be used as input for a second assessment of the Earth-Moon transfer phase, whereas no results are directly interesting for [Boere, 2009]. Actually, the study of the second phase was performed by using reference payload masses from the launchers' user manuals. Therefore, by having payload masses larger than the reference ones, the results obtained in [Zuccarelli, 2009] can be refined.

Table 6.44: Vega: ΔV budgets and propellant masses needed for Earth-Moon transfer from each orbit inclination.

LEO orbit inclination	3 body transfer ΔV	3 body transfer propellant mass
[deg]	[m/s]	[kg]
5	6,820	2,661
28.7	4,584	2,184
51.6	4,688	2,078

Table 6.45: Payload masses available in low lunar orbit relative to Earth-Moon transfer method.

	High thrust transfer LLO payload mass	Low-thrust transfer LLO payload mass ($I_{sp} = 1000$ s)	Low-thrust transfer LLO payload mass ($I_{sp} = 1500$ s)	3 body transfer LLO payload mass
Launcher	[kg]	[kg]	[kg]	[kg]
Ariane 5	8,698	17,052	19,110	8,591
Proton M	5,027	16,406	18,386	9,885
Atlas V 552	9,163	17,152	19,222	9,634

6.8 Launch schedule for the lunar base mission

From the results obtained in this work and from [Zuccarelli, 2009], accounting for some rough assumptions for the landing phase, a schedule of the entire development of the lunar mission will be shown. The entire mission requires a huge effort that cannot be taken only by one space agency but that has to be shared between the international space community. It is a huge effort in terms of money and capabilities and the International Space Station experience has demonstrated that international cooperation is the best strategy to reach such a dream.

The schedule is presented in Table 6.46: the grouping of the expeditions is made by year and a crew expedition every two cargo launches is performed in order to assemble the base structure and mount the scientific equipment.

The first goal is to guarantee communication coverage on the Moon, for this reason the first launch will be used to put two satellites into a Halo orbit around the Lagrangian L_2 point. For this first launch the total payload mass is 0.8 tons, therefore the Vega will be used.

Then, the lunar base building phase can start. The modules will be brought directly to the base site, so that these massive structures do not have to be transported over large distances. However, no crew will be present when the lunar base parts are delivered due to safety considerations.

Initially, the base will be delivered and assembled. Then the emergency and the spaceport modules will be delivered and assembled. The last step of the building phase consists in delivering the rovers and the telescope.

When both the lunar base and the spaceport are completed, the construction phase ends and the operative phase begins. Astronauts will be sent for permanent residence. They will land on the spaceport and travel to the lunar base with the unpressurized rover, over a distance of about 10 km. The pressurized rover is needed for longer sortie. However, it is uncertain if this 6 tons rover (see Table 2.2) will be brought to the lunar base. Currently, it has not been designed yet. It is assumed that the lander is capable of staying 180 to 210 days on the lunar surface [NASA, 2005], meaning that the astronauts will replace each other after this period. Moreover, a cargo supply² per year of circa 8 tons is required, [Baker and Eichstadt, 2005]. It consists of water, oxygen, food, nitrogen, etc. That value does not take into account the mass of equipment that is needed when something on the base needs to be repaired or replaced due to a failure. This mass depends on the particular situation of the failure and will therefore not be taken into account for the normal

² http://www.nasa.gov/mission_pages/station/structure/isstodate.html

Table 6.46: Launch schedule for the lunar mission to settle a permanent base on the South Pole of the Moon.

Launch No.	Year	Cargo/Element(s)	Crew	Mass [ton]
1	2015	Communication satellites		
2	2015	Airlock module 1 base		5
3	2015	Supporting structure + shell module 1 base		3.7
4	2015		Crew expedition	
5	2015	Airlock module 2 base		5
6	2015	Supporting structure + shell module 2 base		3.7
7	2015		Crew expedition	
8	2015	Airlock module 3 base		5
9	2015	Supporting structure + shell module 3 base		3.7
10	2015		Crew expedition	
11	2015	Airlock module 4 base		5
12	2016	Supporting structure + shell module 4 base		3.7
13	2016		Crew expedition	
14	2016	Payload base		4
15	2016	Payload base		4
16	2016		Crew expedition	
17	2016	Payload base		4
18	2016	Payload base		4
19	2016		Crew expedition	
20	2016	Payload base		4
21	2016	Payload base		4
22	2017		Crew expedition	
23	2017	Payload base		4
24	2017	Payload base		4
25	2017		Crew expedition	
26	2017	Airlock emergency module		5
27	2017	Supporting structure + shell emergency module		3.7
28	2017		Crew expedition	
29	2017	Airlock spaceport module 1		5
30	2017	Supporting structure + shell spaceport module 1		3.7
31	2017		Crew expedition	
32	2017	Airlock spaceport module 2		5
33	2018	Supporting structure + shell spaceport module 2		3.7
34	2018		Crew expedition	
35	2018	Payload emergency module		3
36	2018	Payload emergency module		3.5
37	2018		Crew expedition	
38	2018	Payload spaceport module		3
39	2018	Payload spaceport module		3.5
40	2018		Crew expedition	
41	2018	Payload spaceport module		3
42	2018	Payload spaceport module		3.5
43	2018		Crew expedition	
44	2019	Unpressurized and cargo rovers		0.7
45	2019	Pressurized rover		6
46	2019		Crew expedition	
47	2019	Telescope		1.2
48	2019		Crew expedition	

supply mass. For this reason another cargo supply of circa 4 tons per year can be assumed to cover these kind of problems.

Since the three launchers analyzed give payload masses that differ only by one ton from each other, all of them might be used. Two of them may be used for cargo launches while the third one for crew launches. Moreover, the schedule for the maintenance phase is presented in Table 6.47.

Table 6.47: Schedule for the maintenance phase of the base.

Launch No.	Year	Cargo/Element(s)	Crew	Mass [ton]
1	2020		Crew expedition	
2	2020	Supply		4
3	2020		Crew expedition	
4	2020	Supply		4
5	2020	Supply		4

Chapter 7

Conclusions and Recommendations

This chapter will present conclusions based on the results achieved during the research so far reported. Then recommendations for further improvements in the software and for the logistic strategy of the mission will be given.

7.1 Conclusions

1. *The Ariane 5 ESC-A performs better than the Atlas V 552 version by 1.4 tons and the Proton M by almost 2.4 tons, achieving a final payload mass of 25,420 kg.*

Actually, the Proton M has higher performances than the other two launchers but the azimuth constraints penalize it heavily during the optimization process. Table 7.1 shows the final payload mass obtained. Anyway, still the largest reference payload for a circular orbit at 185 km altitude is given by the Atlas V HLV, that, because of inefficiencies of the software used, was not optimized as well as the other vehicles. The Atlas V HLV is said to be able to deliver 28,660 kg in the aforementioned parking orbit.

Table 7.1: Best payload masses for the launchers. The solutions with an asterisk do not satisfy the path constraints or the orbital elements tolerances.

Optimization type	Proton M	Atlas V 552	Ariane 5 ESC-A
1D optimization	23,091	22,993	24,000
2D optimization	23,005	22,726	25,420
3D optimization	23,073*	24,141	19,150*

2. *The multi-objective optimizer DG-MOPSO equals or slightly outperforms the single-objective PSO optimizer.*

The performance of the algorithm may be mainly due to the double grid embedded. This double grid generated in the objectives space is used to keep track of the least and the most crowded areas. The double grid, that is composed of outer grids divided in inner grids, is meant to move the individuals to the less crowded ones in order to have a uniform distribution of solutions. It could be that this particular feature spreads the particles also in the least crowded areas where optimal solutions are difficult to be found. Table 7.1 proves that the optimal results are either equal to higher than those obtained with the single-objective PSO.

3. *Optimizations of the Vega ascent trajectory give payload masses higher than the user manual's reference.* This score is mainly due to the fact that less information about the path constraints are available with respect to other launchers. The vehicle did not have its maiden flight yet and the only known mechanical constraint is about the axial acceleration. More important constraints are needed, like

the dynamic pressure and the bending load, in order to assess correctly the real performances of the launcher. Anyway, with the assumptions made, the optimizations performed are very useful as they give an insight of the capabilities of the rocket.

4. *The RSS of the path constraints together with the payload mass as objectives does not perform as well as the RSS of the orbital elements and cannot be used as a measure of the goodness of the trajectory.*
As experienced in the two-objective optimizations, this objective does not improve the quality of the solutions found with the RSS of the orbital elements. Moreover, when the violations of path constraints are divided into two groups and used as objectives, there is an unbalance in the measure of the violation along one of the two groups. This is caused by the larger effect that the bending load has on the other and that appears to be the most difficult constraint to satisfy. On the other hand, this division, together with a single-optimization, helps in identifying the most difficult constraints to be satisfied by a certain launcher.
5. *The bending load, that is the most violated constraint, is the toughest one that a launcher has to cope with and affects the accuracy on the eccentricity.*
In the largest part of the runs, the bending load is the critical constraint that determine the goodness of a solution. Usually, it is violated more often with a good aerodynamic configuration (higher lift coefficients and lower drag coefficients) because launchers have higher velocities (due to lower drag). Moreover, this constraint also affects the accuracy on the eccentricity. In fact, a launcher, flying with a higher velocity, flies a steeper trajectory, in order to cope with the bending load and avoid high angles of attack. With respect to a worse aerodynamic configuration, it has a higher altitude when the guidance (using a bi-linear tangent law) becomes effective in steering the rocket itself towards the final orbit and, consequently, the accuracy on the eccentricity is not met.
6. *The angles of attack generated are quite high and expose the launchers' safety to risks.*
The high angles of attack are due to the fact that the gravity turn phase, flown by all the stage except the last one, is optimized in the neighbourhood of the reference trajectory. The reference phase is an ideal gravity turn that assumes pitch angles equal to the flight path ones. As the pitch angles are optimized at the nodes in which the phase is divided, in a range around the flight path angle, high angles of attack generate in those specific regions. This means that the optimizer is not always able find better values that can cope with the bending load constraint (as the angle of attack is involved).
7. *The Ascent Module software is not able to cope with engines in which a sharp reduction of the throttle level of the engine is used.*
There are some launch vehicles (e.g., Delta IV Heavy and Atlas V HLV) in which, to avoid high accelerations, the throttle level is changed rapidly and almost instantaneously. As the throttle profile is linearly interpolated between the optimal values found at the nodes selected by the user, the variation of the thrust along the trajectory is not sharp enough. The way this option is implemented does not permit to cope with high acceleration when the thrust becomes way higher than the weight of the vehicle. This is a discriminant for the vehicles that can be optimized.
8. *The coast arcs do not have shown any consistent increment of the performance in terms of payload.*
The implementation of the coast arcs between the stages theoretically should raise the altitude at which a launcher can get, by spending less propellant mass. On the other hand, it is true that at the end of the coast arc the velocity would be lower, therefore more time would be needed in order to reach the injection velocity.
9. *The application of constraints stricter than the real ones can help in finding better solutions not achievable by means of real constraints.*
It might be weird that this approach works but, in this very case, very good solutions (for Atlas V 552) were found applying stricter constraints that were violated but still within the original values. This case might mean that the optimizer is not good enough or the constraints handling method is not sufficiently good or adapt to the problem. On the other hand, relaxation of constraints might give better solutions than these since the evolution of the swarm tends to achieve the optimal points.

Table 7.2: Launch schedule for the lunar mission to settle a permanent base on the South Pole of the Moon.

Launch No.	Year	Cargo/Element(s)	Crew	Mass [ton]
1	2015	Communication satellites		
2	2015	Airlock module 1 base		5
3	2015	Supporting structure + shell module 1 base		3.7
4	2015		Crew expedition	
5	2015	Airlock module 2 base		5
6	2015	Supporting structure + shell module 2 base		3.7
7	2015		Crew expedition	
8	2015	Airlock module 3 base		5
9	2015	Supporting structure + shell module 3 base		3.7
10	2015		Crew expedition	
11	2015	Airlock module 4 base		5
12	2016	Supporting structure + shell module 4 base		3.7
13	2016		Crew expedition	
14	2016	Payload base		4
15	2016	Payload base		4
16	2016		Crew expedition	
17	2016	Payload base		4
18	2016	Payload base		4
19	2016		Crew expedition	
20	2016	Payload base		4
21	2016	Payload base		4
22	2017		Crew expedition	
23	2017	Payload base		4
24	2017	Payload base		4
25	2017		Crew expedition	
26	2017	Airlock emergency module		5
27	2017	Supporting structure + shell emergency module		3.7
28	2017		Crew expedition	
29	2017	Airlock spaceport module 1		5
30	2017	Supporting structure + shell spaceport module 1		3.7
31	2017		Crew expedition	
32	2017	Airlock spaceport module 2		5
33	2018	Supporting structure + shell spaceport module 2		3.7
34	2018		Crew expedition	
35	2018	Payload emergency module		3
36	2018	Payload emergency module		3.5
37	2018		Crew expedition	
38	2018	Payload spaceport module		3
39	2018	Payload spaceport module		3.5
40	2018		Crew expedition	
41	2018	Payload spaceport module		3
42	2018	Payload spaceport module		3.5
43	2018		Crew expedition	
44	2019	Unpressurized and cargo rovers		0.7
45	2019	Pressurized rover		6
46	2019		Crew expedition	
47	2019	Telescope		1.2
48	2019		Crew expedition	

10. *When using heuristic optimization methods, always remember that they do not guarantee the convergence of the solution. On the other hand, the application of huge populations might give a feeling of confidence and certainty in covering the search space.*

The higher the number of optimization variables the higher the volume of the search hyperspace that might be covered. However, one has to realize that there is a huge difference in covering a two-dimensional search space with a 100 particles and a 15 or 20-dimensional hyperspace with the same number of particles. The density of the particles should be increased as the dimensions of the search space increase, even if computational time is sacrificed.

Answering the research question

A thorough analysis of the ascent trajectories have been reported in this work. Several launch vehicles have been reviewed and their performances have been optimized. In addition, with the work presented in Zuccarelli [2009] and the first preliminary results (assuming realistic values for the I_{sp} of the propellant used) from Boere's work, a positive conclusion can be drawn about the mission to the Moon to build a lunar base: a 4 to 5 tons payload can be delivered on the lunar soil.

From the computations performed, and assuming a crew expedition on the Moon every two cargo expeditions in order to assemble the base, 4.5 years would be needed to build the base. However, a tight schedule should be followed for this to occur and no delays due to failures or other issues are permitted. As this is not possible to foresee, events not considered here, that would shift the date of delivery of the base, might occur. Moreover, this would be the ideal case in which no problems about funds from governments will present. A total of 48 launches should be accounted for, of which 16 are manned.

If the beginning of the whole mission occurs in 2015, the base would be ready before July 1, 2020. Anyway, space agencies should start planning right away further details of the mission, hardware and backup plans in order to meet the dates. Assessment of the base structure can be analyzed in more details by experts and the building of the first modules should start within a few years to meet the starting date.

Table 7.3: Schedule for the maintenance phase of the base.

Launch No.	Year	Cargo/Element(s)	Crew	Mass [ton]
1	2020		Crew expedition	
2	2020	Supply		4
3	2020		Crew expedition	
4	2020	Supply		4
5	2020	Supply		4

A schedule like the one presented in Table 7.2 does not take into account delays due to a failure in one of the phases of the mission. This scenario can have two implications:

1. The complete mission is delayed until the new module or payload is manufactured and ready to fly;
2. The launch schedule goes on by trying to anticipate the launches that should follow later on in the programme.

The first scenario would miss the deadline set by the requirements because a time period of about 1-1.5 years is needed to build a new module. The second scenario would imply that the modules scheduled for successive missions should be already available and the astronauts should be prepared and trained enough to be able to assemble it.

If the building phase is completed successfully, the operational phase would foresee a crew of three astronauts replaced every six months and 2 to 3 supplies expedition every year are needed as shown in Table 7.3.

From the manpower and economic point of view, such endeavour cannot be pursued and endorsed by any single space agency or government and yet international cooperation would be the best solution.

7.2 Recommendations

The Ascent Module software

- It would be better to think differently the structure of the software. Right now, the phases of the ascent are integrated one after the other in only one propagation. The new structure should have a propagation per phase where the integrator stops after each phase has been completed and starts again for the next phase. This approach in the structure permits to debug the code in a faster and more direct way, aiming for a more reliable software.
- Implementation of the thrust profile of booster or/and stages. If a launch vehicle has a given thrust profile, it does not make any sense to optimize that profile. The trajectory analysis and optimization should be as closely as possible to reality and this has to take into account real characteristics of the vehicle itself. Moreover, the optimization of the throttle level should include the ability to have bang-bang control of the same (that is the way the throttle is controlled in the Delta IV Heavy and Atlas V HLV).
- An adaptive grid could be implemented in which the position of the nodes is either optimized or decided by the user. This approach would also solve the problem of the instantaneous throttle variations.
- A constraint about the integrated heat flux should be introduced. This is needed in order not to expose the launcher to long flight time in the atmosphere. A long staying in the atmosphere leads to a high

heat flux accumulated on the structure that might damage more seriously the launcher than the peak heat flux.

- An analysis of the falling stages should be included in order to assess the risks that these have on populations and inhabited areas. The analysis shall be done by propagating the falling trajectory of the stages and this should be executed phase-wise (i.e., the entire falling phase is propagated in one go).
- The mass of the vehicle has to be included in the state vector (together with position and velocity) that is propagated. By excluding the mass from the state vector, the user is very likely to deal with a very complicated, tedious and exposed to errors code.
- The use of classes and objects shall be introduced in order to avoid global variables that easily lead to undesired errors.
- Use of ANSI C standard language has to be made. The experience with the software in the beginning of the programming phase has been a nightmare and a challenge at the same time. Some Integrated Development Environments (IDE) make use of their own compilers that inevitably deal in different ways with the code. The standards are available to give users as few mistakes as possible. However, the challenge consists in learning how to deal with these issues, which is not the purpose of a thesis work.

Optimizers/Optimization

- Assess other constraints-handling methods. The current method to handle path constraints uses a linear evaluation. However, other methods as quadratic (without letting the constraints to get higher values than the maximum limit), logarithmic and exponential can be evaluated for this specific problem.
- When a large number of optimization variables is used, a large number of population's particles should be used as well. This idea should have a higher efficiency in covering larger part of the search space. As this approach would increase further the computation time, use of parallelization can be made.

Lunar mission

- It is warmly suggested having the complete mission to be an international cooperation. Any other approach would be a too big effort and more likely to be a complete flop. Moreover, a more tight collaboration than that for ISS is needed as the project is more challenging and difficult than ISS itself.
- Even though the mission is feasible with existing launchers, a new, with a higher capability, vehicle is recommended. Even though the vehicle is not ready for the first launches, it might give a help and shorten the building phase or, in case of delays, can be helpful to catch up with the schedule.
- A manned vehicle is highly needed for the accomplishment of the whole mission. Right now, the only manned vehicle available is the Russian Soyuz that is not meant for lunar missions or landing. Anyway, a project¹ for a lunar version of the Soyuz has already been discussed, the Advanced Crew Transportation System. If this would be built, its mass would be higher than 7.2 tons for sure, that is the actual mass of the spacecraft, because there is need for landing structures and motors and other hardware. Assuming a mass of about 9 tons for the new spacecraft and a space tug of 20 tons (of which 3 tons is the weight of the structural mass), with the assumption about the I_{sp} , it would be possible to land about 5 tons on the Moon. This means that at least two launches are needed if an improved Soyuz is used with the use of a Earth-Orbit Rendezvous.
- The more suitable transfer method should be chosen according to the building phase schedule and the time of flight of the transfer itself. For the schedule sketched in Table 7.2, less space for the low thrust transfer is left because of the long time of flight in the order of months. The time of flight of the "3-body" transfer will still be longer than that of the high thrust one, therefore, for the very tight plan here reported the most suitable transfer method is this last one.

¹ http://www.russianspaceweb.com/soyuz_acts.html

Bibliography

- Anderson, J. D., 2001. Fundamentals of Aerodynamics, 3rd Edition. McGraw-Hill.
- Arianespace, 2006. Vega User's Manual. Arianespace.
- Arianespace, 2008. Ariane 5 User's manual. Issue 5, revision 0 Edition.
- ASTOS, 2007. Astos Model Reference Manual. Astos Solutions.
- Baker, J. D., Eichstadt, F., 2005. Commercial cargo transport service for iss. *Acta Astronautica* 57 (2-8), 257–265.
- Bhasin, K. B., Warner, J. D., Anderson, L. M., 2008. Lunar communication terminals for nasa exploration missions: Needs, operations concepts and architectures. 26th International Communications Satellite Systems Conference.
- Bodkin, D. K., Escalera, P., Bocam, K. J., 2006. A human lunar surface base and infrastructure solution. In: Space 2006.
- Boere, M., 2009. Base on lunar south pole, taking it one step further, literature study, Delft University of Technology.
- Brandhorst, H. W., Rodiek, J. A., O'Neill, M. J., Eskenazi, M. I., 2006. Ultralight, compact, deployable, high-performance solar concentrator array for lunar surface power. In: 4th International Energy Conversion Engineering Conference and Exhibit.
- Brusch, R. G., 1976. Trajectory optimization for the atlas/centaur launch vehicle. Conference on Decision and Control and Symposium on Adaptive Processes.
- Bryson, A. E. J., Ho, Y.-C., 1979. Applied Optimal Control. John Wiley and Sons Inc.
- Castellini, F., 2008a. Global optimization techniques in space mission design. Master's thesis, Politecnico di Milano.
- Castellini, F., 2008b. Sta ascent module verification and validation document. Tech. rep., ESA.
- Chang, K., 2010. Billions for nasa, with a push to find new ways into space.
URL <http://www.nytimes.com/2010/02/02/science/space/02nasa.html?ref=science>
- Chapman, D. R., 1959. An approximate analytical method for studying entry into planetary atmospheres. TR R-11, NASA.
- Chun, W., Brady, D., Conrad, K., 2006. Lunar surface mobility. In: Space 2006.
- Chung, H., Alonso, J. J., 2004. Multiobjective optimization using approximation model-based genetic algorithm. AIAA.
- Chung, M.-K. J., Weinstein, S. S., 2004. Trajectory design of lunar south pole-aitken basin sample return mission. In: AIAA/AAS Astrodynamics Specialist Conference and Exhibit.

- Coello Coello, C. A., Lechuga, M. S., 2002. Mopso: A proposal for multiple objective particle swarm optimization.
- Coello Coello, C. A., Toscano Pulido, G., Lechuga, M. S., 2004. Handling multiple objectives with particle swarm optimization. *Evolutionary Computation*.
- COESA, 1976. U.s. standard atmosphere. TM-X 74335, NASA.
- Cornelisse, J. W., Schoyer, H. F. R., Wakker, K. F., 1979. *Rocket Propulsion and Spaceflight Dynamics*. Pitman, London.
- Deb, K., Pratap, A., Agarwal, S., Meyarivan, T., 2000. A fast elitist multi-objective genetic algorithm: Nsga-ii. *IEEE Transactions on Evolutionary Computation* 6 (2).
- Duhamel, T., 1989. Re-entry and atmospheric transfer trajectories software. Met-ratt-ten-315, Matra Espace.
- Eberhart, R. C., Shi, Y., 2000. Comparing inertia weight and constriction factors in particle swarm optimization. *Evolutionary Computation* 1, 84-88.
- Fieldsend, J. E., 2004. Multi-objective particle swarm optimization ethods. Tech. rep., University of Exeter, Department of Computer Science.
- Fincannon, J., 2008. Characterization of lunar polar illumination from a power system perspective. In: 46th AIAA Aerospace Sciences Meeting and Exhibit.
- Fischer, H. M., 2005. Trajectory and orbital mechanics, ascent of Launchers, Orbits and Orbital Transfers. URL http://www.ieec.fcr.es/english/formacio/cva/apunts/H.M._Fisher/CVA_hfr_od1.pdf
- Gath, P. F., 1998. Improvements to a hybrid algorithm for rapid generation of 3-d optimal launch vehicle ascent trajectories. Master's thesis, Universitat Stuttgart.
- Gath, P. F., 2002. Camtos - a software suite combining direct and indirect trajectory optimization methods. Ph.D. thesis, Universität Stuttgart.
- Goldberg, D. E., 1989. *Genetic Algorithms in Search, Optimization, and Machine Learning*. Addison-Wesley Professional.
- Hall, C., 2003. Reference frames for spacecraft dynamics and control. URL <http://www.aoe.vt.edu/~cdhall/courses/aoe4140/refframes.pdf>
- Hamera, K., Mosher, T., Gefreh, M., Paul, R., Slavkin, L., Trojan, J., March 2008. An evolvable lunar communication and navigation constellation architecture. In: *Aerospace Conference, 2008 IEEE*.
- Hand, D. B., 2005. Integrated crew exploration and base assembly system for moon/mars/beyond missions. In: *1st Space Exploration Conference: Continuing the Voyage of Discovery*.
- Hill, K., Parker, J., Born, G. H., Demandante, N., 2006. A lunar l2 navigation, communication, and gravity mission. In: *AIAA/AAS Astrodynamics Specialist Conference and Exhibit*.
- Hofstetter, W. K., Wooster, P. D., Crawley, E. F., 2007. Analysis of human lunar outpost strategies and architectures analysis of human lunar outpost strategies and architectures analysis of human lunar outpost strategies and architectures. In: *AIAA Space 2007 Conference and Exposition*.
- Hoy, T. D., III, L. B. J., Persons, M. B., Wright, R. L., 1988. Conceptual analysis of a lunar base transportation system. *The Second Conference on Lunar Bases and Space Activities of the 21st Century*, NASA.
- ILCDOVER, 2008. <http://www.ilcdover.com/>. URL <http://www.ilcdover.com/>
- ILS, 2009. *Proton Launch System Mission Planner's Guide*. International Launch Services.

- Isakowitz, S. J., Hopkins, J., Hopkins, J. P. J., 2004. International Reference Guide to Space Launch Systems, 4th Edition. AIAA.
- Jansch, C., Schnepfer, K., Well, K. H., 1990. Ascent and descent trajectory optimization of ariane v/hermes. AGARD Preprints.
- Kemp, R., 2008. An introduction to genetic algorithm for neural networks.
URL http://www.msm.cam.ac.uk/phase-trans/2006/ga_html_files/ga.html
- Kennedy, J., Eberhart, R. C., 1995. Particle swarm optimization. In: Proceedings IEEE international conference on Neural Network.
- Knowles, J. D., Corne, D. W., 1999. The pareto archived evolution strategy: A new baseline algorithm for multiobjective optimisation. Proceedings of the 1999 Congress on Evolutionary Computation, Piscataway.
- Knowles, J. D., Corne, D. W., 2000. Approximating the non-dominated front using the pareto archived evolution strategy. Evolutionary Computation.
- Kolenkiewicz, R., Putney, W., 1965. Injection conditions for lunar trajectories. Tech. Rep. TM X-55390, NASA.
- Kosmann, W. J., Bocam, K. J., 2006. A recommended lunar exploration architecture. In: IAC.
- Larson, W. J., Wertz, J. R., 1999. Space Mission Analysis and Design. Microcosm Press.
- Lesieutre, D. J., Love, J. F., Dillenius, M. F. E., 1996. High angle of attack missile aerodynamics including rotational rates - program m3hax. AIAA 96-3392.
- Lockheed Martin, 1999. Atlas Launch System Mission Planner's Guide, Atlas V Addendum. International Launch Services.
- Lockheed Martin, 2007. Atlas Launch System Mission Planner's Guide. Lockheed Martin Corporation.
- Lu, P., Griffin, B. J., Dukeman, G. A., Chavez, F. R., 2008. Rapid optimal multiburn ascent planning and guidance. Journal of Guidance, Control and Dynamics 31 (6).
- Luke, R. A., 1993. Software design of 6dof guidance approximations in 3dof ascent simulations. Simulation.
- Malmstrom, R. W., Lo, A., Brown, N. S., Haney, G., 2006. Continuous communications to the moon's south pole. In: Space 2006.
- Mandl, F., 1988. Statistical Physics. Wiley and Sons.
- Markl, A. W., 2001. An initial guess generator for launch and reentry vehicle trajectory optimization. Master's thesis, Institut für Flugmechanik und Flugregelung der Universität Stuttgart.
- Michalewicz, Z., Arabas, J., 1994. Genetic algorithms for the 0/1 knapsack problem. Lecture Notes in Computer Science. Springer Berlin / Heidelberg.
- Mooij, E., 1997. The Motion of a Vehicle in a Planetary Atmosphere. Delft University Press.
- Mooij, E., 1998. Aerospace-plane flight dynamics, analysis of guidance and control concepts. Ph.D. thesis, Delft University of Technology.
- Moore, R. E., 1966. Interval Analysis. Prentice-Hall.
- Mosher, T. J., Kwong, J., 2004. Returning to the moon at a modest cost: The shackleton mission. In: Space 2004 Conference and Exhibit.
- NASA, 2005. Exploration systems architecture study. Tm-2005-214062, NASA.
- Nedjah, N. (Ed.), 2010. Multi-Objective Swarm Intelligent Systems. Springer.

- Nedjah, N., Mourelle, L. M. (Eds.), 2006. Swarm intelligent systems. Springer.
- NIMA, 1997. Department of defense world geodetic system 1984. TR 8350.2, NIMA.
- Noomen, R., 2008. Mission geometry and orbit design, lecture Notes, Delft University of Technology.
- Ortega, G., 2008. Sta mission for a moon base, eSA-ESTEC, The Netherlands.
- Pagano, A., 2008. Ascent trajectory for a lunar mission, literature study, Delft University of Technology.
- Palmer, G., Buning, P., Yanowitz, H., Venkatapathy, E., 1996. Three-dimensional computational analysis of complex launch vehicle configurations. *Journal of Spacecraft and Rockets* 33 (1).
- Paredes, E. S., Navarro, A., 2005. Some staging locations considered for lunar pre-positioning. In: *Space 2005*.
- Park, S.-Y., Vadali, S. R., 1998. Touch points in optimal ascent trajectories with first-order state inequality constraints. *Journal of Guidance, Control and Dynamics* 21 (4).
- Perkins, F. M., 1966. Derivation of linear-tangent steering laws. Tr-66-211, Aerospace Corporation.
- Regan, F. J., Anandakrishnan, S. M., 1993. Dynamics of Atmospheric Re-entry. AIAA.
- Reyes-Sierra, M., Coello Coello, C. A., 2006. Multi-objective particle swarm optimizers: A survey of the state-of-the-art. *International Journal of Computational Intelligence Research* 2 (3).
- Roberts, M., 1988. Inflatable habitation for the lunar base. LPI Contribution (652).
- Shampine, L., Watts, H., Davenport, S., 1976. Solving non-stiff ordinary differential equations - the state of the art. *SIAM Review* 18, 376-411.
- Shan, J., 2009. Dynamic of space vehicles.
URL <http://www.yorku.ca/jjshan/>
- Shi, Y., Eberhart, R. C., 1998. Modified particle swarm optimizer. In: *The 1998 IEEE International Conference on Evolutionary Computation*.
- Space Communication Architecture Working Group, 2004. Nasa space communication and navigation architecture recommendations for 2005-2030. Tech. rep., NASA.
- Sutherland, T., Cunio, P., Khan, Z., 2007. Lunar telescope facility, iDAC3 Results Presentation to the CxAWG.
- Tewari, A., 2006. Atmospheric and Space Flight Dynamics: Modeling and Simulation with MATLAB® and Simulink®. Indian Institute of Technology, Birkhäuser.
- Toscano Pulido, G., Coello Coello, C. A., 2004. A constraint-handling mechanism for particle swarm optimization. *Evolutionary Computation*.
- Toups, L., Kennedy, K. J., 2008. Constellation architecture team-lunar habitation concepts. In: *AIAA Space 2008 Conference and Exposition*.
- Turner, M. J. L., 2001. *Rocket and Spacecraft Propulsion: Principles, Practice and New Developments*. Springer.
- ULA, 2007. Delta IV Payload Planners Guide. United Launch Alliance.
- Vallado, D. A., 2001. *Fundamentals of Astrodynamics and Applications*, 2nd Edition. Microcosm, Inc.
- Visser, H. G., 2007. Aircraft performance optimization. Delft University of Technology.
- Volpe, R., Udomkesmalee, G., 2009. Mobility and robotic systems.
URL <http://www-robotics.jpl.nasa.gov/index.cfm>

- Vukelich, S. R., Stoy, S. L., Burns, K. A., Castillo, J. A., Moore, M. E., 1988. Missile datcom, volume 1 - final report. Tech. rep., McDonnell Douglas Missile Systems Company.
- Wakker, K. F., 2007. *Astrodynamics I, Lecture Notes*. Delft University of Technology.
- Well, K. H., 2004. Neighbouring vehicle design for a two-stage launch vehicle. In: *Advanced Design Problems in Aerospace Engineering: Advanced Aerospace Systems*. Vol. 1. Springer US.
- Woytach, J. M., Zakrajsek, J. F., Oswald, F. B., McEntire, K. J., Hill, G. M., Abel, P., Eichenberg, D. J., Goodnight, T. W., Zakrajsek, J. J., McKissock, D. B., 2005. Exploration rover concepts and development challenges. Tm-2005-213555, NASA.
- Zandbergen, B. T. C., 2008. *Thermal rocket propulsion, Lecture Notes*. Delft University of Technology.
- Zipfel, P. H., 2007. *Modeling and Simulation of Aerospace Vehicle Dynamics*, 2nd Edition. AIAA.
- Zuccarelli, V., 2009. Earth-moon transfer orbits. Master's thesis, Delft University of Technology.

Appendix A

Aerodynamic data

Many problems have been encountered in finding and obtaining these data during the thesis work. Then, in order to proceed with the work, some assumptions had to be made to compute or apply the aerodynamic data taken from other launchers so that this study could be reliable. In the following sections, the assumptions, the codes, the approaches tried and followed are explained.

A.1 The Near's *M3HAX* code

At the very beginning of the study, the main idea was that to use some software that would have been able, given the dimensions and the shape of the launch vehicle, to compute and determine the aerodynamic characteristics (drag and lift coefficients) of the vehicle itself.

The attention was put on the code *M3HAX* developed by Near Inc. (further information can be found at <http://www.nearinc.com/>). This code, that is now named *MISL3*, is based on the equivalent angle of attack methodology and various experimental data bases to predict the longitudinal and lateral-directional aerodynamic characteristics of missiles at angle of attack up to 90° , [Lesieutre et al., 1996]. The equivalent angle of attack method has been developed by Nielson Engineering and Research Inc. (NEAR). The method assumes that:

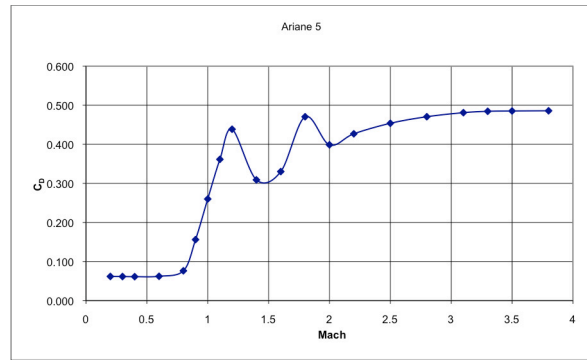
the panel loading for a given panel angle-of-attack is unique. With this method the panel angle of attack is computed including the effect of panel roll orientation with respect to the free stream velocity vector, panel proximity to the fuselage or to other panels, and external vortex flow field effects. Then the isolated panel characteristics are interpolated at the panel equivalent angle of attack to yield the panel load when mounted on a body in combination with other surfaces [Vukelich et al., 1988].

The simplicity of the software consists in the fact that giving the shape of the vehicle, that resemble that of a missile, and the conditions for which data are wanted, as angle of attacks and mach numbers, aerodynamic data are computed. Attention has to be put on the shape of the vehicles since these have to be modeled using simple geometrical shapes; therefore also the output data have to be handled carefully since they are valid for the simple geometric shape.

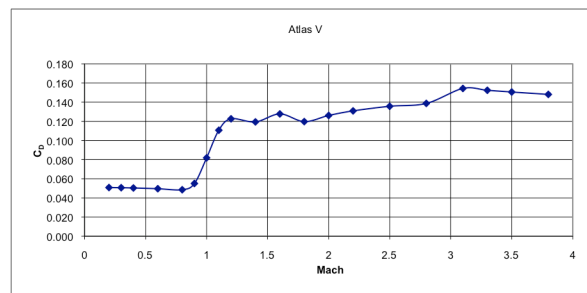
All the models created were processed for angles between 0° and 15° and between 0 and 3.8 Mach. The *M3HAX* code divides the body in segments on which the loads are computed including the effect due to free stream and nonuniform flow fields, [Lesieutre et al., 1996].

However, the results obtained from *M3HAX* were not completely satisfying. Although [Lesieutre et al., 1996] state that *M3HAX* predicts quite well body alone loads, the results obtained were not sufficiently reliable and doubts arose on whether to use them or not. The results obtained are showed in Fig. A.1, where only drag coefficient profiles for the central core of three launchers (Ariane 5, Atlas V and Delta IV Heavy) are depicted.

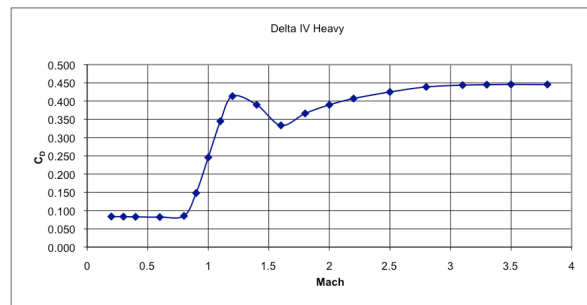
As Fig. A.1 shows, some details of the profiles look a bit strange at first glance. For instance, in the Ariane 5 profile (Fig. A.1a), a double peak can be seen: the first peak, as one might expect, is present right after the transonic speed ($M = 1$), but right after that, instead of a decreasing drag coefficient versus



(a) Ariane 5 drag coefficient profile.



(b) Atlas V drag coefficient profile.



(c) Delta IV Heavy drag coefficient profile.

Figure A.1: Drag coefficient versus Mach number profile computed using *M3HAX*.

Mach behaviour, a second peak is present and the drag coefficient keeps increasing as the number of Mach increases.

Something strange as well happens in the profile of the Atlas V and Delta IV Heavy (Fig. A.1b and A.1c). The drag coefficient profile has a peak in the transonic region but then keeps increasing for higher numbers of Mach (Atlas V) or decreases and then increases again for higher numbers of Mach (Delta IV Heavy).

Since the output obtained by the *M3HAX* did not resemble a typical drag coefficient profile, with the coefficients increasing in the transonic region and then decreasing and remaining almost constant at higher number of Mach, we decided not to make use of this code and the relative data.

A.2 Drag: Ariane 5 and the Dnepr profile assumptions

As we obtained a copy of the software ASTOS, from Astos Solutions (<http://www.astos.de/>), a drag coefficient profile for the Ariane 5 was available. Assuming that, with quite high probability, the profile is for 0° angle of attack, we have a basis on which build up some assumptions to extrapolate data for the other

launchers.

The same happened with the source code of STA AM that has been used for this work. The code, developed at ESA-ESTEC, was provided with an input file for the Dnepr launcher. In this case the aerodynamic data (drag and lift coefficients) for different angles of attack and Mach numbers were present.

Therefore the author has decided to build up the launchers' data by taking as reference those available from Ariane 5 and Dnepr and apply some assumptions that would have permitted to have reliable data to work with.

First of all, [Palmer et al., 1996] have drafted a table that specifies the contribution given by each part of the vehicle to the total drag of the same. The launch vehicle considered in this case is the Conestoga 1620 provided with six solid rocket motor strap-on boosters that surrounds the core motor. Scaling the Conestoga 1620 to the boosters-provided launchers (Ariane, Atlas and Delta) we obtain a table in which the contribution of the boosters, of the central core and of the structural components to the overall drag are given. Table A.1 has been obtained noticing that the contributions of the core motor and of the single booster are in the ratio 1:1. Furthermore, the Table A.1 applies to a vehicle provided with 2 boosters.

Table A.1: Launcher's components contribution to overall vehicle drag.

Component	Before boosters separation	After boosters separation
Core motor	26.6	100
Boosters	53.2	-
Structural components	20	-

From this table and by using the Ariane 5 profile, the drag coefficient profile for the same launcher can be derived for the core only. This procedure permits to have aerodynamics data for the Ariane 5 configuration right after the boosters' jettison.

In order to obtain also the drag coefficients for higher angles of attack, we assumed that the single drag coefficient, for the same mach number, increases linearly. The increment has been computed using the following procedure:

1. At each Mach number, the increase per degree is computed using the coefficients at at 0° and at 5° of angle of attack;
2. The increase per degree is then averaged over the Mach number range between 0.5 and 10;
3. This last value is then divided by the Dnepr reference area so that the coefficients can be scaled by the other launchers' reference areas and be applied to them.

The approach followed to obtain the data for the Atlas V, Atlas V HLV, Delta IV Heavy and Proton are similar to the previous one. First, the single drag coefficient has been divided according the contributions of the core, of the boosters and of the structures following Table A.1. Then, the values, for each Mach number, have been scaled using the reference area of Ariane 5's core and booster in order to have a drag coefficient profile per unit area of the single components. Next, for each launcher, the coefficients have been scaled up using the reference area of each element and summed up. Eventually, the linear increase has been applied to obtain profiles at different angles of attack and also profiles for the after-boosters-jettison configuration.

Concerning the Vega, since this launcher does not have any booster, approximately has a missile shape and its reference area is the same as the Dnepr's one, the same 0° angle of attack profile of drag coefficients has been assumed and then it has been computed also for higher angles.

A.3 Lift: USAF Missile DATCOM code

In 1981 McDonnell Douglas was asked to develop a code able to give a preliminary analysis of the aerodynamic forces and moments acting on a vehicle. Missile DATCOM can be compared to the aforementioned *M3HAX* code since it makes use of the same methodology described before, i.e., the equivalent angle of attack. The approach used in Missile DATCOM to compute forces and moments is the "component build-up": an

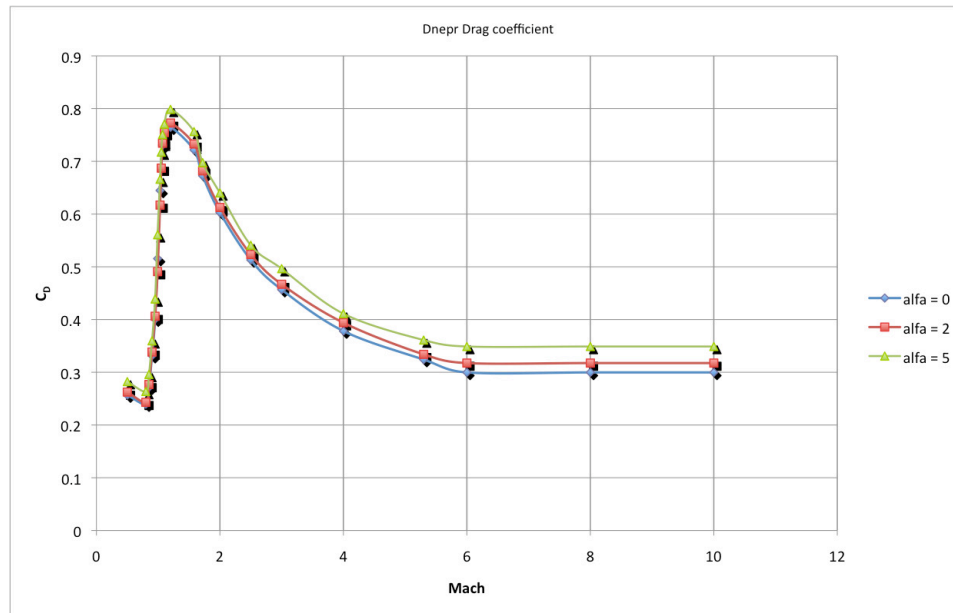


Figure A.2

estimation of the body and fin panels is made, then interference effects are summed to give the overall aerodynamics.

This software has been used to compute the lift coefficients of the launchers needed since it proved to give profiles more reliable than *M3HAX*'s ones, at least when comparing them with the lift coefficients of the Dnepr.

Therefore, the procedure followed to compute the lift coefficients for each launch vehicle is here described:

1. Create the model of the central core, with shape and dimensions, for each launcher and make Missile DATCOM compute the lift coefficients for angles of attack between 0° and 15° and between 0.2 and 3.2 Mach;
2. For each booster, the lift coefficients are considered to be the 60% of central core's ones and are scaled to the booster's reference area;
3. Boosters' coefficients are summed to the central core's ones.

Of course, for the after-boosters-jettison configuration, the central core coefficients only are used.

A.4 Sensitivity analysis

A sensitivity analysis of the model has been performed in order to understand in which measure drag and lift aerodynamic data affect the outcome of the trajectory simulation model.

Sensitivity analysis can be used by decision makers to give advices and suggestions to modellers. The decision makers are the users of the model created. In this sense, from the results obtained they might help the modellers to improve the model, or give them a better understanding of the system. Other purposes for which sensitivity analysis is used are: testing robustness of the model, identifying important variables, searching for errors in the model, simplifying the model or coping with the poor or missing data. The case considered here is the lack of data and the validity of the software. Poor data refers to the fact that, aerodynamic coefficients have been obtained from several assumptions that also might not be true because a particular aspect of the problem may be not known.

Lift

Concerning the lift, the contribution of one booster to the lift coefficient profile has been derived by assuming it equal to the 60% of the core only coefficient. Subsequently, it has been scaled with its reference area. Summarizing:

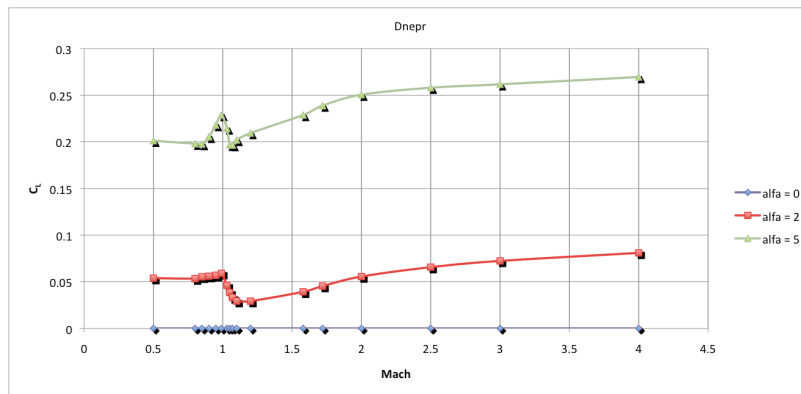
$$C_L = C_{L_{core}} + 0.6 \cdot C_{L_{core}} \cdot N_{booster} \cdot \frac{S_{booster}}{S_{core}} \quad (\text{A.1})$$

where $C_{L_{core}}$ is the lift coefficient computed by using Missile DATCOM.

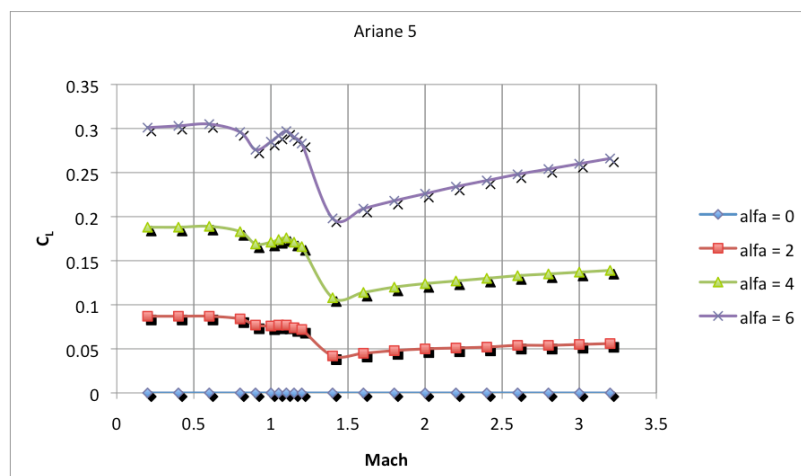
For this specific analysis, the lift coefficients of every launcher have been increased and decreased by $\pm 10\%$.

Drag

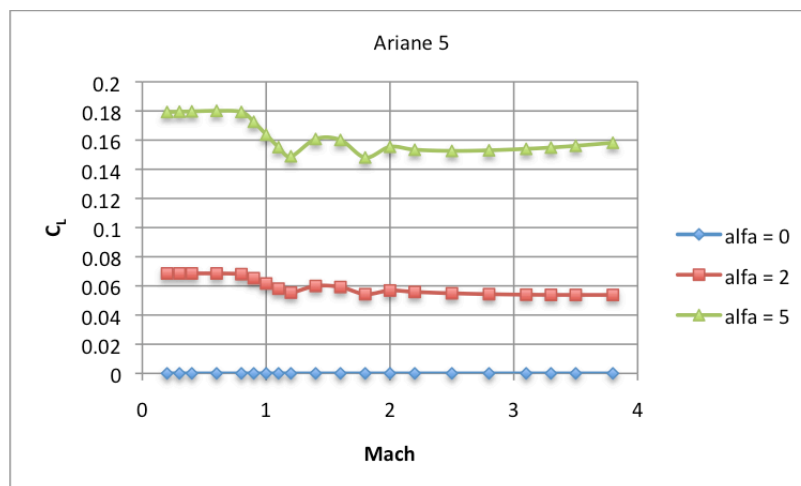
Concerning the drag and following the same approach used for the lift, the increase, computed from the Dnepr to obtain profiles at higher angles of attack, has been varied. The increase has been varied by $\pm 10\%$.



(a) Dnepr lift coefficient profiles.



(b) Ariane 5 lift coefficient profiles (Missile DATCOM).



(c) Ariane 5 lift coefficient profiles (*M3HAX*).

Figure A.3: Comparison of the lift coefficient profiles. For the Ariane 5, it only concerns the central core. Attention has to be paid on the behaviour of the profiles.

Appendix B

Launch vehicles data description and trajectory configuration settings

In this Appendix, a collection of data about the launchers used for the mission analysis is presented. Data concern about structural and propellant masses, rocket motors data and performances and dimensions. Moreover, for each launcher, also tables with the configuration settings (i.e., constraint limits, presence of coast arcs, circularization burn and final orbital elements) of the two and three-objectives optimizations are made available.

B.1 Vega

B.1.1 Property data

Table B.1 is a summary of data available in [Arianespace, 2006].

Table B.1: Vega characteristics. Vega launch vehicle system description (based on [Arianespace, 2006]).

	Stage 1	Stage 2	Stage 3	AVUM Upper Stage
Engine	P80FW	Zefiro 23	Zefiro 9	RD-869
Average Thrust	Sea level: 2,261 kN	Sea level: 1,196 kN	Vacuum: 225 kN	Vacuum: 2.45 kN
I_{sp}	Vacuum: 280 s	Vacuum: 289 s	Vacuum: 295 s	Vacuum: 315.5 s
Propellant mass	88.365 t	23.906 t	10.115 t	550 kg
Dry mass	7.431 t	1.845 t	833 kg	418 kg
Gross mass	95.796 t	25.751 t	10.948 t	968 kg
Fairing mass	490 kg			

B.2 Proton M

B.2.1 Property data

Table B.2 is a summary of Proton data taken from [ILS, 2009]. It has to be noted that the Proton M 4-stages (with Breeze upper stage) is used for payload being injected into GTO orbits.

Table B.2: Proton M characteristics. The performances of the stages are reported for the Proton launch vehicle (based on [Isakowitz et al., 2004]).

	Stage 1	Stage 2	Stage 3
Engine	RD-253 (6 engines)	RD-0210 (3 RD-465 and 1 RD-468) (4 engines)	RD-0212 (RD-473) (1 core engine + 1 vernier engine – 4 nozzles)
Average Thrust (total)	Sea level: 9.5 MN Vacuum: 10.5 MN	Vacuum: 2.39 MN	Vacuum: main: 583 kN Vernier total: 31 kN
I_{sp}	Sea level: 285 s Vacuum: 317 s	Vacuum: 327 s	Vacuum: 327 s
Propellant mass	419.4 t	156.1 t	46.6 t
Dry mass	31 t	11.7 t	4,185 kg
Gross mass	450 t	167.8 t	50.6 t

B.3 Atlas V 552

B.3.1 Property data

Concerning the Atlas V, the version 552 has been chosen since in the series 5 of the vehicle it is the most powerful. The second digit “5” indicated the number of boosters used and the last digit “2” indicates the number of engines in the Centaur upper stage (in this case is the Dual Engine Centaur, DEC).

Table B.3: Atlas V 552 characteristics. The performance for Atlas V 552 are reported (based on [Isakowitz et al., 2004]).

	Atlas V SRB	Atlas V – Stage 1	Centaur III – Stage 2
Engine	SRB (Aerojet) (5 boosters)	RD-180	RL10A-4-2 (2 engines)
Average Thrust	1,361 kN (per motor)	Sea level: 3,827 kN Vacuum: 4,152 kN	DEC: 198.4 kN
I_{sp}	Sea level: 245 s Vacuum 275 s	Sea level: 311.3 s Vacuum: 338 s	450.5 s
Propellant mass	42.5 t	284.1 t	20,830 kg
Dry mass	4,052 kg	20,743 kg	DEC: 2,106 kg
Gross mass	46.5 t	304.8 t	DEC: 22,936 kg
Fairing mass	4,394 Kg (long version, 26 m length)		

B.4 Ariane 5 ESC-A

B.4.1 Property data

Ariane 5 vehicle has been refined through the years and now the most powerful version is the ECA. This Ariane 5 makes use of the ESC-A upper stage (provided with HM7-B engine). In the last years, a new upper stage has been designed, the Vinci engine, that is able to provide a thrust of 180 kN against the 67 kN provided by the ESC-A. However, the development and testing of the new upper stage have been delayed and slowed down. Therefore, based on the readiness and reliability of the Ariane 5 ECA, this latter has been chosen (see Table B.4).

Table B.4: Ariane 5 ESC-A characteristics. The performances of the boosters, of the core stage and of the upper stage are reported (based on [Isakowitz et al., 2004]).

	EAP booster	EPC core stage	Cryogenic Upper Stage
Engine	P241 Ariane 5 ECA (2 boosters)	Vulcain 2 Ariane 5 ECA	ESC-A (HM7B)
Average Thrust	Vacuum: 6,470 kN (x2)	Sea level: 960 kN Vacuum: 1,390 kN	67 kN
I_{sp}	Sea level: 250 s Vacuum: 274.5 s	Sea level: 310 s Vacuum: 432 s	447 s
Propellant mass	240.2 t (x2)	172 t	14.9 t
Dry mass	40.3 t (x2)	14.7 t	4540 kg
Gross mass	280.5 t	186.7 t	19,440 kg
Fairing mass		2675 kg	

B.5 Delta IV Heavy

The Delta IV Heavy is an improved version of the Delta IV that makes use of strap-on boosters. The vehicle is a two-stage rocket with two boosters. During the ascent, the central core is throttled down to avoid too high accelerations and, when the boosters are jettisoned, its throttle level is brought back to 100%. Further details are reported in Table B.5.

Table B.5: Delta IV Heavy characteristics. (Based on [Isakowitz et al., 2004]).

	Common Booster Core Stage 1	Stage 2
Engine	RS-68 (Rocketdyne) (3 motors)	RL10B-2 (Pratt & Whitney)
Average Thrust	Sea level: 2,918 kN Vacuum: 3,312 kN (per motor)	110 kN
I_{sp}	Sea level: 365 s Vacuum: 410 s	462.4 s
Propellant mass	199.6 t	27,200 kg
Dry mass	26,760 kg	3,490 kg
Gross mass	226.4 t	30,710 kg

B.5.1 Property data

B.6 Atlas V HLV

B.6.1 Property data

The Atlas V HLV is a two-stage launcher with two strap-on boosters. The thrust of the central core is throttled down to avoid high acceleration, as in the Delta IV Heavy, and then throttled up when the boosters burn-out. A description of the vehicle is given in Table B.6.

Table B.6: Atlas V HLV characteristics. As one can see the boosters of Atlas V HLV use the same engine of the first stage (based on [Isakowitz et al., 2004]).

	Atlas V LRB	Atlas V – Stage 1	Centaur III Stage 2
Engine	RD-180 (Aerojet) (2 boosters)	RD-180	RL10A-4-2 (DEC: Dual Engine Centaur)
Average Thrust	Vacuum: 4,152 kN (per booster)	Sea level: 3,827 kN Vacuum: 4,152 kN	DEC: 198.4 kN
I_{sp}	338.4 s	Sea level: 311.3 s Vacuum: 338.4 s	450.5 s
Propellant mass	286.8 t	286.8 t	20,830 kg
Dry mass	21,902 kg	23,648 kg	DEC: 2,106 kg
Gross mass	308.7 t	310.4 t	DEC: 22,936 kg
Fairing mass		4,395 Kg	

Appendix C

Detailed results

C.1 Proton M

This section contains further results on the accuracies achieved in the runs for the one-objective optimization. Besides this, also path constraints and normalized path constraints are present.

C.1.1 Trajectories accuracy

The plots of the accuracies of the orbital elements are presented hereafter. A particular note is that a strict tolerance (i.e., 0.0001, in runs 7 to 9) on the final eccentricity produces more effect on the final inclination, violating it, than on the eccentricity itself (see Fig. C.3). This behaviour is strange since the inclination is influenced only by the azimuth, the latitude and the longitude and it should not have a correlation with the eccentricity. Anyway, an hypothesis is that the optimizer does not converge since it is not able to find solutions that satisfy the given tolerances but this has to be investigated further.

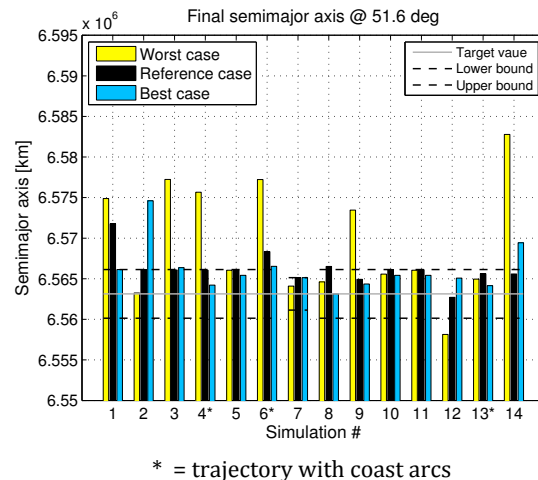


Figure C.1: Proton M: accuracy on the final semimajor axis.

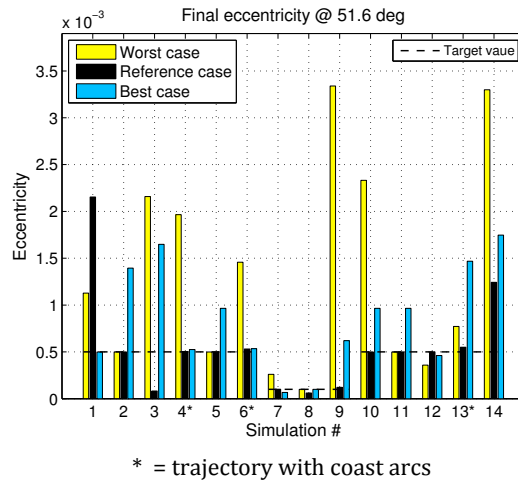


Figure C.2: Proton M: accuracy on the final eccentricity.

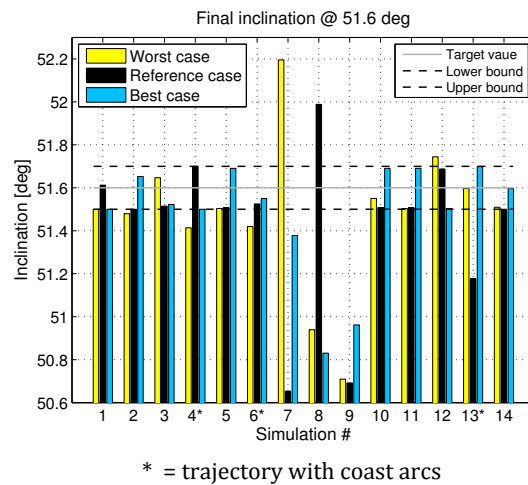


Figure C.3: Proton M: accuracy on the final inclination.

C.1.2 Path constraints violations

As it has been said in section 6.2, all the path constraints are satisfied but the bending load in some cases. However, this violation is mainly due to high angles of attack that arise especially in the gravity turn phase. Then, the effect of a constraint on this angle should be investigated further in the future.

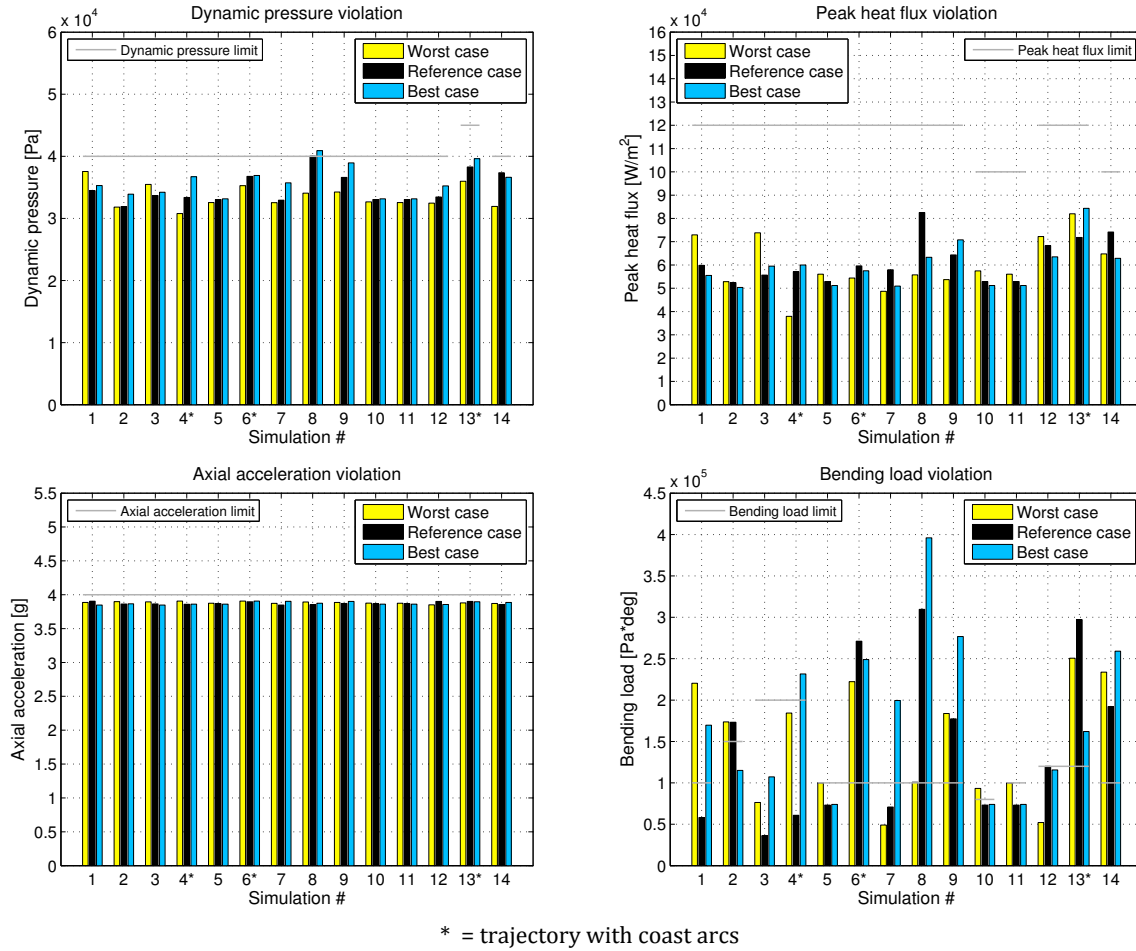


Figure C.4: Proton M: path constraint violations.

C.1.3 Normalized path constraints violations

From the plots of the normalized path constraints it is easier to see which constraint plays a major role and which is more difficult to satisfy. For the Proton M, the bending load has been the toughest constraint and, in some runs, it resulted to be also 3-4 times higher than the set limit. Such large violations would most likely destroy the structure of the launcher and it has to be avoided.

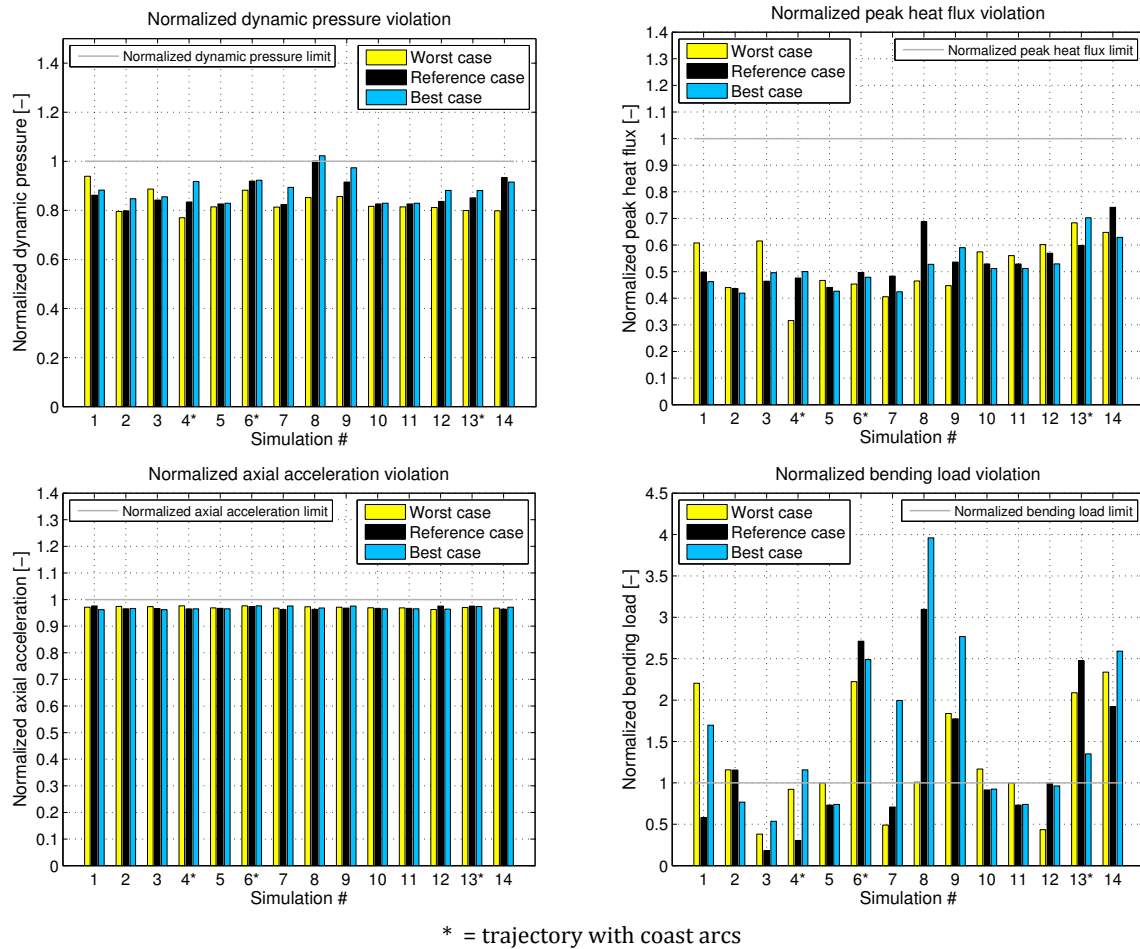


Figure C.5: Proton M: normalized path constraint violations.

C.1.4 Three-objective optimization: 3D view

The 3D view of the complete results of a three-objective optimization could give the user the ability to choose the solution that fits the best his design criteria. However, for a more complete and detailed overview of the results it is always advisable to filter or rank the matrix of the results with a software since it is easier and provide the real values that might not be clear from the plots.

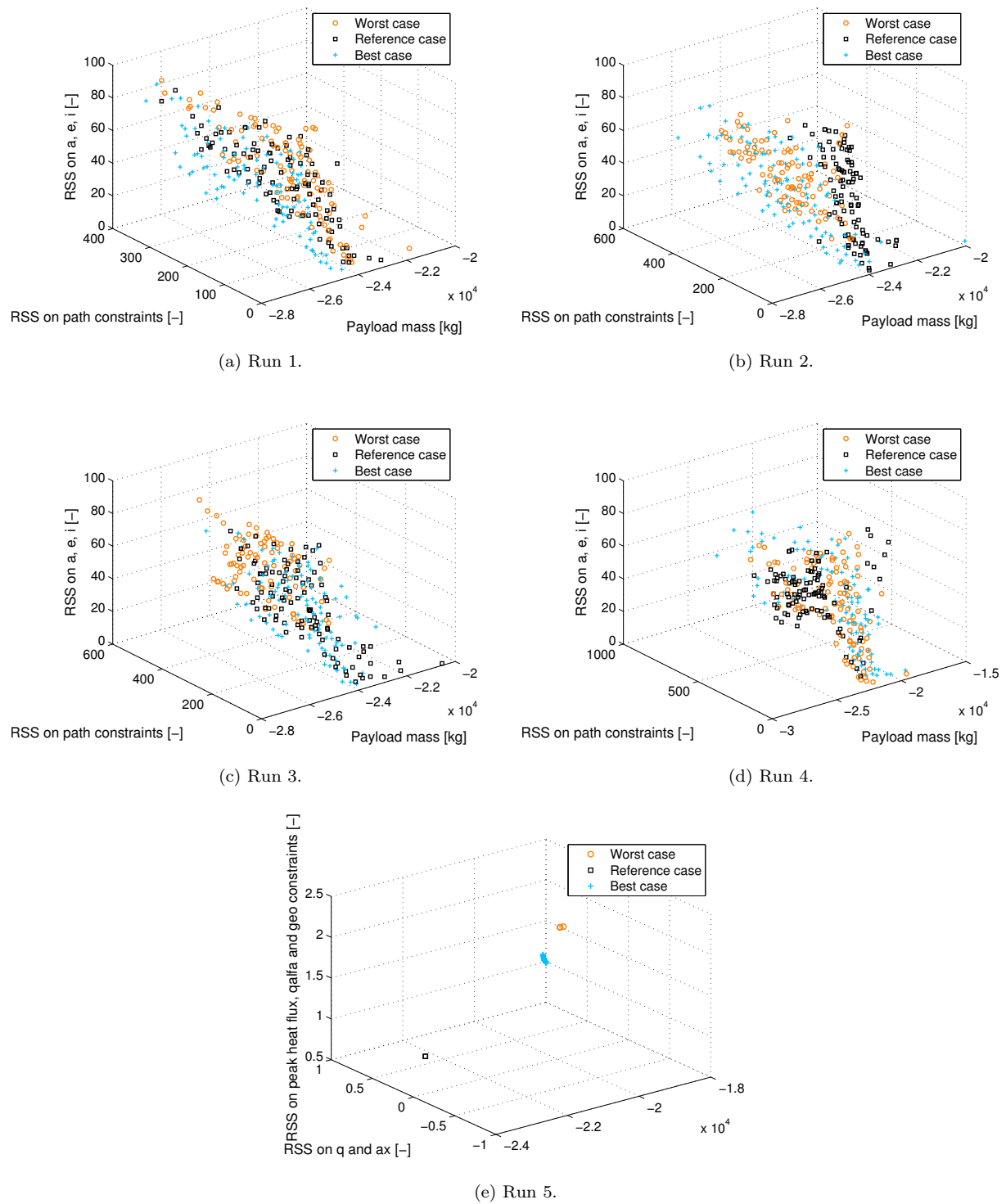


Figure C.6: Proton M: three-objective optimization 3D view.

C.2 Atlas V 552

C.2.1 Trajectories accuracy

The accuracies of the three orbital elements have been discussed in section 6.3.1 and the plots are reported here. It can be highlighted that in 75% of the cases in which the eccentricity tolerance is not respected, also the semimajor axis tolerance is not. The reason for this is that the launcher, while trying to reach the tolerance set on the eccentricity, at some point the set semimajor axis tolerance is satisfied, but not the one of eccentricity. Then, in order to satisfy the eccentricity tolerance, the vehicle keeps flying, but the semimajor axis is already out of its bounds. When this occur, the trajectory simulation is stopped giving an error on both elements.

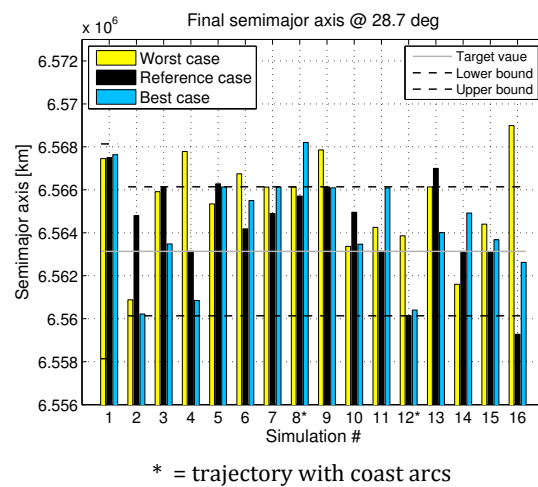


Figure C.7: Atlas V 552: accuracy on the final semimajor axis.

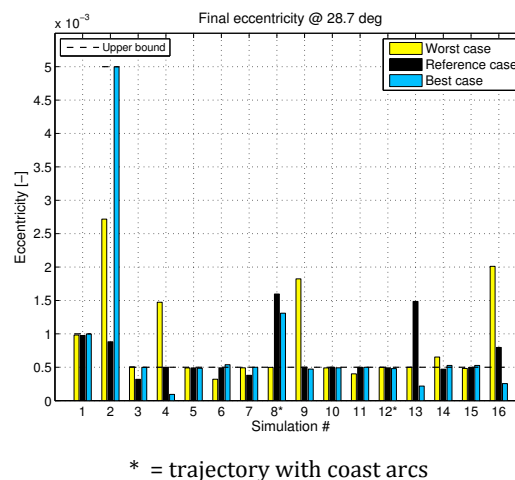
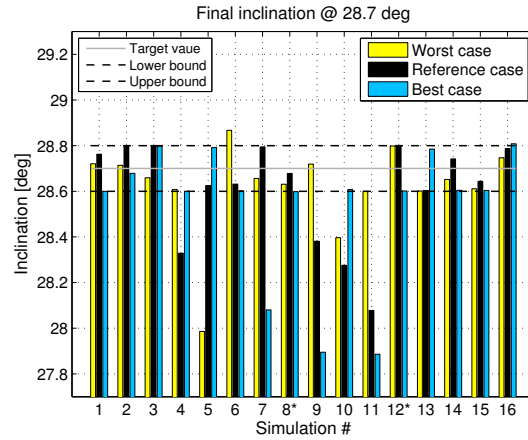


Figure C.8: Atlas V 552: accuracy on the final eccentricity.



* = trajectory with coast arcs

Figure C.9: Atlas V 552: accuracy on the final inclination.

C.2.2 Path constraints violations

The path constraints and their maximum values along the trajectories are depicted in this section. All the optimal trajectories that violate the eccentricity tolerance have also a violation in the dynamic pressure and bending load and this affects all configurations.

In most of the optimal trajectories, both violations of dynamic pressure and bending load occur. This behaviour can be due either to the too high dynamic pressure only or, when this is not violated, to the high angles of attack. The origin of higher angles of attack is due to the optimizer that is not able to find optimal control parameter for the pitch over phase. When this happens, the transition to the gravity turn is not smooth and high angles of attack (of about 10-15°) arise.

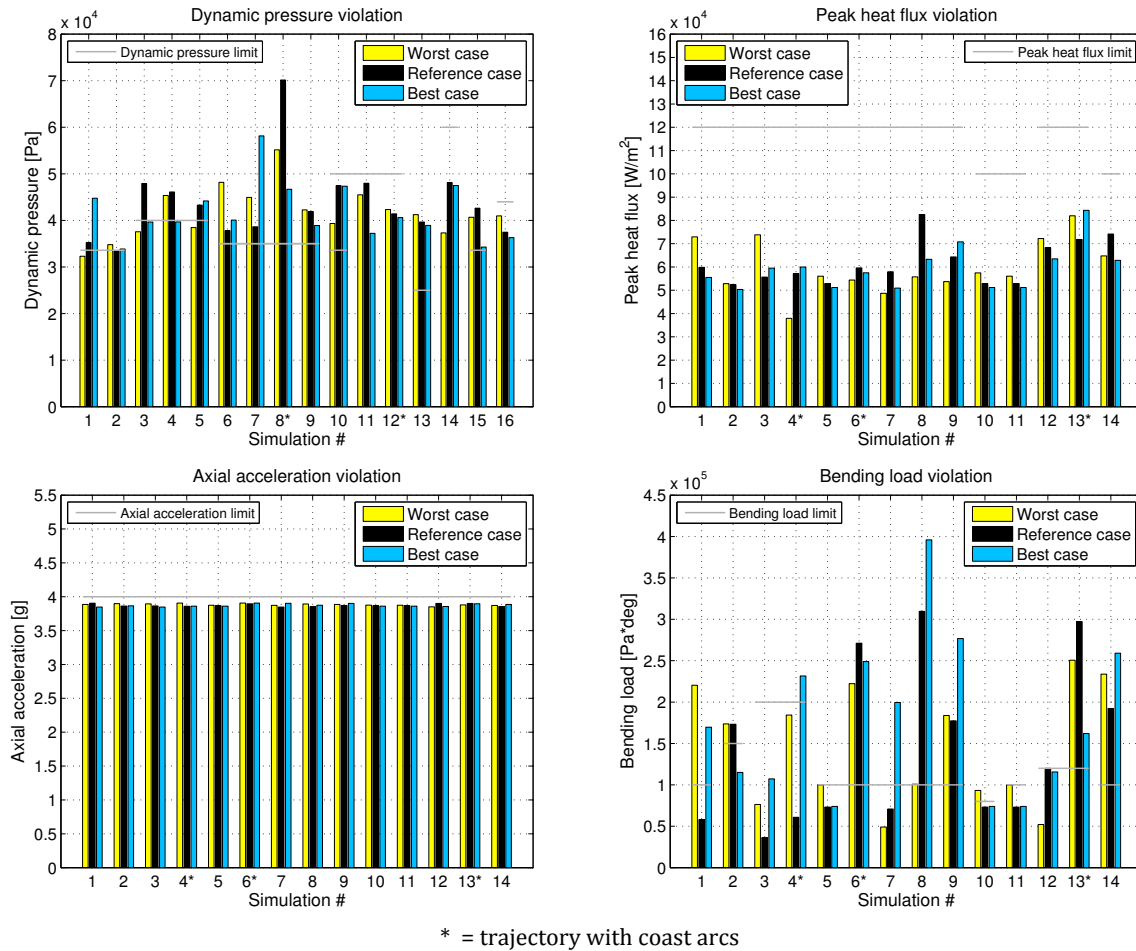
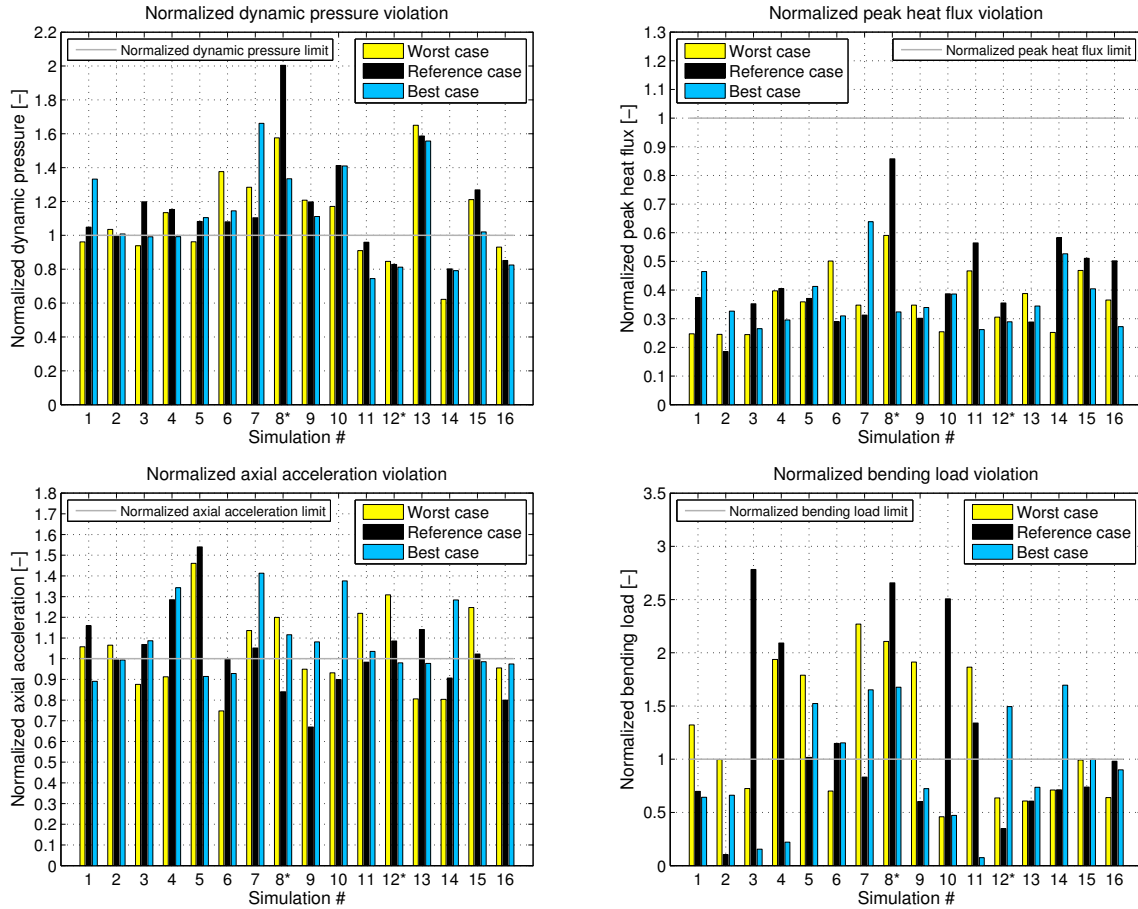


Figure C.10: Atlas V 552: path constraint violations.

C.2.3 Normalized path constraints violations

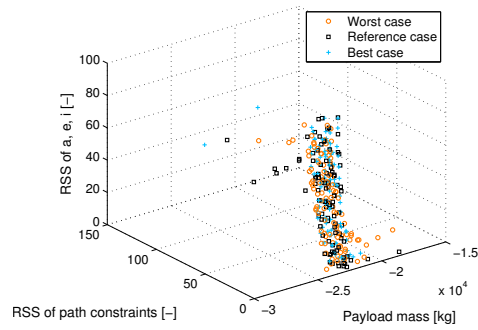
The plots of the normalized path constraints show which of them have a higher influence of the launcher. In this case, the axial acceleration, the bending load and also the dynamic pressure have a large effect on the trajectories. The axial acceleration violation is mainly due to the different strategy for throttle control in the real model and in the one used for this study. Concerning the bending load and the dynamic pressure, the first is due to high angles of attack and dynamic pressure values, whereas the second is violated as the real constraint value was only found late during the research.



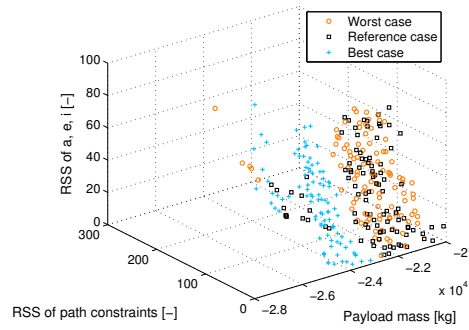
* = trajectory with coast arcs

Figure C.11: Atlas V 552: normalized path constraint violations.

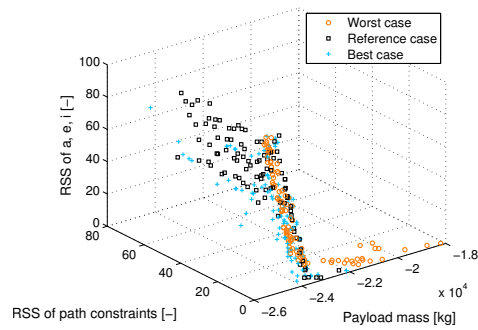
C.2.4 Three-objective optimization: 3D view



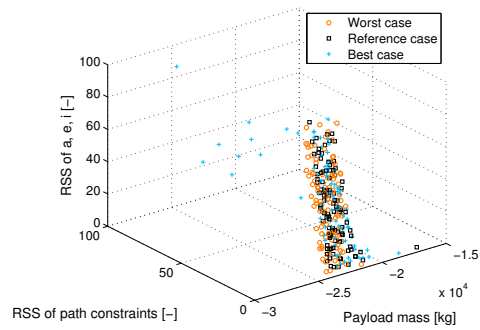
(a) Run 1.



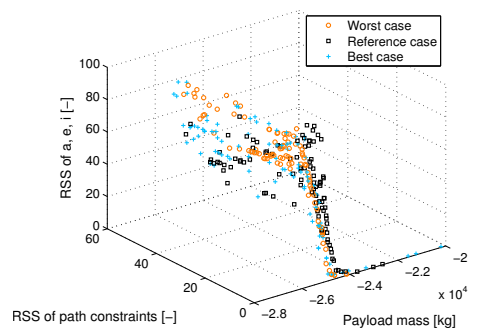
(b) Run 2.



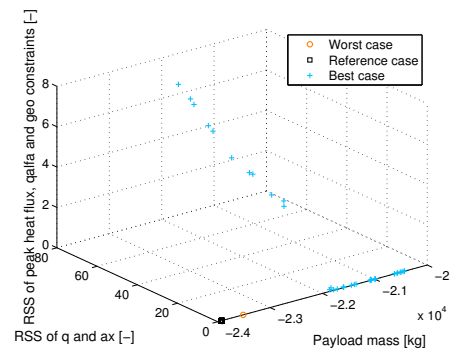
(c) Run 3.



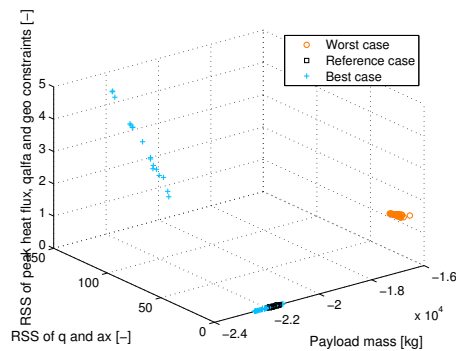
(d) Run 4.



(e) Run 5.



(f) Run 6.



(g) Run 7.

Figure C.12: Atlas V 552: three-objective optimization 3D view.

C.3 Ariane 5 ESC-A

C.3.1 Trajectories accuracy

For the Ariane 5 ESC-A, no violations of the semimajor axis and inclination occur, whereas only in 7 trajectories the eccentricity is violated.

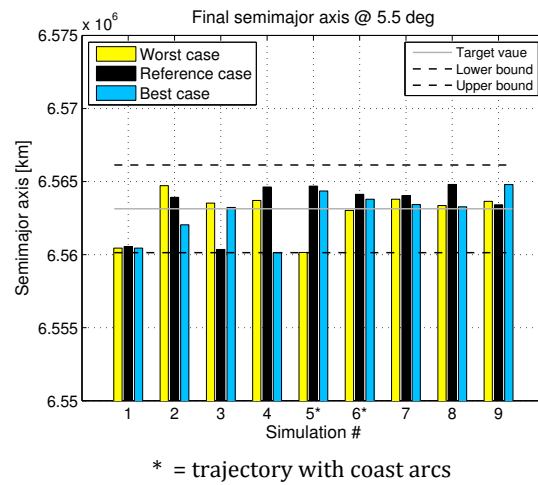


Figure C.13: Ariane 5: accuracy on the final semimajor axis.

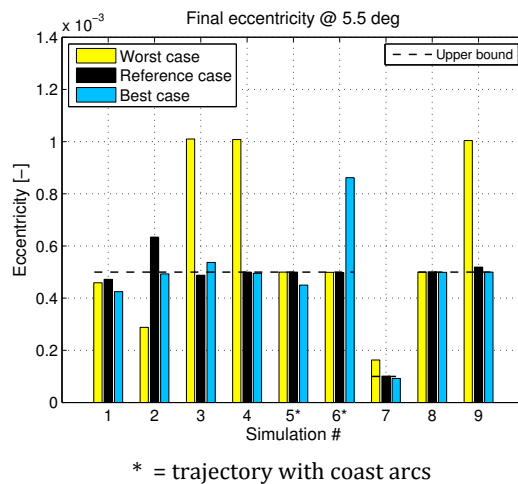


Figure C.14: Ariane 5: accuracy on the final eccentricity.

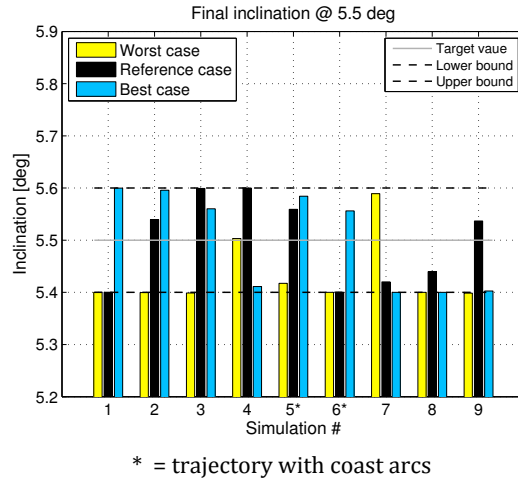
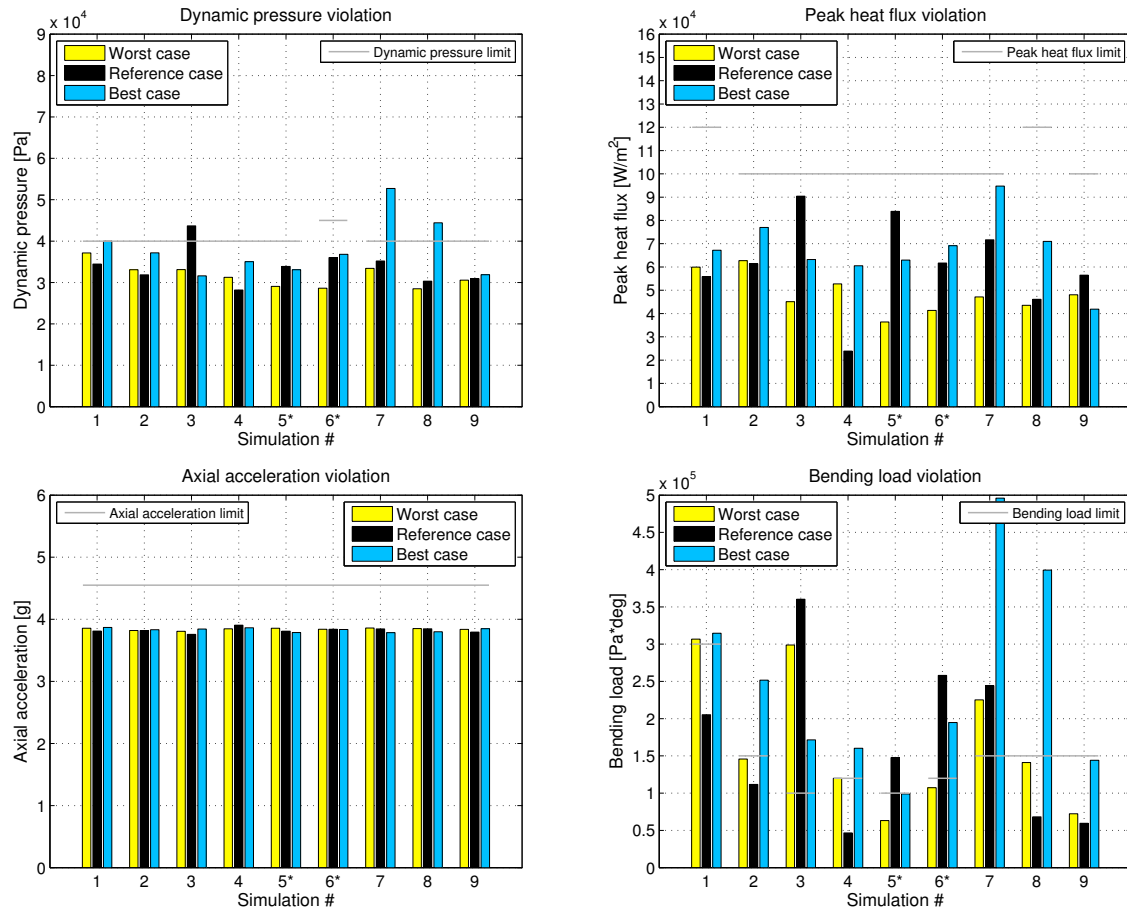


Figure C.15: Ariane 5: accuracy on the final inclination.

C.3.2 Path constraints violations

The Ariane 5 ESC-A copes with all the path constraints but one, the bending load, that is violated several time and in all the aerodynamic configurations.

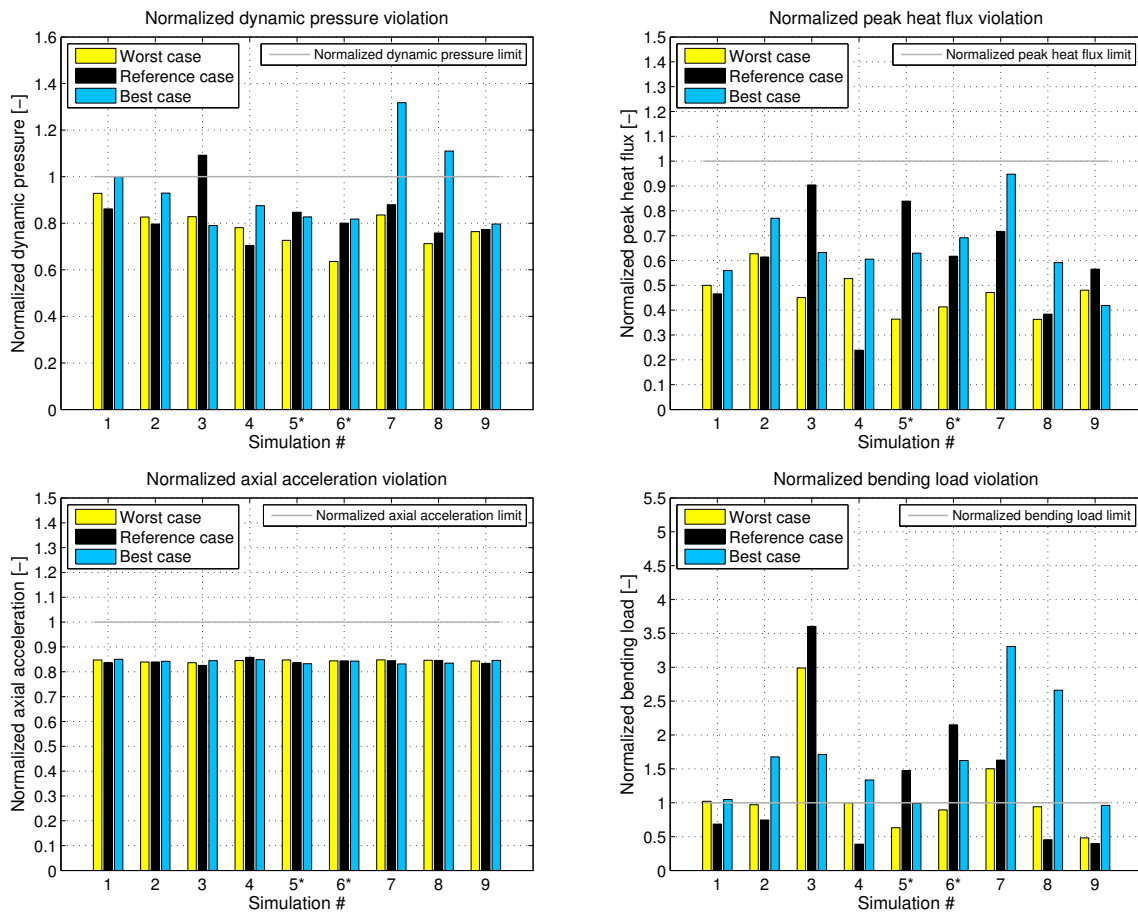
Between the three aerodynamic configurations, the best one, violates more often this constraint. That is related to the higher velocity, less drag and the fact that, maybe, non-optimal parameters for the pitch-over phase have been found. These three factors generate high dynamic pressure and high angles of attack that results in bending load violation. The range azimuth is also violated sometimes and mostly in those trajectories with bending load violations.



* = trajectory with coast arcs

Figure C.16: Ariane 5: path constraint violations.

C.3.3 Normalized path constraints violations



* = trajectory with coast arcs

Figure C.17: Ariane 5: normalized path constraint violations.

C.3.4 Three-objective optimization: 3D view

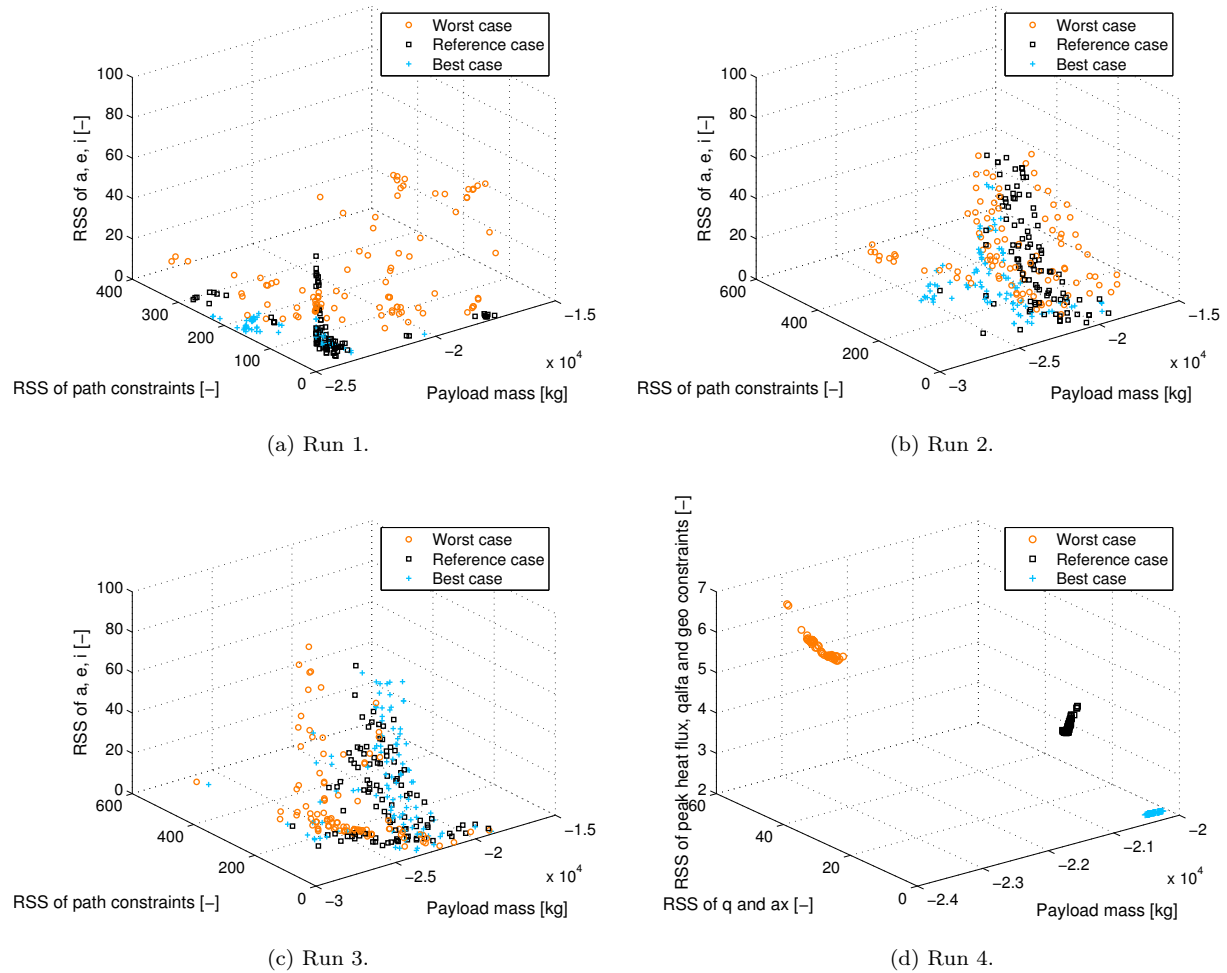


Figure C.18: Ariane 5: three-objective optimization 3D view.